TECHNISCHE UNIVERSITÄT WIEN

MONDRAGON UNIBERTSITATEA

Manufacturing

Co-funded by the European Union

ISTITUTO ITALIANO DI TECNOLOGIA

Master Thesis

Design and Development of Passive Folded-Beam Vibration Isolators for Robotic Reworking in the Automotive Sector

carried out for the purpose of obtaining a double-degree Master's within the EIT Manufacturing Master School, with partner universities Mondragon Unibertsitatea (MU), Arrasate-Mondragón, Spain, and Technische Universität Wien (TU Wien), Vienna, Austria, in collaboration with the Humanoids and Human Centered Mechatronics (HHCM) Laboratory at the Istituto Italiano di Tecnologia (IIT), Genoa, Italy.

Sai Sriram Duddu

TU Wien Mat.No.: 12329617 | MU Mat.No.: 45672

under the supervision of

Univ.-Prof. Dr.-Ing. Sebastian Schlund

Institute for Management Sciences, TU Wien

Prof. Dr. Eñaut Muxika Olasagasti

Faculty of Engineering, Mondragon Unibertsitatea (MU)

with research and funding support from

Dr. Nikos Tsagarakis

Tenured Senior Researcher & Principal Investigator,

Humanoids and Human Centered Mechatronics (HHCM) Laboratory,

Istituto Italiano di Tecnologia (IIT), Genova, Italy

Place and Date

Signature

Affidavit

I confirm that the printing of this thesis requires the approval of the examination board.

Design and Development of Passive Folded-Beam Vibration Isolators for Robotic Reworking in the Automotive Sector

I declare in lieu of oath that I wrote this thesis and carried out the associated research independently, using only the literature cited herein. Verbatim text passages from sources are marked as such.

I confirm that this work is original and has not been submitted for examination elsewhere, nor is it currently under consideration for a thesis elsewhere.

I acknowledge that the submitted work will be checked electronically using suitable state-of-the-art means (plagiarism-detection software). This serves to ensure that the submitted work was prepared in accordance with the high-quality standards and the Code of Conduct for Good Scientific Practice at TU Wien and, by comparison with other student theses, to prevent infringements of my personal copyright.

Place and Date

Signature

"Science is an impersonal study of the workings of nature. An understanding and deciphering of the mysterious alphabet written on the walls of nature makes one a scientist."

— Master E.K

To the lotus feet of the Master,
and with the blessings of my beloved parents …

Acknowledgements

It is often said that a student gains a quarter of his knowledge from his teachers, a quarter through his own intellect, a quarter through his colleagues, and a quarter with the passage of time by self-experience; thus, he learns from different sources and must consciously continue this process of learning throughout his life.

This statement truly reflects my journey through my Master's program, during which I am deeply indebted and sincerely thankful to everyone who supported and encouraged me, helping me come this far in this beautiful and life-changing experience.

Firstly, I would like to express my deep gratitude to the *EIT Manufacturing Master School (EITM)* for sponsoring the scholarship for this Robotics Dual Master's programme and for providing a platform that supported me throughout this three-year journey; the experience of discovering new places and cultures during my studies, together with the support on all documentation, made this path a joyful ride filled with cheerful moments and lasting memories.

Secondly, I feel truly honoured and grateful to have been taught by some of the best and most highly qualified academic lecturers and notable researchers during my first and second years of the Master's programme at *Mondragon Unibertsitatea* and *Technische Universität Wien (TU Wien)*, places that became my second homes and temples of enriched education and innovative research; within these communities I discovered not what to think but how to think, and beyond the academic journey I was able to discover my own character and way of being, learning as an individual all the necessary life lessons for which I am truly indebted to this opportunity.

In particular, I would like to thank **Prof. Dr. Eñaut Muxika Olasagasti** for believing in me from the very start of this Master's journey and for encouraging me in every aspect of my academic endeavours from day one until now; his support, guidance, and help have brought me to this stage, towards the completion of my Master's programme, and I am genuinely grateful for his advice during the course of my studies and, most importantly, for his patience, help, and support as my academic supervisor.

I would also like to thank **Prof. Dr. Sebastian Schlund** for his invaluable support and guidance in supervising this Master's thesis; his constructive and instructive feedback consistently set me back on track and enabled me to progress during my research, and I am genuinely grateful for the permission to pursue my internship and for the support he provided, under which my final year at TU Wien became a successful and fruitful experience.

I further wish to express my deep gratitude for the strong support and encouragement

provided by **Dr. Nikolaos Tsagarakis**, who offered me the platform and opportunity to prove myself by conducting my research internship and Master's thesis; because of him I was able to complete this thesis successfully and also become part of the EU project *MAGICIAN*, and under his esteemed guidance, mentorship, and support in the Humanoids and Human Centered Mechatronics laboratory at the *Istituto Italiano di Tecnologia (IIT)* I found what became my true home during the last year of my academic journey, an experience that words can scarcely capture, in a place I had only dreamt of—full of marvellous robotic and mechatronic equipment—which I believe to be one of the best hardware laboratories I have seen so far, and the opportunity and space to work there was indeed a dream come true; from day one he constantly guided me and provided feedback and suggestions that I regard as true gems for a young researcher, and in this place almost everything I had studied in theory came to life in practice, so that the motivation and support I received in every aspect are, in what this thesis has become, a testament to his guidance and to the help of my lab colleagues.

I am also grateful to **Mr. Lorenzo Baccelliere** for mentoring me in 3D CAD modelling and for sharing valuable academic and life advice that I will remember throughout my lifetime; without his feedback and instructions, the current design of the vibration isolators would not have been possible, and I am truly thankful for his generous support in proofreading my drawings.

Special thanks go to **Dr. Luca Muratore** and **Dr. Ioannis Sarakoglou** for their support on the software aspects and for providing the necessary force-torque sensor equipment and software licences to conduct my experiments, and finally, I would like to thank **Dr. Davide Torielli** for introducing me in depth to the necessary software and project details, whose patient support and cheerful nature always lifted me whenever I encountered hurdles during my time at IIT.

Apart from these proficient mentors, lecturers, and researchers, I am truly blessed to have been surrounded by a great community and enthusiastic people throughout my three-year European journey, to whom I am profoundly grateful.

With all these amazing people whom I have met, I learned something truly beneficial—not only about academia or research, but also about how to live, to be happy, and to remain cheerful—which I believe is the ultimate aspect of life, not merely to be understood but to be experienced in its beauty.

Abstract

This thesis presents the design, development, and validation of passive vibration isolators for robotic reworking operations in the automotive sector. Industrial robots are increasingly deployed to replace tedious, repetitive, and physically demanding finishing tasks traditionally performed by human workers, and several automation solutions already exist in this domain. However, most of these solutions give limited attention to vibration effects at the tool, even though such disturbances can reduce accuracy, degrade surface quality, and destabilise force control. This study addresses this gap by focusing specifically on vibration isolation at the end-effector level, proposing passive structural solutions to improve robotic finishing performance.

To establish the operating requirements, the vibration disturbances generated by a representative finishing tool were experimentally characterised using a six-axis force–torque sensor. This analysis identified the dominant frequency ranges that informed the design of the isolator.

Building on these findings, two passive vibration isolator concepts based on folded-beam flexures were developed: (i) a conventional folded-beam isolator and (ii) a novel Stewart-based folded-beam isolator, which represents a unique contribution of this work. Both designs were modelled, simulated, and optimised through modal and static analyses, then fabricated as metal prototypes. The prototypes were subsequently evaluated through bench-top vibration tests under realistic operating conditions.

The results show that both isolators effectively attenuate vibration disturbances, with the Stewart-based configuration demonstrating superior performance, particularly at higher operating speeds. These findings highlight the potential of robust, low-cost, and entirely passive structural isolators to enhance robotic finishing operations by reducing vibration effects. In doing so, they enable smoother tool operation, more stable force feedback, and improved surface quality in automotive reworking tasks.

Kurzfassung

Diese Dissertation präsentiert die Konzeption, Entwicklung und Validierung passiver Schwingungsisolatoren für robotergestützte Nachbearbeitungsprozesse im Automobilsektor. Industrieroboter werden zunehmend eingesetzt, um monotone, repetitive und physisch belastende Finishing-Aufgaben zu ersetzen, die traditionell von menschlichen Arbeitskräften durchgeführt wurden. Obwohl in diesem Bereich bereits zahlreiche Automatisierungslösungen existieren, berücksichtigen die meisten nur unzureichend die Schwingungseinflüsse am Werkzeug. Solche Störungen können jedoch die Genauigkeit verringern, die Oberflächenqualität beeinträchtigen und die Stabilität der Kraftregelung negativ beeinflussen. Diese Arbeit schließt diese Lücke, indem sie sich gezielt auf die Schwingungsisolation auf Endeffektorebene konzentriert und passive strukturelle Lösungen zur Verbesserung robotischer Finishing-Prozesse vorschlägt.

Zur Definition der Konstruktionsanforderungen wurden die von einem repräsentativen Finishing-Werkzeug erzeugten Schwingungsstörungen experimentell mithilfe eines sechsdimensionalen Kraft-Momenten-Sensors charakterisiert. Diese Analyse lieferte die dominanten Frequenzbereiche, die als Grundlage für die Isolatorauslegung dienten.

Aufbauend auf diesen Erkenntnissen wurden zwei passive Schwingungsisolator-Konzepte entwickelt, die auf Faltbalken-Flexuren basieren: (i) ein konventioneller Faltbalken-Isolator und (ii) ein neuartiger Stewart-basierter Faltbalken-Isolator, der einen originellen Beitrag dieser Arbeit darstellt. Beide Konzepte wurden mittels modaler und statischer Analysen modelliert, simuliert und optimiert und anschließend als Metallprototypen gefertigt. Die Prototypen wurden anschließend in praxisnahen Labortests auf ihre Schwingungsisolationseigenschaften untersucht.

Die Ergebnisse zeigen, dass beide Isolatoren Schwingungsstörungen wirksam dämpfen, wobei die Stewart-basierte Konfiguration insbesondere bei höheren Betriebsgeschwindigkeiten eine überlegene Leistung erbrachte. Diese Ergebnisse verdeutlichen das Potenzial robuster, kostengünstiger und vollständig passiver Strukturisolatoren zur Verbesserung robotischer Finishing-Prozesse, indem sie Schwingungseinflüsse reduzieren und so einen gleichmäßigeren Werkzeugbetrieb, stabileres Kraftfeedback sowie eine verbesserte Oberflächenqualität bei automobilen Nachbearbeitungsaufgaben ermöglichen.

Contents

1 Introduction and Motivation

In today's technological world, everything from smartphones in our pockets to the precision mechanisms in jet engines, secondary manufacturing processes play a pivotal role in transforming raw material shapes into valuable products that define our modern-day living. Nowhere is this more apparent than in the automobile sector, where secondary processes are essential for creating the complex, more reliable and visually appealing components and body parts that make up every vehicle. While primary manufacturing processes like stamping, casting provide the basic forms such as chassis, which act as a skeleton that provides the initial structure to panels, doors and bonnets, it is where the surface finishing operations, such as sanding, grinding and polishing, that give these parts the smoothness and a finished appearance demanded by both manufacturers and consumers. These finishing operations are used to remove minor surface imperfections, weld beads and tool marks, ensuring a uniform smooth finish, which is then painted [1]. This not only enhances the visual appearance but, more importantly, also improves the fit by enhancing corrosion resistance, resulting in better paint adhesion and overall vehicle durability. Thus, secondary manufacturing processes with surface finishing at the forefront are indispensable for transforming simple raw forms into the refined, safe, and high-performance components and devices integral to modern living.

1.1 Overview on Sanding, Grinding and Polishing Operations

Grinding : Grinding is a precision material removal process that utilises abrasive wheels or belts to shape and finish workpiece surfaces to tight tolerances. The grinding wheel consists of numerous abrasive grains, each functioning as a microscopic cutting tool. This process achieves high-dimensional accuracy and superior surface integrity, making it vital for components such as engine parts, bearings, and cutting tools [2].

Typical grinding operations include surface grinding for flat parts, cylindrical grinding for rotational components, and centerless grinding for high-throughput tasks. The process operates at higher cutting speeds compared to conventional machining, generating significant heat; thus, it requires coolant to prevent thermal damage. Material removal occurs primarily via microchip formation, analogous to turning or milling, but at a much finer scale [2]. The choice of abrasive—aluminium oxide, silicon carbide, cubic boron

nitride, or diamond—is determined by the workpiece material. Control of wheel speed, feed rate, and depth of cut is crucial to achieving a balance between material removal rate, surface finish, and workpiece integrity.

Sanding : Sanding is a surface finishing process that smooths and flattens workpiece surfaces using coated abrasives. It is essential for removing surface blemishes and preparing substrates for subsequent operations such as painting or coating [3]. Abrasives are bonded to paper, cloth, or mesh backings in a range of grit sizes from coarse to ultra-fine, enabling controlled refinement of surfaces.

Sanding can be performed manually with sandpaper or mechanically using belt, orbital, or drum sanders. In woodworking, sanding eliminates saw marks and provides a uniform finish. In metalworking and automotive contexts, it removes oxidation, rust, and paint, ensuring the proper blending of repairs. Optimal sanding employs a grit progression from coarse to fine, minimising surface scratches and imperfections. Cutting speeds typically range from 10 to $15\mathrm{m/s}$ [3], with platen pressure adjusted for effective abrasive belt utilisation.

Polishing : Polishing is a delicate finishing process employing sub-micron abrasives, often combined with liquids, to generate smooth, lustrous, or mirror-like surfaces. It is generally a “wet” process and may use soft pads or rotating wheels impregnated with abrasives.

This finishing process typically removes microscopic scratches and irregularities, enhancing both aesthetics and functional properties such as corrosion resistance and cleanability. It is crucial in industries requiring high surface integrity, including medical devices, optics, and automotive and aerospace components. Polishing can be performed manually or with machines; techniques include buffing, using flexible wheels, and lapping for extreme flatness. Typical wheel speeds reach $2300\,\mathrm{m/min}$, with grit sizes ranging from 20 to above 120, depending on the required finish. Pre-polished surfaces must be of high quality to ensure effective polishing. Material removal is minimal, often measured in microns, and polishing is commonly the final step in surface finishing [1].

In all these processes, abrasive materials with higher hardness are moved against the workpiece, generating frictional forces that affect material removal and surface refinement. The desired surface characteristics and the nature of the workpiece material dictate the selection of operation, abrasives, and process parameters. A general finishing process is illustrated in Figure 1.1.

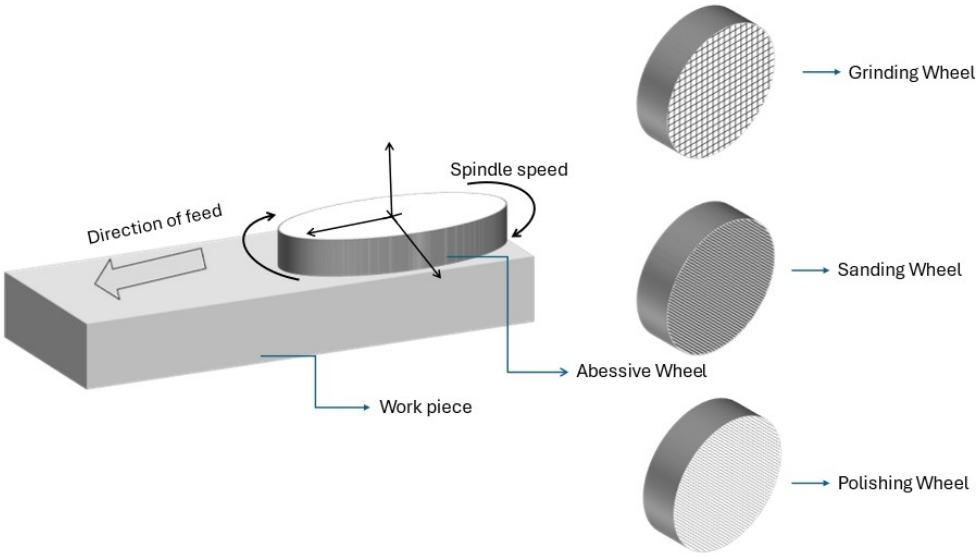

Figure 1.1: Schematic illustration of abrasive finishing processes.

1.2 Manual Operating Surface Finishing Tools and Equipment

Generally, most surface finishing operations, such as grinding, sanding, and polishing, are done manually with the help of a dedicated set of tools and equipment designed for specific operations. In Figure 1.2, there is a list of some of the essential tools that are used explicitly in the Automobile production lines, and most of these tools are rotary-based tools where a rotating disc with abrasive materials is made in contact with the workpiece. Even though there are some tools with reciprocating features, such as the Jitterbug sander and an orbital sander, which not only rotate around a fixed axis but also orbit because of their eccentricity, most of these tools are handheld. They are controlled manually by the experienced personnel on the shop floor.

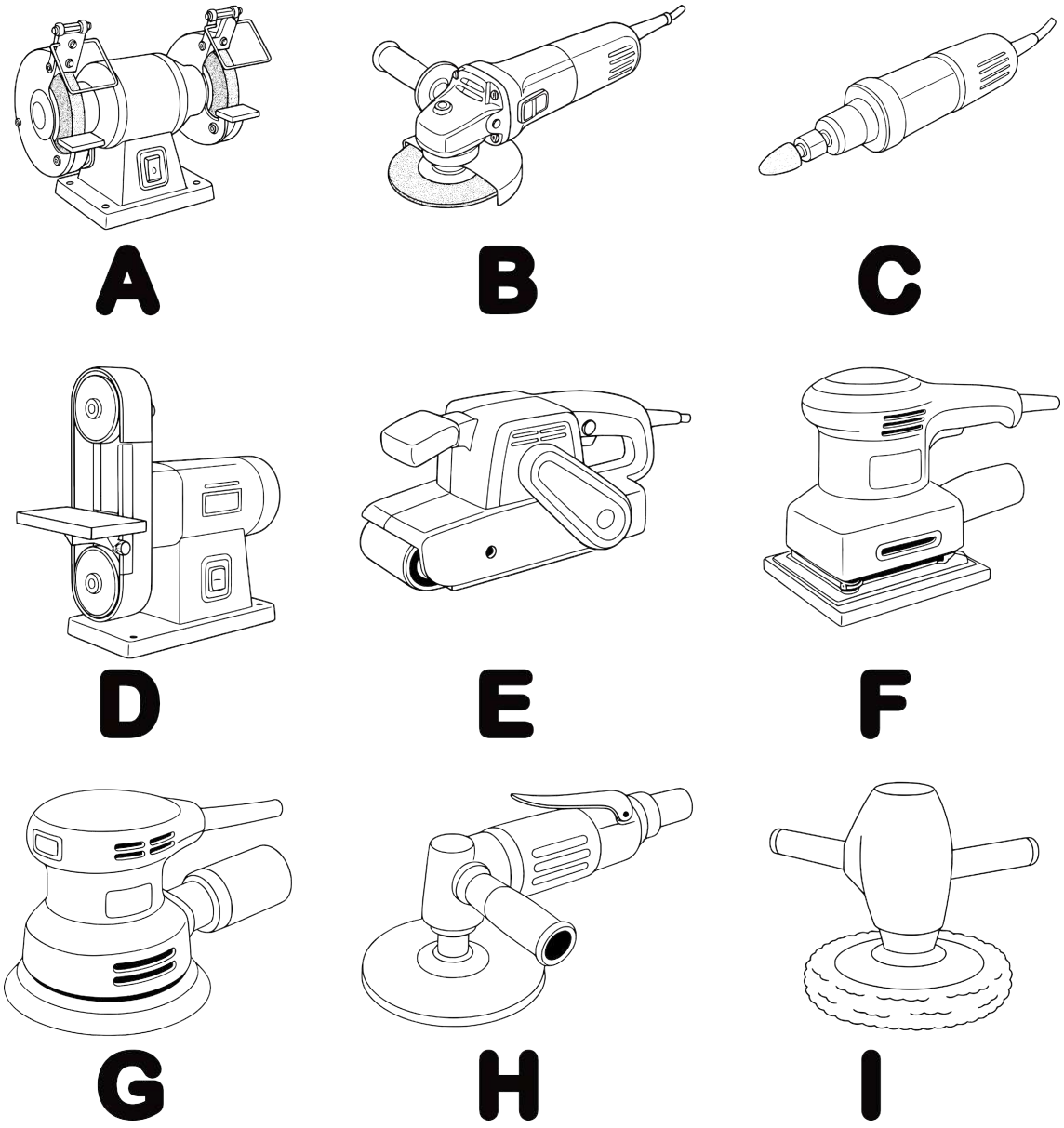

Figure 1.2: Few Important Surface Finishing Tools which are extensively used in Grinding, Sanding and Polishing operations. (a) Bench Grinder, (b) Angle Grinder, (c) Die Grinder, (d) Stationary Belt Sanding Machine, (e) Hand Sander, (f) Jitterbug Sander, (g) Orbital Sander, (h) Right Angle Sander, (i) Vertical Polisher.

1.3 Health Effects Caused by Manual Machining Operations

Most industrial workers engaged in manual handling for prolonged periods, or beyond prescribed safety limits, are likely to experience health issues. In the automobile sector, assembly line workers frequently use a range of tools to install components and body parts onto the car chassis. Among these, surface-finishing tools are heavily employed, and their operation generates undesirable vibrations.

These effects are often underestimated for smaller handheld tools, yet they can lead to adverse outcomes such as **hand–arm vibration syndrome**. Tools that typically produce substantial vibrations include rotary power tools—mainly orbital sanders and polishers—as well as reciprocating tools such as jitterbug sanders [4].

Hand–arm vibration refers to the oscillatory motion transmitted to a worker's hands and arms during the use of vibrating tools. In automotive manufacturing, handheld surface-finishing tools—such as grinders, polishers, and particularly sanders—are widely used on assembly lines for tasks including smoothing welds, sanding vehicle body panels, and polishing painted surfaces. Given that workers may operate these tools for extended hours per shift, hand–arm vibration exposure is a **significant occupational concern** in this industry.

1.3.1 Exposure Limits and Standards

International standards provide methodologies for evaluating and managing hand-arm vibration. **ISO 5349-1 and 5349-2** are key standards that describe how to measure vibration at the tool handle and calculate the daily exposure in m/s^2. **ISO 8041** defines the performance requirements for vibration measuring instruments to ensure accuracy [5]. Under this Directive, any power tool sold in Europe must be accompanied by declared vibration emission values measured under standardised conditions. These ISO and EN standards provide guidelines for both manufacturers and employers to assess vibration risks consistently.

The risk from a vibrating tool depends on its vibration magnitude, which is measured in m/s^2 and duration of exposure. Table 1.1 illustrates approximate safe exposure times before reaching the EU exposure limit (5 m/s² over an 8-hour workday), for different constant vibration magnitudes [6, 5].

Table 1.1: Vibration Emission Levels of Typical Automotive Assembly Tools - [6, 5]

Tool Type	Vibration Magnitude (m/s^2)	Typical Task Example
Pneumatic Orbital Sander	2 – 11	Paint prep, surface finishing
Pneumatic Angle Grinder	6 – 12	Weld removal, edge grinding
Electric Polisher	1.5 – 6	Paint polishing, buffing
Reciprocating File/Saw	4 – 8	Metal filing/cutting

1.3.2 Hand-Arm vibration Syndrome and Cumulative Trauma Health Effects

Chronic exposure to hand-arm vibration can lead to a collection of injuries known as **Hand-Arm Vibration Syndrome (HAVS)**. HAVS is a progressive condition encompassing damage to nerves, blood vessels, and other tissues in the hands and arms. Workers suffering from HAVS often report **pain, stiffness, and clumsiness** in their hands as shown in Figure 1.3. The condition adversely affects quality of life, with chronic pain and loss of hand function that can lead to anxiety, sleep disturbances, or depression in some cases. Indeed, research from [7] has shown that workers with HAVS have poorer self-reported mental health and physical functioning compared to the general population.

Figure 1.3: Hand-Arm Vibration Syndrome (HAVS) results from the use of handheld power tools [8]

In Europe, surveys indicate that roughly 1 in 5 workers (20%) are exposed to vibration

from tools or machinery for at least a quarter of their work time. A 2017 pan-European working conditions survey reported that about 20% of EU workers experienced such regular vibration exposure [9]. High-risk sectors include construction, manufacturing, mining, forestry, and agriculture, which are fields where vibrating handheld tools are commonly used.

1.3.3 Respiratory Risks from Dust Exposure

In addition to HAVS, workers involved in surface finishing operations also face several lung and respiratory diseases from inhaling dust and particulates. During these operations, a noxious cloud of fine dust composed of both the base metal and the abrasive particles, such as aluminium and chromium, was released [10]. These particle sizes vary with the material and grit, but often coarse dust tends to settle. In contrast, fine dust remains airborne longer. It can be inhaled deeply into the lungs, which causes chronic respiratory diseases like inflammation, pneumoconiosis and also **chronic obstructive pulmonary disease (COPD)**.

Epidemiological data in Europe show that occupational exposures to vapours, gases, dust, or fumes account for roughly 15% of COPD cases and about 15% of adult asthma cases [11]. Asthma is the most common work-related lung disease, with one European study attributing 1 in 7 severe asthma exacerbations to occupational exposure [11]. Overall, it's estimated that around 10% of all chronic respiratory disease deaths in the EU are due to occupational exposures, a significant portion of which comes from inhaling dust and particles in industries like manufacturing and autobody work [11].

1.4 Vibration Ranges of various Tools used in Manufacturing Sector

It is evident that vibrations generated by the tools ultimately lead to severe health problems. It has been evaluated from [4] that most of these tools do vibrate within a narrow frequency range between **35 Hz and 150 Hz**. Also, the dominant fundamental frequencies for each specific tool are summarised in the Table 1.2.

Here, the palm grip orbital sander was measured to have a higher frequency with respect to other tools. This is because of its structural design and the functionality, which will be discussed in detail later.

Table 1.2: Dominant Frequencies of Some of the Important Tools used in the Manufacturing Sector [4]

Tool Description	Frequency (Hz)
Hand grip orbital sander	90
Palm grip orbital sander	150
Right angle sander	45 / 80
Light-duty right-angle sander	70
Jitterbug sander	100
Vertical polisher	100

1.5 Foundation of the Study – Motivation

Surface finishing operations in the automotive industry, particularly sanding, are highly repetitive, physically demanding, and typically carried out in noisy and dusty environments. Traditionally performed manually, these tasks expose workers to adverse conditions such as Hand-Arm Vibration Syndrome (HAVS) and are often executed under strict time constraints. Such challenges highlight the need for innovative solutions that improve both efficiency and working conditions.

Automation, primarily through robotic arms, offers a promising alternative. However, despite existing research and commercial solutions, a key limitation remains unresolved: vibrations generated by general surface finishing tools. These vibrations not only degrade surface quality but also reduce the accuracy, efficiency, and durability of robotic arm performance. Without addressing this issue, the full potential of the robotic automated reworking process cannot be realised.

To overcome this limitation, this thesis proposes the design and development of a passive compliant end-effector specifically aimed at vibration isolation. The study outlines the reasoning behind this design, its operating principles, and its role in enhancing the effectiveness of robot reworking. By focusing on vibration mitigation—an aspect often overlooked in prior work—this research contributes a novel mechanical solution that improves process stability, adaptability, and automation outcomes in automotive reworking.

1.6 Research Question

This thesis addresses the following research questions:

Q1. How can the resonant frequency of a commercially available random orbital sanding tool be determined, along with its frequency ranges corresponding to different operating speeds?

Q2. What are the design challenges and constraints in developing a vibration isolator that is compact, lightweight, and incorporates minimal moving parts, enabling its integration into a robotic system while maintaining passive operation?

Q3. What are the challenges in optimising the design of a folded-beam vibration isolator to achieve an effective isolation range? Specifically, what is the optimal geometry that minimises transmitted vibration while maintaining structural integrity under loading, subject to constraints of frequency and mass, also simultaneously offering 6-DOF vibration isolation?

1.7 Outline of the Thesis

This current study is organised into eleven chapters, as illustrated in Figure 1.4.

The first part introduces the background and context of the work. Chapter 1 presents the motivation and objectives of the study. At the same time, Chapter 2 provides an overview of the EU project under which this research is carried out, including its scope and impact on the automotive sector. Chapter 3 reviews the current state of the art in robotic sanding and grinding, discussing existing approaches in both research and industrial contexts.

The preceding part focuses on vibration isolation. Chapter 4 presents a study of vibration isolation principles and relevant theoretical background, and Chapter 5 provides a vibration analysis of the sanding tool, supported by experimental testing.

The middle part of the thesis is dedicated to the design of the isolator system. Chapter 6 details the design of an initial tool mount interface, while Chapter 7 addresses the modelling of a vibration isolator unit element. Chapters 8 and 9 focus on the modelling

and design of folded-beam vibration isolators, beginning with a conventional approach and then introducing a novel folded-beam design. Both analytical modelling and computational tools, including Computer-Aided Design (CAD) and Finite Element Analysis (FEA), are employed.

The final part, presented in Chapter 10, covers the development of the isolator prototype and the experimental validation of different vibration isolation designs, including comparisons and refinements of the prototype. Chapter 11 concludes the thesis with a summary of findings and outlines future research directions.

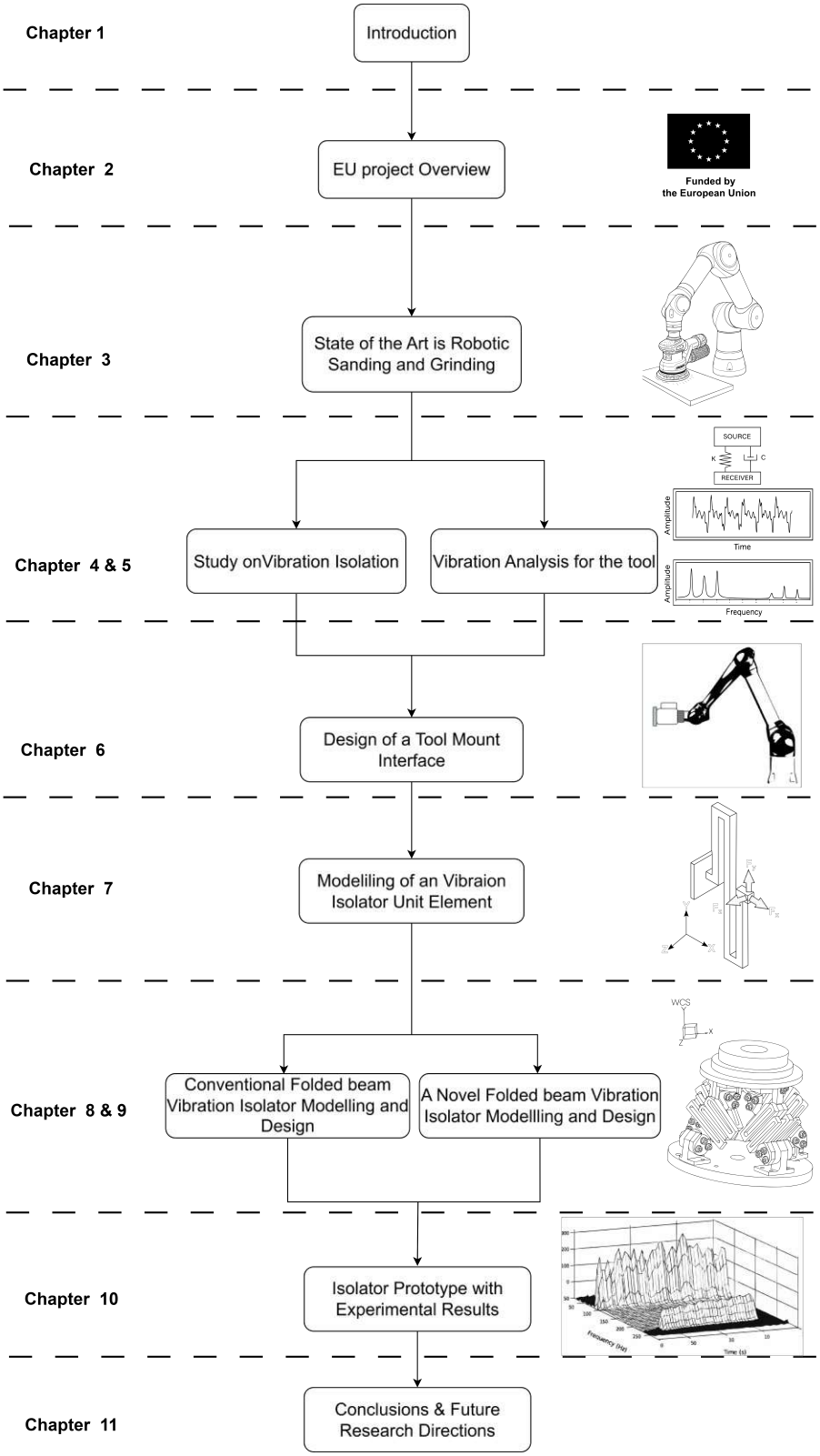

Figure 1.4: Thesis Outline

2 MAGICIAN – An EU Funded Project

In modern consumer markets, the aesthetic quality of products plays a critical role in shaping customer perception and acceptance. High-end luxury items as well as mid-range necessities, such as automobiles, are expected to be defect-free and visually appealing, particularly when they are in the direct sight of consumers. Consequently, stringent production standards are applied to ensure high surface quality. Especially in the automotive sector, achieving these standards often requires considerable physical effort from workers, who are tasked with addressing defects on car body parts, frequently under conditions that may compromise occupational health and safety.

The project **MAGICIAN (iMmersive leArninG for ImperfeCtion detectIon and repAir through human-robot interactioN)** [12] is taking on the challenges both in physical and mental ways for the skilled workers who are doing this dull repetitive rework job. To automate repetitive and demanding tasks while maintaining a safe and effective production time, this EU project promises to adopt a human-centred approach, enabling a sustainable transition towards human-robot collaboration in manufacturing based on trust and safety.

2.1 Workflow and Methodologies

The MAGICIAN project aims to bring a profound innovation in the manufacturing world, addressing the "improving human working conditions and satisfaction" use case. This Magician project proposed a robotic approach for autonomously detecting and reworking defects in semi-finished car body parts before they are sent for the final paint job process. Generally, in industry, this activity requires a skilled workforce that must inspect and rework defects within a defined time frame, which involves physically and cognitively demanding operations on manufacturing production lines.

Figure 2.1 better showcases the overall workflow steps which will be taking place in this phase. When a semi-finished car body is completed with its assembly, it then approaches the operation areas, and the operators make their first decision based on visual perception. If the defect is grossly evident, the classification can be made immediately. But in other cases, if the defect is observed from different viewpoints with special lighting, or when required, the defect is further inspected by touching and feeling the surface. This defect is classified by type, such as weld spatter, deformation, scratches, and dents, and also

based on their severity. In the next phase, another team plans and executes a sequence of rework operations by a sanding tool.

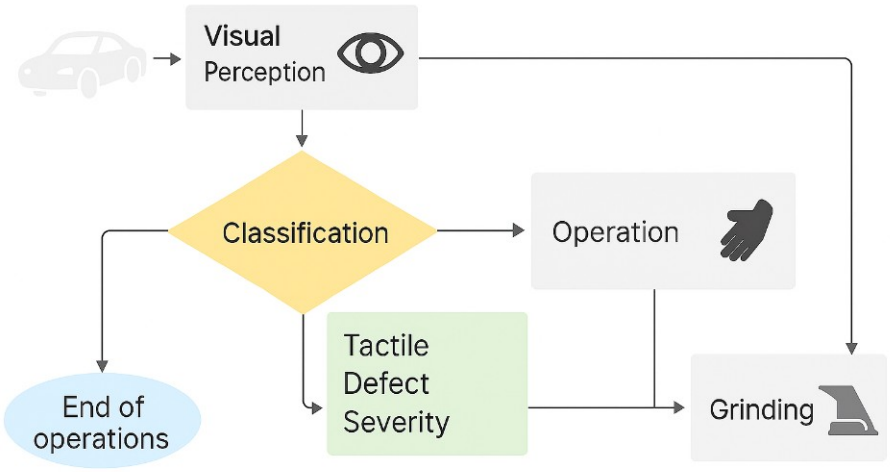

Figure 1: the human-based workflow

Figure 2.1: Human-Based Workflow for inspecting and addressing the defects.

With the Recent advancements in the domain of Artificial Intelligence (AI), which have paved the way toward human-centred approaches to the robotic automation of such operations. This Magician project aims to bring them to industrial maturity, for we will develop sensing technologies and methodological approaches to learn the human expertise in defect classification and reworking. Then, the development of advanced robotic technologies will enable us to replicate human operations with the required accuracy, thereby satisfying the timing constraints of the production process.

Some of the Methodologies for applying robotic technologies in defect reworking require a precise and clear understanding of how humans sense and classify defects, also what strategies they use to scan relatively large areas in search of minor defects and the way to excute the surface finishing operations along with this there is also a strict cycle time constratints duing the production process which requires an adequate prioritisation of the activities and optimisation of their sequence. To address this in the current project, there will be specifically two robotic solutions that will emerge, of which one is going to inspect the defects and analyse them, which we term as a **Sensing Robot (SR)** and the other to decide optimal reworking operations, which we termed as **Cleaning Robot (CR)**.

The SR and the CR can be used separately, with the humans remaining in charge of some of the activities, or in combination, with the CR operating on the defects identified by the SR[13]. In brief, these technologies will lead us to the following scenarios where

the car body reaches the station where SR thoroughly scans the entire body and applies markers related to the type of severity of the defect, so that in the next station, one or more CR's that remove the defects in the prescribed areas accordingly.

Lastly, this project adopts a **"Human-Centred Approach"** to understand problems from the point of view of the individual, the collective, and society, aiming to develop human-robot solutions that are desirable to use, safe, trustworthy, feasible to implement, and societally viable. Thus, the human perspective is thoroughly integrated into the development of the MAGICIAN, starting from the design of the system as a whole, down to the various interfaces between its components and human operators.

2.2 Current Research Objective and Outcomes

In the current study, we primarily consider the module of a cleaning robot by modelling and designing a sanding tool end effector for a commercial collaborative robotic arm, specifically the Doosan H2515 series, which will perform the task of reworking car body parts. Here is the main functional block for the robot-based defect reworking, as shown here in Figure 2.2.

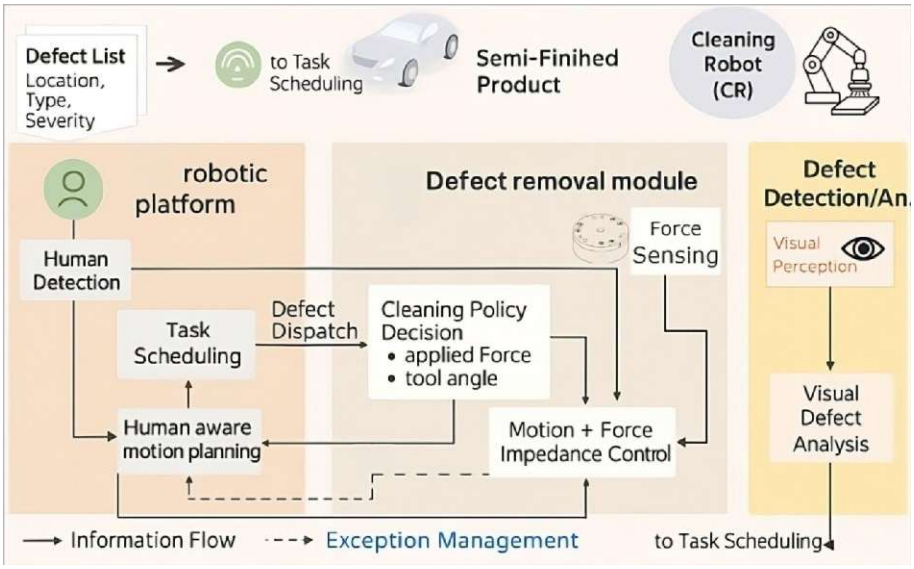

Figure 2.2: Cleaning Robot (CR) Framework for Defect Removal.

Here, when the semi-finished (Body in White) car body reaches the defect reworking work-station, each specific model comes along with an annotated list of defects that are obtained from the defect analysis. This list is processed by a task scheduling module, which then determines the optimal sequence of reworking operations to be executed by the robot. The robot is equipped with a specialised sanding tool end effector, featuring a

force torque sensor and a specialised vibration isolator, to perform these operations.

Whenever a defect is processed, it is dispatched to the Cleaning policy decision module, which, based on the defect type and severity, determines the operation parameters, including the tool angle, direction of motion, and the respective forces to be applied. This information is then passed to the human-aware motion planner, which determines the operation trajectories, taking into account the possible presence of humans in the near periphery. The controller module then approaches the operation area along the desired trajectory. During the operation phase, the controller controls motion and impedance. So when the task is completed, the defect is analysed by a camera module on the end effector to verify the correct reworking.

Mainly, during this study, we will concentrate on the Development and integration of a surface finishing tool with a customised end effector and its mounting clamp, along with a vibration absorption interface, which will be used to carry out reworking operations smoothly on car body parts. As concerns the end-effector design, our approach will be to develop specialised end-effector interfaces that permit the direct and robust mounting of a finishing tool while providing intrinsic features that accommodate the adaptation of the tool onto the car surface, while reducing at the same time the amount of chattering that affects the performance of the robotic system. To this aim, different vibration absorption or isolation components will be explored and integrated in the structure of the specialised end-effector interface.

So the CR, which is tested and piloted in this project will prevent workers form engaging in strenuous and hazardous tasks such as mechanical vibrations on the wrists and limbs along with decreased exposure to the fine metallic dust associated to the task of sanding these defects thus improving the safety and well being which in turn translate into a reduction of workers engaging in health hazardous activities.

2.3 Project's Impact on the Manufacturing Sector

The global market for manufacturing automation is experiencing rapid expansion. The robotics market was valued at USD 27.73 billion in 2020, projected to grow to USD 74.1 billion by 2026 [14]. Similarly, the defect detection in the manufacturing market is expected to increase from USD 3.5 billion in 2021 to USD 5.0 billion by 2026, driven by the need for automated quality control, adherence to health and safety regulations, and a shortage of skilled labor [15].

Advancements in defect detection systems, machine vision, and related technologies are key to improving production efficiency and consistency. Furthermore, the artificial

intelligence (AI) in the manufacturing sector is forecasted to rise from USD 2.3 billion in 2022 to USD 16.3 billion by 2027, reflecting growing integration of AI into industrial operations [16].

These trends are visually summarised in Figure2.3, illustrating the comparative market growth across the three segments.

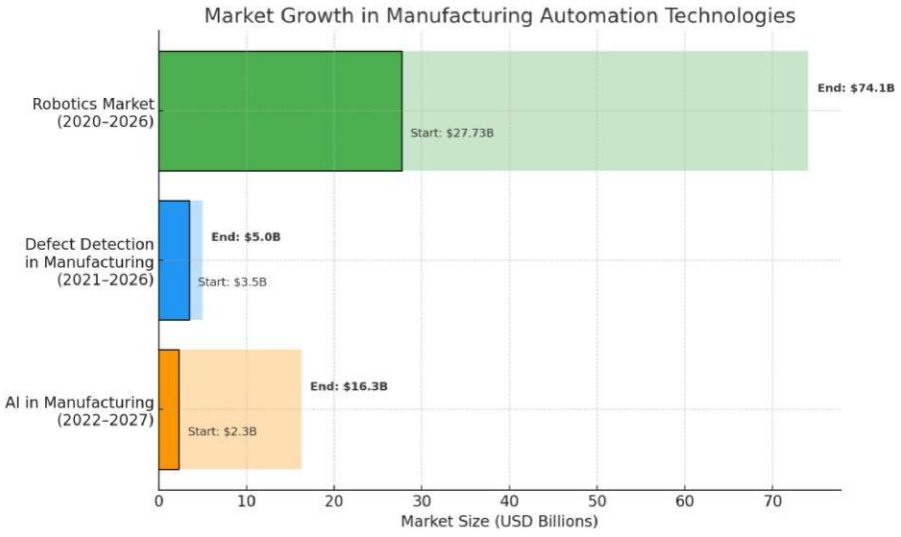

Figure 2.3: Market growth in three automation technology areas.

The MAGICIAN outcomes are expected to generate a significant impact in the above-mentioned automation areas by improving the working conditions of workers involved in non-ergonomic, physically strenuous, and hazardous activities. With the integration of autonomous robots in Manufacturing tasks and the generalisation of MAGICIAN innovations, it is expected to generate long-term impacts in the quality of working conditions in several additional fields, especially in manufacturing, e.g., the aerospace industry, shipbuilding, production of manufacturing components, etc [13].

More particularly, this project presents a transformative approach to automated defect detection and removal in manufacturing, uniquely integrating AI, Robotics, and human-centred design. This approach encompasses industrial efficiency, workforce well-being, and sustainability, setting a precedent for future applications of collaborative robotics in complex and hazardous environments.

2.4 Defects that need to be Addressed

In this project we were primarily focused on specific category of defects as shown in the Figure 2.4 that which were going to occur during the building process of the automobile

body parts which were gone through lots of machining and different joining methods such as continuous or spot welding which cause weld spatters and craters on the surface which some time becomes very hard to detect and difficult to remove.

Also Since most of these components are been manufactured in different locations which could lead to tiny scratches and dents which could from with the metal surface internal stresses or with a cause of accumulated excess metal grains on the top of the body parts here in Table 2.1 with estimates the typical ranges for the following defects and for some is very difficult to detect with the naked eye but significantly effect in the upcoming paint job process.

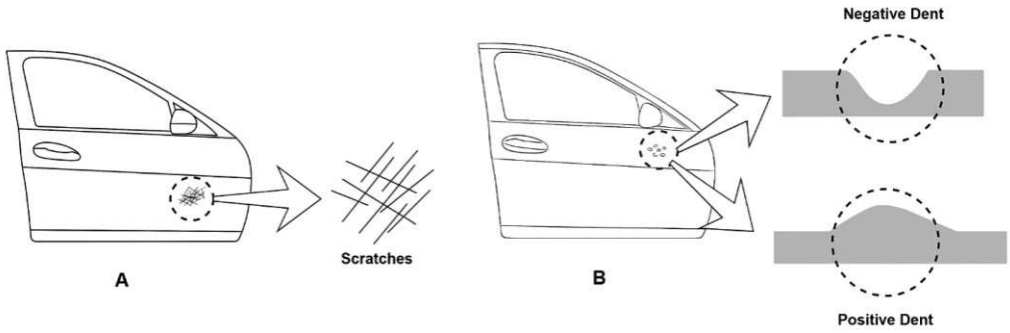

Figure 2.4: Types of defects shown on the Car front door panel, (a) Scratch Defects,(b) Positive & Negative Defects.

Table 2.1: Size Range of the Defects occur on the automobile body parts [17]

Defect Type	Size Range
Scratches	Tens to hundreds of μm
Dents	0.2 mm up to several mm
Craters	Tens of μm to mm-size

Understanding the overall framework of the Autonomous cleaning process, as well as the types of defects addressed by the cleaning robot during the surface finishing process, provides insight into selecting the proper tool and choosing an appropriate abrasive to handle these defects.

3 Surface Finishing Automation Technologies – A Literature Review

In general, surface finishing operations are mandatory across virtually every field of product design, ranging from microscopic chip-level components to large macroscopic structures such as wind turbine blades. These operations are essential before releasing the final product to its customers. Since surface finishing is typically classified as a low material removal rate (**low-MRR**) process, it is most often performed during the final stages of manufacturing, after obtaining a semi-finished product.

To properly investigate the latest technologies and techniques in this domain, it is often beneficial to examine the historical timeline of technological evolution. Figure 3.1 presents an illustrative historical timeline depicting the advancements in surface finishing operations across various industries.

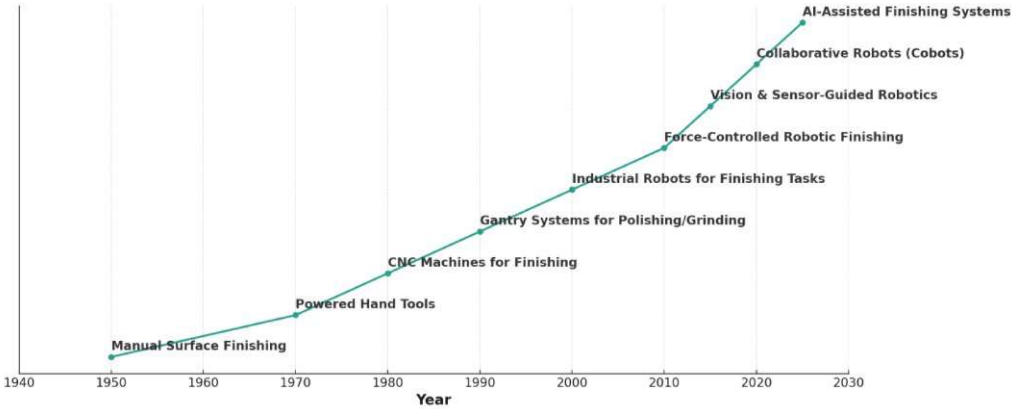

Figure 3.1: A historical timeline illustration of the key technologies used in surface finishing operations across various industries.

As this may be evident, the use of automated control technologies, such as computer numerical control (CNC) and other gantry-type systems, was mainly utilised on the industrial shop floor, which operated on larger surface areas, including ship hulls, rocket vessels, and during the manufacture of wind turbine blades.

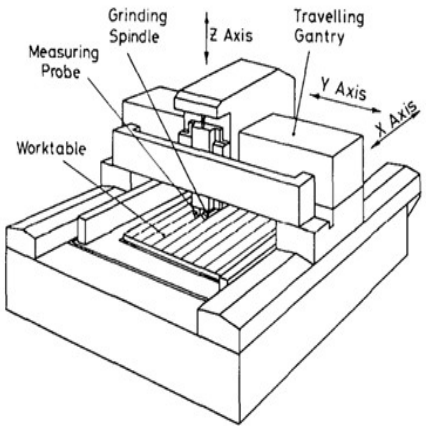

(a) CNC Grinding Machine configuration used for large optical mirror manufacturing[18].

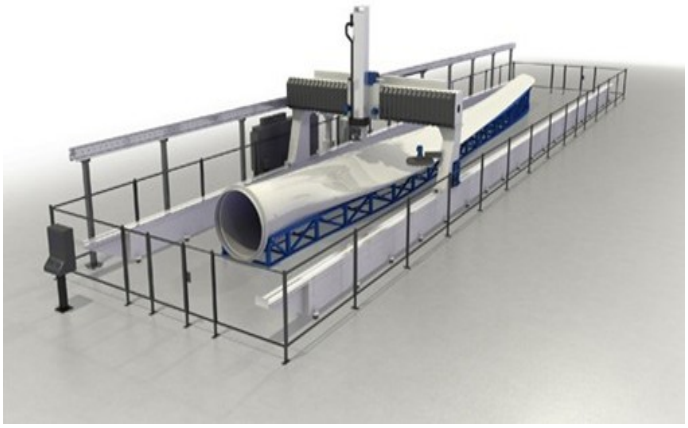

(b) Large 5-axis Agile Gantry System that is used in Wind blade manufacturing [19].

Figure 3.2: Designs of the CNC Grinding Machine

3.1 Transition from CNC to Industrial Robot

By the end of the 20th century and the beginning of the 21st century, most surface finishing processes began transitioning from traditional methods, such as CNC machines and gantry systems, towards the incorporation of industrial robots. This shift introduced new possibilities in manufacturing complex components. Compared to their predecessors, robots offer adaptability in place of large, rigid, and constrained structures, providing a significantly larger and extendable workspace. Furthermore, with a reasonable price point, they present a cost-effective solution [20] for small- and medium-scale industrial sectors.

However, it is worth noting that the primary obstacle in utilising robots for precision machining lies in their comparatively lower accuracy and repeatability relative to traditional CNC machines. A detailed comparison of these aspects is presented in Table 3.1 [21].

Despite these limitations, numerous effective solutions have recently been developed to mitigate manipulator stiffness issues and positioning errors in industrial machining applications. These advancements, in turn, help maintain the accuracy and repeatability required in precision manufacturing. Some of these state-of-the-art technologies and methods will be discussed in the subsequent section.

Whilst multi-axis CNC machines have become the mainstream approach in many manufacturing areas, in most industries, the high cost and limited flexibility of CNC grinding machines discourage their use. Consequently, industrial robots have emerged

Table 3.1: Comparison of CNC Machine vs Industrial Robot for machining applications [21].

Indicator	CNC Machine	Industrial Robot
Accuracy	0.005 mm	0.1–1.0 mm
Repeatability	0.002 mm	0.03–0.3 mm
Workspace	Limited	Large
Workspace extending	Impossible	Possible by adding extra actuated axis
Kinematic architecture	Cartesian	Serial
Number of actuated axes	3 or 5	6+
Kinematic redundancy	None	Yes, 1 *dof* at least
Complexity of trajectory	Suitable for 3/5 axes machining	Any complex trajectory
Relation between actuated and operational space	Linear	Non-linear
Actuator feedback	Single encoder	Single or double encoders
Mechanical compliance	Relatively high	Relatively low
Compliance error compensation	Not required	Mechanical (gravity compensators), algorithmic (off-line and/or on-line)
Dynamic properties	Moderate, homogeneous within the workspace	High, heterogeneous within the workspace
Control algorithm	Continuous path control	Point-to-point control; continuous path control
Programming language	Standardized G-code language	Manufacturer-specified languages (KRL, V+, Karel, RAPID, Inform, etc.)
Manufacturing flexibility	Single or several similar operations	Any type of operation
Price	Competitive for 3-axis tools; expensive for 5-axis tools	Competitive for 6 *dof* robots

as an appealing alternative, offering a large workspace, high flexibility, and advanced sensing capabilities that enable easy adaptation to changing conditions.

3.2 Transition from Industrial Robots to Collaborative Robots

The term *Collaborative Robotics*, often referred to as "cobots," represents a paradigm shift in industrial automation. This transition moves away from traditional industrial robots—typically caged and isolated from human workers—towards systems designed for safe, direct interaction with humans in shared workspaces to accomplish useful tasks [22]. Importantly, collaboration is defined by the *application and usage*, not merely by the device itself. According to **ISO 8373:2012** [22], a collaborative operation occurs when robots and humans work together in a defined workspace, while a *collaborative robot* is specifically designed for direct interaction with a human.

Over the past decade, technological advances in actuation, perception, control, and safety have enabled cobots to function effectively alongside humans, combining the efficiency and accuracy of automation with the flexibility, dexterity, and decision-making abilities of skilled operators. This human-centric approach is driven by improvements in robot safety standards, sensor integration, intuitive programming, and risk-reduction methodologies [22, 23].

3.2.1 Research Shift toward Collaborative robots

In recent years, there has been a significant increase in both research and application of collaborative robots in the context of human–robot collaboration (HRC). As illustrated in Figure 3.3, the number of published HRC studies involving cobots has risen markedly since around 2014, whereas the number of studies using traditional industrial robots has remained relatively constant or declined. Early HRC research primarily employed conventional industrial robots; however, the introduction and proliferation of cobots—such as the DLR LWR-III, KUKA *iiwa*, ABB *YuMi*, and Universal Robots—have accelerated both academic research and industrial adoption [24].

This transition is primarily driven by industry demands for flexible automation solutions that can reduce operational costs, save workspace, and adapt quickly to changes in production requirements, all while ensuring worker safety and maximising productivity [23].

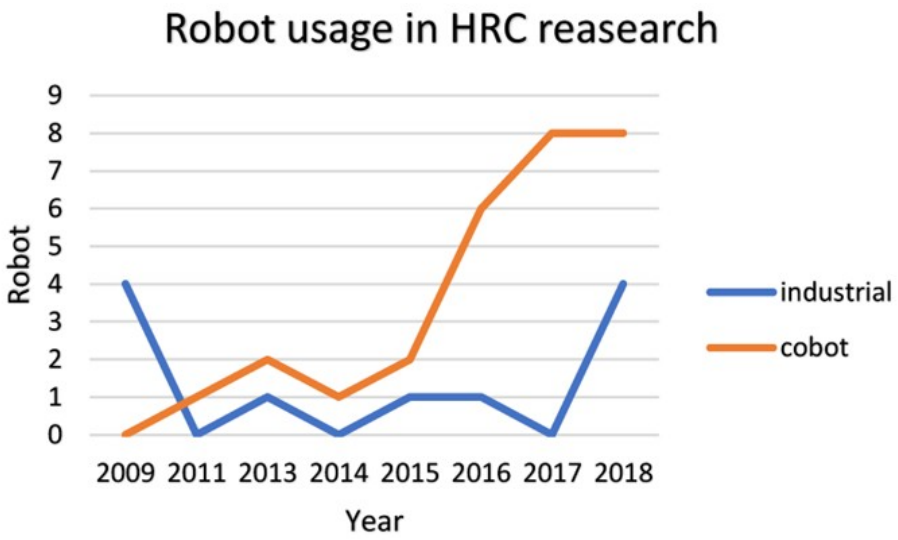

Figure 3.3: Number of reviewed studies employing industrial robots and collaborative robots (cobots) in human–robot collaboration (HRC) between 2009 and 2018 [24]. The vertical axis indicates the count of studies considered in the review.

3.2.2 Advantages and Importance of Collaborative Robots in Industrial Applications

Collaborative robots (cobots) offer several key advantages over traditional industrial robots, particularly in human-robot collaborative tasks such as surface finishing. They are easier and faster to set up, more adaptable to changing tasks, and require less floor space and lower initial investment. Table 3.2 presents a comparison across critical factors between conventional industrial robots and collaborative robots.

3.3 State of the Art in Robotic Surface Finishing Operations

Robotic surface finishing refers to the use of programmable robots to perform tasks such as sanding, grinding, polishing, and buffing of workpiece surfaces. Traditionally, these operations have been labour-intensive, requiring skilled workers to achieve smooth finishes or to remove surface defects. They are also dirty and ergonomically challenging tasks, often involving dust, vibration, and awkward postures when performed manually [25]. The increasing importance of surface finishing technologies can be inferred from the growing number of annual publications since 2008, as illustrated in Figure 3.4 [26].

In the present study, we primarily examine developments from the last decade, be-

Table 3.2: Comparison between conventional industrial robots and collaborative robots based on various factors [23].

Factor	Industrial Robots	Collaborative Robots
Deployment	Hard to deploy	Easy to deploy
Programmability	Hard and time-consuming	Easy to program
Flexibility	Hard to adapt, one task	Quickly adapts to changes
Space consumption	High	Low
Cost	Expensive	Low cost, high precision
Weight	>50 kg	<29 kg
Human–Robot Interaction	Minimal, job security concerns	High, secured job for operators
Productivity	Increases overall productivity	Also increases worker productivity
Safety	Minimal, caged operation	Advanced, safe close-proximity interaction
Force sensors	Generally absent	Present
Sensors & Machine Vision	Minimal, basic	Advanced, high-end integrated

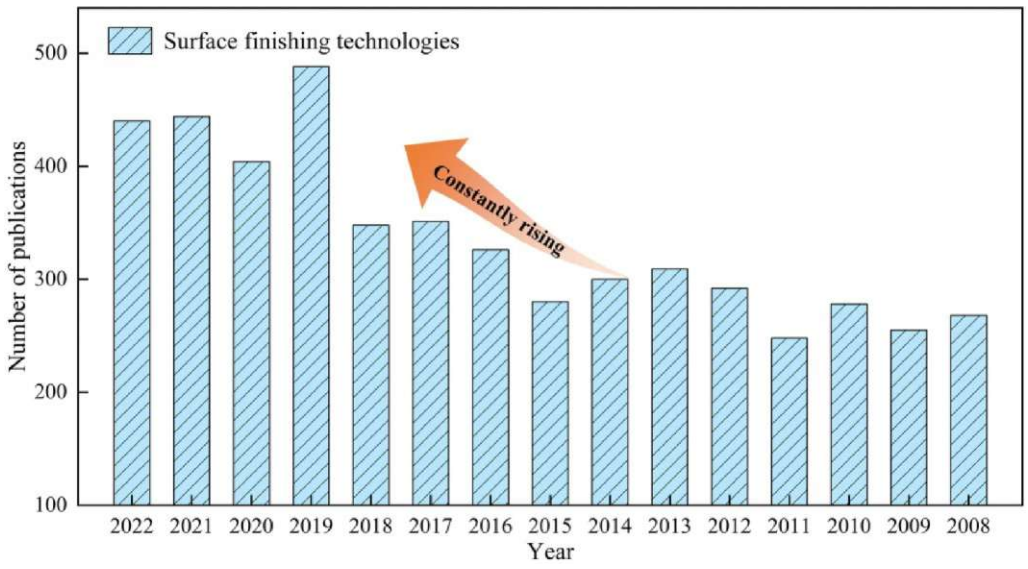

Figure 3.4: Annual publications on surface finishing technologies since 2008 [26].

ginning in 2015. A brief overview is provided of the key techniques that enable robotic surface finishing, along with a breakdown of applications in sanding, grinding, and polishing within both industrial and collaborative robot contexts.

3.3.1 Active Compliance and Force Control

Maintaining a constant pressure or contact force between the tool and the workpiece is essential for achieving uniform material removal in sanding, grinding, and polishing. Most modern robotic finishing systems employ *active compliance control*, i.e., using force-sensor feedback in a closed-loop system to adjust the robot's motion, thereby regulating contact force in real time [27]. This force-control approach has become the mainstream control scheme for many high-precision robotic operations.

A commonly observed strategy in the literature is the implementation of *impedance* or *admittance control*. Passive compliant tools, such as flexible sanding pads or belt-grinder contact wheels, can absorb minor height variations; however, they offer limited adaptability and are unsuitable for high-precision applications [27].

In general, compliant force-control strategies can be categorised into five main types [28]:

1. **Impedance control** [29]
2. **Hybrid force/position control** [30]
3. **Adaptive control** [31]
4. **Admittance control** [32]
5. **Intelligent control** (e.g., fuzzy control) [33]

Impedance Control Strategy: The control system illustrated in Figure 3.5 is designed to ensure safe and efficient interaction between a robot and its environment during polishing operations [29]. The controller operates by continuously comparing the robot's desired position and force with the actual position and force measured when the tool makes contact with the workpiece. Functionally, it behaves as a virtual spring–damper system, dynamically adjusting the robot's compliance based on discrepancies between the commanded and measured values. This strategy is particularly advantageous in applications where both safety and surface quality are critical, as it limits excessive contact forces while allowing the robot to adapt effectively to uncertainties in the operating environment [29].

Hybrid Control Approach: The control system illustrated in Figure 3.6 is implemented to enable precise force regulation, even in the presence of strong vibrations generated by the polishing tool [30]. The approach simultaneously manages both the robot's position along the desired path and the contact force applied to the workpiece. It is

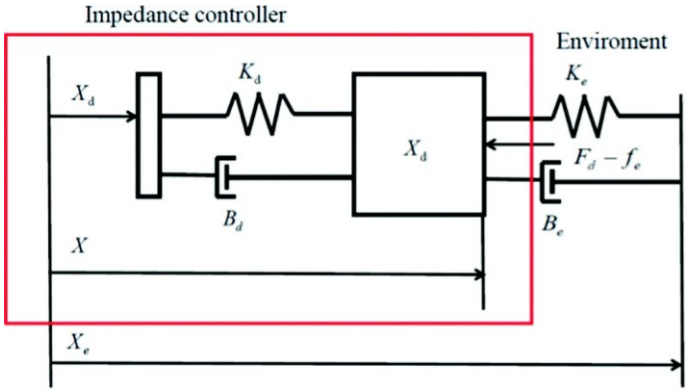

Figure 3.5: The one-dimensional physical interaction model of impedance controller and environment [29].

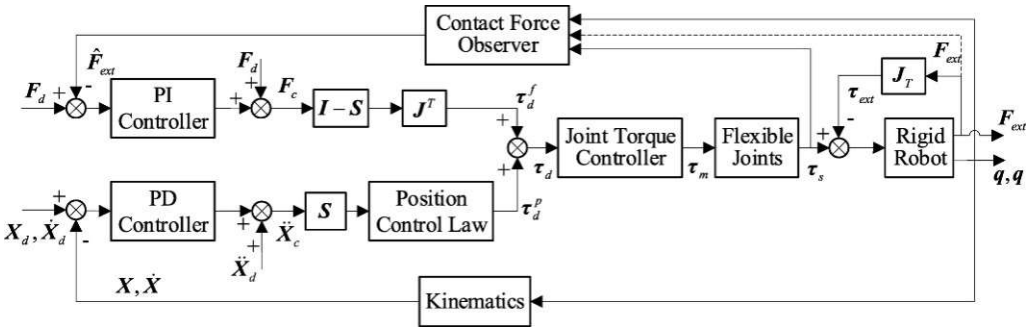

Figure 3.6: Design scheme of the hybrid position/force control [30].

realised by dividing the control actions between a position-based *proportional–derivative (PD)* controller and a force-based *proportional–integral (PI)* controller, which are coordinated through a layered joint torque controller. As demonstrated in [30], this method achieves reliable and smooth polishing performance, producing high-quality surface finishes while maintaining a consistent contact force without the need for additional multi-axis force/torque sensors.

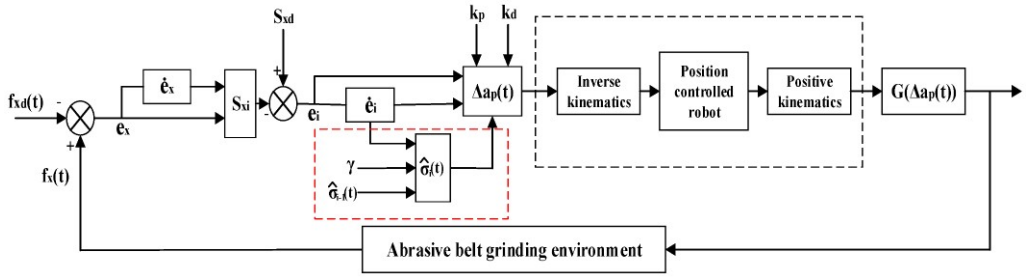

Figure 3.7: Control Flow process for the Adaptive Sliding-mode iterative control [31].

Adaptive Sliding-Mode Control (SMC) with Iterative Learning Control (ILC): The control architecture illustrated in Figure 3.7 ensures accurate force regulation using only a one-dimensional (*1D*) force sensor [31]. The system operates by continuously comparing the actual grinding force with a predefined desired force. Based on the force

error and its rate of change, the controller computes a slight positional offset to adjust the robot's motion perpendicular to the contact surface. Robustness and adaptability are enhanced through the SMC component, which suppresses disturbances and improves stability in the presence of nonlinearities or uncertainties. The ILC component refines control performance over repeated grinding cycles by updating an adaptive term based on the force error dynamics from the previous iteration. Through the ILC mechanism, the *robot learns* from prior passes, progressively reducing force fluctuations and improving process consistency. Overall, this combined strategy effectively replaces multi-axis force sensors with a simplified force estimation model, significantly reducing cost and complexity [31].

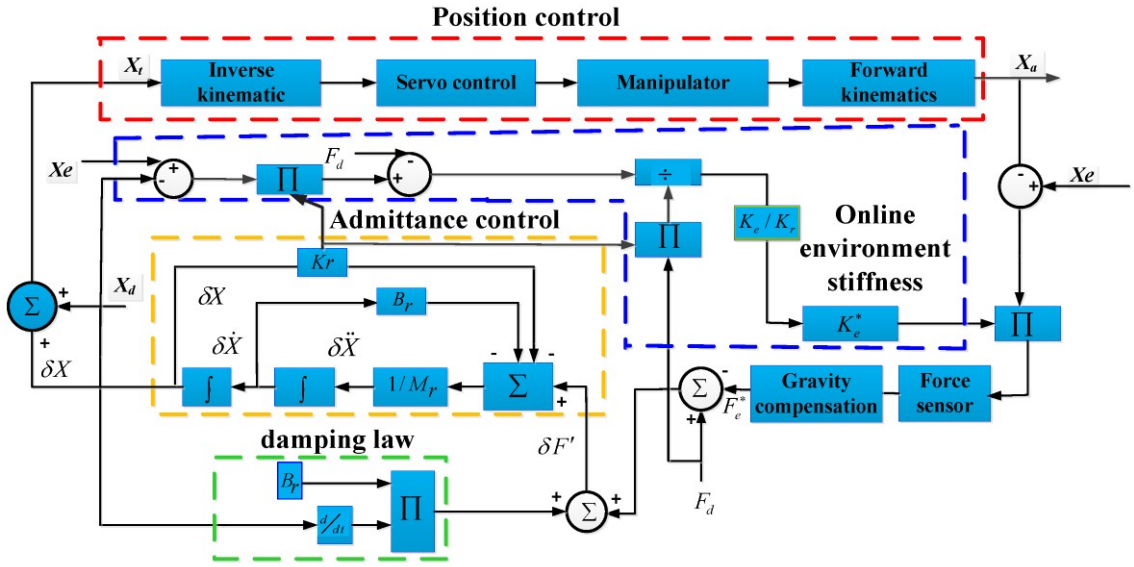

Figure 3.8: Schematic diagram of an online admittance controller with gravity compensation [32].

Admittance Control Strategy: The system illustrated in Figure 3.8 employs real-time force feedback to regulate the pressure applied by the tool [32]. An admittance controller continuously monitors and adjusts the robot's response to surface variations by adapting stiffness and damping parameters in real time. Gravity compensation is incorporated to eliminate the influence of the tool's weight, ensuring that the measured contact force reflects only the interaction with the surface. By combining position control, adaptive force regulation, and continuous environment sensing, the robot achieves uniform polishing quality, even for intricate and curved geometries [32].

Fuzzy Logic Control Strategy: The system illustrated in Figure 3.9 integrates sensor feedback and human-inspired reasoning through a fuzzy logic controller [33]. The controller continuously monitors the tool's torque and the robot's position relative to the workpiece, enabling real-time adjustment of the robot's movement. Instead of

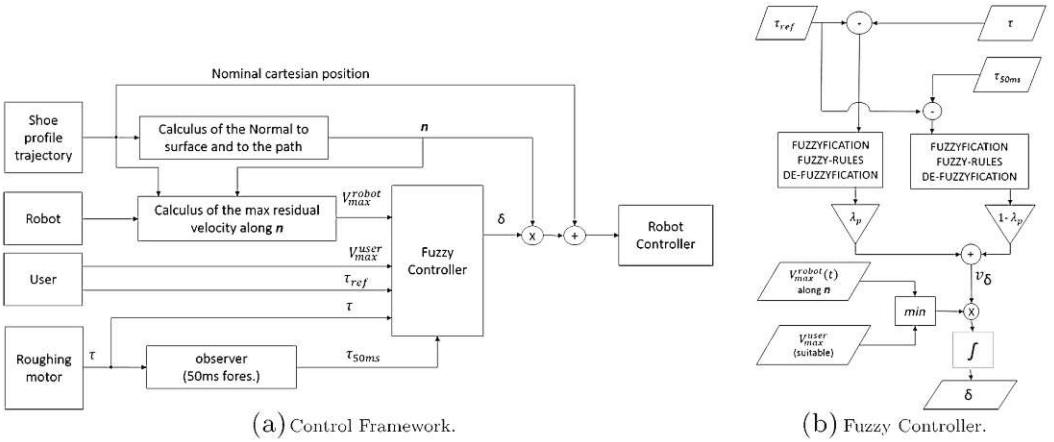

Figure 3.9: The proposed control architecture panel (a) the overall control framework, panel (b) is the detailed view of the fuzzy controller [33].

strictly maintaining a constant force, the fuzzy controller interprets the measured signals and applies intuitive rules to adapt the robot's approach gently. This flexible, adaptive strategy closely mimics the decision-making of skilled human workers, resulting in a robust, smooth, and responsive control system that can handle unpredictable challenges and make automation feasible for tasks traditionally reliant on human expertise.

From the above research literature, it is evident that maintaining a steady contact force greatly improves surface consistency in terms of its roughness parameters, which is particularly suitable for machining complex geometrical surfaces. Overall, force-controlled compliance through advanced control algorithms is a foundational technique in robotic surface finishing.

3.3.2 Specialised End-Effectors and Tools

In general, there are two main configurations for implementing robotic surface finishing processes, as illustrated in Figure 3.10. In the first configuration (Figure 3.10a), the finishing tool is fixed to a workbench or a rotating table, while the robotic arm manipulates the workpiece. In the second configuration (Figure 3.10b), the finishing tool functions as the robot's end-effector and is mounted at the tip of the robotic arm, while the workpiece remains fixed on the work table.

In this study, we focus on the setup shown in Figure 3.10b, where the end-effector is mounted on the robotic arm and the workpiece, for example, an automobile body, is placed on a moving bench. The end-effector is compact and lightweight, enabling precise and flexible manipulation by the robot.

For surface finishing operations, a wide variety of end-effector tools has been developed.

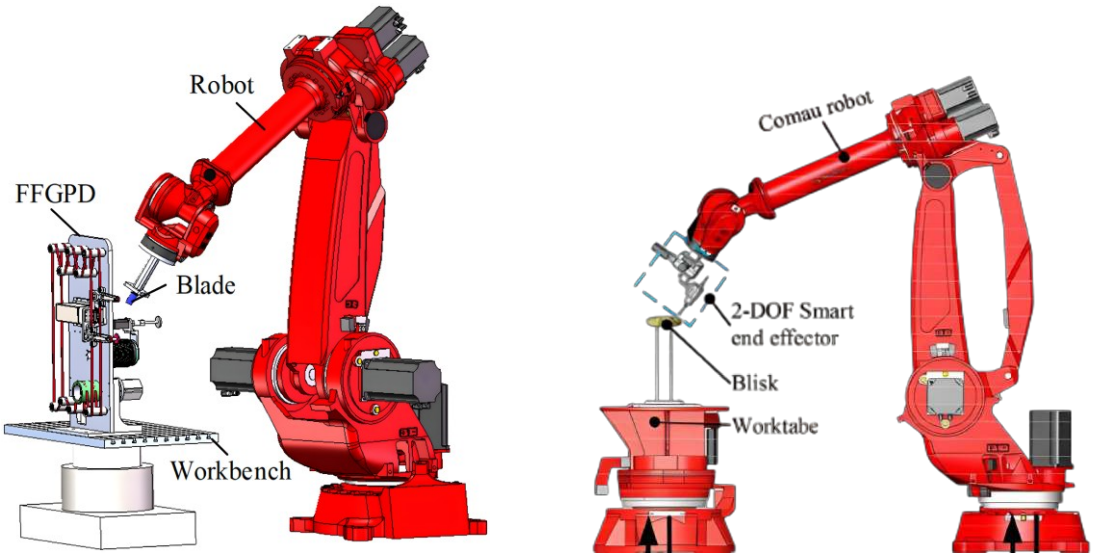

(a) End-effector full-feature grinding and polishing device (FFGPD) mounted on a workbench; the workpiece is attached to the robotic arm [34].

(b) Two-DOF smart end-effector on the robot arm; the workpiece is fixed on the work table [35].

Figure 3.10: Arrangement of the robotic surface finishing system.

These include abrasive belt grinders, grinding disks, flap wheels, orbital sanders, polishing wheels, buffs, and other types of finishing devices. Compared with manual finishing, robotic finishing enables precise regulation of contact forces through force control, which is generally classified into two main approaches: passive compliance and active compliance [36].

In the design of end-effectors for passive compliance tools, components such as springs [37] or compliance mechanisms such as flexures [38] are commonly used. In contrast, active compliance tools are equipped with components like voice coil motors [39], pneumatic cylinders [40], magnetic actuators [41], and traditional actuators such as stepper or servo motors [35, 42]. In some cases, a combination of both active and passive compliance is employed, resulting in a hybrid compliance control system [36].

The compliant end-effector (CEE) described in [36] is a modular design combining both *active* and *passive* compliant mechanisms, used for polishing operations as illustrated in Figure 3.11. This design primarily consists of a flexible beam capable of elastic deformation, acting as a passive damping component. Furthermore, this component can also detect the contact force, which is calculated from its deflection and stiffness coefficient, thereby eliminating the need for an external force sensor. The flexible beam frame is fixed to a series of parallel-arranged pneumatic cylinders, which move back and forth once the polishing tool contacts the workpiece surface, maintaining a constant contact force during machining.

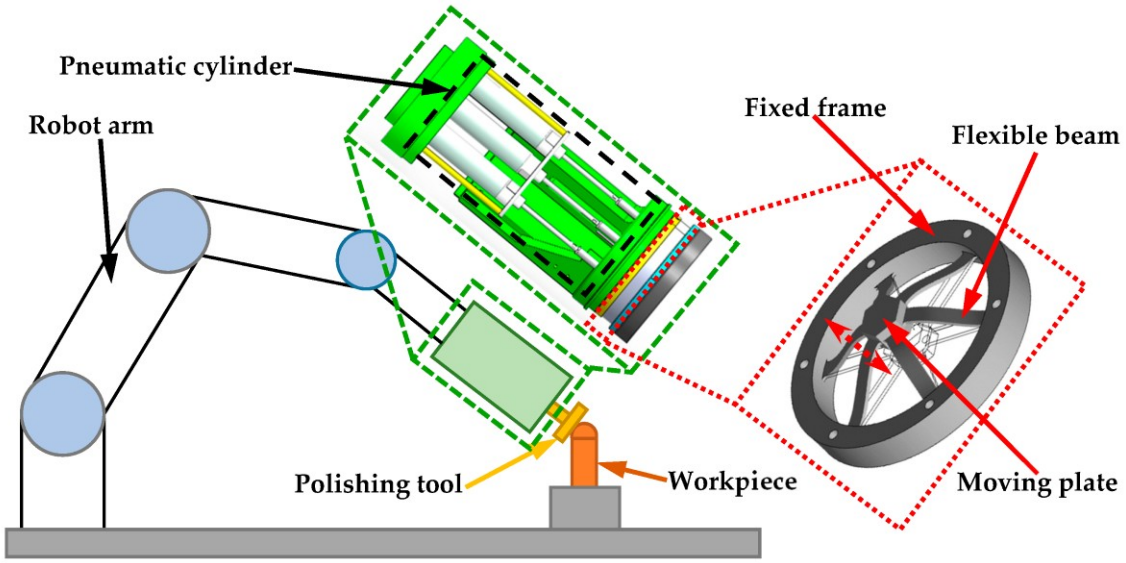

Figure 3.11: A Schematic diagram of the proposed compliant end effector mechanism installed onto a robotic arm [36].

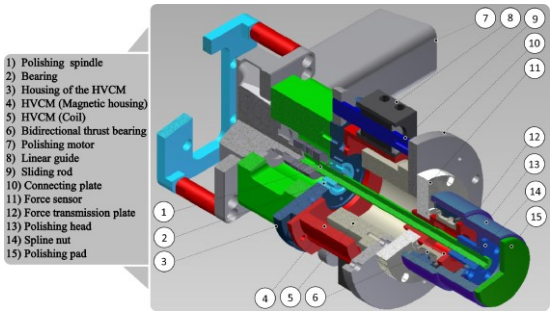

(a) A sectional view of the proposed force-controlled end effector [39]

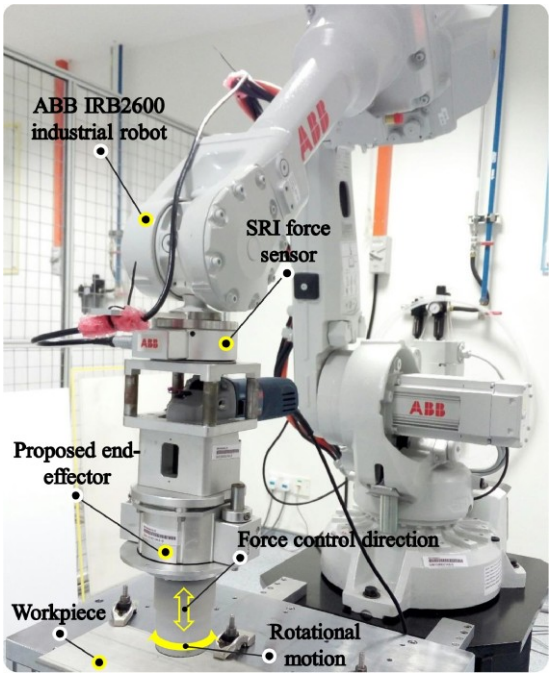

(b) The experimental set-up of an ABB IRB2600 industrial robot mounted with the proposed end effector [39]

Figure 3.12: An active polishing end effector design

A novel **force-controlled end-effector** design [39] for automated robotic polishing operations, shown in Figure 3.12, operates as a "mini–robot" in a macro–mini system [43]. In this design, both the polishing motor and the spindle remain stationary; instead, the polishing spindle incorporates a spline shaft that transmits rotational motion to a spline nut, which is connected to the polishing head. A linear hollow voice coil motor (HVCM) enables *active compliance*, while a strategically placed donut-shaped force sensor, positioned close to the polishing head, provides accurate contact force measurement.

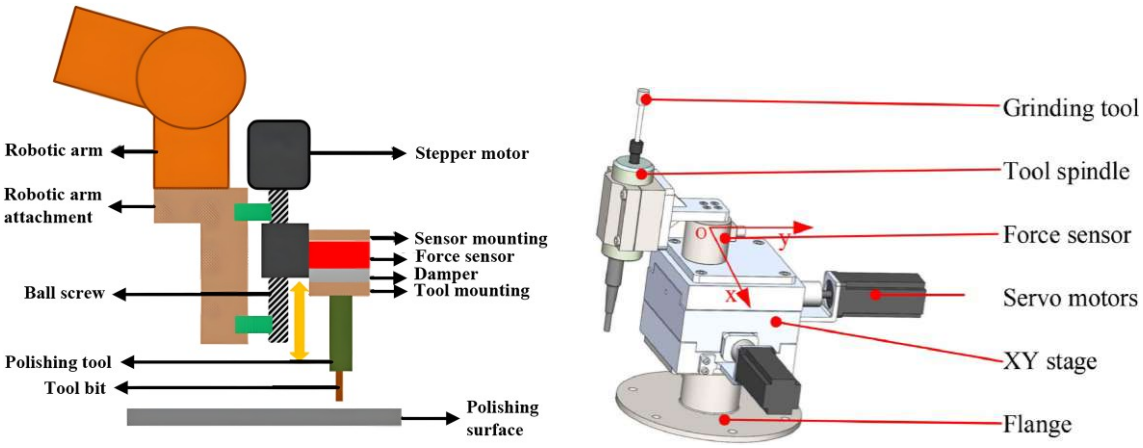

(a) Stepper motor with the ball screw mechanism for the robotic polishing system [42]

(b) Configuration of the 2-DOF smart end effector with a X-Y stage feed directions [35]

Figure 3.13: Actuator-based end effector tool interfaces.

From the work in [42], an end-effector for robotic polishing applications, illustrated in Figure 3.13a, features a modular linear motion mechanism driven by a stepper motor and ball screw. The linear motion mechanism enables the precise application of polishing force along the tool's normal axis. Additionally, a six-axis force sensor is integrated to provide real-time feedback, enabling direct force control during finishing.

Another advanced end-effector developed in [35] for grinding curved surfaces, shown in Figure 3.13b, features a **2-DOF XY stage** actuated by servo motors and equipped with a three-axis force sensor. By enabling micro-motion adjustments in both X and Y directions, the system maintains a constant contact force during the grinding process. Experimental results demonstrate that this approach significantly improves contour accuracy and surface quality compared to traditional constant-force methods, making it effective for finishing complex curved surfaces.

In [41], a passive vibration suppression system is integrated into a smart end-effector, as illustrated in Figure 3.14a. This system is equipped with a precision linear stage for fine adjustment of the tool position. Central to its design are two custom-built **eddy current dampers (ECDs)**. When the spindle generates vibrations, the magnets move relative

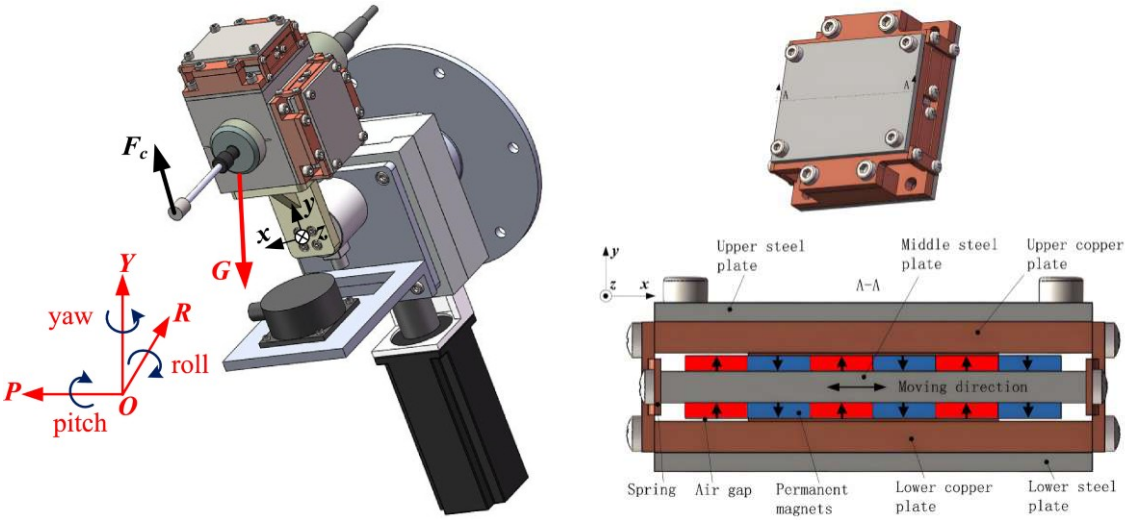

(a) Model of the smart end effector tool interface [41]

(b) Cross-section design of the Eddy Current Dampers (ECD) for damping the structural vibrations [41]

Figure 3.14: Eddy Current Dampers (ECD) Vibration Suppression System.

to the copper plates, producing eddy currents as shown in Figure 3.14b. These currents, by Lenz's law, create opposing electromagnetic forces that passively damp vibrations across a broad frequency range, without the need for external power or active feedback. Overall, the system enables precise real-time control of the polishing force, while the passive ECDs enhance surface quality by minimising vibration-induced defects.

In the work of [37], the authors developed an *active compliant force-controlled end-effector* as shown in Figure 3.15a. A key feature is the inclusion of a low-impedance *series elastic actuator* (SEA) structure. The core of the design is a spring interface, as shown in Figure 3.15b, positioned between the actuator and the grinding tool, which provides mechanical compliance and enables precise force control. By optimising the spring stiffness, the end-effector achieves a balance between compliance and dynamic response, reducing mechanical disturbances and improving the stability of force application. In essence, the compliant end-effector acts like a smart, shock-absorbing hand for the robotic grinder.

A novel *passive end-effector interface*, shown in Figure 3.16, based on a constant-force mechanism [38], has been developed for robotic polishing applications. Unlike traditional active compliance systems that rely on force sensors, actuators, and complex control algorithms to regulate contact force, this design utilises a purely mechanical approach. The mechanism is based on the *stiffness combination method*, which ingeniously combines a *positive-stiffness* structure, such as a multi-layer flexure (MLF)[44], with a *negative-stiffness elastic element* consisting of a bistable mechanism[45]. The end-effector maintains

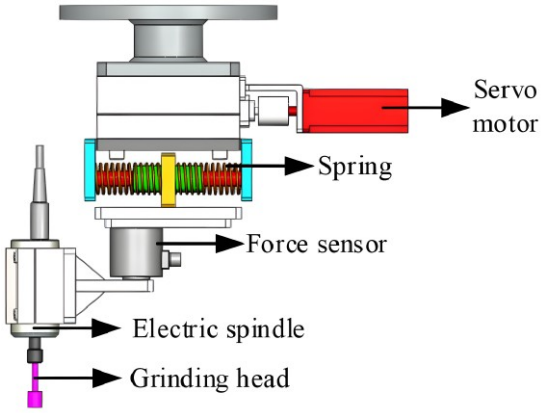

(a) Model of the smart end effector tool with the springs added between the ball screw system of the grinder tool

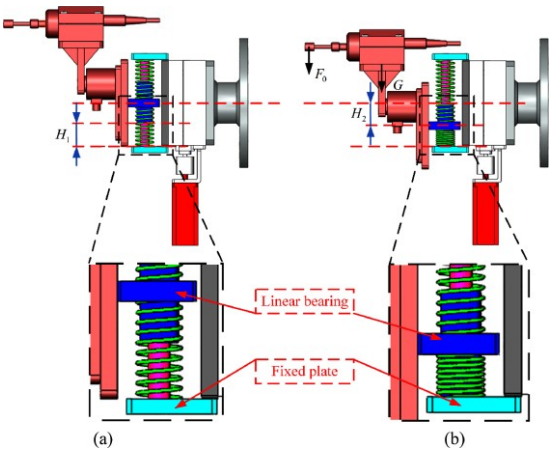

(b) Schematic diagram of the spring stiffness selection for the compliant force-controlled end-effector: (a) initial compression position of the spring; (b) position of the spring compression under the load, gravity and contact force

Figure 3.15: Active elastic grinding tool end effector [37] .

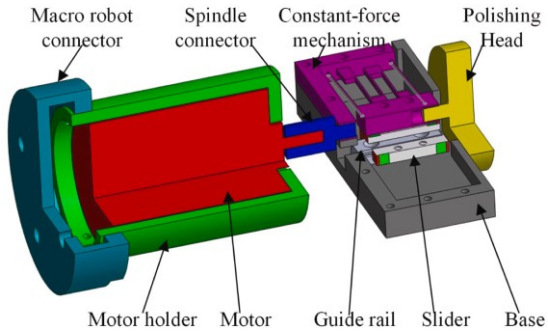

(a) Section view of the designed passive end effector based on a constant force mechanism for robotic polishing

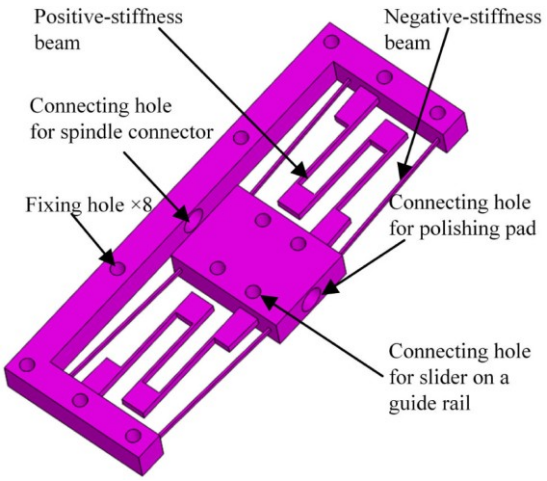

(b) CAD model of the designed constant-force mechanism, which is composed of the positive-stiffness structure (multi-layer flexure) and negative-stiffness structure (bistable beam)

Figure 3.16: passive flexure element based end effector polishing tool[38] .

a nearly constant contact force within a specific range of motion, regardless of minor variations in surface height or robot position. This constant-force capability eliminates common issues found in active systems, such as force overshoot at initial contact and large force fluctuations. Additionally, the entire end-effector is designed as a modular unit, which can be easily changed if a different force value is needed, and also simplifies its connection to the motor and polishing head. During experimental studies, this design achieved high force accuracy, typically within ± 0.3N[38], along with effective vibration isolation.

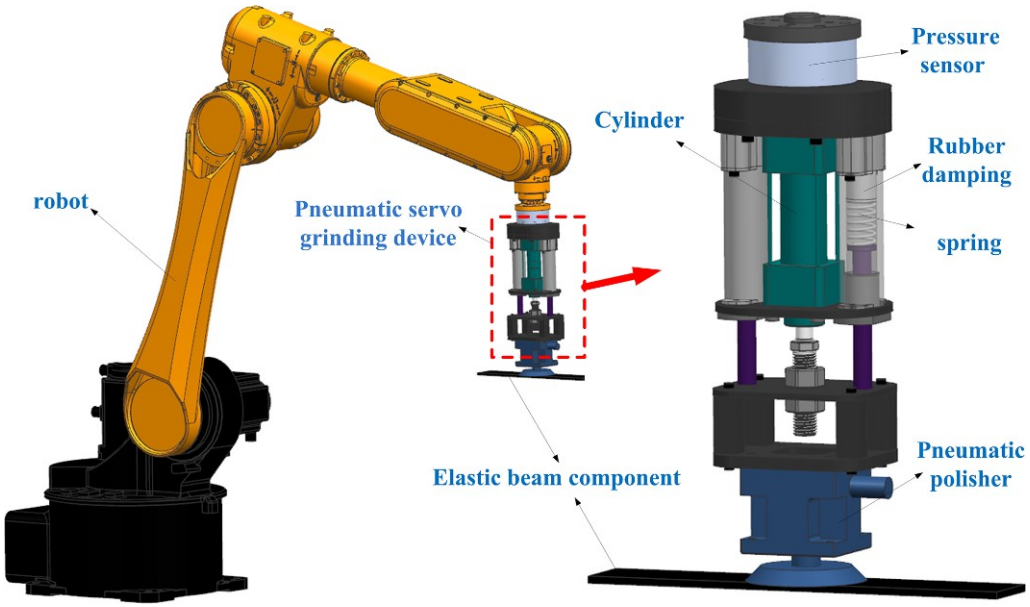

Figure 3.17: Structure composition of the robotic grinding system through pneumatic servo control [40].

The developed end-effector, as illustrated in Figure 3.17, is a *pneumatic servo grinding device* mounted on a robot [40], incorporating a pneumatic cylinder, grinder, and pressure sensor for real-time force control. Its pneumatic interface enables precise regulation of contact force by controlling air pressure via an electromagnetic servo valve, which is continuously monitored by the pressure sensor to measure the actual contact force. Additionally, this design dynamically compensates for the vibrations and force fluctuations induced by the elastic deformations of the workpiece [40], which is especially important for high-quality robotic surface finishing of thin-walled or elastic components. The end-effector operates using a *passive compliance control method*, where the robot is primarily responsible for trajectory control. At the same time, the grinding device manages the contact force through a flexible joint. This approach reduces dependence on the robot body and decouples force control from position control. The core of its force control mechanism is a pneumatic servo system [40], which regulates the mass flow. The pneumatic servo system enables the device to independently maintain a steady, desired grinding force on the workpiece, even when the workpiece itself is vibrating or

deforming.

3.4 Commercial robotic surface finishing end effectors

In the domain of commercially available robotic surface finishing, end-effectors are critical for automating labour-intensive work. A key feature of these tools is their *compliance/force control*, which enables the robot to maintain a constant pressure against irregular surfaces while also monitoring the allowable forces required for specific finishing operations, much like a human expert would do. It is observed that most of the force control types integrate either active or passive force control mechanisms.

During this study, we investigated several major commercial end-effector interface solutions, with all their essential features presented in Table 3.3, such as force control methods, payload capabilities, and compliance stroke ranges. These interfaces are primarily used in industrial applications, including aerospace, metal fabrication, and the automotive sector. All these interfaces are shown in Figure 3.18.

The landscape of commercial robotic surface finishing end-effectors is diverse and rapidly advancing. Modern robotic finishing end-effectors integrate various compliance techniques with active force control to ensure consistent results across different surfaces, effectively mimicking the sense of "human touch" to produce high-quality and accurate products. Each solution balances force, compliance stroke, and payload along with control sophistication to suit different use cases, ranging from aggressive material removal using industrial robots to fine finishing with collaborative robots.

Table 3.3: Commercial robotic end-effectors for surface finishing with force/compliance capabilities.

Vendor & Model	Force Control Type	Force Range	Compliance Stroke	Payload / Tool	Typical Application	Special Features
FerRobotics ACF Series [46]	Active (servo-pneum.)	100–800 N (model dep.)	11–98 mm	25–350 Nm torque	Automotive; aerospace; grinding; sanding	Gravity compensation; quick integration
ATI AOV-10 [47]	Passive (pneum.)	7–67 N (1.5–15 lbf)	13 mm (max)	2.68 kg tool; 10,000 RPM	Paint sanding; blending; finishing	Axial float; reduced path teaching
PushCorp AFD Series [48]	Active/Passive (servo-pneum.)	120–956 N (model dep.)	20–36 mm	12–97 kg payload (model dep.)	Heavy grinding; sanding; foundry work	Force compensation in all directions
Nordbo NAC-S20-150 [49]	Active (pneum.)	Up to 150 N (push), 110 N (pull)	20 mm	16 Nm moment; 2.6 kg unit	Polishing; sanding; automotive; wood	Web config; compact; IP67
Suhner EFC-02 [50]	Active (electric)	Up to 200 N	20 mm	4 kg unit; payload max 15 kg	Grinding; sanding; tight spaces	All-electric; data logging; compact
OnRobot Sander [51]	Active (via FT sensor + robot)	Up to ∼100 N*	Limited (via pad/robot)	1.2 kg sander	Light-duty; cobots; plastics; paint	Plug-and-play; electric; easy setup
Schunk PCFC [52]	Passive (pneum.)	18–240 N	12 mm	∼3.5 kg unit; 4 kg payload	Polishing; industrial robots	Gyro/gravity compensation; sensor option
IPR ZN/Z-Axis Comp. [53]	Passive (spring/pneum.)	9–714 N	8–12 mm	0.2–18.3 kg unit; 1–300 kg payload	Assembly; some sanding	Modular sizes; Z-collision detection
Bosch Rexroth Smart Flex Effector [54]	Active (electromech.)	(Sensor only; no actuation)	±6 mm	6 kg payload	Assembly; inspection; finishing	6D force/position feedback; IP54

Figure 3.18: Commercial Robotic Surface Finishing End Effectors, (A) FerRobotics Active Contact Flange (ACF) [46], (B) ATI Axial Orbital Vane (AOV)- 10 [47], (C) PushCorp Adjustable force device (AFD) Smart-X series [48], (D) Nordbo Active Compensation NAC-S20-150 unit [49], (E) Suhner Electric force compliance EFC-02 [50], (F) OnRobot Sander [51], (G) Schunk Pneumatic Compliance Force Control PCFC [52], IPR z-compensation unit [53], Bosch Rexroth Smart Flex Effector [54].

3.5 Design Considerations and Areas for Further Development

Analysis of the above-stated end-effector designs, from both research and commercial solutions, reveals that they all serve a primary purpose: enabling robots to perform surface finishing tasks with a consistent and controlled force. This capability ensures compliance and provides force feedback, allowing robots to adapt to varying part geometries and surfaces, thereby achieving high-quality and uniform finishes.

It is evident that most of these interfaces are attached to industrial robots capable of handling heavy payloads with high accuracy in a dedicated environment called a *work cell* [20], as shown in Figure 3.19. In such a configuration, an ABB IRB 6640 six-axis articulated robot operates in a dedicated work cell environment, where there is no human intervention, and the cell itself acts as a protective barrier between the human worker and the industrial robot.

Figure 3.19: Machining changeable robotic workcell (*courtesy SIR SpA–Italy*) [20].

Furthermore, most industrial robots are usually not equipped with built-in force/torque sensors to monitor the contact force during machining operations [55]. The absence of built-in sensors is one of the primary reasons why the aforementioned end-effector interfaces are equipped with force/torque sensors, which enable force and gravity compensation, as well as monitoring of the resultant force applied to the workpiece.

In the context of human–robot interaction (HRI), it is essential that the robot be equipped with integrated joint torque sensors [56]. Equipping robots with such sensors

is the central aim of the **MAGICIAN** project, which focuses on a human-centred design strategy to advance automation while promoting human–robot collaboration in manufacturing. Recognising the importance of this capability has driven the shift toward collaborative robotic arms designed explicitly for HRI, where each joint of the robot is equipped with a torque sensor [30]. An example is shown in Figure 3.20, depicting a **Dexterous Collaborative Robotic Arm (DCRA)**, a 7-DOF robotic manipulator [30], where all joints (marked in the Figure 3.20) are equipped with a joint torque sensor at the load side of each actuator.

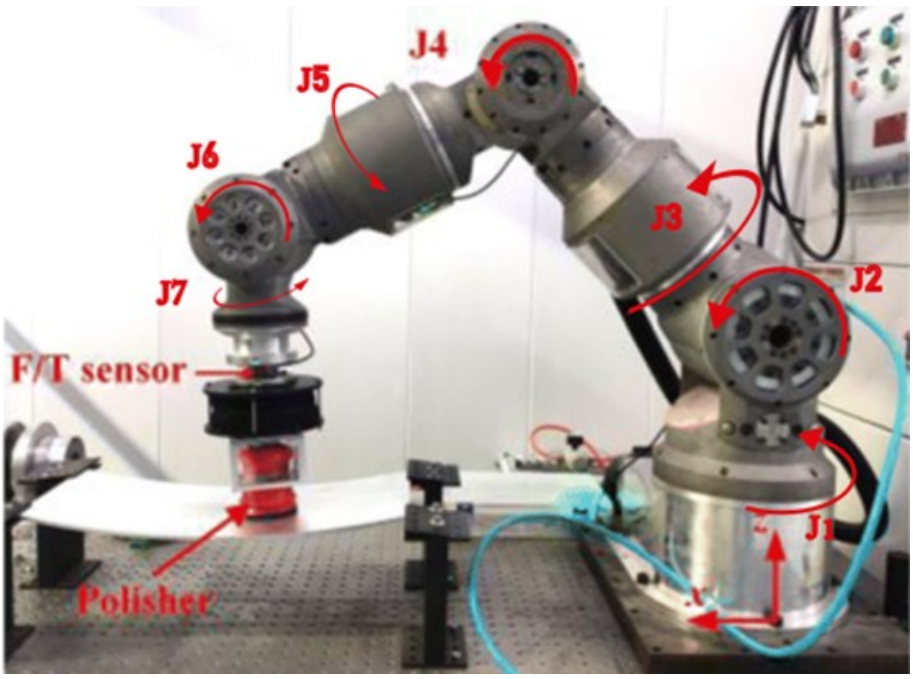

Figure 3.20: The dextrous collaborative arm (DCRA) and the robotic polishing system, with each of the seven joints, are equipped with the joint torque sensors [30].

Thus, for the current MAGICIAN Project, the application of robotic technologies to reproduce human operations is essentially a socio-technical activity, as everyday human–robot collaborative work practices involve interactions and communications among humans and robots within complex infrastructures, making the collaborative robot the most suitable choice.

After finalising that our robot will be a collaborative arm instead of an industrial arm, there are additional factors that need to be considered when designing the end-effector tool. As discussed previously, collaborative robots (*cobots*) generally have a smaller payload capacity compared to industrial robots. When the end-effector is attached directly to the robotic arm, vibrations generated by the operation of the tool can cause imperfections during machining operations, producing *chatter* at higher work speeds. This chatter leads to poor surface finish and increased roughness [57].

The factor of vibration has thus become a crucial consideration. All the previously discussed end-effector interfaces lack mechanisms to effectively suppress or isolate these vibrations, although some research designs [41, 38, 40] have demonstrated partial compensation. However, these designs were mainly effective along the tool's normal axis (transverse direction) but lacked suppression capability in other directions, such as radial or in-plane vibrations generated by the machine tool. The limitation of directional suppression will be further investigated and analysed in the subsequent chapters.

The requirement to isolate chatter vibrations caused by tool rotation guided the finalisation of the mechanical design requirements. A mechanism—whether mechanical, electrical, or pneumatic—must ultimately be capable of attenuating these vibrations. The persistent issue of machine chatter has therefore become the primary driving force for further investigation into concepts and methods for reducing these undesirable vibrations.

In the subsequent chapters, an in-depth overview of the physics of vibration isolation is provided, followed by an examination of current trends in vibration control to identify concepts and methods relevant to the final design of the end-effector interface. Further state-of-the-art examples are revisited in later chapters, where they are directly integrated into the design and modelling of the vibration isolation platform for the end effector interface.

4 An Overview on Vibration and its Attenuation

4.1 Introduction to Vibration and Control

In physics, bodies are often termed as "rigid," meaning they are non-deformable and possess infinite stiffness. However, in the real world, there are no truly rigid bodies; every object exhibits some degree of elasticity, allowing it to deform under stress and return to its original shape when the stress is removed. Any physical structure with both inertia and elasticity, when subjected to energy input, whether by a sudden impact or a periodic excitation, will tend to oscillate (vibrate) when disturbed. Any motion that repeats itself after a fixed interval of time is called *vibration* or *oscillation* [58].

A vibratory system generally includes: (i) a means of storing potential energy, such as a spring or other elastic element, (ii) a means of storing kinetic energy, such as mass or inertia, and (iii) a means by which energy is gradually dissipated, such as a damper [58], as illustrated in Figure 4.1. During vibration, the system alternates between transferring potential energy into kinetic energy and vice versa. When the system is damped, energy is dissipated during each cycle of oscillation exponentially. It must be replenished by an external source if a state of steady vibration is to be maintained [58].

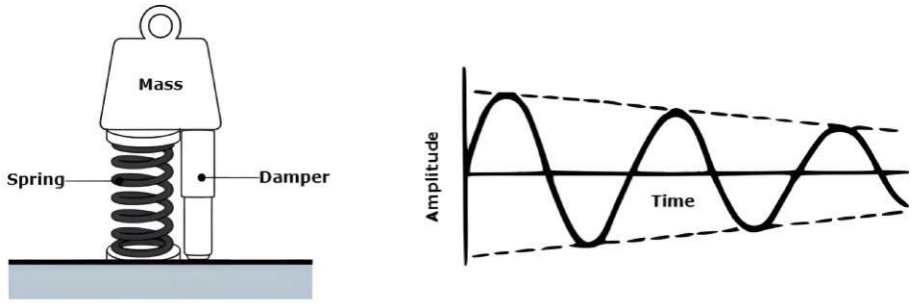

Figure 4.1: Spring mass damper system on left with decay of oscillations on right

These vibrations, when left uncontrolled, can cause the system to oscillate at its *natural frequency* indefinitely, which may ultimately lead to *resonance*. Resonance can result in adverse effects, such as noise, fatigue, or loss of precision, which can potentially lead to system failure or damage.

The basic model for a simple *single degree of freedom* (SDOF) system is illustrated in

Figure 4.1. In this configuration, a mass m is attached to a spring of stiffness k and a damper (or dashpot) with damping coefficient c. According to [59, 58], vibration can be classified in several ways; however, the most significant classifications are illustrated in Figure 4.2.

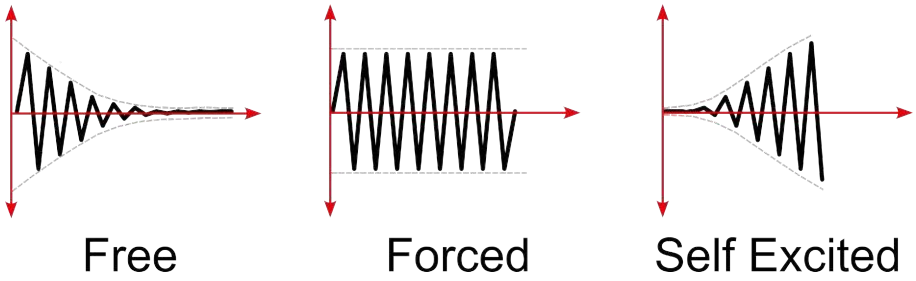

Figure 4.2: General Classification of Vibrations

Free Vibrations: If a system, after an initial disturbance, is left to vibrate on its own, the resulting motion is referred to as *free vibration*. In this case, no external forces act on the system, and over time, the oscillations gradually decay due to the presence of damping. A classical example of such oscillations can be observed in a simple pendulum model. As illustrated in Figure 4.2a, the amplitude of motion diminishes progressively with respect to time.

For a single degree of freedom (SDOF) system, the equation of motion for free vibration is illustrated in Figure 4.3.

The equation of motion for a damped single degree of freedom (SDOF) system is given by:

$$m\ddot{x}(t) + c\dot{x}(t) + kx(t) = 0 \tag{4.1}$$

where $x(t)$ is the displacement of the mass from equilibrium, $\dot{x}(t)$ is the velocity, and $\ddot{x}(t)$ is the acceleration. The stiffness coefficient k (units: N/m) characterises the elastic

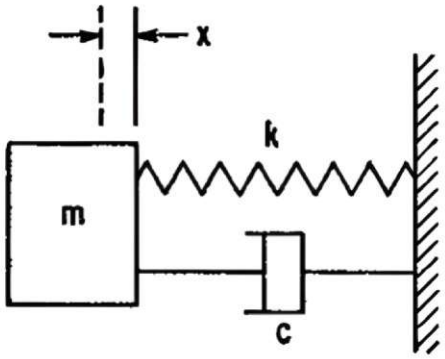

Figure 4.3: Single degree-of-freedom system with a viscous damper [59].

restoring force, and the **damping coefficient** c (units: N·s/m) characterises the resistive force produced by the damper.

For a given system that is undamped ($c = 0$), the solution is a simple harmonic motion that reduces to:

$$m\ddot{x}(t) + kx(t) = 0, \tag{4.2}$$

And the general solution is a simple harmonic motion:

$$x(t) = A\cos(\omega_n t) + B\sin(\omega_n t) \tag{4.3}$$

where ω_n is the *natural angular frequency* of the system. Assuming a non-trivial sinusoidal solution of the form:

$$x(t) = Xe^{j\omega t} \tag{4.4}$$

and substituting the above into Eq.(4.2) and solving we obtain the natural angular frequency as:

$$\omega_n = \sqrt{\frac{k}{m}} \tag{4.5}$$

with units of rad/s. The natural frequency in Hz is then:

$$f_n = \frac{\omega_n}{2\pi} \tag{4.6}$$

In a damped system ($c > 0$), free vibrations decay over time. The *critical damping coefficient* is given by:

$$c_c = 2\sqrt{km} \tag{4.7}$$

If the damping coefficient is equal to the critical damping coefficient, the system will return to equilibrium in the shortest time interval without oscillating. Moreover, the *damping ratio* is defined as

$$\zeta = \frac{c}{c_c} \tag{4.8}$$

where c_c is the critical damping coefficient [59].

For an underdamped system where $\zeta < 1$, the system oscillates at a slightly reduced rate than the *damped natural frequency* given by

$$\omega_d = \omega_n \sqrt{1 - \zeta^2} \tag{4.9}$$

With amplitude decay is $e^{-\zeta \omega_n t}$. Where $\zeta \geq 1$, the system is critically damped or overdamped, and oscillations cease altogether. In typical engineering structures, systems are often underdamped, thus exhibiting oscillatory responses. Damping is beneficial for isolation because it dissipates vibratory energy, thereby reducing the transfer of energy.

Forced Vibrations: If a system is subjected to an external force that repeats in nature, the resulting vibration is known as *forced vibration*. Examples include diesel engines, machine tools, and home appliances. From Figure 4.2b, it can be seen that a constant interaction of an external source causes the system to oscillate over time, maintaining a defined amplitude throughout the system.

The equation of motion for a single-degree-of-freedom (SDOF) system under forced vibration is expressed as

$$m\ddot{x}(t) + c\dot{x}(t) + kx(t) = F(t) \tag{4.10}$$

where $F(t)$ is the externally applied force.

If $F(t) = F_0 \cos(\omega t)$, then the particular solution is of the form:

$$x_p(t) = X \cos(\omega t - \phi) \tag{4.11}$$

where:

- ω = forcing frequency
- X = amplitude (depends on ω, ω_n, ζ)
- ϕ = phase lag

Self-Excited Vibrations: If the frequency of an external force coincides with one of the natural frequencies of the system, a condition known as *resonance* occurs, leading the system to undergo dangerously large oscillations. Such oscillations can cause issues such as noise, fatigue, and even catastrophic failure or damage to the entire system, as evident from Figure 4.2c.

The general equation of motion for a self-excited vibration system is given as:

$$m\ddot{x} + c\left(x, \dot{x}\right)\dot{x} + kx = 0 \tag{4.12}$$

where $c(x, \dot{x})$ can be **negative** during part of the motion, leading to energy input instead of dissipation.

In our current study, the machine tool falls under the category of *forced vibrations*, where, over time, the system's oscillations tend to become consistent, which may ultimately lead to chatter or a poor surface finish.

4.2 Mode shapes - Eigenvalue Problem

For systems with multiple degrees of freedom (MDOF), there are multiple natural frequencies and associated mode shapes. The free vibration motion can be expressed as a superposition of independent modes. Mathematically, for an N-DOF linear system with mass matrix $\mathbf{M}$ and stiffness matrix $\mathbf{K}$, The undamped free-vibration equation is:

$$\mathbf{M}\ddot{\mathbf{x}} + \mathbf{K}\mathbf{x} = \mathbf{0} \tag{4.13}$$

We seek solutions of the form $\mathbf{x}(t) = \boldsymbol{\phi} e^{j\omega t}$, leading to the **eigenvalue problem** [59]:

$$\left[\mathbf{K} - \omega^2\mathbf{M}\right]\{\boldsymbol{\phi}\} = \{\mathbf{0}\} \tag{4.14}$$

Non-trivial solutions exist only for specific frequencies $\omega = \omega_i$ that satisfy:

$$\det\left|\mathbf{K} - \omega^2\mathbf{M}\right| = 0 \tag{4.15}$$

These ω_i $(i = 1, 2, \ldots, N)$ are the *natural frequencies* that corresponds to the eigenvalues of the MDOF system, and eigenvector $\boldsymbol{\phi}_i$ are the corresponding *mode shape vectors*. Each mode shape is a unique deformation pattern in which all masses oscillate in a fixed ratio.

All mode shapes are orthogonal with respect to $\mathbf{M}$ and $\mathbf{K}$, and any arbitrary motion can be expressed as a combination of the modes. Understanding mode shapes is critical for predicting how complex structures respond to vibrations and for determining where isolators or dampers can be most effectively placed, often targeting specific modes.

4.3 Transmissibility of Vibrations

A key metric for vibration isolation is *transmissibility*, denoted T. Transmissibility is defined as the ratio of response amplitude to input amplitude in steady-state forced vibration. There are two main contexts for transmissibility: **force transmissibility** and **displacement transmissibility** [60].

Transmissibility (T) quantifies how much of the input vibration is transmitted to the mass above the isolator [59].

$$T = \frac{\text{Output amplitude}}{\text{Input amplitude}} \tag{4.16}$$

Force transmissibility is the ratio of force transmitted to the base with respect to the applied force [58]:

$$T_f = \frac{F_{\text{source}}}{F_{\text{base}}} \tag{4.17}$$

$$T_F = \sqrt{\frac{1 + (2\zeta r)^2}{\left[1 - r^2\right]^2 + (2\zeta r)^2}} \tag{4.18}$$

where $r = \omega/\omega_n$ is the *frequency ratio* and $\zeta = c/c_c$ is the *damping ratio*.

Damping (ζ) reduces peak amplification but slightly worsens isolation at very high frequencies.

A linear isolator effectively reduces vibration only when the excitation frequency exceeds about 1.4 times the system's natural frequency [60]. If the excitation frequency is lower, then the system is in *amplification region*, as illustrated in the figure 4.4 (C).

Displacement Transmissibility: is the ratio of the motion of the isolated mass with respect to the motion of the base [58].

$$T_d = \frac{x(t)}{y(t)} \tag{4.19}$$

$$T_d = \frac{1}{\sqrt{(1 - r^2)^2 + (2\zeta r)^2}} \tag{4.20}$$

Here, T_d is the displacement transmissibility of a viscous-damped single-DOF system

as a function of frequency ratio $r = \omega/\omega_n$ for various damping ratios ζ, with curves labeled as shown in Figure 4.4(D).

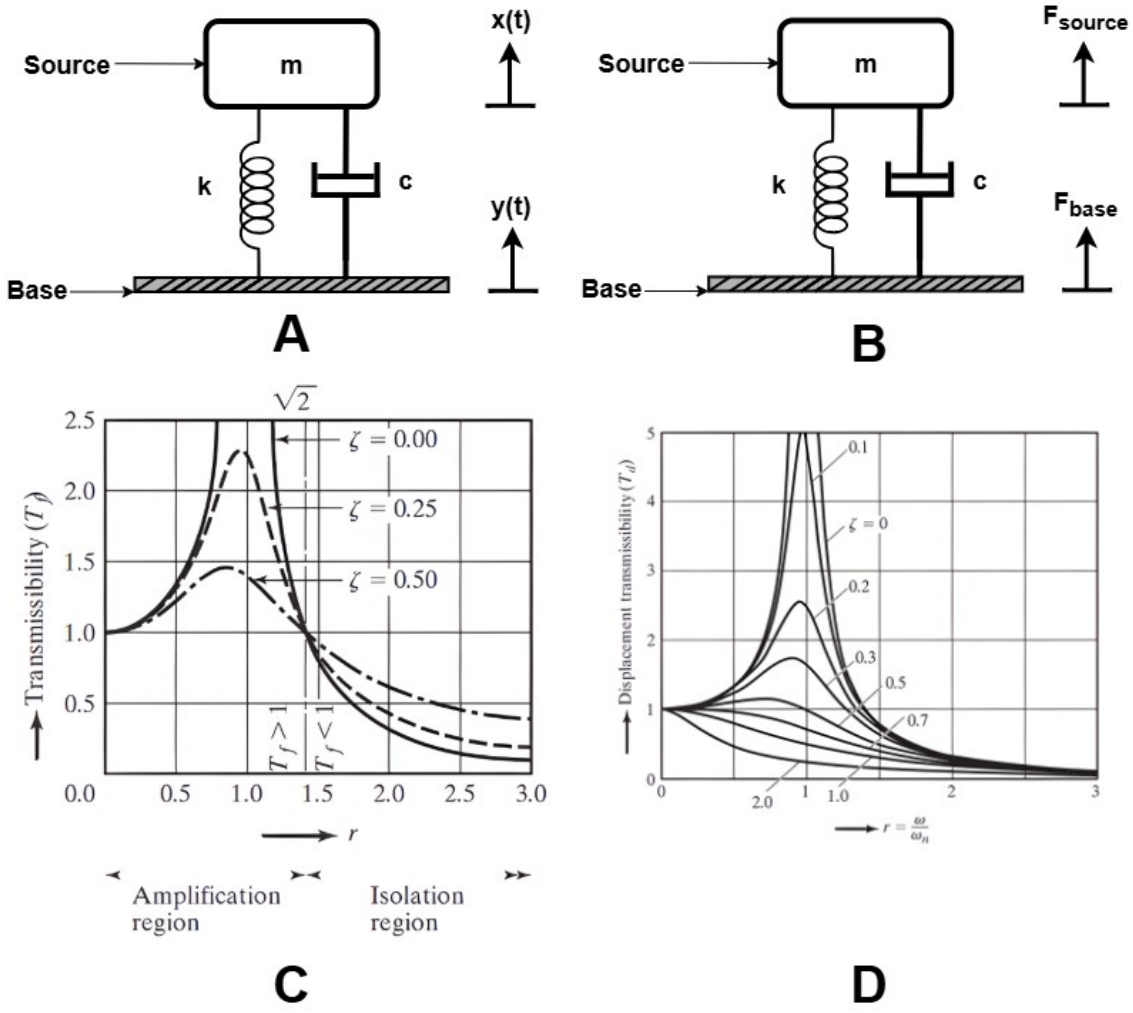

Figure 4.4: (A) Single-degree-of-freedom system with mass m having displacement $x(t)$ and base displacement $y(t)$; (B) Similar system where the mass m experiences a force F_{source} and the base experiences F_{base}; (C) Variation of force transmissibility T_F with respect to frequency ratio r [58]; (D) Variation of displacement transmissibility T_D with respect to frequency ratio r [58].

The transmissibility T depends strongly on the frequency ratio $r = \frac{\omega}{\omega_n}$ and the damping ratio ζ [58]. Here, ω is the excitation (forcing) frequency of the base vibration, and ω_n is the undamped natural frequency of the isolator system. For $r \ll 1$ (excitation frequency well below the natural frequency), $T \approx 1$, meaning the mass follows the base motion with little or no isolation. At resonance ($r \approx 1$) and for low damping, transmissibility reaches a maximum, $T \gg 1$, indicating strong vibration amplification. For $r > 1$, transmissibility decreases, and when $r > \sqrt{2}$ (for light damping), $T < 1$, so the system begins to provide isolation. This region, often referred to as the *super-resonant region*, is the desired operating regime for vibration isolation design, typically with $r > 1.4$–2 [58].

Thus, the border between amplification and isolation occurs at $r = \sqrt{2}$ for lightly damped systems, where $T = 1$; for $r < \sqrt{2}$ vibrations are amplified, while for $r > \sqrt{2}$ isolation is achieved.

There is one trade-off evident from the plot in Figure 4.4(C), where adding damping helps around resonance but degrades high-frequency isolation, because the damper itself transmits some force at high speeds (as damping forces grow with frequency).

Another essential property, evident from the transmissibility formula, is that as ω_n is lowered, r becomes larger for a given forcing frequency ω, thereby improving isolation. The relationship between natural frequency and transmissibility explains why a low natural frequency, achieved by incorporating a soft suspension, is desirable for isolating low-frequency vibrations [60]. However, lowering stiffness has limits, as it can cause the entire system to sag or become unstable; the goal, therefore, is to achieve low-frequency isolation without sacrificing load support capability or stability [60].

Insertion loss: a practical, decibel (dB)-based way to specify and measure the effect of an isolator, especially for higher-frequency systems [61].

The insertion loss D is defined as:

$$D = 20 \log \frac{V_{R,HM}}{V_{R,SM}} \tag{4.21}$$

Here, $V_{R,HM}$ is the velocity amplitude of the receiver when it is hard-mounted (HM) to the source, and $V_{R,SM}$ is the velocity amplitude of the receiver when it is soft-mounted (SM) to the source [61]. Insertion loss quantifies, in dB, the reduction in vibration at the receiver when an isolator is inserted, compared to when it is directly hard-mounted to the source [61].

Effectiveness: This is defined as the ratio of the receiver vibration amplitude when directly connected to the source to the amplitude when the isolator is present. Commonly, effectiveness is also described as the transmissibility ratio. In general, higher effectiveness means better isolation [62].

$$E = \left| \frac{V_{R0}}{V_R} \right| \tag{4.22}$$

Here, E is the effectiveness, V_{R0} is the velocity amplitude of the receiver with a rigid connection, and V_R is the amplitude when the isolator is attached.

A common measure of effectiveness in percentage is:

$$\text{Effectiveness (\%)} = (1 - \text{Transmissibility}) \times 100\%$$

4.4 Vibration control methods

Modern vibration control strategies are commonly categorised into passive, active, and semi-active methods [63]. All these methods were aimed to attenuate the vibrations but differ in their control and in their use of external energy or feedback methods as depicted in Figure 4.5.

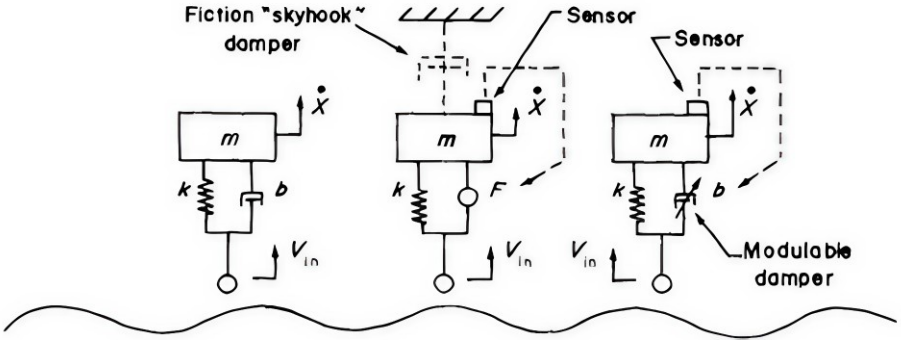

Figure 4.5: Classification of different vibration control methods in a simple single-degree-of-freedom susspension models, (A) is the passive conventional suspension typically consists of elements such as spring and damper, (B) a reperesentation of active vibration control system having an active force generator what behaves like a damper which is operated on state variable feedback loop, (C) finally a semi-active modulable damper like a conventional hydraulic shock absorber which utilises little power to perform the necessary modulation [63].

4.4.1 Active, Passive, and Semi-Active Vibration Control

Active Vibration Control (AVC) involves the use of external actuation and feedback control to counter vibrations in real time. An active control system typically includes sensors, such as accelerometers or strain gauges, to measure vibration; a controller, which computes the desired counter-force using a control algorithm; and actuators to apply forces or moments to the structure. Since the actuators require external power to generate forces, active control systems inject energy into the mechanical system.

The controller uses the sensor measurements to decide how to "cancel" the incoming vibration, often using strategies like feedback regulation or feedforward cancellation of disturbances. For example, an active vibration isolation table might sense motion in the table and command electromagnetic actuators to push or pull against the motion, thus holding the table steady.

Active control systems utilise feedback or feedforward control algorithms to generate forces that counteract unwanted vibrations, employing actuators such as electromagnetic

devices, hydraulic cylinders, or piezoelectric stacks. These active systems are adaptable and can react to changing excitation frequencies and conditions, potentially isolating even below the natural frequency. Active systems can add damping or even create an effective *negative stiffness*, actively countering the forces causing vibration [60], which yields superior vibration attenuation across a broad frequency range and under varying loads. Active systems can be highly effective but are more complex, costly, and potentially unstable if not properly designed [59].

Passive vibration control refers to all vibration mitigation approaches that use fixed, time-invariant physical components, like springs and dampers, without any active feedback or external energy input. In a passive system, the components themselves react to motion in ways that reduce vibration transmission. Common passive elements include metal or rubber springs for isolation, viscoelastic or fluid dampers for energy dissipation, and tuned mass dampers or absorbers attached to structures to absorb specific vibrational energy.

Generally, the behaviour of passive systems depends heavily on the design parameters—stiffness, damping values, and geometry. This approach is inherently stable, simple, and requires no sophisticated electronics or controller design. A notable example is the installation of a *tuned mass damper* in one of the world's tallest skyscrapers, Taipei 101, which features a 660-metric-ton suspended mass that operates entirely on passive components, such as cables and hydraulic dampers [64]. Recent passive designs, like *quasi-zero-stiffness* (QZS) mechanisms, use clever geometry, such as buckled beams or magnetic springs, to achieve very low dynamic stiffness around the equilibrium position without sacrificing load capacity [60].

Passive vibration control systems are simple, reliable, and fail-safe, making them a preferred choice in many vibration problems, ranging from a car's shock absorber to satellites, including wheel-balancing mechanisms.

Semi-Active Vibration Control is a hybrid between passive and active methods. A semi-active system cannot inject net mechanical energy into the structure but can modulate its internal properties, such as damping or stiffness, in response to operating conditions. In semi-active systems, parameters of the isolation system are varied based on feedback, without adding mechanical energy to the system [59].

A semi-active control system still uses sensors and a controller, but the controller's command is to adjust a parameter rather than exert a direct force. The controlled element then dissipates or redirects vibration energy in a more optimal way than a purely passive element would. Semi-active systems offer a compromise between effectiveness, energy consumption, and complexity, and have found wide application in civil engineering and

automotive suspensions. Standard devices include magnetorheological (MR) dampers and controllable springs [59].

The trade-off is that while semi-active control is *adaptive*, it cannot achieve the same level of performance as fully active control in some scenarios. Since it can only dissipate energy, it cannot counteract persistent forces at very low frequencies.

4.5 Vibration Isolation Concept and Importance

Vibration isolation refers to the reduction of the transmission of vibratory energy from a source, such as a machine, to a receiver, such as a structure or the ground. In this study, the receiver is a robotic arm, and the isolation is achieved by interposing a resilient element, typically a spring and/or a damper, referred to as an *isolator*. Its primary purpose is to protect sensitive equipment and to reduce the vibrations that could propagate to the receiver to acceptable levels [62], as illustrated in Figure 4.6.

Isolator design aims to make the isolator's natural frequency as low as possible compared to the disturbing frequency. The rule of thumb is that if an isolator has a natural frequency f_{iso}, it will attenuate frequencies above this value [58].

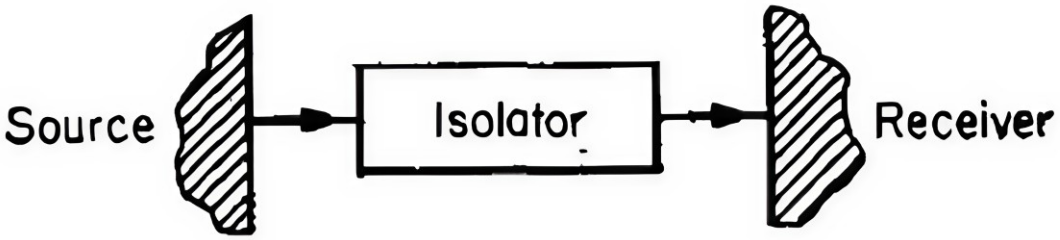

Figure 4.6: Schematic and mobility diagram of source, isolator and receiver [62].

A well-designed isolator should introduce a significant *mobility mismatch* between the vibration source and the receiver, as a greater mismatch results in more effective attenuation of transmitted vibrations. The isolator must support the full static load without exceeding its allowable deflection or losing effectiveness [58]. Ensuring adequate load-bearing capacity guarantees that the resonance frequencies do not coincide with the operating range, thereby preventing amplification of vibrations.

The importance of vibration isolation lies in its ability to protect sensitive equipment from both low- and high-frequency disturbances, ensuring the reliable operation of machinery, electronics, and precision instruments [61]. Additionally, proper vibration isolation reduces noise and mechanical wear, thereby extending the service life and performance of the protected systems.

4.6 Machining Forces and Causes of Vibrations in Tools

As discussed in the previous chapters, handheld surface finishing tools such as grinders and sanders generate significant vibrations during machining operations. A primary source of these vibrations is machine chatter, which arises from the interaction of dynamic machining forces with the tool–workpiece system. This phenomenon is also encountered during automated robotic finishing processes, where the tool is mounted on a robot and similar force–tool interactions occur. Therefore, understanding these forces is crucial for designing an end-effector tool holder for collaborative robots.

An illustration is shown in Figure 4.7, representing the dynamic model of the machining forces generated during a finishing operation between the tool and the workpiece [65], with the tool held by a robotic manipulator. This ideal compliant finishing system captures the coupled, direction-dependent nature of vibrations and tool response. It has been clearly shown in [65] that, in most surface machining processes, vibrations are more likely in the *tangential* direction. The higher likelihood of tangential vibrations arises because the system's stiffness is usually lower in that direction compared to the *normal* direction, due to relatively low process stiffness tangentially [65]. Such tangential vibrations leave chatter marks on the workpiece surface. In these operations, any imbalance or geometric error is translated into periodic forces.

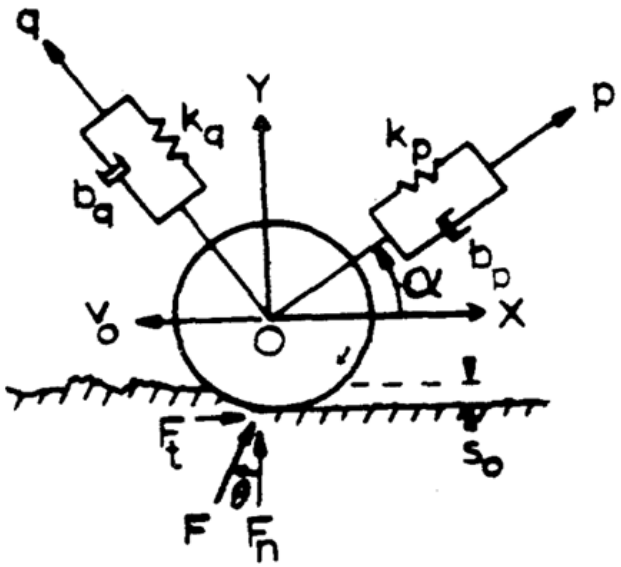

Figure 4.7: Typical Surface finishing process model, where F_n and F_t are the normal and tangential components with respect to the surface. Two principal axes, p and q, define the system's principal stiffness and damping directions, represented as k_p, k_q, b_p, and b_q. These represent the mechanical compliance of the robot, oriented at an angle [65].

The roles of stiffness and damping are crucial. Higher stiffness in the normal direction

reduces static deflection, thereby improving surface finish and accuracy. However, excessive stiffness in all directions can amplify transmitted vibrations [65]. Similarly, adequate damping is essential for dissipating vibratory energy and suppressing chatter.

Optimal compliance design for robotic reworking tool holders strongly depends on parameter optimisation, which influences the overall stiffness and damping, while keeping the maximum vibration amplitudes minimal. These are essential conditions for achieving accuracy, stability, and optimal material removal rates. Ultimately, determining which design provides the best overall grinding performance should depend on the magnitude of the deflections as well as the degree of stability in the machining forces [65].

In this section, we have presented an overview of the essential concepts and terminology that will be used in the upcoming design of the vibration isolator end effector. In the subsequent chapters, this thesis will present experimental investigations into the vibrations generated by the handheld tool and discuss methods for mitigating them. The experimental and analytical work will then be followed by the modelling of the prototype versions of the direct-mount interface for the collaborative robot, and finally, the design of a passive vibration isolator based on the principles described here.

5 Vibration Analysis for the Random Orbital Tool

As noted in the earlier chapter, each machining operation has a dedicated tool suited for the process, such as grinding, sanding, and polishing operations. In this study, the focus is on defects that arise after the components are prepared and assembled, particularly in the automobile **"Body in White"** stage, where defects such as dents (mainly positive dents), scratches, and spatters are of primary concern.

Since these defects are minor in nature, there is no need for aggressive machining such as grinding. Instead, a milder process, such as sanding, is preferred. Accordingly, the chosen finishing operation involves selecting an appropriate tool to address this task. The scope is therefore narrowed to a specific category of finishing machine tools, namely sanders, which are mostly handheld devices.

In this chapter, the selection of a suitable sanding tool is presented, along with experiments conducted to estimate the vibrations produced by the tool.

5.1 Selection of Random Orbital Sander

In the current market, several types of sanding tools are available, including belt, sheet, and orbital sanders. Among these, orbital sanders—particularly random orbital sanders—are preferred in surface finishing applications because their combined rotary and orbital motion produces a more uniform finish. As shown in Figure 5.1, compared with conventional orbital sanders, random orbital sanders leave fewer visible sanding marks and ensure more even material removal, making them well-suited for addressing surface defects in this study.

Following an initial survey of commercially available random orbital sanders, the DeWalt DCW210 (Figure 5.2) was identified as the most suitable option for this research. This tool was selected because it is compact, lightweight (0.93 kg without battery), and provides an eccentric orbital stroke of 2.6 mm with a variable speed range of 8,000–12,000 Orbitals per minute (OPM), which meets the requirements for robotic integration [67]. Furthermore, unlike many other commercial sanders, it allows customisation, making it an appropriate choice for end-effector mounting on the robotic arm.

Figure 5.1: Comparison between orbital and random orbital sanding processes (Source: Fine Homebuilding [66]).

Figure 5.2: Selected random orbital sander: DeWalt DCW210 (Source: DeWalt [67]).

5.2 Current State of the Art in Vibration Analysis for the Sanding Tool

As discussed in the earlier section, there are several research papers and monographs on vibration analysis for machine tools, particularly surface finishing tools. These tools are of special concern because, during automated operations, they can transmit significant vibrations to the robotic arm and other sensitive equipment, primarily due to vibratory chatter generated during reworking processes. In particular, orbital sanders have been observed to create unweighted acceleration magnitudes in the range of 10 m/s^2 to 300 m/s^2 [68].

Designing a vibration isolator for the orbital sanders is a bit challenging because the machine's dynamic characteristics are complex and multi-directional [69]. Here are the internal components that comprise a general orbital sanding tool, which is illustrated in Figure 5.3, where the machine's critical internal parts are shown. In general, sanders are simplified into four main parts [68], namely the housing, rotor, soft nylon posts, and the grinding pad.

It's been observed that High levels of vibration are generated due to the rotating eccentric masses and rotor pad imbalance during operation [70]. Through literature, it has been observed that accurately locating and analysing the cause of vibration amplitudes requires a reliable dynamic model of the orbital sander for both designing better tools and equipment and for effective vibration control. Researchers from [68, 70] had built an experimental measurement setup to measure the tool's vibration frequency range.

5.2.1 Experimental Approaches for Determining Vibrations

To investigate the vibrational forces generated by the sander tool, a research setup was designed under free-free conditions, where the tool was suspended using ropes and left hanging in mid-air, subjected only to its self-weight, as shown in Figure 5.4.

In the first case, as illustrated in Figure 5.4a, authors [69] used experimental modal analysis (EMA) to extract the dynamic properties of the tool. The physical sander is then prepared with up to 72 node points, which helps capture the shape and vibratory response of the tool. Then **impact testing** is performed by striking the tool in this condition and recording its response. The collected data is then run through the Frequency response function (FRF) from which the modal mass, damping and stiffness for different modes of vibration frequencies are derived.

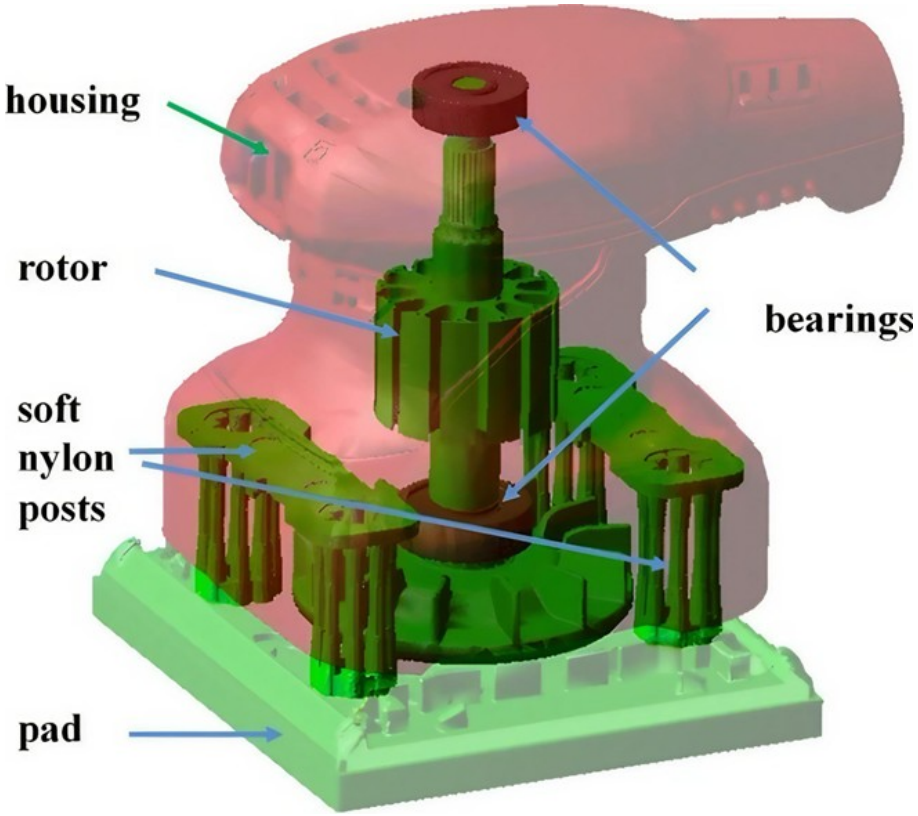

Figure 5.3: Assembled version of the critical parts in a typical orbital [68]

(a) The impact testing setup for the orbital sander in a free-free condition [69].

(b) Experiment to measure the acceleration of the housing[70].

Figure 5.4: Experimental Modal Analysis

To capture this Data, Tri-axial accelerometers are mounted on the top of the sander to capture the accelerations in all three principal directions, by doing the spectrum measurement for capturing the Vibration spectrum of the tool. Overall, this experiment conducted by [69] showed that the tool's first three vibration modes are in the range of $50 - 350Hz$. Additionally, the results show that the highest vibration level occurs along the z-direction.

In a similar experiment, the authors in [68] first conducted a modal analysis, as shown in Figure 5.4b, selecting six points on the sander housing for the test. Three directional accelerometers were then mounted at four locations on the top of the housing. The sander was suspended by a string and operated at 13,500 rpm for 120 seconds, during which acceleration time histories were collected along three directions. A **frequency domain analysis (FFT)** was subsequently performed to identify the dominant peak at the rotor speed, thereby revealing the true source of vibration.

The results indicated that most of the dominant vibration energy occurred along the Y-axis. Furthermore, the unbalanced force generated by the eccentric mass of the rotor was identified as the primary cause of housing vibrations [68].

In essence, these research studies show that orbital sander vibrations are mainly from the internal design of the rotor imbalance. Additionally, conducting experimental research is crucial for determining the key vibrations and natural frequencies of the tool.

5.3 Current Approach for Determining Vibration for the Tool

By now, it can be understood that before starting the design of the end-effector tool for the robotic arm, it is essential to determine the natural frequency of the sanding tool so that the vibration isolator can be designed accordingly, in a way that attenuates the vibrations generated by the tool. For the selected sanding tool, it is necessary to identify its excitation frequencies while the tool is operating. To achieve this, experimental techniques proposed by [68, 69] can be employed to identify the frequency modes and thereby determine the tool's operating frequency range.

In the present approach, a force–torque sensor is employed instead of a triaxial accelerometer to determine the fundamental frequencies of the tool. This choice is motivated by the availability of an in-house developed force–torque sensor at the Humanoids and Human-Centred Mechatronics (HHCM) Laboratory of the Italian Institute of Technology, which will be used extensively throughout this study.

Six-axis force–torque sensors are devices designed to measure forces and torques along all three spatial axes, providing a complete picture of sensitive mechanical interactions. These sensors have been widely employed in the domain of automation and robotic applications [71]. The core of these sensors is an elastomer that deforms when subjected to external forces and moments, which are measured using transduction methods, most commonly resistive strain gauges as sensing elements [71].

These sensors operate by converting deformation strains into electrical signals, which are then mapped to the corresponding force and torque values using a calibration matrix unique to each sensor design [71]. In the present context, a force–torque sensor can be used to detect the vibrations generated by the random orbital sanding tool by capturing both observable and minute fluctuations in force and torque that occur when the tool is turned on or when it interacts with the workpiece. These vibrations produce dynamic, high-frequency changes in the measured force and torque signals along all six axes. Converting these measured signals into the frequency domain enables the quantification of vibration characteristics, such as amplitude and dominant frequencies, of the tool.

For the current task, we utilised a 6-axis force–torque sensor, specifically the **FT-45** [72], due to its compact and robust structure. It provides a data rate of $1kHz$ for real-time communication and works with Ethernet or EtherCAT network architectures. An image of the FT-45 sensor and its characteristics is shown in Figure 5.5 and Table 5.1.

Figure 5.5: 6 axis force torque sensor (FT - 45) [72].

Parameter	**FT-45**
Dimensions (D × H) mm	45 × 20.8
Load Range	
- Fz	±1000 N
- Fx, Fy	±500 N
- Mx, My, Mz	±20 Nm
Resolution	
- Fx, Fy, Fz	250 mN
- Mx, My, Mz	5 mNm

Table 5.1: Specifications of the FT-45 force–torque sensor [72].

Since this current sensor is quite suitable for analysing the vibration generated by the tool, which is absolutely quite below the load ranges, with this sensor, we will be conducting an experimental test to determine the tool's exciting frequency range.

5.4 Free-Fixed condition Experiment

So far, we have explored different methodologies and techniques that could assist us in performing the vibration analysis for the current orbital sanding tool. During this experimental testing, the tool is turned on and is free to rotate, where one end of the side of the grinding face will be free, and on the other end of the tool will be constrained to a rigid beam. The general overview of the experimental setup was illustrated in Figure 5.6.

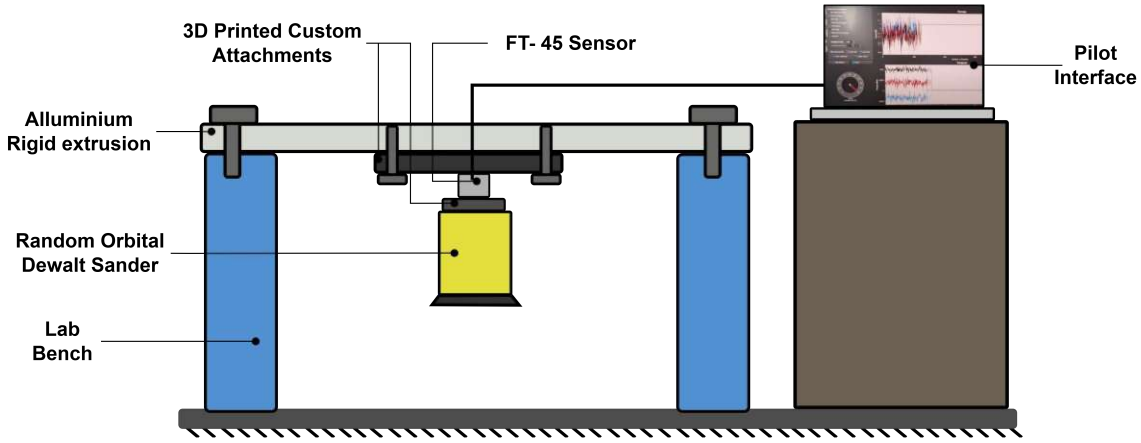

Figure 5.6: A general illustration of the Experimental Setup for collecting the data.

In this setup, the orbital sander was slightly modified to fit with the force–torque sensor. For this purpose, a top-cap interface was designed and 3D-printed to hold the sensor, which was then tightly fastened to the existing mounting holes of the tool, as shown in detail in Figure 5.7. The force–torque sensor was subsequently attached to another 3D-printed rectangular plate, which was rigidly bolted to an aluminium extrusion profile that itself was firmly secured to the laboratory bench on both sides. Since the sensor is capable of Ethernet connectivity, data retrieval was straightforward and efficient.

After the experimental setup was completed, the sensor was connected to a laptop via an Ethernet cable. Proprietary laboratory software, **"SensLiveView"**, was then used to collect and record the force–torque sensor data.

Before the start of the experiment, a few essential parameters needed to be fixed; one of them was the sample rate, which was set to **1000 Hz**. The sample rate was chosen based on the Nyquist criterion for sampling and to eliminate aliasing [59]. Each experimental run lasted only **20 seconds**; that is, the data obtained from the force–torque sensor was recorded for about 20 seconds. During the experiment, there was no human interaction or any other external interference with the tool, as it was fixed to a rigid frame. This setup was designed to replicate the conditions of the tool when it is mounted on the robotic arm. Tests were conducted over the entire speed range of the sanding tool; in the

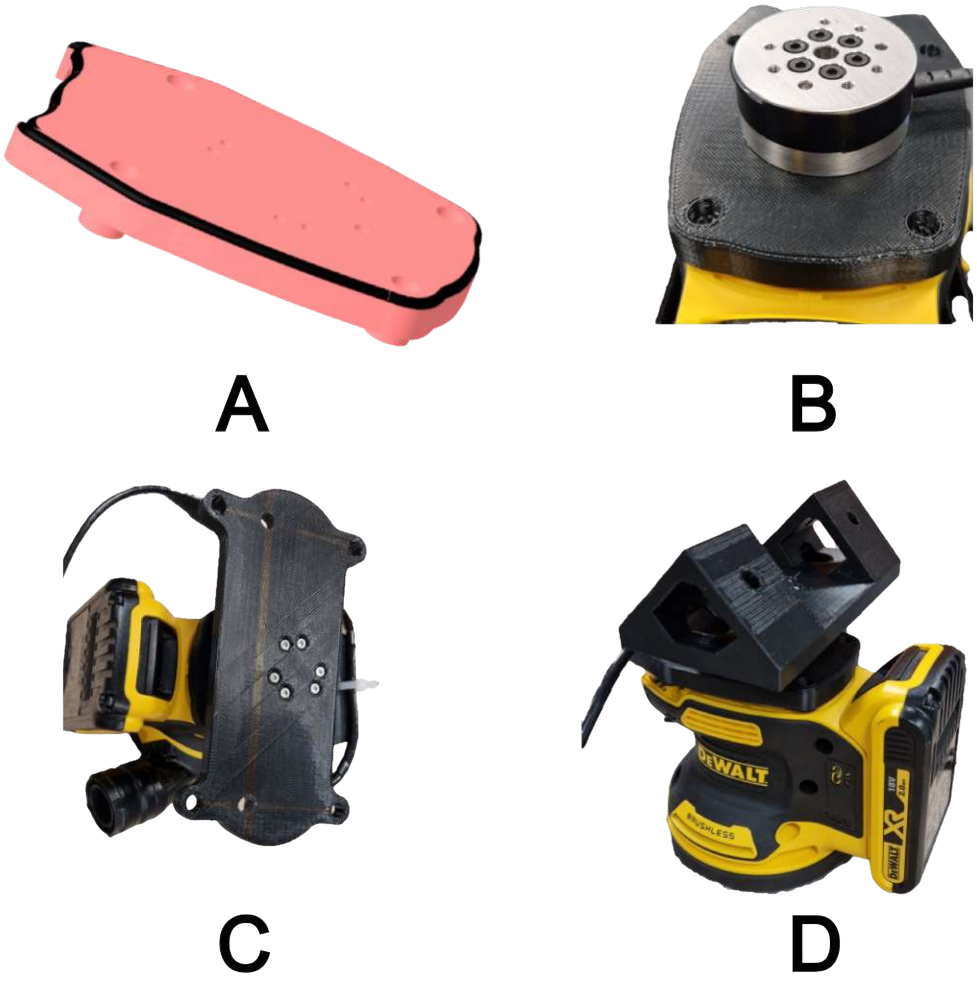

Figure 5.7: (a) CAD model of the modified Top cap for the tool, (b) Mounting of the FT sensor onto the modified 3D-printed cap, (c) A 3D-printed part for fixing the tool onto the aluminium extrusion, (d) A 3D-printed wedge-shaped part which is used to fix the tool in $45°$ orientation.

case of the DeWalt sander, this corresponded to seven speeds.

During this testing, three different experiments were performed by altering the tool mount angle from zero degrees to forty-five degrees, and then to a ninety-degree orientation. Within all three experiments, the data were collected under the same parameters. By doing this, the total orientation range of the tool once mounted on the robotic arm could be mimicked, allowing observation of whether any discrepancies in the frequency characteristics occurred as the tool orientation changed.

From all these experiments, only forces were considered, not torques. The exclusion of torques was justified because, as observed during testing, the changes in torques were minute compared to the changes in forces. Therefore, the analysis concentrated only on

the forces generated while the tool was in motion.

5.4.1 Zero Degree Orientation

Initially, the tool is fixed vertically downwards, which we considered as the zeroth position starting from the bottom, which is shown in the Figure 5.8. In this orientation, we conducted a recording of the force data for approximately 20 seconds each over the entire speed range of the tool (1-7 speeds).

Figure 5.8: Tool fixed in the vertical downward zero-degree orientation

Once all the force data has been recorded, while the tools are in free rotation, the data, obtained in comma-separated value format, is then plotted in the MATLAB environment. Here, one of the force graphs for $speed - 6$ with respect to time in seconds is shown in Figure 5.9.

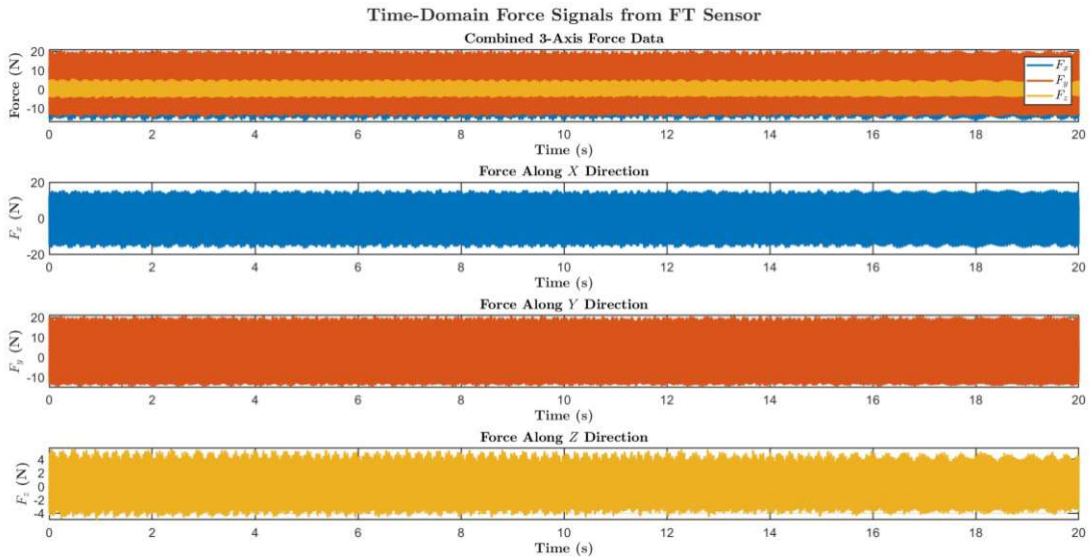

Figure 5.9: Force-time domain Plot when the tool is in zero orientation recoded for $speed6$.

From the above figure, it can be evaluated that the magnitudes of force along the x and y (radial) directions, with Root Mean Square (RMS) values of **9.68** and **11.1**N, are

greater than the force along the z (axial) direction, which has an RMS value of **2.802**N. This difference indicates that the dominant forces are generated in the planar directions while the sanding disc is rotating. Because the orbital sander has some eccentricity, once the disc is in motion, it generates oscillations in addition to rotations, creating a mass imbalance in the x and y directions. The resulting imbalance produces considerable disturbances in these directions. Furthermore, the remaining data plots for the other five speeds consistently show a minimum force magnitude along the z-direction.

Now, according to the experimental analysis mentioned in [68, 69, 70], the force data in the time domain were converted into the frequency domain, as illustrated in Figure 5.10. This plot was obtained after performing a Fast Fourier Transformation (FFT) on the resulting time-domain force data for $speed; 6$.

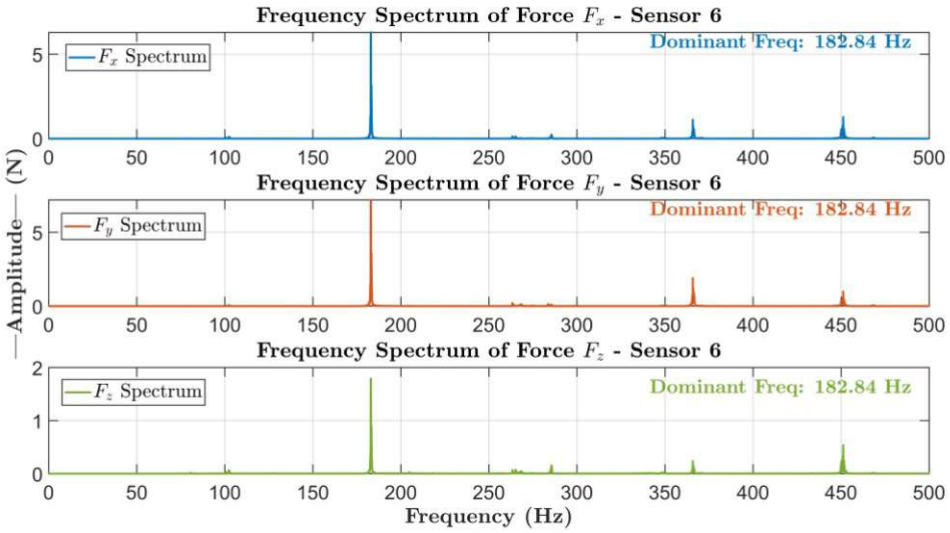

Figure 5.10: Amplitude-Frequency domain plot for the force-time domain plot in zero orientation recoded for $speed - 6$.

Here is the Frequency spectrum plot, which is far clearer and cleaner to analyse and inspect the fundamental frequency of the tool at $speed - 6$, which is evident with a significant spike that is around 182.84 Hz, which corresponds to the primary excitation frequency of the tool during its operation. The presence of a strong peak is detected in all axes, indicating that the vibration at this frequency is being transmitted and detected in every direction. Additionally, other smaller peaks appear at higher frequencies around 350 Hz and 450 Hz, which represent the higher harmonics or sub-harmonics components generated by non-linearities in the system, such as imperfections in tool motion or structural resonances of the setup. Several-minute peaks are typically attributed to random noise, such as electronic interferences or minor dynamic responses of the structure and sensor. This frequency-domain analysis confirms that the primary source of force fluctuation is periodic and dominated by the tool's operational dynamics.

A comprehensive analysis of all the data recordings we have analysed them in the frequency domain spectrum over the entire speed range of the tool, and here is the final table and bar chart of the natural frequencies of the tool shown in Table 5.2 and in Figure 5.11.

Table 5.2: Statistical Summary of FT Sensor RMS Force Measurements and Natural Frequencies Across Tool Speeds in Zero Orientation.

Tool Speeds	Axis	Natural Frequency (Hz)	RMS (N)	Total RMS (N)
1	X-axis	150.8925	2.9651	6.6448
	Y-axis	150.8925	5.4127	
	Z-axis	150.8925	2.4625	
2	X-axis	159.4420	4.6438	8.1364
	Y-axis	159.4420	6.4245	
	Z-axis	159.4420	1.8338	
3	X-axis	165.5917	4.6611	8.5802
	Y-axis	165.5917	6.9363	
	Z-axis	165.5917	1.9447	
4	X-axis	171.3914	7.1291	11.6906
	Y-axis	171.3914	8.9448	
	Z-axis	171.3914	2.4159	
5	X-axis	171.3914	7.1291	11.6906
	Y-axis	171.3914	8.9448	
	Z-axis	171.3914	2.4159	
6	X-axis	182.8409	9.6801	14.9929
	Y-axis	182.8409	11.1008	
	Z-axis	182.8409	2.8025	
7	X-axis	189.6905	12.9407	19.2743
	Y-axis	189.6905	12.9585	
	Z-axis	189.6905	6.0096	

As we can observe from the statistical summary table, which specifies Root Mean Square (RMS) forces, the total RMS increases with tool speed for all axes. Higher tool speeds lead to greater overall force magnitudes and larger fluctuations. Among the three axes, the **Y-axis** consistently records the largest in RMS forces, thereby having the tool's dominant vibration and force transmission occur in this direction. This observation can

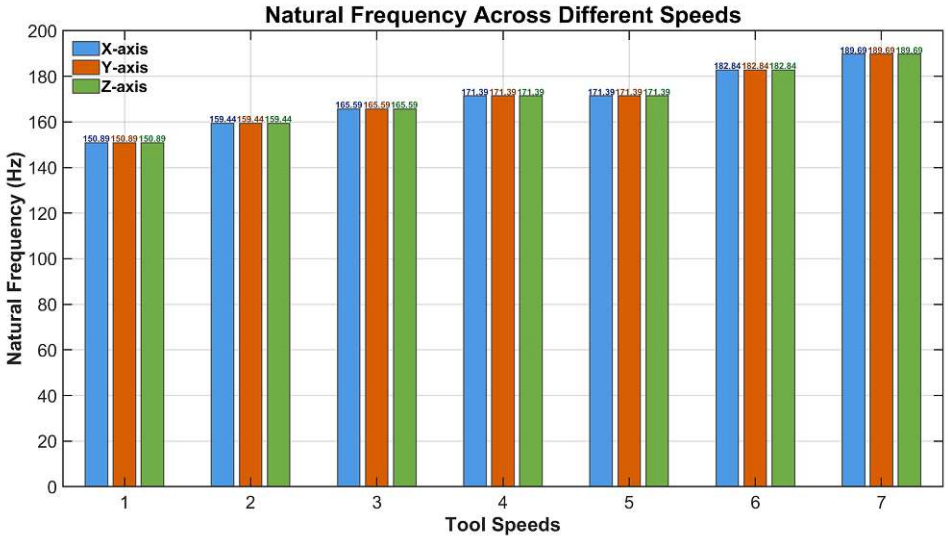

Figure 5.11: Bar Chart of Natural Frequency vs. Tool Speed for Each Force Axis - Zero Orientation.

also be found in a prior research study [68], which identifies a common factor affecting the cause of vibrations. It has also been observed that as tool speed increases, amplitudes of RMS force signals also increase, which in most of the mechanical systems, where higher rotational speeds induce large dynamic forces, occurs both through increased imbalance and higher interaction forces with the mounting structure.

Additionally, from the natural frequency bar chart, it can be observed that the dominant frequency increases with tool speed, indicating a linear relationship between tool speed and the measured natural frequency. The natural frequency extracted from the force signals rose from approximately **151 Hz** at the lowest speed to nearly **190 Hz** at the highest speed, consistent with the expected relationship between rotational speed and vibration frequency. Furthermore, all three axes exhibited the same natural frequency levels at each speed, suggesting that the tool's vibration is strongly governed by its rotational speed and that the structure may be dynamically coupled. Such dynamic coupling could represent a potential limitation for tool operation, as higher vibration magnitudes can lead to increased wear and cause unnecessary chatter between the sanding tool and the workpiece.

This experimental study demonstrates an explicit mapping between speed and measured natural frequency, ranging from **151 Hz to 190 Hz**, which validates both the FT sensor measurement process and the assumed tool dynamics. The observed mapping highlights the importance of considering the dominant frequencies of the tools when designing the vibration isolator. Consequently, a similar trend was observed during experiments conducted in different tool orientations.

5.4.2 Forty Five Degree Orientation

This time, the tool is aligned in a $45°$ orientation, as shown in Figure 5.12. The same experiment is also repeated for all tool speed ranges, using the same parameters.

Figure 5.12: Tool fixed at a forty-five degree angle.

By repeating the same procedural steps that were in detail mentioned in the zero orientation case, the recorded force signals, being in the force domain, are converted to the frequency domain using FFT. A comprehensive table was generated for the current orientation of the tool, along with other crucial parameters such as RMS.

Here is the Table 5.3 that summarises the force statistics and dominant natural frequencies which are measured by the FT sensor over the entire range of speeds, also the final Bar chart Figure 5.13 to show the different natural frequencies across all the tool speed and base axes.

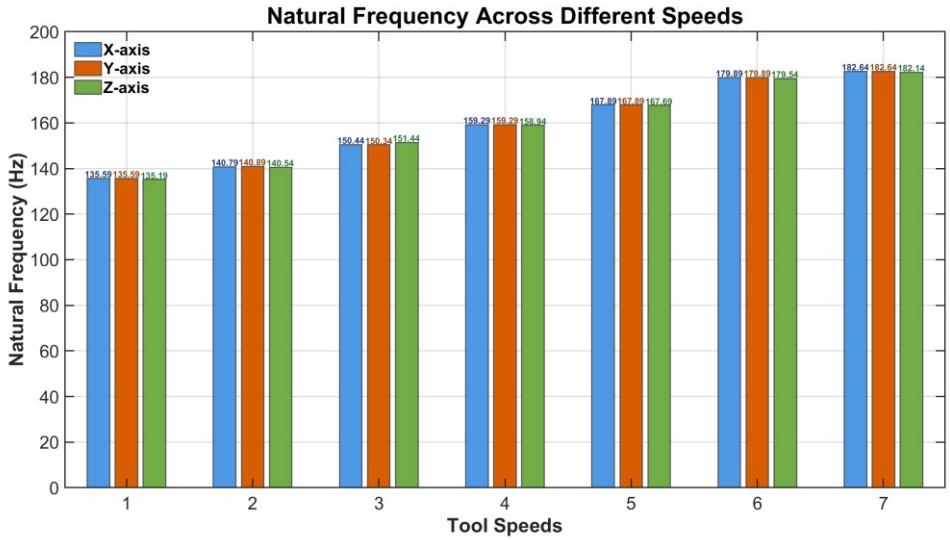

Figure 5.13: Bar Chart of Natural Frequency vs. Tool Speed for Each Force Axis - Forty-Five Degree Orientation

Here, the natural frequencies across all axes increase with tool speed, as observed in the zero orientation. However, at lower speeds, the values are slightly reduced compared

Table 5.3: Statistical Summary of FT Sensor RMS Force Measurements and Natural Frequencies Across Tool Speeds in Forty-Five Degree Orientation.

Tool Speeds	Axis	Natural Frequency (Hz)	RMS (N)	Total RMS (N)
1	X-axis	135.5932	3.0696	5.6895
	Y-axis	135.5932	3.7822	
	Z-axis	135.1932	2.9399	
2	X-axis	140.7930	2.2560	5.7803
	Y-axis	140.8930	4.4649	
	Z-axis	140.5430	2.8960	
3	X-axis	150.4425	2.6479	9.1372
	Y-axis	150.3425	5.7545	
	Z-axis	151.4424	6.5851	
4	X-axis	159.2920	5.2517	9.5064
	Y-axis	159.2920	7.0129	
	Z-axis	158.9421	3.6892	
5	X-axis	167.8916	15.9674	23.7692
	Y-axis	167.8916	8.9528	
	Z-axis	167.6916	15.1613	
6	X-axis	179.8911	8.0375	20.1809
	Y-axis	179.8911	8.7677	
	Z-axis	179.5411	16.3032	
7	X-axis	182.6409	5.0694	18.7345
	Y-axis	182.6409	10.0978	
	Z-axis	182.1409	14.9438	

to the zero orientation, resulting in greater compliance and a softer system response. At higher speeds, the Z-axis exhibits natural frequencies that are slightly offset from the X and Y axes, indicating anisotropic behaviour. The observed anisotropy is likely due to the tool's mass distribution and the altered loading direction in the 45-degree setup.

The RMS values, especially for the **Z-axis at higher speeds from 5–7**, are substantially higher than in the zero orientation. The increased RMS values reflect greater force transmission along Z, which is consistent with a 45-degree tilt exposing the Z-axis to larger dynamic loads.

Compared to the zero orientation, mounting the tool at $45°$ results in slightly lower

natural frequencies ranging from around **135.59 Hz to 182.64Hz**. There, while designing the vibration isolator, this range of frequency domain should also be taken into account to model an effective solution.

5.4.3 Ninety Degree Orientation

Lastly, the tool is fixed horizontally in a ninety-degree orientation from its original vertical downward position, as shown in Figure 5.14. The same set of experimental parameters was set, and the recording of the force data was collected for a duration of $20 seconds$.

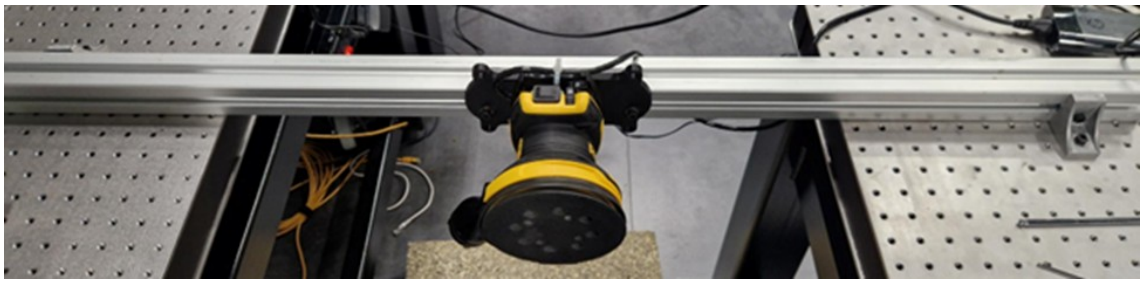

Figure 5.14: Tool fixed in a Ninety-degree angle position

After the recordings were collected, the data was then run through FFT analysis for obtaining the dominant frequency and other statistical results just similar to its predecessors, which is detailed under the Table 5.4, along with a bar chart plotting out all the dominant frequencies over the entire speed range of the tool, which is illustrated in the Figure 5.15.

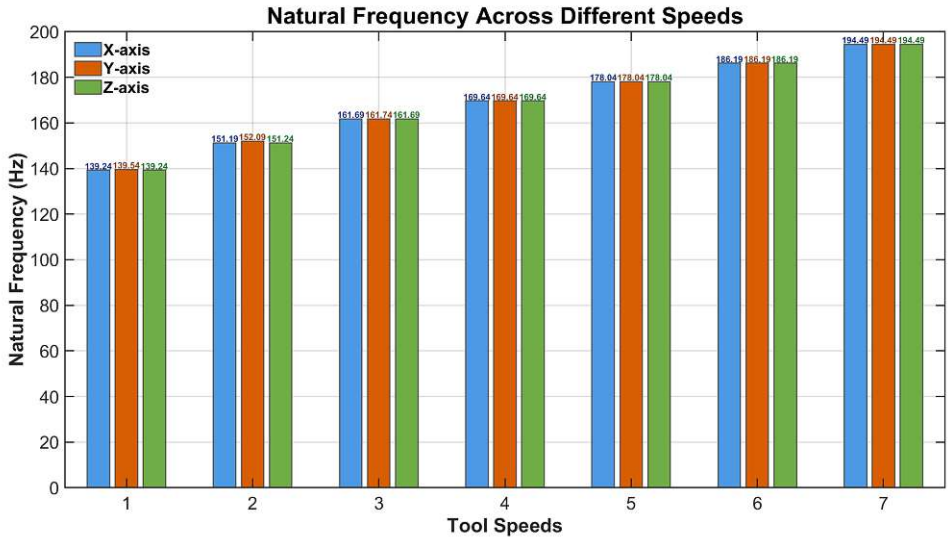

Figure 5.15: Bar Chart of Natural Frequency vs. Tool Speed for Each Force Axis Ninety-Degree Orientation

Table 5.4: Statistical Summary of FT Sensor RMS Force Measurements and Natural Frequencies Across Tool Speeds in Ninety-degree Orientation.

Tool Speeds	Axis	Natural Frequency (Hz)	RMS (N)	Total RMS (N)
1	X-axis	139.2430	15.8947	17.2236
	Y-axis	139.5430	3.2974	
	Z-axis	139.2430	5.7567	
2	X-axis	151.1924	10.3069	13.1563
	Y-axis	152.0924	3.9856	
	Z-axis	151.2424	7.1394	
3	X-axis	161.6919	4.6834	10.4207
	Y-axis	161.7419	5.3551	
	Z-axis	161.6919	7.6144	
4	X-axis	169.6415	3.1029	12.4223
	Y-axis	169.6415	6.9183	
	Z-axis	169.6415	9.8399	
5	X-axis	178.0411	7.0787	15.4937
	Y-axis	178.0411	8.8764	
	Z-axis	178.0411	10.5430	
6	X-axis	186.1907	9.6228	18.5250
	Y-axis	186.1907	11.1538	
	Z-axis	186.1907	11.2326	
7	X-axis	194.4903	13.1368	23.1034
	Y-axis	194.4903	13.9270	
	Z-axis	194.4903	12.9317	

Similar to its previous experiments, the natural frequencies for all axes increase with speed, reaching the highest value of $\approx$ **194** Hz at $speed - 7$ in every axis. This shift upward suggests the system is stiffer and is less compliant when mounted vertically. Also, the three axes' natural frequencies remain closely aligned at each speed, affirming that the primary excitation is still set by tool speed and the structure's fundamental modes.

The RMS values for the X-axis are higher at lower speeds compared to the Y and Z axes, unlike the other orientations. However, at higher speeds, the RMS values along the Y and Z axes are also larger. Additionally, at the highest speed, the force distribution is nearly uniform across all axes. It is observed that no single axis consistently dominates

in RMS across all speeds except at $speed - 7$, for which the distribution of vibration among the three axes becomes more balanced. We can say that at higher speeds, the tool vibrates in a more isotropic manner, which likely results from the increasing dominance of rotationally induced dynamic forces of the tool, which excite the tool and its mounting structure more uniformly, thereby reducing the effect of the initial anisotropic geometry.

Finally, the overall dominant frequency range is from **139.24 Hz to 194.49 Hz**, which is higher than in its previous experiments. Ultimately, the vibration mitigation design parameter must also consider these domain frequencies while modelling the isolator.

5.4.4 Experimental Observations and Discussion

So far, the experimental analysis to find the dominant frequencies of the tool has been conducted. Some of the crucial parameters and observations that will be important when designing the isolator for the tool end effector arm. One of the most essential parameters, critical to determining the range of the tool's natural frequency which was obtained during these tests, it is now evident that the natural frequency of the tool increase with increase in it's speed also the vibration magnitude along the radial direction is greater than the tool's axial direction which explains the behaviour of the random orbital motion of the tool.

In turn, this makes it essential to design the isolator so that it can attenuate both radial and axial vibrations. Still, in the case of axial vibration, their magnitude gets diminished once the tool is in contact with the workpiece, thereby absorbing most of the axial vibrations generated by the tool. Here is the final summary table, which indicates the average RMS forces experienced in each orientation condition, as illustrated in Table 5.5.

It is evident from the summary table that across all three orientations, both the distribution of dynamic forces and the effective frequency range of the tool are strongly influenced by the mounting orientation. From the first zero-degree orientation, the average RMS force along the Y direction is higher, followed by the X direction. This behaviour establishes that the tool's orbital motion is highly responsible for generating Vibration disturbances that could affect the operation of the tool, which is attached to the robotic arm, onto the workpiece. Similar behaviour could be seen in the other orientations, where a substantial amount of vibrations are being developed along these directions. This specific observation is essential during the design of the vibration isolator.

Finally, by considering the overall frequency ranging from **135 - 195 Hz** over the entire tool orientation span in the first quarter ($0 - 90°$). Additionally, this coincides with the tool's operational workspace when it is connected to the robotic arm.

Table 5.5: Summary of average force RMS values and frequency ranges for different tool orientations.

Experiment	Direction	AVG Force RMS (N)	Frequency Range (Hz)
Zero degree Orientation	X-axis	7.02	150.89 – 189.69
	Y-axis	8.67	
	Z-axis	2.84	
Forty-five degree Orientation	X-axis	6.04	135.59 – 182.14
	Y-axis	6.98	
	Z-axis	8.93	
Ninety degree Orientation	X-axis	9.13	139.24 – 194.49
	Y-axis	7.65	
	Z-axis	9.30	

In the upcoming chapters, we will delve into the design and modelling of an interface attachment for the tool to be directly assembled onto the robotic arm, followed by an in-depth study and analysis to design the best suitable vibrational isolator for the Dewalt random orbital Sanding tool.

6 Direct Tool Mounting Interface

So far, we have developed an in-depth understanding of the study's aim, along with an analysis of state-of-the-art technologies and their comparison, thereby establishing the necessity of an autonomous finishing system. We also conducted preliminary experiments to investigate the dynamics of the sanding tool, followed by vibration analysis.

In this chapter, we present the design and modelling approaches for developing an end-effector interface suitable for integration with a collaborative robot. In this research, we employ a Doosan 6-DOF robotic arm equipped with the tool end-effector interface. As with any engineering design process, we begin by establishing the *design criteria*, constraints, and performance characteristics that must be satisfied during the modelling of the end-effector interface.

6.1 Mount Design Criteria and Constraints

From Chapter 5, it is evident that the sanding tool interface must be equipped with a force–torque (F/T) sensor. The inclusion of the F/T sensor is essential for measuring the forces exerted by the robot on the workpiece during processing. By measuring the actual forces experienced by the tool and comparing them to the commanded forces, the sensor enables the implementation of a closed-loop feedback system. Beyond this, several additional design considerations (DC) and constraints were identified:

- **DC-1:** The end-effector should be compact and robust when mounted on the robot, without any shaking or instability during tool operation.
- **DC-2:** The tool should accommodate a commercial F/T sensor and allow manual mounting with minimal time and effort.
- **DC-3:** The design should contain few or no moving parts to ensure robustness in handling reworking tasks in a multidirectional domain. It should be a direct, passive solution that does not require external power sources, unlike active devices.
- **DC-4:** As this design is intended to mount a commercial handheld sanding tool (DeWalt sander) onto the robotic arm, the integration should require minimal or no modifications to the sander itself.
- **DC-5:** Since vibration attenuation is a key objective, the design must be modular to allow flexibility in incorporating a vibration isolator. The design should therefore support two scenarios: (i) without an isolator interface and (ii) with an integrated

isolator.

All of these design considerations and constraints are essential to ensure smooth and effective use of the sanding tool, while also enabling accurate acquisition of force feedback signals.

6.2 Doosan H2515 Collaborative Robotic Arm

As discussed in the earlier chapter regarding the framework of the cleaning robot, the operation is designed to sand the surface defects that were identified. For this task, we have selected the **Doosan H2515** collaborative robotic arm. This arm belongs to the H-series (High Power), which represents the most potent class of collaborative robots. It is a 6-DOF manipulator with a total arm weight of 72 kg, a payload capacity of 25 kg, and an operating radius of 1500 mm [73].

A unique feature of this arm is its six integrated joint torque sensors, one in each joint, which enable precise, responsive, and safe force/impedance control. The presence of these sensors makes the robot particularly well-suited to sanding operations. In addition to its high performance, the H2515 is designed for human–robot collaboration, offering high collision sensitivity. It is also equipped with an in-built gravity compensator, allowing for cost-effective operation across a wide range of applications, such as palletising, assembly, inspection, and automotive bodywork. Moreover, all of these tasks can be performed with nearly half the power consumption of comparable 6-axis articulated robots [73].

With these key features, the Doosan H2515 is the most suitable choice for this study, as it closely aligns with the essential requirements of a cleaning robot. An illustration of the robot, including its links, joints, and corresponding rotational axes, is provided in Figure 6.1. Furthermore, Table 6.1 summarises critical parameters such as joint angle limits and joint speed limits. These parameters are essential for the design of the end-effector interface, as they define the geometrical and volumetric constraints, thereby establishing the allowable design envelope for the interface module.

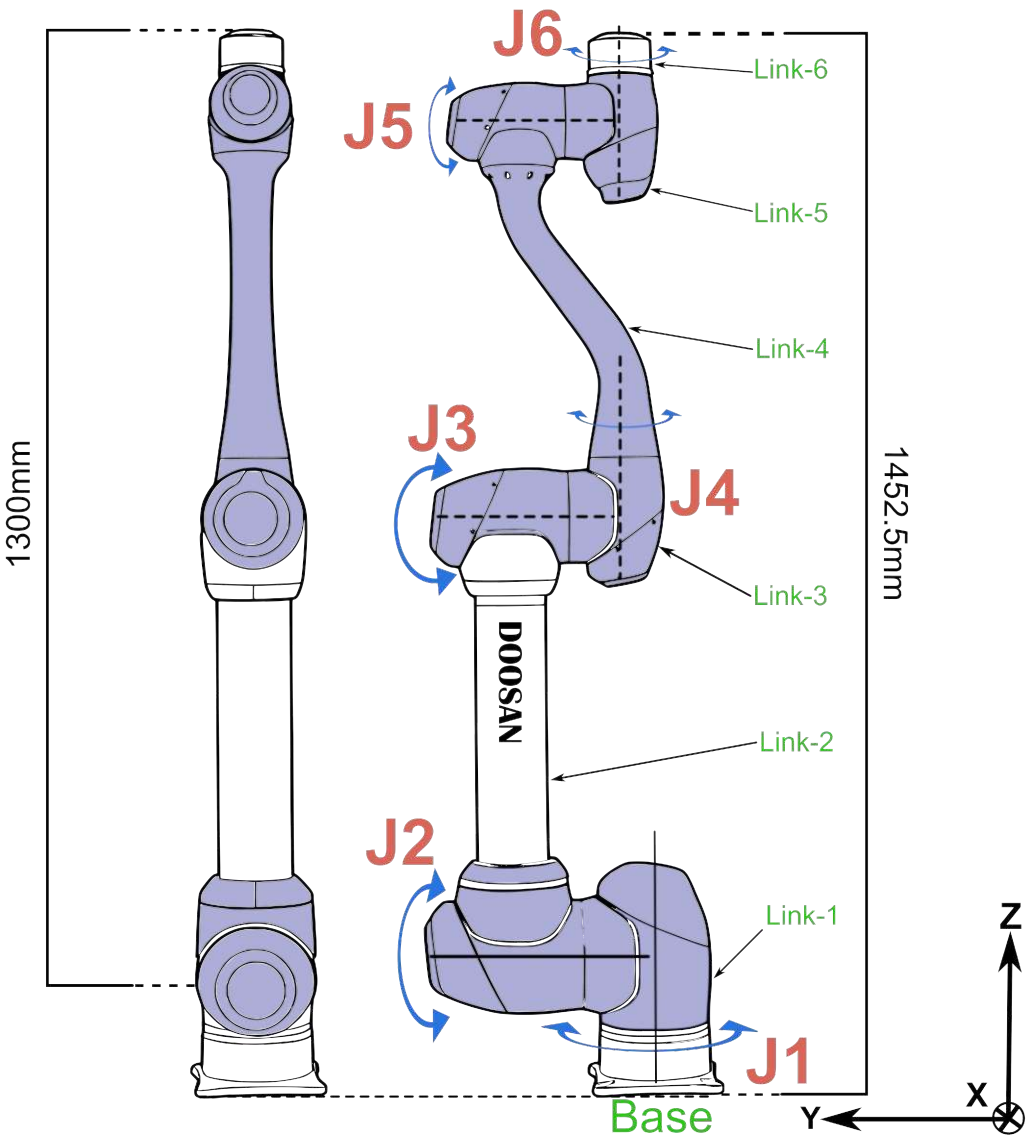

Figure 6.1: Doosan H2515 Structure

Table 6.1: Doosan H2515 Collaborative Robot – Joint Angle, Speed, Robot/TCP and Safety Limits [73].

Parameters		Normal			Reduced			Tolerance
		Min	Max	Default	Min	Max	Default	(+/-)
Joint Angle Limits	J1 (degree)	-360	360	-360∼360	-360	360	-360∼360	3/3
	J2 (degree)	-125	125	-95∼95	-125	125	-95∼95	3/3
	J3 (degree)	-160	160	-145∼145	-160	160	-145∼145	3/3
	J4 (degree)	-360	360	-360∼360	-360	360	-360∼360	3/3
	J5 (degree)	-360	360	-135∼135	-360	360	-135∼135	3/3
	J6 (degree)	-360	360	-360∼360	-360	360	-360∼360	3/3
Joint Speed Limits	J1 (degree/s)	0	100	100	0	100	100	10
	J2 (degree/s)	0	80	80	0	80	80	10
	J3 (degree/s)	0	100	100	0	100	100	10
	J4 (degree/s)	0	180	180	0	180	180	10
	J5 (degree/s)	0	180	180	0	180	180	10
	J6 (degree/s)	0	180	180	0	180	180	10
Robot/TCP Limits	Force (N)	0	1200	243	0	1200	122	–
	Power (W)	0	1600	800	0	1600	650	–
	Speed (mm/s)	0	2500	2000	0	2500	1500	–
	Momentum (kgm/s)	0	400	200	0	400	122	–
	Collision Detection Sensitivity (%)	1	100	75	–	–	–	–
Safety I/O	Speed Reduction Ratio (%)	–	–	–	1	100	20	–

6.3 Design and Prototyping of a Direct End Effector Tool Interface

Before delving into the design and modelling of the end effector, initial modifications were made to the commercial *Dewalt* sanding tool. A relay module (24 V DC coil, 8 A switching current, DPDT – Double Pole Double Throw) and a 3-way female M8 sensor–actuator connector were integrated into the tool. These were connected to the tool's power inlet switch, enabling control of the tool via the Doosan robot's digital I/O port located at Link 6. Consequently, the tool's ON/OFF operation can be executed directly through Doosan's command line interface.

6.3.1 End Effector Interface Modelling

Throughout this study, we employed **PTC Creo**, a powerful 3D CAD software that provides advanced parametric modelling and simulation capabilities, to develop the final tool interface.

As previously mentioned, the manual *Dewalt* sanding tool can be easily customised. The first design task involved modelling a top holder capable of securing the force–torque (F/T) sensor. This placement ensures that whenever the tool contacts the workpiece, both the applied forces and the reactive forces generated during sanding can be accurately measured. Thus, mounting the F/T sensor directly above the tool was considered a practical design choice.

Since no CAD model or technical drawing of the Dewalt sander was available, a simplified reference model was created based on the tool's weight, including its battery module, totalling 2.492 kg. This approximate model served as the basis for designing the end-effector interface. Using the manufacturer's tool cap and hole spacing dimensions as a reference, a top holder interface was created with the required parameters.

For this work, the chosen sensor is the *ATI Industrial Automation F/T Mini58*[74], a compact and high-strength six-axis force/torque sensor well-suited to the application. To avoid exposing the actual sensor to potential damage during preliminary trials, a dummy force–torque module replicating its dimensions ($58\ mm$ diameter and approximately $30\ mm$ height) was modelled. The manufacturer's CAD and technical drawings were used as references for this dummy model, which was employed during initial testing and calibration of the robot. Once the system's stiffness and damping parameters were tuned, the dummy module was replaced with the actual F/T sensor.

To attach the tool to the robot, a flange module was designed. This flange securely connects to another flange mounted on the F/T sensor, with both parts fixed using screws and pins for stability. The flange attached to the F/T sensor replicated the hole pattern of the sensor's mounting interface. Meanwhile, the flange designed to connect to the Doosan arm at Link 6 adhered to the standardised ISO 9409-1-50-4-M6 interface [75], featuring a 50 mm pitch circle diameter (PCD) with M6 threaded holes. Manufacturer-provided technical drawings were used as a reference during the modelling of this flange.

Finally, all components were rigidly assembled using screws and dowel pins. The detailed illustration of the complete end effector tool interface, along with the exploded view of the mount assembly, is shown in Figure 6.2. All parts were initially fabricated using 3D printing to verify fit and alignment before CNC machining of the final assembly.

6.3.2 Metal Prototype Version of the Tool End Effector

All drawings prepared for machining were drafted in accordance with the **UNI ISO 8015** standard. Dimensional tolerances were specified under tolerance class "m", while geometric tolerances followed class "K", ensuring acceptable limits of variation in both geometry and form. Threaded features conformed to ISO metric thread tolerances, with class 6H applied for internal threads and class 6g for external threads, thereby guaranteeing standardisation and interchangeability across components.

For machining, the selected material was **ERGAL 70** (AA 7075), an aerospace-grade aluminium alloy. This alloy was chosen for its excellent strength-to-weight ratio, good corrosion resistance, and superior machinability, making it highly suitable for ensuring the mechanical performance and reliability required of the tool end effector.

The final machined components of the tool module are illustrated in Figure 6.3.

6.3.3 Assembly and Installation of the Tool

The finished machined parts were assembled along with the 3D-printed side cap, as shown in Figure 6.4, which serves to protect the sander from dust and debris.

The fully assembled tool was then mounted onto the robotic arm, as illustrated in Figure 6.5, and the tool's digital ON/OFF connector was wired into Doosan's digital I/O pins. This complete setup was positioned near a test car door panel for subsequent integration and experimental evaluation.

In this chapter, we have detailed the design and modelling process of developing the direct tool end-effector interface and achieving a functional prototype. The final

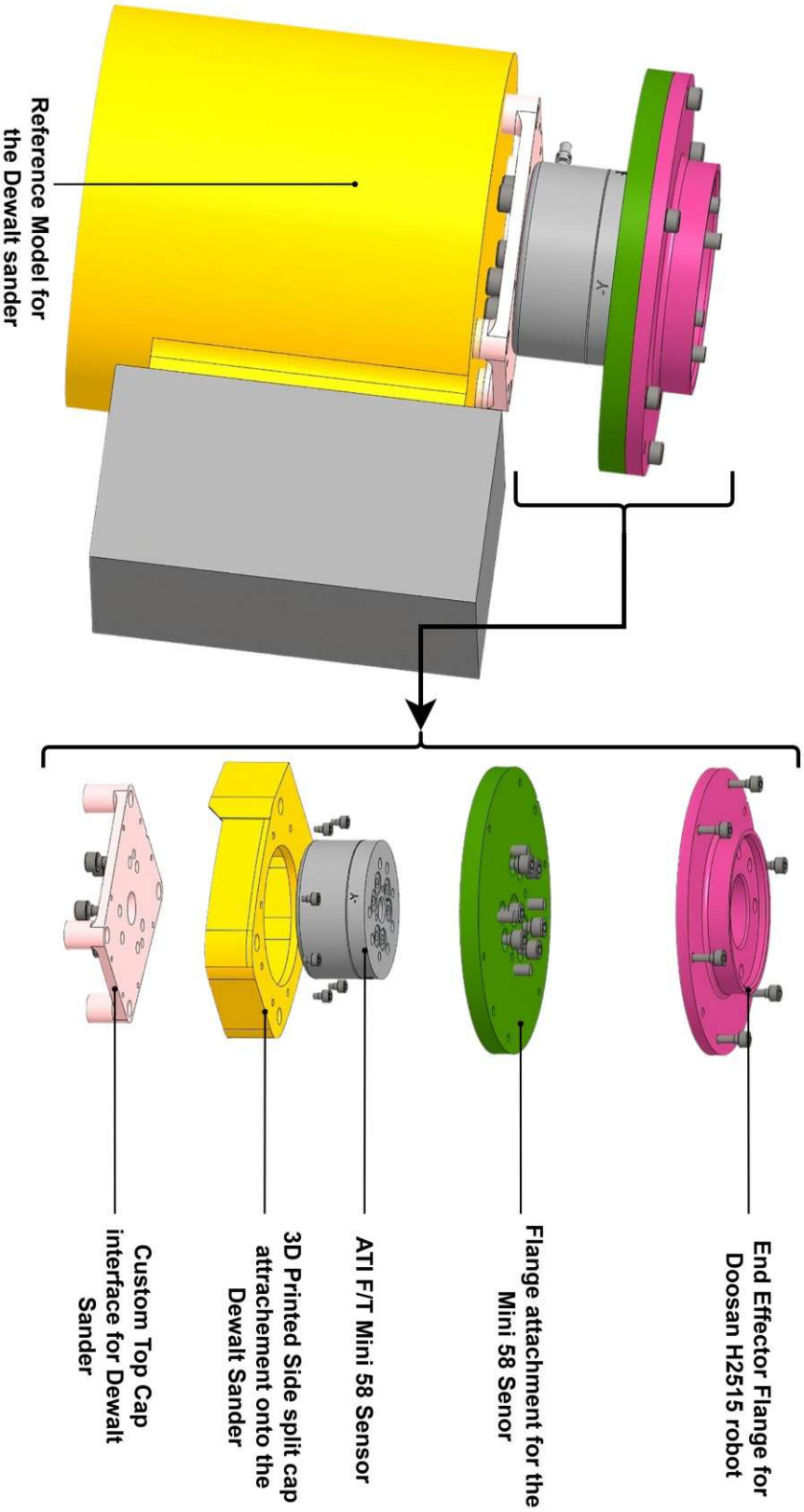

Figure 6.2: Model of the assembled end-effector tool interface with the corresponding exploded view of the attachment interface.

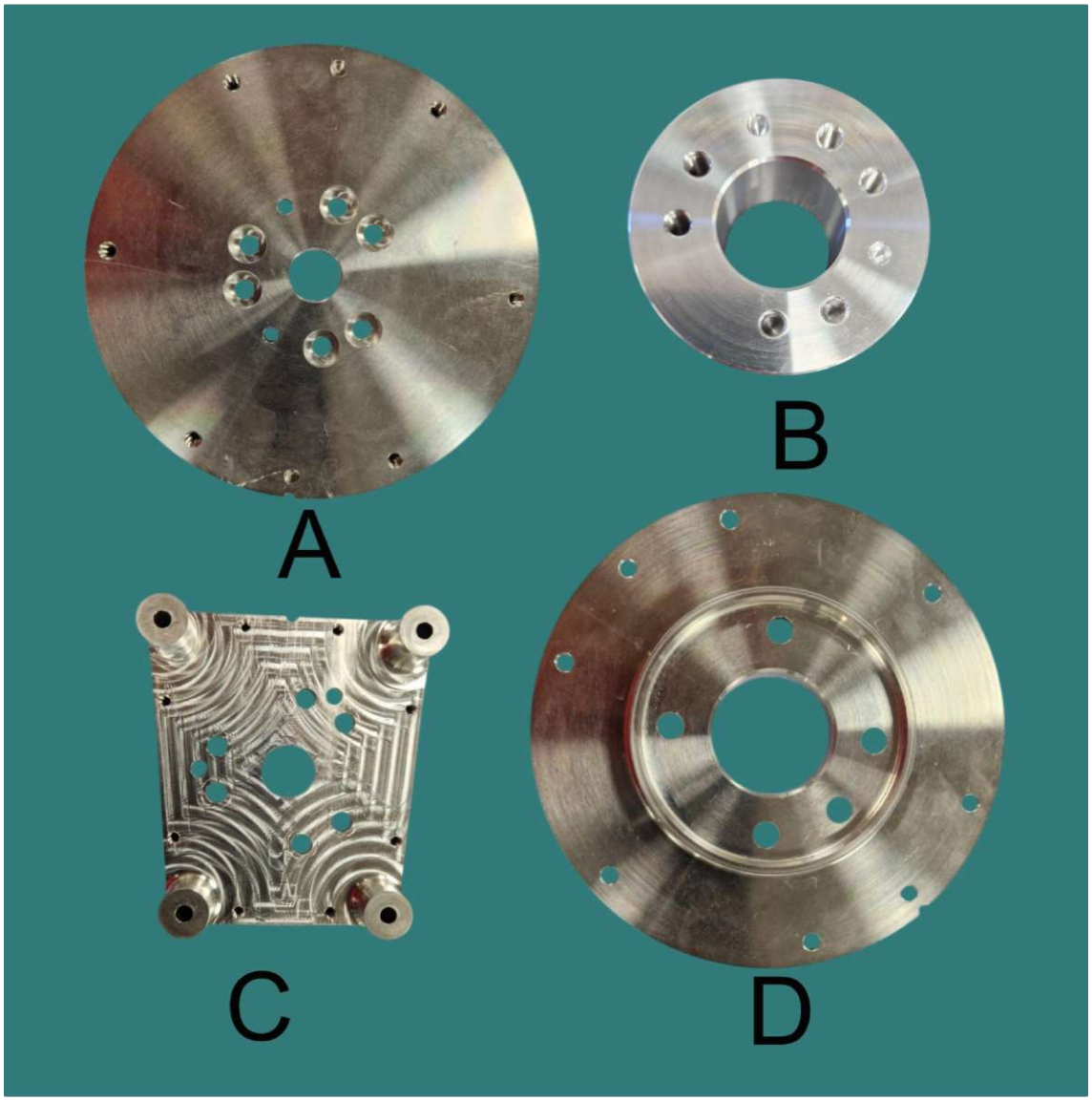

Figure 6.3: Machined components for the attachment interface, a) flange for the F/T sensor, b) Dummy F/T sensor component, c) Custom top cap for Dewalt tool, d) Doosan robot Joint-6 end-effector flange.

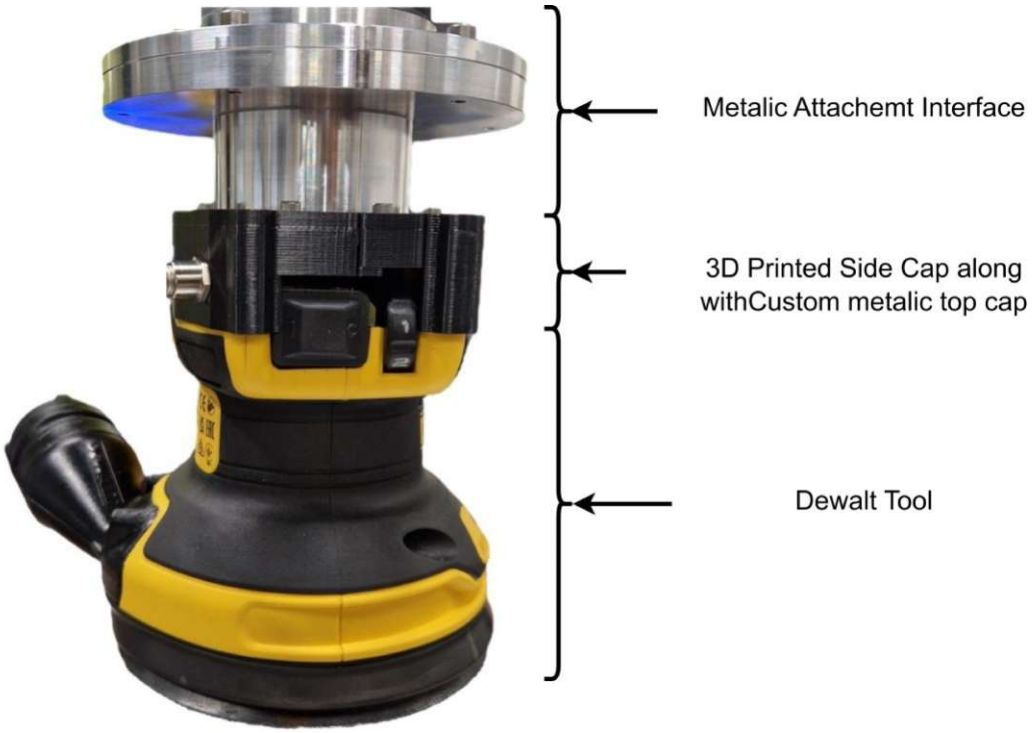

Figure 6.4: Assembled Prototype of the End Effector Tool.

assembled tool interface was successfully attached to the Doosan H2515 robot, where it was validated both in simulation and through initial real-time testing. In the upcoming chapters, we will focus on the design and modelling of a vibration isolator interface, which will ultimately be integrated between the tool and the robot to suppress undesirable vibrations during operation.

Figure 6.5: A Custom Autonomous Sanding Robot Workcell – End effector tool attached to the Doosan H2515 robot arm, along with the car front door.

7 Design and Modelling a Vibration Isolator Element

Until now, we have examined the ideologies and various state-of-the-art end-effector interfaces, both from research and commercial perspectives, along with their design characteristics and working principles. We also conducted real-time experimental testing on the tool to identify its dominant frequencies, followed by modelling and building a working prototype direct interface module to which the sander was fixed.

In this chapter, we now move to the core of our main objective: the design and modelling of a vibration isolator interface, which will be positioned between the tool and the robot to mitigate unwanted vibrations. This interface is expected to ensure more accurate and precise functioning of the force/torque sensors and the robot itself during finishing operations. We will also review insights from state-of-the-art vibration isolation systems and adopt an analytical approach in designing a suitable spring component. Subsequently, we will model the proposed design, perform a Finite Element Analysis (FEA) to verify its structural integrity, and conduct optimisation studies to determine the best possible solution that meets the current research requirements.

7.1 Isolator Design Criteria and Constraints

Similar to the attachment interface, the isolator must be developed based on a set of essential design criteria and constraints, in addition to those defined earlier in Chapter 6. These are as follows:

- **DC-6:** Similar to the design criteria for the attachment interface, the proposed solution must be a robust, compact, and lightweight structure, since it will be mounted onto the robot, which has a limited payload capacity and operates under dynamic conditions.
- **DC-7:** The proposed solution must be a purely passive isolation component, with few or no moving parts, and must not require any external power input. The requirement for a passive design without external power is also a fundamental research constraint within the *MAGICIAN* project.
- **DC-8:** The module should be fully adaptable to the previously modelled attachment interface without any major design modifications. Such adaptability ensures that

the FT sensor, mounted to the robot's flange, can be easily connected to the isolator.

With these three critical design criteria, we surveyed both past and current solutions in the domain of passive vibration isolators. Numerous in-depth research studies and monographs offer valuable insights into vibration isolation and control methods. In this study, several relevant research methodologies were analysed to inform the design of our isolator system.

7.2 State of the Art in Passive Vibration Isolation Systems

In general, as described in Chapter 4, passive vibration control systems consist of three primary components: a spring, a dashpot (damper), and a mass. Together, these elements generate control forces that counteract structural motion without requiring external power. Such passive systems are widely applied, from simple suspension systems in automobiles to large seismic vibration absorbers in bridges and high-rise buildings.

The majority of passive vibration control systems can be grouped into three categories [76]:

1. **Energy Dissipators:** These function by converting kinetic energy generated by structural motion into heat or electricity, thereby reducing vibration amplitudes. They rely on irreversible energy transformation processes within the structure.
2. **Dynamic Vibration Absorbers (DVA):** These work by transferring vibrational energy from the primary structure to an auxiliary system that is specifically tuned to mitigate resonant responses.
3. **Vibration Isolators:** These aim to shield the structure from external disturbances by introducing elements that modify the system's dynamic characteristics, typically lowering its natural frequency and thereby reducing the transmission of vibratory forces. Such isolation techniques are particularly effective in protecting structures from hazardous environmental excitations by preventing resonance with dominant disturbance frequencies.

An overview of these three categories is illustrated in Figure 7.1.

In our current design, we focus on exploring possible techniques and methodologies regarding vibration isolator systems, particularly **elastic isolators**, since they contribute most significantly to vibration attenuation. These isolators typically consist of spring elements, rubber mounts, or air springs, which function by providing mechanical compliance and thereby reducing the transmission of vibrational energy between the source and

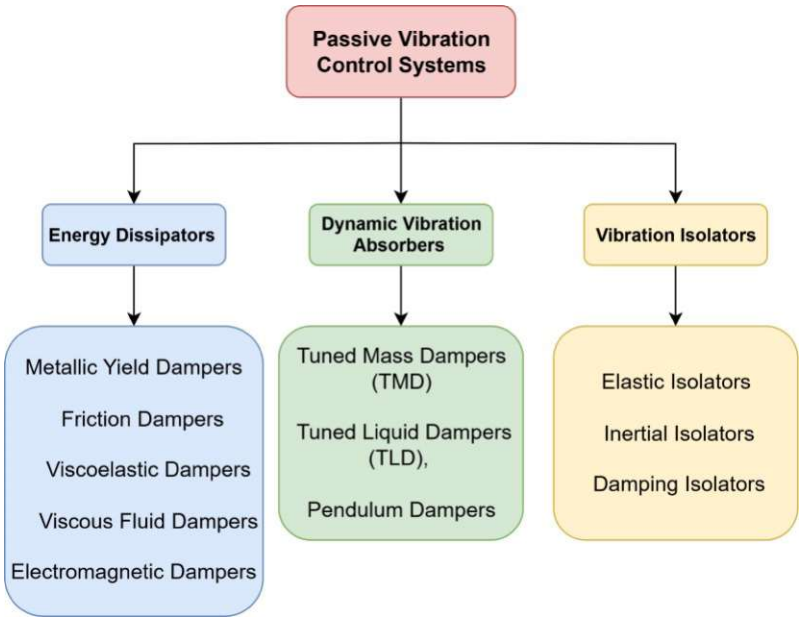

Figure 7.1: Classification of the Passive Vibration Control Systems.

the receiver. A few reference designs were studied before developing our own isolator system.

Our initial idea was to use a simple rubber padding between the robot and the tool, so that vibrations would not be transferred. This approach is attractive because of its compactness, low cost, and inherent damping properties. However, several limitations and risks are associated with this design choice. As demonstrated in [77], the **dynamic stiffness** of rubber is significantly higher than its static stiffness. With increasing excitation frequency, the dynamic stiffness also increases, which can lead to reduced isolation or even amplification. Moreover, rubber modules are strongly **temperature-dependent**, which alters their damping properties. In addition, long-term usage can result in creep, gradually reducing both stiffness and damping [78]. Because of these limitations, rubber padding alone cannot be considered a reliable isolator solution in our design.

7.2.1 Limitations of Linear Vibration Isolation Systems

Most primary isolator components, such as springs and dampers, are inherently linear in nature, and thus fundamentally constrained by a narrow, adequate bandwidth and limited adaptability [79]. From the earlier discussions, it is clear that the effectiveness of a linear isolator is primarily governed by the frequency ratio between the external excitation and the system's natural frequency. For effective isolation, this ratio must typically **exceed** $\sqrt{2}$.

In practice, however, external excitation frequencies are dictated by operational or environmental conditions and cannot be readily adjusted. Consequently, achieving the required frequency ratio depends on lowering the system's natural frequency. Yet, excessively reducing stiffness undermines the isolator's ability to support the system's mass, compromising both **structural integrity and load-bearing performance** [80]. Furthermore, while damping is beneficial for mitigating resonance-induced vibrations, it is detrimental at higher frequencies, where damping forces grow with frequency, thereby reducing isolation effectiveness beyond resonance.

Thus, **linear systems are inherently inadequate for suppressing broadband, low-frequency vibrations commonly encountered in real-world applications**, such as random shocks and wide-spectrum disturbances in machinery and structures.

7.2.2 Need for Nonlinear Isolators

To overcome these limitations, nonlinear vibration isolators have emerged as a critical advancement. Unlike linear systems, nonlinear isolators exhibit **variable stiffness and damping characteristics**, dynamically adapting to the amplitude and frequency of incoming excitations. This adaptability enables superior performance across a broader frequency range, including low-frequency excitations where linear isolators fail.

A schematic comparison of linear and nonlinear vibration isolation systems is shown in Figure 7.2 [80].

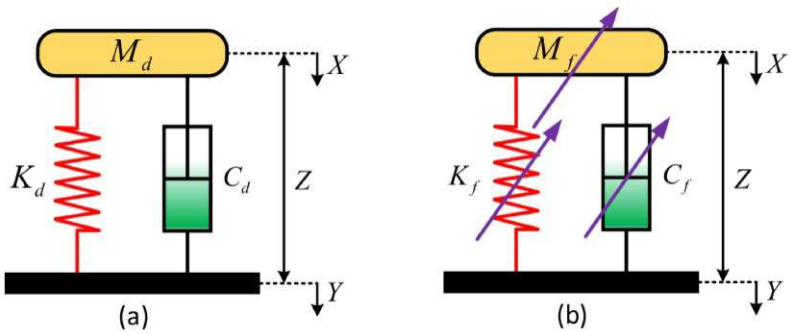

Figure 7.2: Schematic diagram of vibration isolation systems: (a) Linear vibration isolation system; (b) Nonlinear vibration isolation system [80]. where $Z = X - Y$ is the relative displacement between the source and receiver and $X$and Y represent their absolute displacement.

Here, the motion of the system for linear vibration isolation systems having an equivalent mass M_d, damping C_d, and stiffness K_d as constants is described by a linear differential equation:

$$M_d\ddot{Z} + C_d\dot{Z} + K_dZ = -M_d\ddot{Y} \tag{7.1}$$

Also, the dynamic equation for the nonlinear vibration isolation system can be given by:

$$M_f\ddot{Z} + C_f\dot{Z} + K_fZ = -M_f\ddot{Y} \tag{7.2}$$

In Equation 7.1, all of the inertia, stiffness, damping, and restoring forces maintain a direct proportionality relative to acceleration, velocity, and displacement. In contrast, in Equation 7.2, the same parameters exhibit nonlinear behaviour. Here $M_f\ddot{Z}$ represents the *nonlinear inertial force*, $C_f\dot{Z}$ is the *nonlinear damping force*, and K_fZ is the *nonlinear restoring force* [80]. This adaptability enables superior isolation performance across a broader frequency range, particularly at low frequencies where linear systems are ineffective.

Thus, incorporating nonlinear behaviour not only improves vibration suppression and operational bandwidth but also facilitates additional functionalities, such as mechanical energy harvesting and advanced dissipation mechanisms like *nonlinear energy sinks* [79]. Therefore, the adoption of nonlinear vibration isolators is essential for overcoming the inherent constraints of linear systems.

Hereafter, we will particularly examine some of the passive nonlinear vibration isolator designs and their workings.

7.2.3 A Survey on Nonlinear Passive Vibration Isolators

Nonlinear passive vibration isolators are typically categorised into three main groups based on the dominant physical nonlinearity that drives their isolation behaviour. They are classified as shown in Figure 7.3.

As observed from review and survey papers, most isolators fall under the category of *restoring-force nonlinear isolators*[79, 80, 81]. A typical subset is the **negative stiffness** and **quasi-zero-stiffness (QZS)** mechanisms. QZS systems combine a positive stiffness element with a negative stiffness mechanism, as shown in Figure7.4, to produce a near-equilibrium dynamic stiffness close to zero while still maintaining a high static stiffness. The resulting QZS configuration provides very high compliance to low-frequency vibrations while still supporting significant static loads [80].

From these mechanisms, we have analysed a few isolator concepts that could potentially

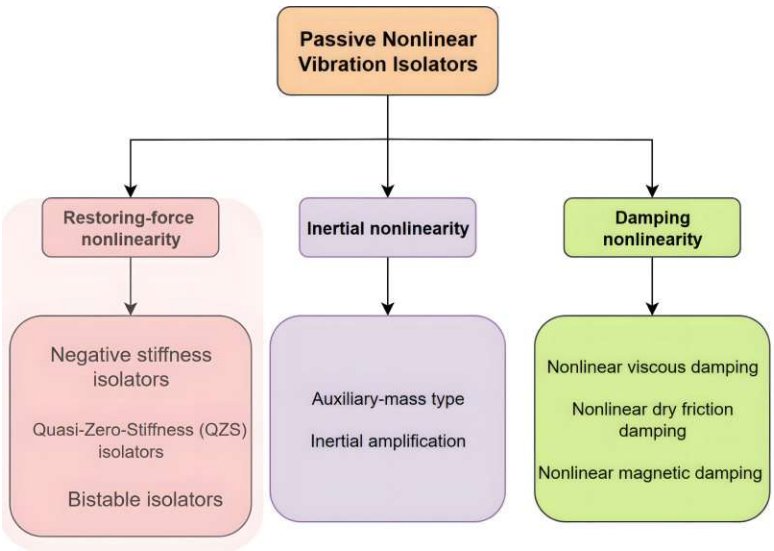

Figure 7.3: General classification of Passive Nonlinear Vibration Isolators.

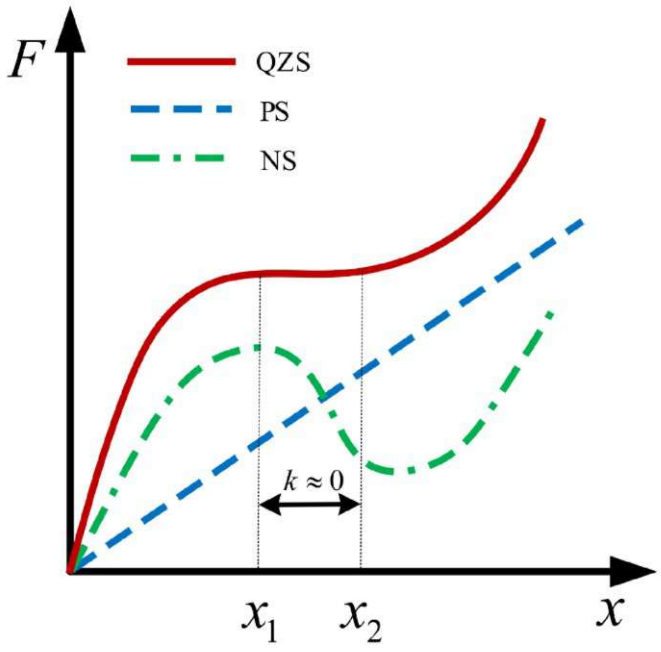

Figure 7.4: Force-displacement relationship of **QZS** vibration isolator. Here, **PS** is the positive stiffness, and **NS** is the negative stiffness, and the combination of both gives a Quasi-Zero-Stiffness mechanism [80].

be implemented in our current use case. One such approach was proposed in [82], introducing the **geometric anti-spring (GAS) isolator**. This design falls within the restoring-force nonlinearity class and is specifically recognised as a QZS mechanism. The schematic of this system, shown in Figure 7.5, is designed to achieve ultra-low frequencies (greater than $3.6\ Hz$) for vibration isolation, where attenuation becomes effective above this frequency. The study further demonstrated that this mechanism can carry high loads, making it particularly suitable for precision applications [82].

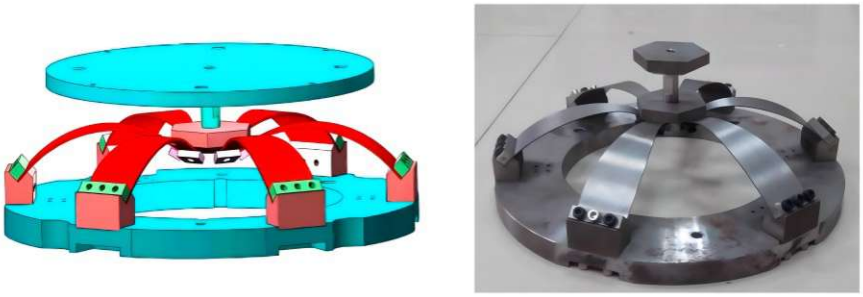

Figure 7.5: Model of the geometric anti-spring (GAS) isolator. Left: schematic representation of the GAS mechanism. Right: initial prototype version [82].

The GAS isolator operates by arranging multiple specially shaped cantilever blade springs in a symmetric pattern, where the lower ends of the blades are rigidly fixed to the base. In contrast, the upper ends are connected to a central load platform. With the application of load, the system's geometry and orientation of the springs create an *anti-spring effect* by leveraging high nonlinear restoring forces [82]. Unlike traditional linear isolators, this design is compact and enables a very low natural frequency without sacrificing load capacity or requiring impractically large springs.

In research [83], a vibration isolation system is investigated that utilises a *negative stiffness structure (NSS)* to enhance low-frequency vibration suppression. The system combines two symmetric negative stiffness elements, which are coupled in parallel with a bar and slide block assembly, along with a conventional positive stiffness spring and a damper that supports the payload's static weight, as shown in Figure 7.6. This parallel arrangement enables the overall dynamic stiffness to be drastically reduced, approaching zero near equilibrium without sacrificing static load capacity.

Since stiffness is directly proportional to frequency, both simulation and experimental results demonstrate that this isolator achieves effective vibration isolation for frequencies as low as 0.1 Hz up to approximately 10 Hz in the critical low-frequency region. Consequently, the system's resonance frequency can be designed much lower than what is achievable with traditional linear isolators. Additionally, due to the negative stiffness property, this mechanism exhibits a *softening behaviour*, which shifts the frequency

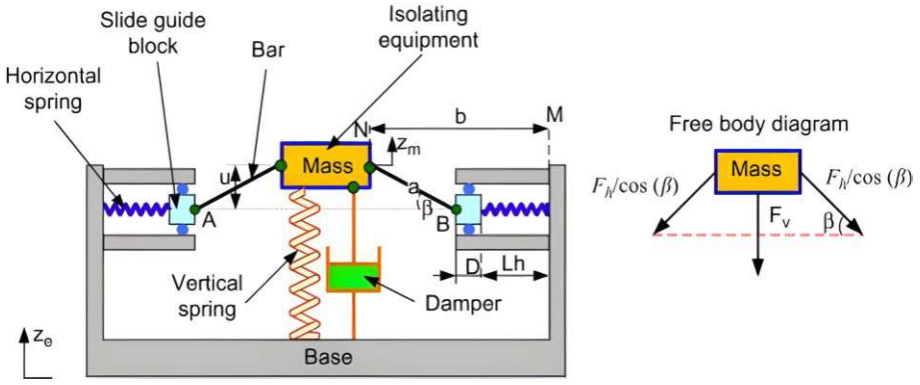

Figure 7.6: Configuration of the proposed Mechanical model of isolation system [83].

response curve and suppresses resonance, resulting in minimal vibration transmission.

A unique design and concept proposed by researchers in [84] introduced a *mechanical metamaterial vibration isolator*, which consists of architected materials whose unique wave or energy-control properties arise mainly from their structure rather than their composition. The mechanism, shown in Figure 7.7, is designed for perfect *energy shielding* by recirculating energy between itself and the energy source, rather than absorbing or transmitting vibrations to the payload. This unit cell consists of a hexagonal frame with strategically placed springs and bars that support a central mass. When external vibrations or disturbances are applied, the metamaterial's special geometry and coupling ensure that the force transmitted to the payload remains nearly constant. As a result, the payload is effectively isolated from vibrations across the full frequency range.

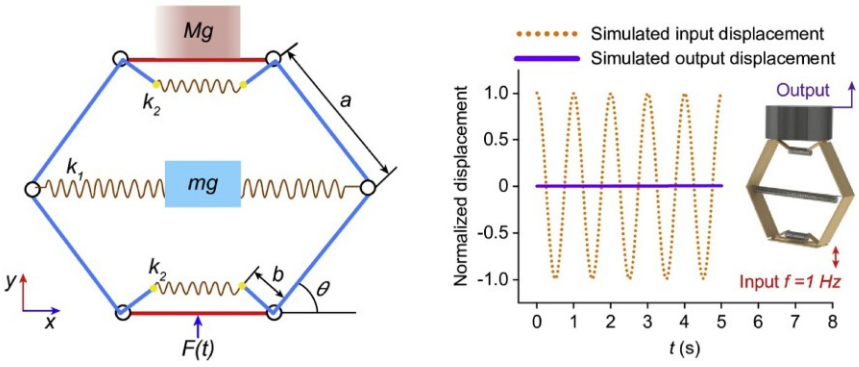

Figure 7.7: mechanical metamaterial vibration isolator. Left: Illustration of the unit cell design. Right: Performance of the proposed vibration isolator at 1 Hz [84].

The behaviour of this isolator mechanism is fundamentally different from classic quasi-zero-stiffness (QZS) or negative stiffness isolators, which typically provide isolation only within a limited band and can transmit low-frequency vibrations ranging from as low as 0.1 Hz up to at least 25 Hz. Most importantly, this mechanism offers truly *multi-directional isolation*, in which both vertical and horizontal vibrations can be blocked

simultaneously [84]. This mechanical metamaterial introduces a new paradigm for vibration isolation, delivering passive, broadband, and multi-directional shielding that is highly robust to disturbances across nearly the entire practical frequency spectrum. This breakthrough makes it a significant advancement for both engineering and scientific applications.

The mechanism depicted in Figure 7.8 is a *Linkage Anti-Vibration Structure (LAVS)*, which utilises a tunable compensation mechanism combining linear positive and negative stiffness. This structure consists of a symmetric polygonal frame (SPS) equipped with oblique linear springs to generate negative stiffness, paired in parallel with a vertical linear spring that provides positive stiffness [85]. This QZS isolation platform is specifically designed for multi-directional vibration isolation (both vertical and lateral) due to its symmetric linkage configuration, which can be tuned for different payloads and application scenarios.

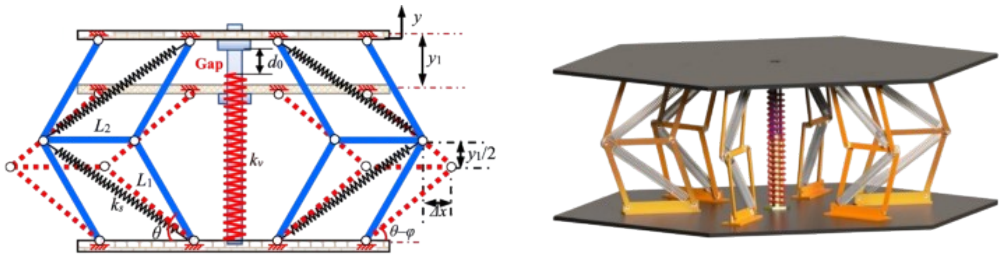

Figure 7.8: Symmetric Polygonal Structure (SPS) isolator.Left: Schematic diagram of a novel linkage anti-vibration structure (LAVS) via linear positive and negative stiffness compensation mechanism. Right: Design of a vibration isolation platform based on the proposed LAVS [85].

The typical frequency range for the LAVS system offers substantial attenuation in the low-frequency range of $0.16 - 10\ Hz$, spanning a broadband isolation region [85]. By precisely tuning the geometric parameters and spring stiffness, an enhanced QZS zone can be achieved over a significant displacement range. This advanced passive isolator is particularly suited for precision instruments, engineering equipment, and applications requiring stability under variable loads and broadband vibration suppression. The mechanism is both robust and tunable, thereby overcoming the limitations of traditional QZS isolators, which often provide only a narrow QZS zone or suffer from high nonlinearity.

From Figure 7.9, which presents a compact, lightweight nonlinear metastructure designed for vibration isolation, based on *bio-inspired quasi-zero-stiffness (QZS)* principles. It falls under the category of **high static and low dynamic stiffness (HSLDS)** isolators [86]. The core structure is a bistable mechanism consisting of two inclined beams that buckle and exhibit negative stiffness due to snap-through instability. At the same time, semicircular arches provide positive bending-dominated stiffness. By carefully

tuning the geometry and arrangement, these opposing stiffness effects combine to create a broad displacement region where the overall stiffness approaches zero—the QZS region. Experimental results [86] confirm that this metastructure achieves substantial vibration attenuation in the low-frequency range, typically from around 3 Hz up to 25 Hz.

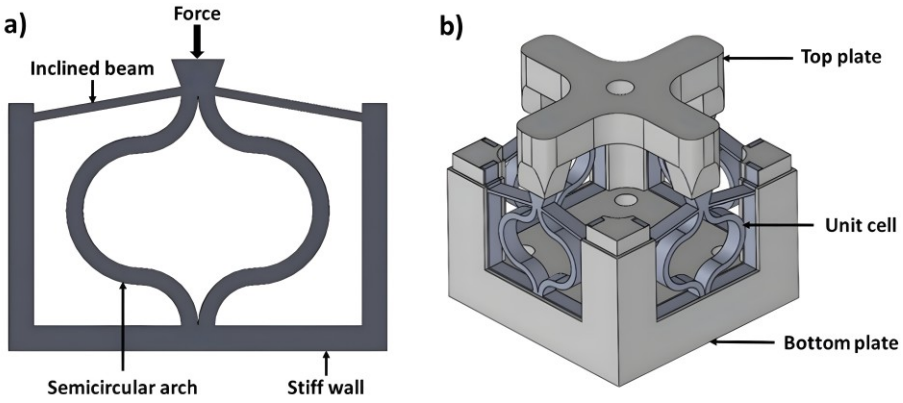

Figure 7.9: Compact nonlinear metastructure. Left: Unit cell of the core structure. Right: Arrangement of the Metastructure isolator [86].

The multi-cell design mentioned in Figure 7.9 ensures multi-directional vibration suppression, making it well-suited for sensitive instruments and industrial applications. The payload is supported on the top plate, resting on the bottom plate, which provides substantial load-bearing capacity. However, as with most QZS/HSLDS isolators, the operational zero-stiffness band is limited to a specific displacement range, and nonlinear effects such as jump phenomena or hysteresis may occur under large excitations. These novel architected structures, with their unusual engineering geometries, exploit compliance to achieve unique static and dynamic properties.

These studies represent some of the essential references analysed for potential adaptation to our current use case. All of these isolator designs are robust and compact, and analysing these works provided valuable insights and design ideas for modelling our own isolation system. However, despite their effectiveness in isolating vibrations, several critical limitations were identified, which prevented their direct adoption in this work.

7.2.4 Limitations in Current Vibration Isolator Mechanisms

One of the primary constraints is that the current tool operates in a frequency range of 135–195 Hz, which falls within the high-frequency regime. The high operating frequency makes most low-frequency isolators unsuitable for adaptation in this study. As highlighted above, the nonlinear isolators discussed are primarily effective in the low- to mid-frequency isolation ranges. Since the tool requires **multi-degree-of-freedom (MDOF)** isolation—such as that offered by metamaterials—most of the QZS and negative

stiffness structures reviewed are more effective in single-degree-of-freedom (SDOF) applications. While one potential design based on a symmetric polygonal structure offers promise, it has a complex assembly process and carries significant instability risks during operation.

Another major limitation is that the final isolator model will be attached to a robotic arm, which itself is a dynamic system. In such cases, most QZS and negative stiffness mechanisms lose much of their theoretical isolation performance when oriented or rotated. Furthermore, their performance is highly sensitive to the precise tuning of geometric and spring parameters; once tuning is lost, retuning is required. Although a few designs provide high-frequency isolation, most offer only a narrow and specific isolation range.

Ultimately, all the reviewed designs rely on spring and damping components to achieve vibration isolation. For the next phase of this research, however, we consider the adoption of more compliant structures that can provide tunable stiffness ranging from near-zero to prescribed values. Such compliant mechanisms may enable improved broadband and high-frequency isolation, greater robustness against instability, and better adaptability to dynamic MDOF environments.

For these reasons, the subsequent analysis in this work focuses on identifying and developing more suitable isolation designs that can deliver broadband, high-frequency vibration attenuation.

7.3 Folded Beam Vibration Isolation Systems

All of the previously mentioned vibration isolator mechanisms were shown to be efficient in mitigating vibrations in the low-frequency domain, typically where the excitation sources are below $30\ Hz$. However, for our current requirement, the tool operates in the frequency range of $135 - 195\ Hz$, which falls in the high-frequency domain. Therefore, according to the design criteria, the proposed isolator must provide effective isolation at frequencies below $95\ Hz$.

7.3.1 Folded Beam Micro Vibration Isolation Systems in Spacecraft

In the search for isolators capable of attenuating vibrations in our required frequency range, an effective solution can be found in the domain of space applications. Micro-vibrations in spacecraft represent a significant challenge for high-precision missions, as they can degrade the performance of sensitive payloads such as optical telescopes (illustrated in Figure 7.10), cameras, and other scientific instruments. The typical range

of these micro-vibrations is $0.1 - 300\ Hz$, with disturbances above $30\ Hz$ classified as high-frequency vibrations [87]. These vibrations are often induced by internal mechanical components, specifically momentum wheel assemblies (MWA), reaction wheel assemblies (RWA), control gyros (CG), cryocoolers, mobile mirrors, solar array drive mechanisms, and other spinning or moving devices [88].

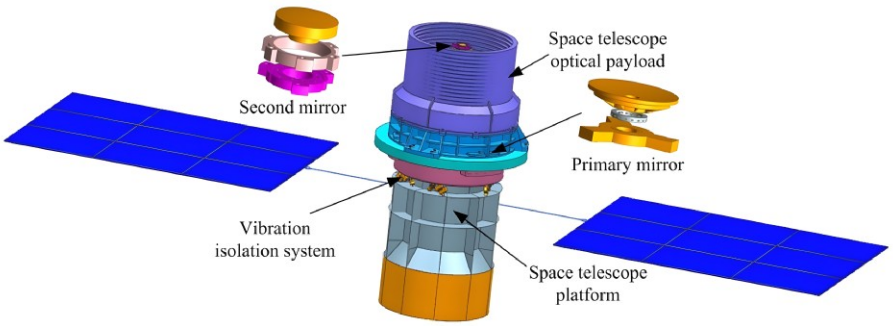

Figure 7.10: Structural model of the space optical telescope [89].

Most of these disturbances arise due to static and dynamic imbalances caused by mass eccentricity relative to the rotational axis, as well as imperfections in bearings [87, 88]. These imbalances inject dynamic forces and moments into the spacecraft structure, which then propagate through mechanical connections to sensitive components.

To mitigate the effects of micro-vibrations, various isolation strategies have been developed. Among these, **passive isolation techniques** are widely adopted in spacecraft because they provide reliable and stable performance without requiring external power. One particularly innovative and effective class of passive isolators is based on the use of *folded beam structures*. Folded beams, often implemented as flexure-based suspensions, are designed to provide high static stiffness sufficient to support the mass of onboard components such as RWAs or MWAs (as shown in Figure 7.11), while simultaneously achieving low dynamic stiffness in the directions of interest. These structures are especially effective in attenuating disturbances in the medium- to high-frequency range above $30\ Hz$ [87].

Unlike viscous fluid or viscoelastic dampers, folded beams rely purely on elastic deformation and structural configuration. Several researchers have designed isolation platforms using folded beams, demonstrating that such platforms can effectively decouple dynamic disturbances above their low resonance frequency without relying on sensitive damping equipment [87, 88].

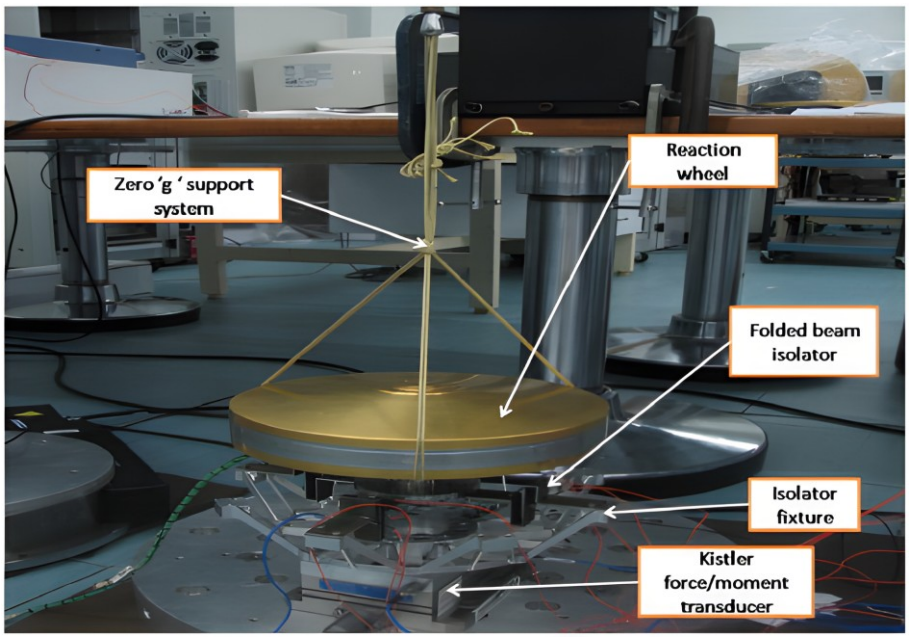

Figure 7.11: Reaction wheel assembly with folded beam isolator [90].

7.3.2 Design and Role of Folded Beam Structures in MEMS Devices

Microelectromechanical systems (MEMS) are miniaturised devices that integrate electrical and mechanical components at the microscale, typically ranging from 0.1 μm to several hundred micrometres. These devices enable sensing, actuation, and signal processing functions in a compact form factor [91]. The origins of MEMS technology trace back to the late 1950s and 1960s, with the invention of the silicon strain gauge and the integrated circuit. Over the past decades, MEMS has rapidly advanced, driving innovations across domains such as aerospace, biomedical engineering, and consumer electronics [91].

Within MEMS, the design of compliant suspension structures is critical for achieving high sensitivity and low noise in devices such as accelerometers, gyroscopes, and RF switches. Folded beams represent a specific subset of *serpentine springs*, characterised by multiple zig-zag or snake-like patterns. An example is depicted in Figure 7.12, where a gold proof mass is suspended by numerous serpentine springs in the form of folded beams. These structures provide mechanical support while allowing in-plane or out-of-plane displacements in response to external forces. Folded beams are particularly preferred in MEMS because they enable the realisation of low and controllable spring constants within a compact footprint, which is crucial for high-sensitivity accelerometers [91].

The working principle of serpentine and folded-beam springs relies on their multiple meandering sections, which deform under applied forces, thereby enabling large displacements with relatively low restoring force [92]. This geometry also provides enhanced

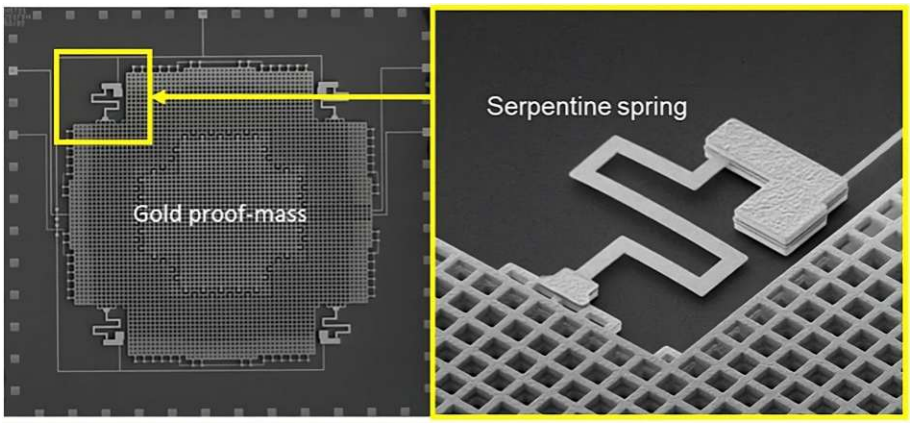

Figure 7.12: Scanning Electron Microscopy image of the gold single proof-mass MEMS capacitive Accelerometer with the Folded beam type Serpentine spring [91].

compliance in the desired direction of motion and can be tuned for specific dynamic and mechanical requirements. Importantly, these structures can be designed to decouple motions in orthogonal directions, minimise cross-axis sensitivities, and provide greater tolerance to fabrication variations.

To design such flexure structures, both analytical models and finite element method (FEM) simulations have been employed. These studies show that the dominant parameters governing the spring constant of folded beams are the beam width and thickness [91, 92]. A general schematic of a typical half-edge folded beam structure is illustrated in Figure 7.13, where the overall length is L, thickness is t, each meander has length a and width w, except for the first and last meanders, which have a width c, with $c = b/2$ where b is vertical lenght of span beams for the half-edge folded beam design.

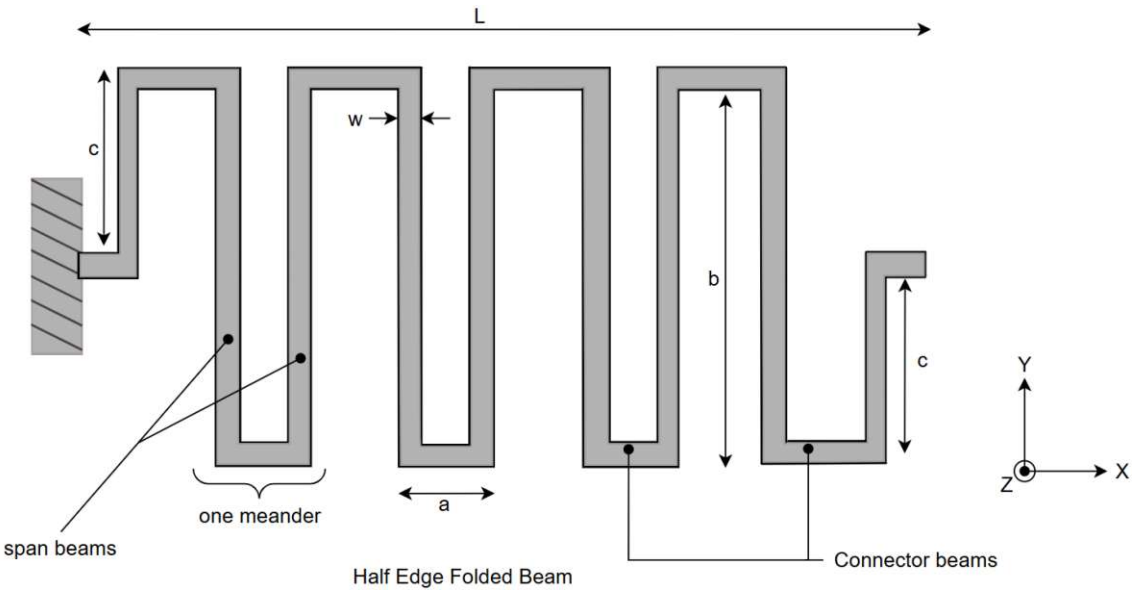

Figure 7.13: Half-Edge Folded Beam Type Serpentine Spring.

In summary, folded-beam spring structures have played a crucial role in both macro- and micro-scale applications due to their compliance, compactness, and tunability. These characteristics make them strong candidates for adoption as isolator elements in vibration isolation systems. Before proceeding to the actual modelling phase, it is necessary to design the complete spring structure with its governing parameters and to derive its stiffness matrix, which will be of order 6×6. With these initial dimensions and parameters, the structure can then be modelled in CAD and analysed using FEM to evaluate its behaviour under loading in different directions. The FEM analysis will provide insight into which directions exhibit higher or lower stiffness. In the following sections, we will also develop an analytical model of a simple one-meander half-edge folded beam as the basis for further analysis.

7.3.3 Analytical Modelling of a Half-Edge Folded Beam Structure

From the previous chapters, we found the fundamental relation between the natural frequency and the stiffness constant with respect to this equation:

$$f_r = \frac{1}{2\pi}\sqrt{\frac{k}{m}} \tag{7.3}$$

Since the stiffness constant k is directly proportional to the natural frequency f_r, it is evident that by altering the stiffness parameter, we can change the natural frequency of any system. In general, stiffness is highly dependent on the structural design parameters.

Unlike traditional coil springs, the stiffness for the serpentine spring structure, which is nonlinear, can be represented in the form of a 6×6 matrix, termed as the *stiffness matrix*. The stiffness matrix for a folded serpentine spring is a symmetric 6×6 matrix that relates forces and moments at the spring ends to corresponding translations and rotations [93]. Each element in that matrix captures either a direct term (diagonal) or a cross-axis term (off-diagonal mechanical coupling).

In most folded structures that are symmetric in design, cross-axis terms cancel at the system level, so they will be zero while performing analytical calculations. The general stiffness matrix 7.4, as discussed in [93], is:

$$\mathbf{K} = \begin{bmatrix} k_{xx} & k_{xy} & k_{xz} & k_{x\theta_x} & k_{x\theta_y} & k_{x\theta_z} \\ k_{yx} & k_{yy} & k_{yz} & k_{y\theta_x} & k_{y\theta_y} & k_{y\theta_z} \\ k_{zx} & k_{zy} & k_{zz} & k_{z\theta_x} & k_{z\theta_y} & k_{z\theta_z} \\ k_{\theta_x x} & k_{\theta_x y} & k_{\theta_x z} & k_{\theta_x\theta_x} & k_{\theta_x\theta_y} & k_{\theta_x\theta_z} \\ k_{\theta_y x} & k_{\theta_y y} & k_{\theta_y z} & k_{\theta_y\theta_x} & k_{\theta_y\theta_y} & k_{\theta_y\theta_z} \\ k_{\theta_z x} & k_{\theta_z y} & k_{\theta_z z} & k_{\theta_z\theta_x} & k_{\theta_z\theta_y} & k_{\theta_z\theta_z} \end{bmatrix} \tag{7.4}$$

Where:

- k_{xx}, k_{yy}, k_{zz} are **direct stiffness terms** for translation along x, y, z.
- $k_{xy}, k_{xz}, \ldots$ are **cross-axis terms** that define translation-to-translation coupling.
- $k_{x\theta_x}, k_{y\theta_x}, \ldots$ are **translation-to-rotation coupling** terms.
- $k_{\theta_x\theta_x}, k_{\theta_y\theta_y}, \ldots$ are **rotation-related terms**.
- The matrix is **symmetric**: e.g., $k_{xy} = k_{yx}$, $k_{x\theta_y} = k_{\theta_y x}$, etc.

This symmetric matrix contains 21 independent terms for flexures, such as serpentine springs. Out of which, in our current analysis, we were only considering the forces that were acting on the folded beam without considering the moment, as shown in Figure 7.14.

From the above figure, which is a simple basic design of a horizontal serpentine spring where the span beam length is l_0 and the length of the connector beam is l_p, with the end beam length $l_1 = l_2 = 0.5\, l_0$. These initial design parameters are obtained from [94], which will serve as the basis for further analytical modelling. All the principal external forces (F_x, F_y, F_z) are acting on the free end of the beam without any external moments.

So the ultimate stiffness matrix with only translational degrees of freedom is reduced from 6×6 to a 3×3 matrix, and all the terms related to moments vanish. The reduced stiffness matrix is:

$$\mathbf{K}_{3\times3} = \begin{bmatrix} k_{xx} & k_{xy} & k_{xz} \\ k_{xy} & k_{yy} & k_{yz} \\ k_{xz} & k_{yz} & k_{zz} \end{bmatrix} \tag{7.5}$$

Now we have only the direct and the cross-axis translational stiffness elements, which in total govern the structure's behaviour under loading conditions. The following spring constants were obtained using the linear equations derived by the principle of **virtual work** in combination with the **unit load method** [94].

The principle of Virtual Work is a fundamental concept in structural mechanics and energy methods. It states that for a system in equilibrium, the total virtual work done by all external forces during a virtual displacement—a kinematically admissible, infinitesimal,

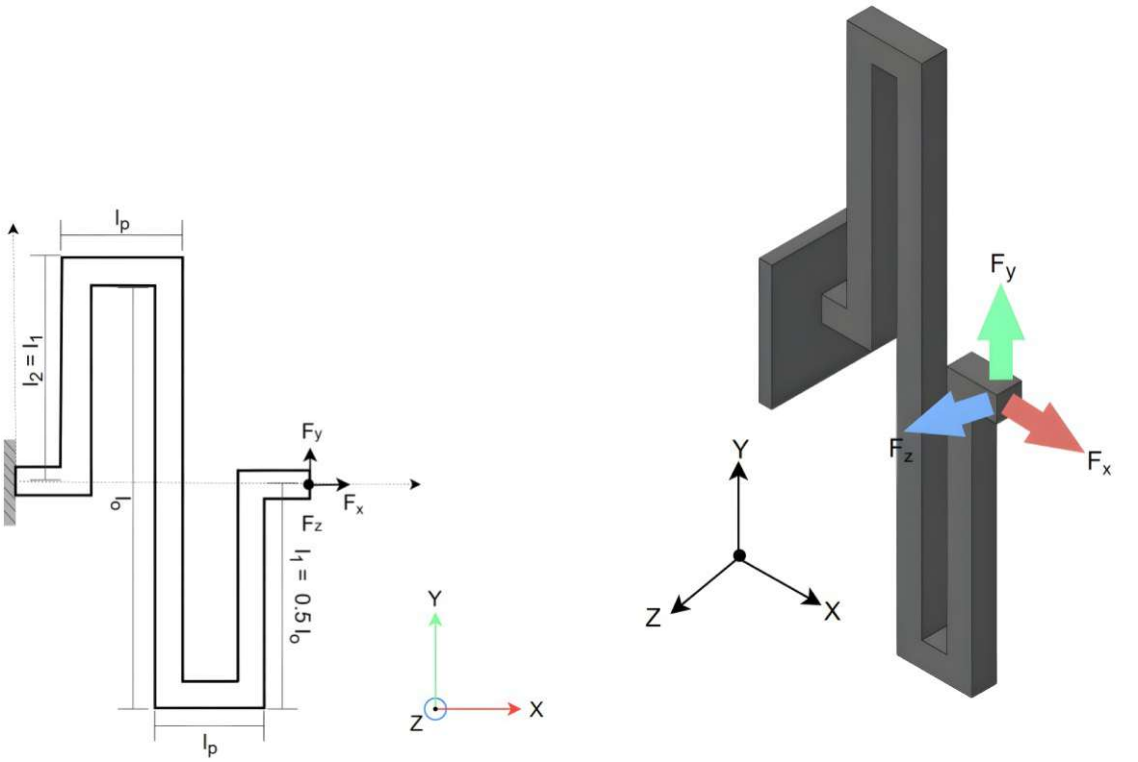

(a) Schematic diagram representing Geometrical parameters

(b) 3D Model with principal forces acting on the free end

Figure 7.14: A simple horizontal half-edge folded beam structure where one end is fixed and the other end is free.

and imaginary displacement consistent with constraints—is zero [95]. The principle can be expressed mathematically as:

$$\delta W = \sum (F_i \, \delta u_i) = 0 \tag{7.6}$$

For a discrete system like a mass–spring assembly, the principle of virtual work states that the work done by the applied external forces during a virtual displacement is equal to the work done by the internal forces in the same virtual displacement [95], that is:

$$\delta W_{\text{ext}} = \delta W_{\text{int}} \tag{7.7}$$

Where:

- δW_{ext} is the virtual work done by external forces,
- δW_{int} is the virtual work done by internal stresses.

In our current case, which is a beam element, the External virtual work:

$$\delta W_{\text{ext}} = \sum_{i=1}^{n} F_i \cdot \delta u_i \tag{7.8}$$

expanded equation 7.8 for forces & moments at nodes:

$$\delta W_{\text{ext}} = \sum_{a=1}^{n_n} \Big(F_{x,a}\,\delta u_a + F_{y,a}\,\delta v_a + F_{z,a}\,\delta w_a + M_{x,a}\,\delta\theta_{x,a} + M_{y,a}\,\delta\theta_{y,a} + M_{z,a}\,\delta\theta_{z,a} \Big), \tag{7.9}$$

Where:

- n_n: number of nodes in the element.
- $F_{x,a}, F_{y,a}, F_{z,a}$: externally applied **nodal forces** at node a in the x-, y-, and z-directions, respectively.
- $\delta u_a, \delta v_a, \delta w_a$: corresponding **virtual displacements** at node a.
- $M_{x,a}, M_{y,a}, M_{z,a}$: externally applied **nodal moments** (torques) at node a about the x-, y-, and z-axes.
- $\delta\theta_{x,a}, \delta\theta_{y,a}, \delta\theta_{z,a}$: corresponding **virtual rotations** at node a.

Then the Internal virtual work is expressed as:

$$\delta W_{\text{int}} = \int_V \sigma : \delta\varepsilon \, dV \tag{7.10}$$

where F_i are external forces, δu_i are the corresponding virtual displacements, σ is the stress tensor, and $\delta\varepsilon$ is the virtual strain.

also the expanded equation 7.10 stress–strain components over the volume:

$$\delta W_{\text{int}} = \int_V \Big(\sigma_{xx}\,\delta\varepsilon_{xx} + \sigma_{yy}\,\delta\varepsilon_{yy} + \sigma_{zz}\,\delta\varepsilon_{zz} + \tau_{xy}\,\delta\gamma_{xy} + \tau_{yz}\,\delta\gamma_{yz} + \tau_{zx}\,\delta\gamma_{zx} \Big)\, dV. \tag{7.11}$$

Where:

- V: volume of the element (or structure).
- $\sigma_{xx}, \sigma_{yy}, \sigma_{zz}$: **normal stresses** in the x-, y-, and z-directions.
- $\delta\varepsilon_{xx}, \delta\varepsilon_{yy}, \delta\varepsilon_{zz}$: corresponding **virtual normal strains**.
- $\tau_{xy}, \tau_{yz}, \tau_{zx}$: **shear stresses** on the xy-, yz-, and zx-planes.

- $\delta\gamma_{xy}, \delta\gamma_{yz}, \delta\gamma_{zx}$: corresponding **virtual shear strains**.

The *unit load method* is a specific application of the virtual work principle, widely used for calculating displacements or rotations at a particular point in a structure, especially in statically indeterminate systems. The unit load method is foundational in deriving spring constants for the folded-beam structure discussed above. Applying the virtual work principle with the unit load method yields the following equation for the displacement and rotation at the point of interest [94]:

$$\delta \text{ or } \phi = \int \frac{N_U N_L}{EA}\, dx + \int \frac{M_U M_L}{EI}\, dx + \int \frac{T_U T_L}{GJ}\, dx \tag{7.12}$$

The notation used in the unit load method is as follows. The linear displacement in the direction of interest is denoted by δ, while ϕ represents the angular displacement (rotation) at the point of interest. The internal forces and moments due to actual applied loads are designated as N_L for axial force, M_L for bending moment, and T_L for twisting moment.

Correspondingly, the internal responses due to a hypothetical unit dummy load are represented as N_U, M_U, and T_U for axial force, bending moment, and twisting moment.

The material and geometric properties essential for these calculations include:

- Young's modulus (E),
- shear modulus $(G = \frac{E}{2(1+\nu)})$, where ν is the Poisson ratio,
- cross-sectional area (A),
- second moment of area or moment of inertia (I),
- polar moment of inertia (J).

In the application of the virtual work principle via the unit load method, the first term of the resulting expression quantifies the contribution from axial deformation, the second term accounts for bending deformation, and the third term represents the effect of torsional deformation. This comprehensive approach allows for accurate calculation of displacements and rotations in beam and spring elements subjected to complex loading conditions.

By applying the following equation, the authors in [94] had calculated the principal spring constants, which are as follows:

The stiffness along the principal x direction is:

$$K_{xx} = \left[\frac{(N+1)l_0^3}{6EI_{z_0}} + \frac{(N+1)l_0^2 l_p}{2EI_{z_p}} \right]^{-1} \tag{7.13}$$

If $l_0 \gg l_p$:

$$K_{xx} \simeq \frac{6EI_{z_0}}{(N+1)l_0^3} \tag{7.14}$$

For stiffness along the principal y direction:

$$K_{yy} = \left[\frac{(2(N+2)l_p)^3}{3EI_{z_p}} + \frac{(8N^3+36N^2+55N+27)l_p^2 l_0}{3EI_{z_0}}\right]^{-1} \tag{7.15}$$

And if $l_0 \gg l_p$:

$$K_{yy} \simeq \frac{3EI_{z_0}}{(8N^3+36N^2+55N+27)l_p^2 l_0} \tag{7.16}$$

Lastly, stiffness along the principal z direction is:

$$K_{zz} = \left[\frac{(2(N+2)l_p)^3}{3EI_{y_p}} + \frac{(N+1)l_0^3}{6EI_{y_0}} + \frac{(N+1)l_0^2 l_p}{GJ_p} + \frac{(8N^3+36N^2+55N+27)l_p^2 l_0}{3GJ_0}\right]^{-1} \tag{7.17}$$

For $l_0 \gg l_p$:

$$K_{zz} \simeq \left[\frac{(N+1)l_0^3}{6EI_{y_0}} + \frac{(8N^3+36N^2+55N+27)l_p^2 l_0}{3GJ_0}\right]^{-1} \tag{7.18}$$

Here, l_0 denotes the length of the spring element orthogonal to the x- and z-axes, while l_p represents the length of the element parallel to the x-axis. The parameter N indicates the total number of foldings, or meanders, within the spring structure. The moment of inertia with respect to the y-axis for the section of the spring element orthogonal to the x and z-axes is denoted as I_{y0}, whereas I_{yp} refers to the moment of inertia with respect to the y-axis for the section of the element parallel to the x-axis. Similarly, I_{z0} corresponds to the moment of inertia with respect to the z-axis for the orthogonal spring element section, and I_{zp} represents the moment of inertia with respect to the z-axis for the spring element section parallel to the x-axis. G is the shear modulus and J_0 is the polar moment of inertia.

By obtaining the principal diagonal, direct translational stiffness terms were determined using the unit load method proposed in [94]. Next for the cross-axial stiffness parameters

such as K_{xy}, K_{xz}, K_{zx}, K_{xz}, K_{yz}, K_{zy}. The cross-axial parameter K_{xy} for the planar folded beam serpentine spring is given in [93] using the same unit load method, which is:

$$K_{xy} = \frac{36EI_aI_b^2}{l_0\left[l_0^2I_a^2(N-2)(N-1)^2 + 3l_p^2I_b^2N(N^2-3) + 2l_pl_0I_aI_bN(2N^2-5N+3)\right]} \tag{7.19}$$

Regarding the K_{xz}, K_{zx}, K_{yz}, and K_{zy} stiffness terms, the finite element method (FEM) analysis of the folded-beam structure shown in Figure 7.14 demonstrates that the deflection along the z-direction, when a force is applied along either the x- or y-axis, is on the order of 10^{-4} mm. This deflection is significantly smaller than the corresponding values along the x and y directions, which are typically in the range of 10^{-1} to 10^{-2} mm. The very small out-of-plane (z-direction) deflections observed in response to in-plane (x or y) loading indicate that the structure exhibits a very high stiffness in the z-direction relative to in-plane directions.

Similarly, when a force is applied in the z-direction, the resulting deflections along the x and y axes are several orders of magnitude smaller than the primary deflection along the z-axis. These results suggest that, for this particular folded-beam structure—which is symmetric with respect to the z-plane—the out-of-plane coupling effects are negligible. Therefore, in the subsequent analytical modelling, only in-plane force components and couplings are considered. The cross-axis stiffness terms K_{xz}, K_{zx}, K_{yz}, and K_{zy} are omitted from the analysis, as their influence on the overall structural response is insignificant.

Now that we have obtained the direct and cross stiffness terms equations, we have numerically calculated the stiffness and deflection parameters when a Unit Loading is applied along the x, y, and z directions independently, under the following geometrical conditions: $l_1 = l_2 = 0.5\,l_0$. Number of repeated folded patterns $N = [0, 1, 2, 3, 4, 5, 7, 10]$, which we start testing from the zero pattern to the 10 pattern repetitions. $l_{mi} = l_{fin}$ which are the end horizontal beams, and $I_{fin} = I_{mi} = I_{zo} = I_{yp} = I_{yo} = I_{zp} = w^4/12$ which represent moment of inertia for a square segment of equal side length of the beam as w and $l_p = 0.1\,l_0$ where l_p is the length of connector beam and l_0 is the length of span beam.

Since we have fixed our material properties as **ERGAL-70 (Aluminum 7075-T6)** which is also used in the previously for prototyping the attachment interface whose mechanical properties such as Young's modulus $E = 7.1700 \times 10^{10}$ Pa and having a Poisson's ratio $\mu = 0.33$, G being the shear modulus $G = E/(2(1+\mu))$ and J is the polar moment of inertia which is numerically given by using standard Engineering

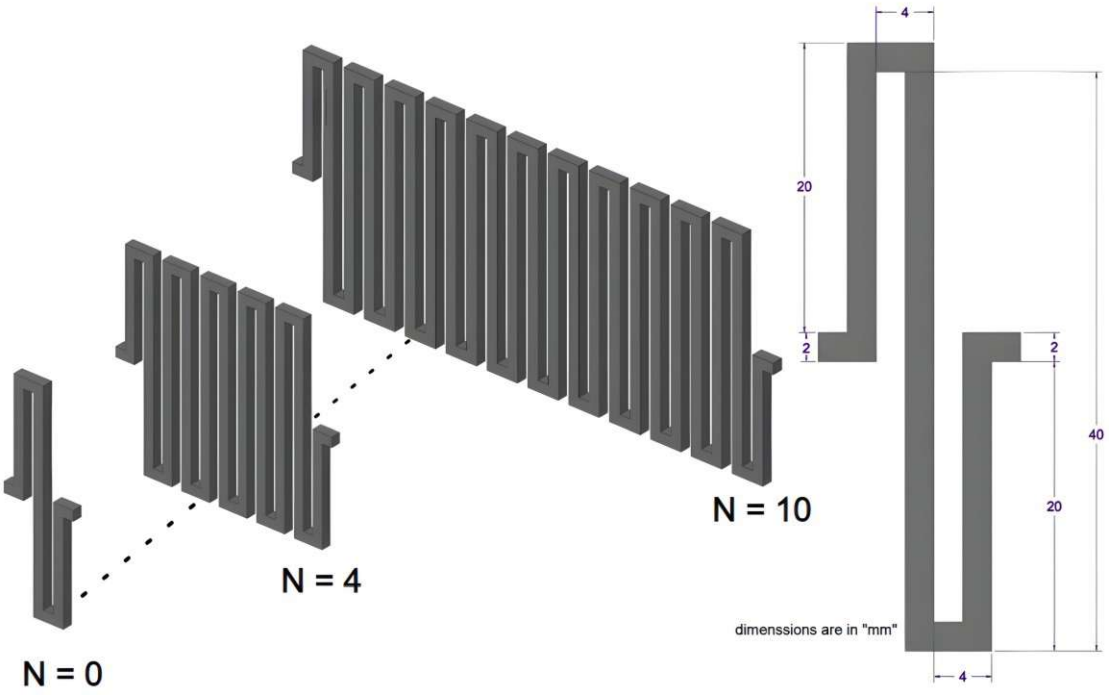

Figure 7.15: The CAD models of the different repeated pattern folded beam structures from zero to ten repetitions, along with the initial design parameters of the folded beam element according to the analytical model.

Approximation for a square cross section as $J \approx 0.141\, b^4$ [95]. Along with all these initial parameters and substituting into the individual translational stiffness coefficients, which are all generated in the `Matlab` code and computed analytically to find how the stiffness and deflection trends are happening with the change in number of fold patterns (N) of the beam element, which are provided in the below Table 7.1.

7.3.4 Finite Element Analysis for the Folded Beam Designs

With the similar parameters as mentioned in the analytical modelling, we modelled eight types of folded beams from zero repetition pattern up to a maximum of ten repetition patterns, as shown in Figure 7.15. These beams were modelled in **Creo Parametric** with all material assignments and other mechanical and design parameters, where the cross section was defined as a 2×2 mm square.

Following this, we proceeded to perform **Finite Element Analysis (FEA)**. Here, Creo provides an inbuilt **Creo Simulation** module, a real-time FEA analysis tool powered by ANSYS solvers. Using this tool, we defined the necessary material and other essential properties, followed by fixing the constraints at one end of the beam and exerting a unit load along the three principal directions. For meshing, Creo employs a *p-type mesh*, which is an approach where the polynomial order of the shape functions within each element is

increased to improve accuracy, rather than refining the mesh by simply increasing the number of elements.

After meshing, a Static Load Analysis Study was carried out, including all the required constraints and parameters stated earlier. This entire process was repeated for different repetitions of the folded beam structures, ranging from $[0, 1, 2, 3, 4, 5, 7, 10]$. For each repetition, three cycles of loading were performed corresponding to the three principal directions: x, y, and z.

A snapshot of one such analysis result is shown in Figure 7.16, representing the outcome for one of the folded-beam cases. Similar analyses were conducted for the y- and z-loading directions. After collecting the results regarding the deflections in each principal direction, the values were uploaded into a numerical MATLAB code to compare the analytical predictions with the FEA simulations. The MATLAB-based comparison enabled both validation of the analytical approach and a detailed inspection of the influence of individual stiffness effects on the folded-beam designs.

Once all the results regarding the deflections in every principal direction were collected, these values were uploaded into the numerical MATLAB code to compare the results obtained analytically with those from the FEA study. This comparison was also used to inspect the behaviour of the individual stiffness effects on the folded beam design.

7.3.5 Validation of the Analytical Model with FEA Results for the Folded Beam Design

The final results obtained after computation using the analytical method with respect to the FEA study were both plotted and tabulated. The tabulated results are presented in Table 7.1. At the same time, the plot showing the trend variation of stiffness along the three principal directions with respect to the change in the number of repeated turns is illustrated in Figure 7.17.

From the following data, it is evident that for the given serpentine folded beam spring, with an increase in the number of turns under unit loading conditions, the overall trend in the stiffness decreases in an exponential order.

In the case of the X-stiffness plot, the stiffness is initially high for a smaller number of turns, but with the increase in the number of turns, the stiffness gradually decreases in a nonlinear fashion. Considering the highest stiffness of around $6900\,\mathrm{N/m}$ for a beam with zero turns, the stiffness tends to decrease with increasing turns, thus increasing the overall length of the beam. For the final case with the maximum number of beam turns, the stiffness reaches approximately $660\,\mathrm{N/m}$, which corresponds to a decrease by almost

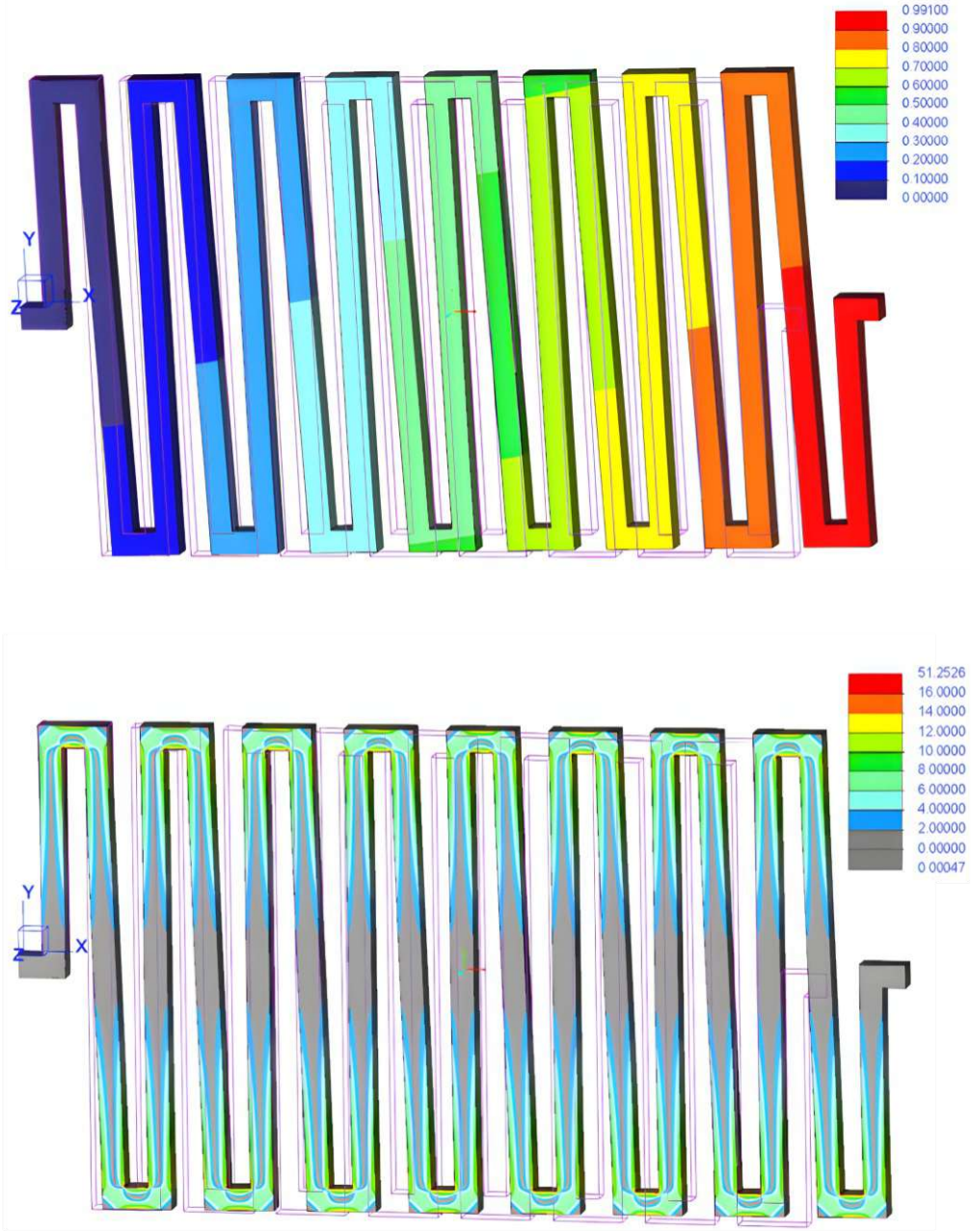

Figure 7.16: Static analysis of a seven-patterned folded beam subjected to a unit force along the x-direction. **Top:** maximum deflection along x (0.991 mm). **Bottom:** maximum von Mises stress along x (51.25 MPa).

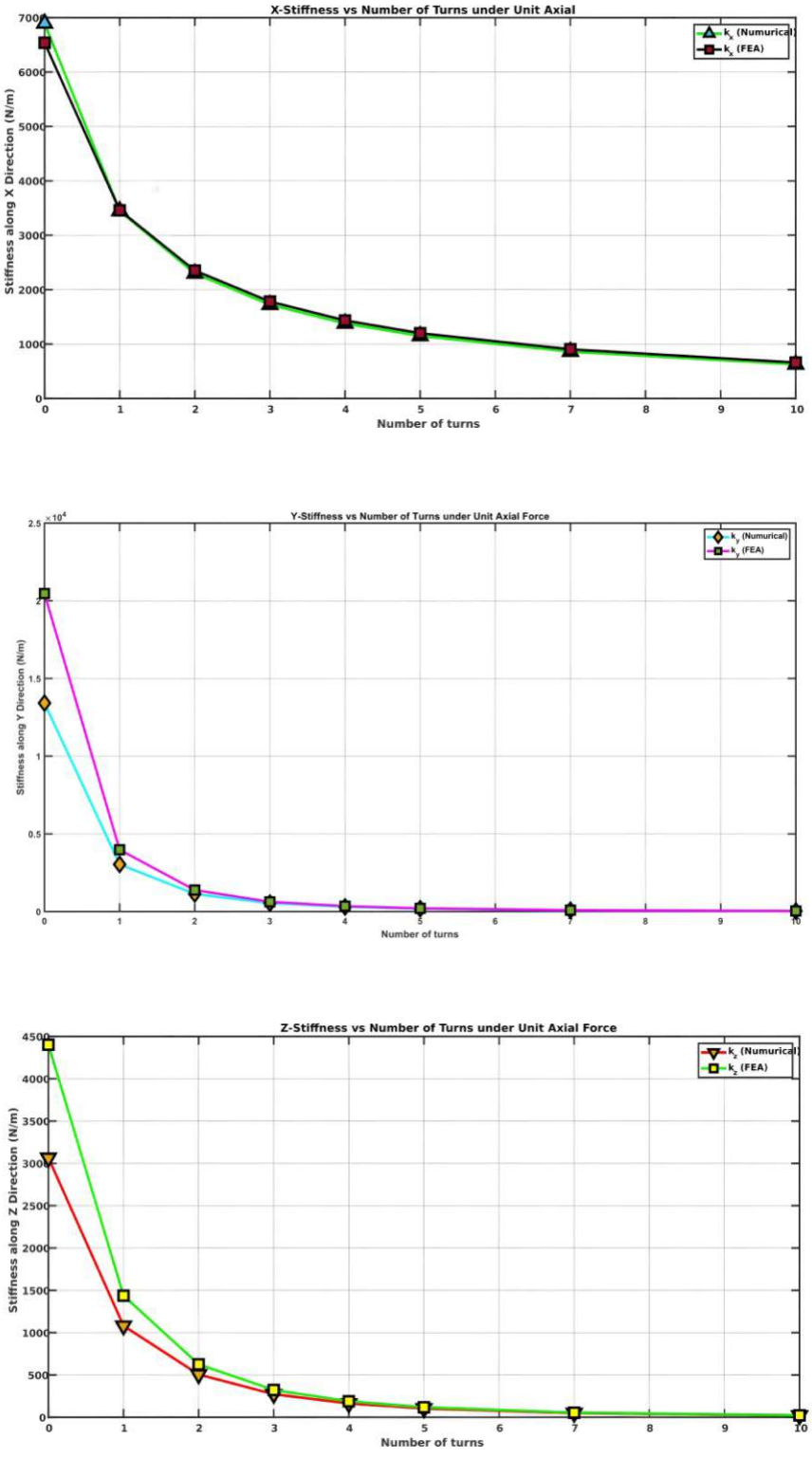

Figure 7.17: Comparison of the Analytical model and FEA stiffness parameters for the folded beam spring under the design set parameters and variation in the number of turns: (top) Variation of stiffness along the X-direction, (middle) Variation of stiffness along the Y-direction, (bottom) Variation of stiffness along the Z-direction.

Table 7.1: Stiffness Results and Percentage Errors

No. of Meanders	X Direction			Y Direction			Z Direction		
	FEA Stiff. X (10^3 N/m)	Analyt. Stiff. X (10^3 N/m)	% Error X	FEA Stiff. Y (10^4 N/m)	Analyt. Stiff. Y (10^4 N/m)	% Error Y	FEA Stiff. Z (10^3 N/m)	Analyt. Stiff. Z (10^3 N/m)	% Error Z
0	6.5385	6.8942	5.44	2.0467	1.3417	34.45	4.4018	3.0647	30.38
1	3.4582	3.4471	0.32	0.3978	0.3036	23.68	1.4368	1.0806	24.79
2	2.3505	2.2981	2.23	0.1383	0.1131	18.23	0.6250	0.5054	19.14
3	1.7807	1.7236	3.21	0.0625	0.0539	13.82	0.3226	0.2728	15.43
4	1.4331	1.3788	3.79	0.0345	0.0297	13.81	0.1887	0.1622	14.04
5	1.1994	1.1490	4.20	0.0204	0.0181	11.33	0.1176	0.1035	11.99
7	0.9038	0.8618	4.65	0.0090	0.0081	9.61	0.0543	0.0492	9.53
10	0.6601	0.6267	5.05	0.0036	0.0033	7.46	0.0224	0.0207	7.65

one order of magnitude.

For the Y-stiffness plot, the initial stiffness is higher compared to the stiffness obtained for a larger number of turns, with an initial value of approximately $2470\,\text{N/m}$ that gradually decreases nonlinearly to about $35.71\,\text{N/m}$ for the maximum number of beam turns. As is evident from the graph, the numerical formulation is better aligned with the FEA analysis, particularly for the case of higher beam turns.

Similarly, for the Z-stiffness plot, the initial stiffness is higher for fewer beam turns, but with the increase in the number of turns, the stiffness simultaneously decreases. The highest beam stiffness is approximately $4400\,\text{N/m}$, while the lowest stiffness is around $20\,\text{N/m}$, showing an exponential decrease with increasing turns.

Also, from Table 7.1, the stiffness values for the folded beam from zero to ten folds indicate that the stiffness along the z-direction is less compared to the other two directions. For the initial cases with fewer turns, the stiffness along the x-direction is smaller than that along the y-direction. However, from around two turns onwards, the stiffness in the y-direction decreases more rapidly than the x-direction, resulting in $K_y < K_x$.

This unusual behaviour is better observed during the modal analysis for the folded beam with no turns ($N = 0$) compared with the beam having two turns ($N = 2$). The modal analysis was performed in *Creo Simulate*, and the results are shown in Figure 7.18. It was observed that the system has six modes, each vibrating in higher harmonics than its predecessor. Both beam designs exhibit their first translational mode along the z-direction, which validates that these structures have less stiffness in that direction and therefore tend to oscillate initially along z under resonant conditions.

However, for higher frequency domains, starting from the second translational mode, differences are observed. For the beam with zero turns in Figure 7.18a, the second

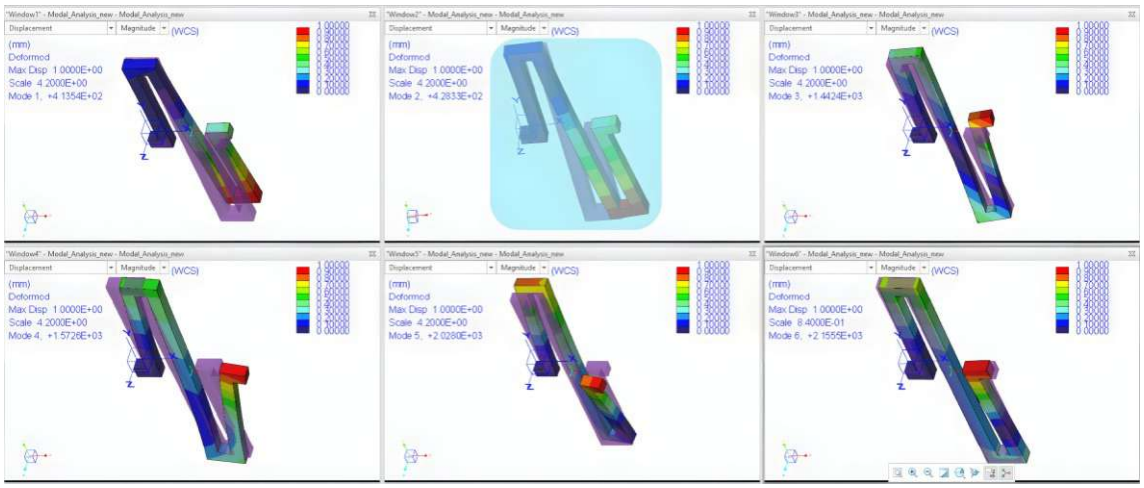

(a) For $N = 0$, the beam's 2nd translational modal frequency is around $428.33\ Hz$ and the structure is vibrating along the x-direction.

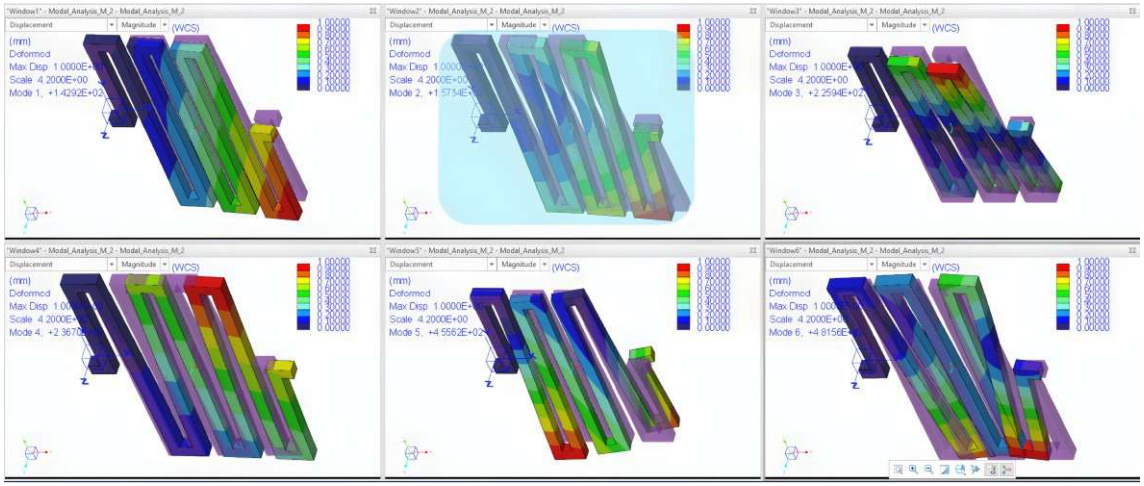

(b) For $N = 2$, the beam's 2nd translational modal frequency is around $157\ Hz$ and the structure is vibrating along the y-direction.

Figure 7.18: Modal analysis results for the folded beam structure under different numbers of turns ($N = 0$ and $N = 2$).

modal frequency corresponds to oscillations along the x-direction, proving that at higher harmonics the structure oscillates along the axis with lower stiffness (K_x smaller than K_y). For the beam with two turns in Figure 7.18b, the second modal frequency is along the y-direction, indicating that in this case $K_y < K_x$.

7.4 Observations and Discussions

The shift in modal frequency comes mainly from the unique geometry of the folded beam. After a certain total length, the beam becomes less stiff. Both the analytical and simulation results clearly show that increasing the number of folds drastically lowers the in-plane stiffness. The reduction in stiffness occurs because each additional zig-zag section increases the total length of the beam, adding more compliant (flexible) parts and making the spring "softer" in its main direction.

It is also observed that each additional meander (fold) produces a noticeable drop in stiffness, which agrees with the results of other studies [93, 96, 94]. A significant advantage of this design is that stiffness and natural frequency can be reduced in a compact space, simply by adding more folds.

The out-of-plane stiffness (along the z-axis) also decreases when more turns are added, but the drop is much smaller compared to the in-plane stiffness (along x and y). The difference arises because in-plane motion is strongly affected by each extra bend, whereas out-of-plane motion is primarily limited by beam thickness and torsional resistance. In simple terms, folded beams become very flexible in-plane but still resist vertical loads to some extent.

Another critical point is that increasing the number of turns changes the ratio between in-plane and out-of-plane stiffness. As more turns are added, in-plane stiffness falls rapidly, while out-of-plane stiffness remains relatively higher. The result is a larger gap between in-plane and out-of-plane resonance frequencies.

The modal analysis also shows that with more folds, the lowest-frequency mode usually corresponds to in-plane deflection. This shift occurs because the in-plane stiffness reduces so much that it dominates the structural response. In contrast, with fewer folds, the first mode may involve some out-of-plane motion at a similar frequency. Overall, folded beams can behave like suspensions that are "tuned" to be soft in one direction (in-plane) while remaining stiff in others, a valuable property also noted in [96].

On the other hand, using too many folds can cause practical problems. Long, thin folded beams may easily buckle, which makes them difficult to manufacture or use safely. For this reason, it is often best to choose a moderate number of folds: enough to reduce stiffness significantly, but not so many that the beam becomes unstable. Further softening can also be achieved by using longer beams or materials with a lower Young's modulus, instead of only adding more folds.

Because of these considerations, ERGAL-70 (Aluminium 7075-T6) was chosen for the

isolator design. This aerospace-grade alloy has good strength, durability under dynamic loads, and a suitable Young's modulus that is neither too brittle nor too ductile. It is also easy to machine and manufacture, which makes it a practical material for the final metal prototype.

In summary, the analytical and simulation results confirm that folded beams can provide strong in-plane flexibility while keeping out-of-plane stiffness relatively higher. This property is helpful for vibration isolation. Based on these results, the next step is to design and model the final vibration isolator, considering both conventional and novel designs. The key observations and insights obtained from the folded beam design analysis are as follows:

Key Insights:

- Increasing the number of folds significantly reduces in-plane stiffness (x and y directions).
- Out-of-plane stiffness (z direction) also decreases, but much less compared to in-plane.
- More folds widen the gap between in-plane and out-of-plane resonance frequencies.
- Modal analysis confirms that higher folds shift the first mode to pure in-plane motion.
- Too many folds may cause buckling and manufacturing issues; a moderate number is optimal.
- ERGAL-70 (Aluminium 7075-T6) is chosen for the isolator due to its strength, machinability, and suitable stiffness.

8 Conventional Folded-Beam Vibration Isolator Design

By now, we have procured a spring element which is better suited for our current purpose, where, unlike a regular helical spring, which is linearly dependent, these unique structures show nonlinear properties. Additionally, unlike traditional springs, which are only used for in-plane displacements, these folded beam structures can also facilitate out-of-plane displacements and angular deflections. Again, all this is achieved in a minimal form factor, making these beam structures an ideal choice for further design of the vibration isolator that will be used as an end-effector on the robotic arm.

Regarding the modelling of folded beam vibration isolators, researchers in the domain of space applications have already designed and modelled isolators to mitigate the micro-vibrations generated from the MWAs and RWAs in satellites, so as not to propagate these vibrations to the base frame and other sensitive equipment. Initially, we will discuss in detail some of the basic designs with folded beam isolators in a more modelling and simulation-oriented manner, rather than delving in-depth into the numerical and analytical methods.

8.1 Modelling of a Flexible Planar Folded Beam Platform

The initial design model of the nonlinear passive isolator is adopted from [97, 90], where the researchers designed an isolated platform with low stiffness mounts for reaction wheel disturbances built from four continuous folded beams arranged orthogonally between a rigid base and a payload interface. This flexible platform was initially modelled in Creo, having similar parameters to those of the zero-turn folded beam modelled earlier with the same design parameters of the folded beam structure modelled in Chapter 7, which is shown in Figure 8.1. In this symmetrical platform structure, the folded beams are placed in a vertical orientation, where the payload's weight is borne along the y-direction. The rotational disturbances of the flywheel are along the x- and z-directions.

Another similar flexible isolator platform using folded beam structures was implemented in [98]. In this case, the folded beams were arranged in a centrosymmetric fashion distributed within the plane that is perpendicular to the spin axis (the momentum

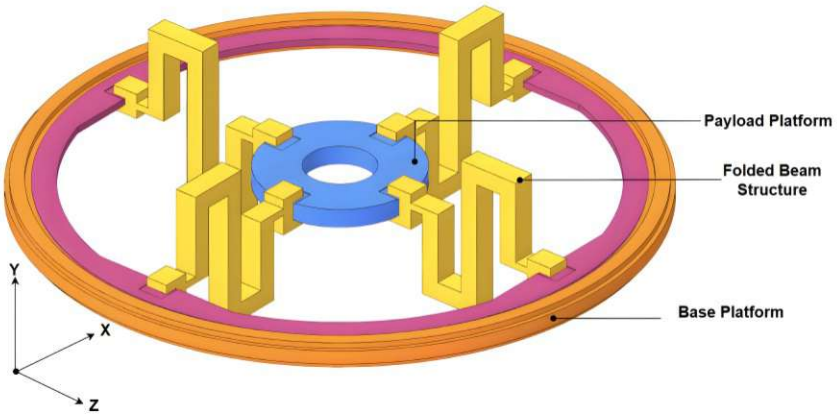

Figure 8.1: CAD Model of the vertical Flexible folded beam isolator.

wheel's spin axis). Each beam in this design is comprised of several zig-zag elements where one end connects to a central circular platform on which the payload (disturbance source) rests, and the other end of the beam is connected to the outer rigid frame. This platform was also modelled in Creo using the geometrical parameters specified in [98], as illustrated in Figure 8.2.

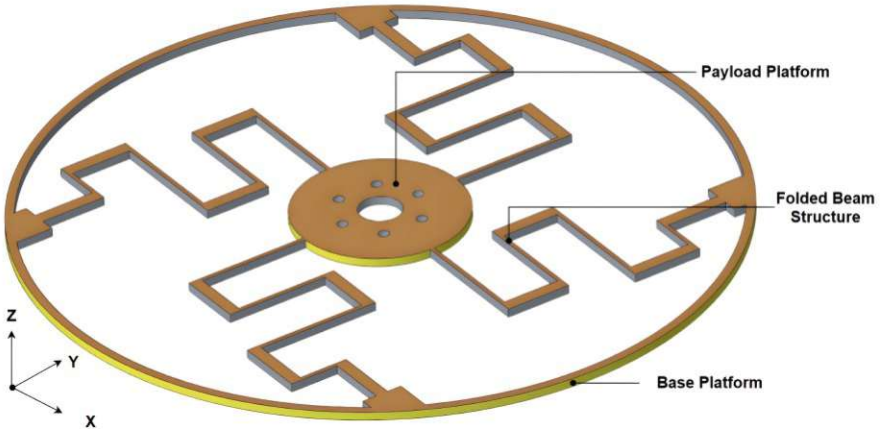

Figure 8.2: CAD model of the horizontal flexible folded beam isolator.

8.1.1 Observed limitations in a flexible folded beam isolator design

Though the above modelled flexible platform folded beam isolators perform optimally by mitigating the micro-vibrations caused by the RWA and MWA mounted on these platforms, they were initially intended to work in zero-gravity environments where the influence of weight is negligible (only mass and inertia are present). Under such conditions, these structures function effectively as vibration isolators since they can

isolate the disturbances caused by the momentum wheel, with no net external force acting on the platform except the self-mass of the system.

However, in our case, we need to install an oscillating sanding tool that will be subjected to vertical forces during polishing operations. The tool exerts a normal force on the isolator platform, for which the above platform designs fail to withstand. The isolator platform proposed in [97, 90] demonstrates that while the folded beams work efficiently in all three translational directions, they exhibit limited compliance in the torsional direction. Specifically, in this design, the vertical blades provide reduced stiffness overall, and increasing the number of folds introduces risks of large static deflections, higher stresses, and potential buckling during operation.

Similarly, the planar folded beam design proposed in [98], though compact and occupying less form factor, also fails to attenuate out-of-plane disturbances. This design tends to be ineffective when applied forces act in the normal direction along the payload platform plane.

Considering these potential limitations, the above modelled platforms were not carried forward for further modelling, as they do not suit the isolation frequency range required for the tool. Hence, alternative designs were explored that could better isolate the vibrations generated by the sander.

8.2 Modelling and Design of a 45° Angled Folded Beam Isolation Platform

From the earlier folded beam flexure platform designs, it is evident that a purely planar arrangement of folded beams is not suitable for our current application. At best, they provide isolation in three degrees of freedom (DOF), whereas a 6-DOF passive isolator is a more appropriate and ideal choice for our purpose. In this section, we design an isolator platform that not only incorporates folded flexures but also addresses the previously mentioned limitations and drawbacks.

8.2.1 Geometry Modelling and coordinates for the 6-DOF isolator platform

Since we have now gathered all the essential information regarding the loading conditions, such as the weight of the tool along with its size constraints, the isolator to be modelled is adapted from earlier versions of 6-DoF isolation platforms, which are described in

detail in [99, 100]. In these works, the authors proposed a passive micro-vibration isolation platform designed to suppress disturbances generated by spacecraft reaction wheels (RWs) within a frequency range of approximately 100 Hz to 600 Hz. Both studies introduced compliant folded-beam flexure-based 6-DoF isolator platforms, where folded-beam structures achieve very low stiffness within a compact form factor, while preserving high load capacity and attitude stability. An additional advantage of folded beams is that they provide high axial as well as torsional stiffness [99], with predictable closed-form mechanics that are ideal for modelling, optimisation, and reproducible fabrication. The conceptual platforms are illustrated in Figure 8.3, where the systems are supported by four symmetrically arranged inclined flexure spring elements, each oriented at a 45° mounting angle.

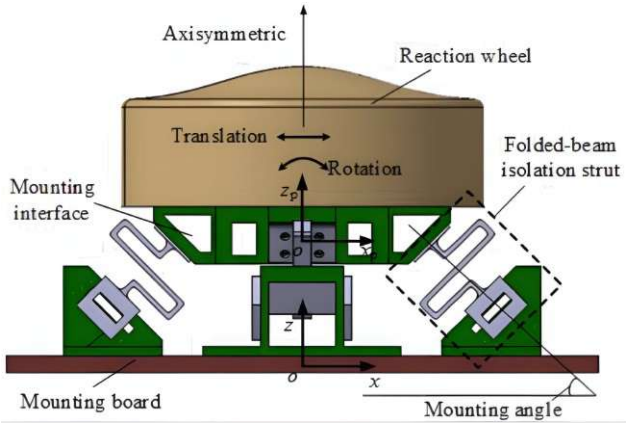

(a) Folded beam isolator platform with folded beam structures [100].

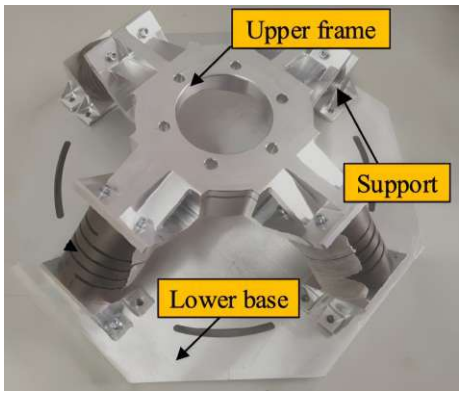

(b) Circular folded beam flexures vibration isolation platform [99].

Figure 8.3: Passive micro-vibration isolation for reaction wheels.

The current model is designed according to the schematic of the passive folded beam 6-DOF isolation platform as illustrated in Figure 8.4, where the design parameters are:

Here:

- $O(X, Y, Z)$ represents the base frame of the isolator platform where the isolator is connected to the robot, here R is the radius of the base circle.
- $o(x, y, z)$ represents the tool frame of the isolator platform where the sanding tool will be mounted, here r is the radius of the tool circle.
- H is the vertical height between the tool frame and the base frame.
- (o_1, o_2, o_3, o_4) are the origin points of the four folded beam flexure, which are distributed across the circumferential direction on the base circle with coordinates $(X_1, Y_1) \ldots (X_4, Y_4)$ representing the mounting points of the flexure elements on the base platform that are evenly spaced.
- The same applies for the tool platform where the flexure elements are connected at

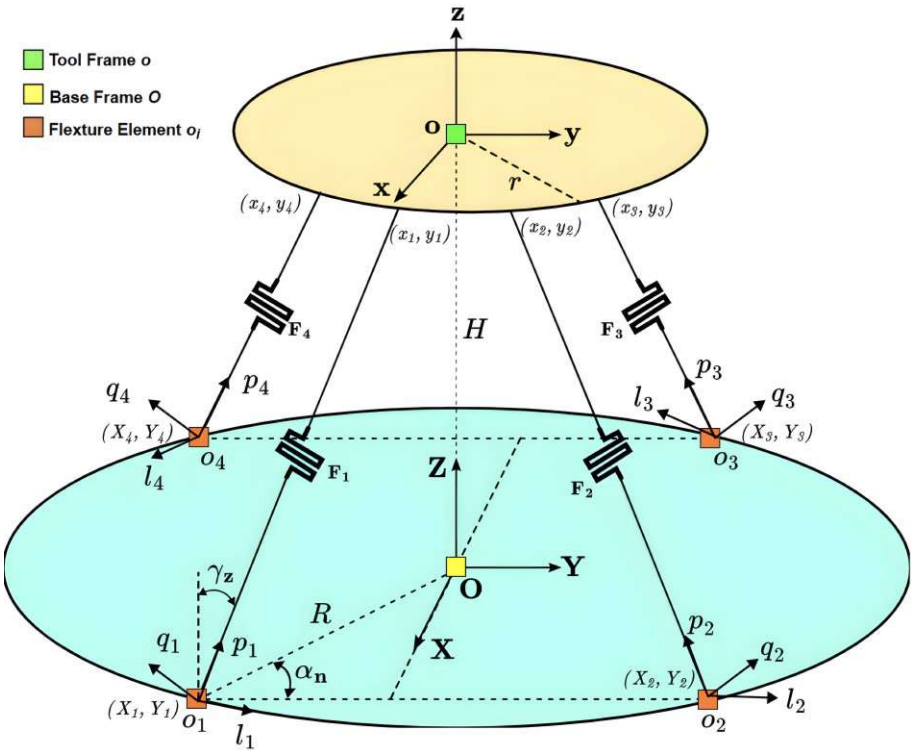

Figure 8.4: Coordinate frames and element placement for the folded-beam isolation platform.

the coordinates $(x_1, y_1) \dots (x_4, y_4)$ with the z axis as H that are also evenly spaced along the tool plane.

- o_{ip}, o_{iq}, o_{il} represent the principal stiffness directions of the folded beam elements.
- α_i is the azimuth rotation angle around the central vertical Z axis of the i-th isolator along the base frame:

$$\alpha_i = \alpha_1 + (i-1)\frac{\pi}{2}, \quad i = 1, \dots, 4 \tag{8.1}$$

Here: α_1 is the azimuth angle of the first isolator element.

- Each folded beam element lies in a vertical plane that is tilted by $\gamma_z = 45°$ toward the top payload, so that the unit's local compliant direction points approximately toward the tool frame origin.
- Lastly, $F_1, \dots, F_4$ are the total lengths of the folded beam elements, which are all equal. The geometrical parameters of the folded beam, such as its width and thickness, and other specifications, are the same as those from the previous chapter design.

The reason for selecting the tilt angle $\gamma_z = 45°$ as the mounting angle is that this configuration allows the platform to attenuate disturbances in multiple directions—radial, axial, and rotational—while maintaining mechanical stability [100]. At this angle (also

noted in [99]), the two coupled radial rocking mode pairs become orthogonal and equal in frequency, which ensures isotropic in-plane isolation. The isotropic isolation is critical because the load excitation (in this case, the tool) can arrive from any horizontal direction. Having identical radial isolation characteristics in both planes guarantees uniform attenuation, minimises directional bias, and reduces cross-axial coupling, thereby avoiding irregular peaks.

Also, the axial and radial stiffness contributions from each element are balanced at $\gamma_z = 45°$, allowing the platform to maintain adequate vertical load capacity and static stability without excessively stiffening in the lateral directions, which would degrade isolation performance since our tool oscillates more along the lateral directions.

With all the above proposed design parameters, we will model the initial version of the isolator platform, then perform simulated modal analysis studies to make sure that the isolator's lowest natural frequency is well below the disturbance source frequency.

We know that the maximum span of the tool's dominant frequency range lies between 135 and 195 Hz. According to the isolator's design criterion—where the disturbance frequency must be at least $\sqrt{2}$ times higher than the isolator's natural frequency—the condition can be written as follows. If the source frequency is f_s, then for effective isolation the isolator frequency f_{iso} must satisfy:

$$f_{\text{iso}} \leq \frac{f_s}{\sqrt{2}} \tag{8.2}$$

From Equation 8.2, the theoretical effective isolator frequency f_{iso} is obtained as 95.5 Hz or lower.

8.2.2 CAD Model of the Conventional 6 DOF Isolator Platform

The initial CAD model version is created in Creo, incorporating all the design parameters stated in the earlier sections. The design model, along with the detailed dimensions of the folded beam element with no turns, is shown in Figure 8.5.

As shown, the mounting angle for the folded beam structures is placed at an angle of 45°. The top and bottom platforms are modelled with diameters of 75 mm and 130 mm, respectively, with an overall vertical height of 45.8 mm. The thickness of both the base and top platforms is set to 4 mm, while the folded beam dimensions remain the same as in the previous isolator designs.

These dimensional values were selected to ensure compatibility with the attachment interface of the robotic arm and to support the static weight of the tool in every direction.

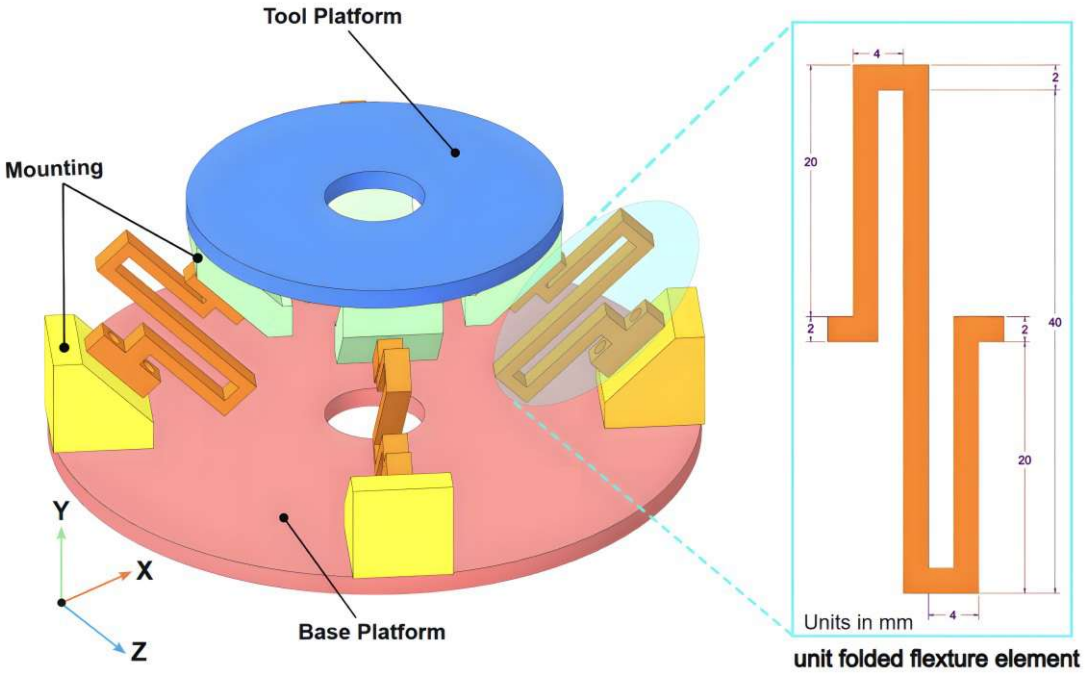

Figure 8.5: CAD Model of the Conventional folded beam vibration isolator.

Furthermore, the platform parameters were chosen in such a way that they remain compatible with the flange design mounted to the Doosan arm, while the top platform is designed to hold the custom top cap of the tool.

This model offers a straightforward and efficient interface with the robotic arm, requiring minimal auxiliary components. The initial design of the isolator platform is subsequently verified using a Finite Element (FE) modal analysis. The respective parameters will be refined through an optimisation study later on until the desired frequency range is achieved.

8.2.3 Modal Analysis of the Conventional Passive Folded Beam Model

Unlike traditional Finite Element (FE) methods, which employ *h-refinement* (subdividing existing elements into smaller ones), `Creo Simulate` adopts the *p-version* (polynomial type) finite element method. The p-version approach relies on increasing the polynomial order on a fixed mesh, making it less sensitive to the initial mesh density. In this design study, the **AutoGEM mesh** feature is used, which primarily provides geometric discretisations. Accuracy improvements are obtained through *p-type adaptability* rather than iterative *h-refinement*.

The designed isolator platform was tested in the FE simulation environment. Initially,

the model was meshed using AutoGEM, which discretises the model into tetrahedral elements and automatically refines the mesh for smaller features. The automatic refinement capability is particularly advantageous for the folded-beam design.

The material properties of *ERGAL 70 (Aluminium 7075-T6)* were assigned to the model. The modal analysis study was then performed with polynomial orders defined as $p_{\min} = 1$ and $p_{\max} = 6$. This setting was observed to yield consistent and robust results without risk of convergence to local minima.

The initial modal analysis results, including the first four mode shapes and their dominant frequencies, are illustrated in Figure 8.6. The corresponding modal data is tabulated in Table 8.1, providing the mode shape behaviour and its characteristics.

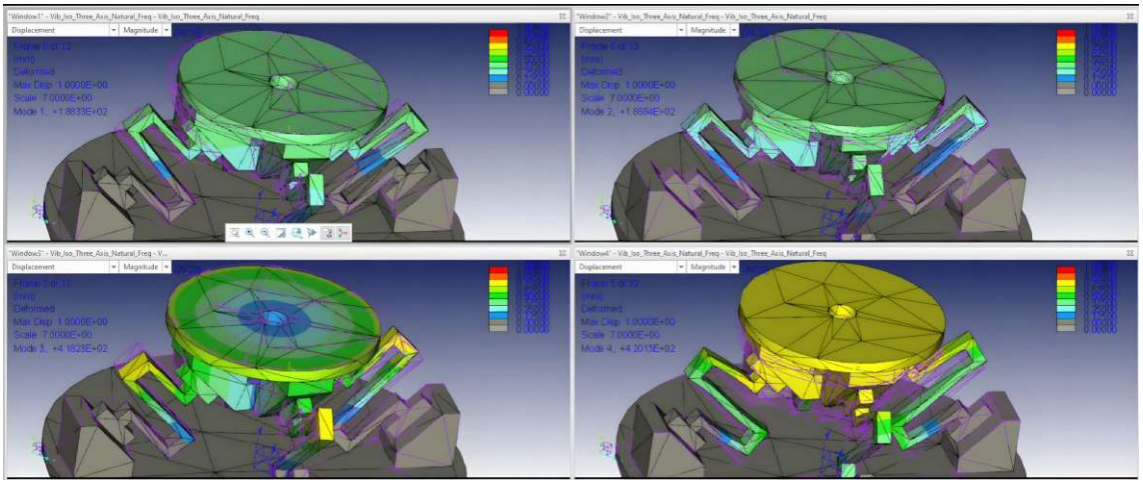

Figure 8.6: Modal Analysis of the first four mode shapes with their respective dominant frequency range for the conventional fold beam isolator platform.

Mode #	Dominant Frequency (Hz)	Modal Description
1	188.33	**In-plane translation** along the lateral direction, **global X-axis**
2	188.84	**In-plane translation** along the lateral direction, **global Z-axis**
3	418.23	**Torsional (yaw) mode** about the vertical axis, rotation around **global Y-axis**
4	420.13	**Out-of-plane translational mode** along the vertical direction, motion primarily along **global Y-axis**

Table 8.1: First four modes of the isolator system with dominant frequencies and technical motion descriptions.

From the initial modal study, it was observed that the dominant frequency range of

the four-folded beam isolator platform lies between 188 Hz and 420 Hz. However, the first two modal frequencies fall within the resonant frequency range of the sanding tool (135 Hz – 195 Hz). The overlap between the tool's frequency range and the isolator's first two modal frequencies makes the system unstable when the tool is connected to the platform. Instead of attenuating oscillations, the system would encounter resonance, ultimately leading to the potential failure of the entire setup.

Previous studies on folded beam isolator platforms have shown that the natural frequencies of such systems are strongly dependent on the **design parameters** of the folded beams. By optimally selecting these parameters, the dynamic behaviour of the system can be altered. Folded beam structures are highly tunable and can be adjusted to achieve the desired stiffness range, thereby modifying the system's natural frequency. For example, the authors in [89] employed numerical optimisation methods, such as *genetic algorithms*, to tune folded beam structures and obtain the required dominant frequency ranges.

8.3 Optimisation Design Study for the Folded Beam Isolator Platform

Since the dominant frequencies of the initially modelled isolator platform are not suitable for the current application, an **optimisation design study** is required. Flexure-based folded beam structures exhibit stiffness properties that are highly sensitive to design parameters; therefore, altering these parameters directly affects the dynamic characteristics of the system.

The objective of the current study is to design an isolator platform with a dominant frequency range below 95.5 Hz. The dimensional parameters of the folded beam (lengths, widths, and thicknesses) serve as the design variables, while the objective functional parameter is the target frequency. This problem naturally falls under the category of **constrained nonlinear optimisation**, since both the objective function and constraints are nonlinear functions of the design variables. These are derived from finite element analysis (FEA) of geometry-dependent structural behaviour.

Several approaches exist under nonlinear programming (NLP) [101], but one of the most widely recognised and effective methods is Sequential Quadratic Programming (SQP).

8.3.1 Sequential Quadratic Programming (SQP)

Sequential Quadratic Programming (SQP) is a Newton-type, gradient-based algorithm specifically designed for solving smooth nonlinear constrained optimisation problems. It is widely regarded as one of the most effective general-purpose optimisation methods because of its strong local convergence properties and its ability to handle complex constraint structures [101].

The core principle of SQP is to approximate the original nonlinear optimisation problem at each iteration by a **Quadratic Programming (QP) subproblem**. This subproblem is derived from:

- a local quadratic model of the Lagrangian function, and
- linearizations of the nonlinear constraints.

This process enables the solution of a sequence of quadratic approximations that converge toward the optimum of the original nonlinear problem. The Sequential Quadratic Programming (SQP) method relies on the construction of the Lagrangian function, expressed as:

$$\mathcal{L}(x, \lambda, \mu) = f(x) + \lambda^\top g(x) + \mu^\top h(x) \tag{8.3}$$

where $\mathcal{L}(x, \lambda, \mu)$ is the Lagrangian, $f(x)$ is the objective function, $g(x)$ and $h(x)$ represent the inequality and equality constraints respectively, and λ, μ are the associated Lagrange multipliers.

In each SQP iteration, the Hessian of the Lagrangian, expressed in matrix form, is given by:

$$\nabla^2_{xx}\mathcal{L}(x, \lambda, \mu) = \nabla^2 f(x) + \sum_{i=1}^{m} \lambda_i \nabla^2 g_i(x) + \sum_{j=1}^{p} \mu_j \nabla^2 h_j(x) \tag{8.4}$$

Here, $\nabla^2_{xx} f(x)$ denotes the Hessian, and $x \in \mathbb{R}^n$, with n being the number of design variables. The Hessian is an $n \times n$ symmetric matrix that is typically approximated using the BFGS (Broyden–Fletcher–Goldfarb–Shanno) update, defined as:

$$
\left.
\begin{aligned}
B_{k+1} &= B_k - \underbrace{\frac{B_k s_k s_k^\top B_k}{s_k^\top B_k s_k}}_{\text{First Correction Term}} + \underbrace{\frac{y_k y_k^\top}{y_k^\top s_k}}_{\text{Second Correction Term}} \\
s_k &= x_{k+1} - x_k \\
y_k &= \nabla_x \mathcal{L}(x_{k+1}, \lambda_{k+1}) - \nabla_x \mathcal{L}(x_k, \lambda_k)
\end{aligned}
\right\} \text{BFGS Update Formulation}
\tag{8.5}
$$

Where B_k is the current Hessian approximation of the Lagrangian with respect to the design variables x, this is an iteratively updated approximation that maintains symmetry and positive-definiteness. Also here, s_k is the design step vector (the change in design variables after iteration k), and y_k is the change in the Lagrangian gradient between iterations (capturing how the gradient shifts from x_k to x_{k+1}).

- The *first correction term* in Eq. 8.5 removes outdated curvature information along the last step direction s_k.
- The *second correction term* adds updated curvature information based on the most recent gradient change y_k.

After applying the BFGS update, the Hessian together with linearised constraints defines the following QP subproblem:

$$
\begin{aligned}
\min_{d} \quad & \frac{1}{2} d^\top B_k d + \nabla f(x_k)^\top d \\
\text{s.t.} \quad & g(x_k) + \nabla g(x_k)^\top d \leq 0, \\
& h(x_k) + \nabla h(x_k)^\top d = 0
\end{aligned}
\tag{8.6}
$$

Here, d represents the search direction. Solving the quadratic subproblem yields a candidate search direction, which is then scaled using a merit-function line search to balance improvement in the objective function against constraint satisfaction [101].

This entire iteration terminates when the set of all the desired equations and inequalities, which are known as *Karush–Kuhn–Tucker (KKT)* conditions, falls below a specified numerical tolerance, ensuring that the computed solution satisfies the optimality conditions within acceptable numerical error.

8.3.2 SQP Framework in Creo Simulate Optimisation Study Analysis

In Creo Simulate, the optimisation design study obtains a solution to an objective feature parameter while being constrained to a set of rules specified in the form of allowable ranges for model dimensions and other analysis feature parameters [102]. In general, the Creo Simulate engine has two types of algorithms: **Sequential Quadratic Programming (SQP)** and **Gradient Projection (GDP)**. It is observed that SQP is faster and more robust compared to GDP. The SQP framework is embedded within a CAD–FEA loop [102]:

1. The design variables, e.g., dimensions and material parameters, are updated according to the computed search direction.
2. The CAD model is regenerated, respecting geometric equality constraints directly in the parametric definition.
3. The model is meshed using the polynomial (p) method with adaptive polynomial order refinement to ensure consistent solution accuracy between iterations, and reanalysed using Creo Simulate's finite element solver.
4. Modal frequencies, stresses, displacements, or other performance metrics are extracted for use in objective and constraint evaluations.

This tightly integrated SQP–CAD–FEA loop enables the optimisation to be geometry-aware and mesh-consistent, which is critical for maintaining accurate and differentiable objective and constraint functions in structural and modal optimisation.

Here is a general pseudo-algorithm 8.1 code of SQP for constrained optimisation in Creo Simulate.

8.3.3 Formulating the Hyper Design Parameters

To conduct the optimisation design study in Creo, initially, we need to set some boundaries and constraints to perform the design study, which iteratively adjusts the selected design variables within a defined variable space to achieve a specified goal that will be our objective function while satisfying design limits, which will be considered as constraints. In this current optimisation study, the goal quantifies the performance measure to be maximised or minimised, the design limits enforce allowable bounds on other measures, and the variable space defines the permissible range for each design variable. For this current study definition, we set the following parameters and measures as **goals, design limits, and variables**:

Algorithm 8.1: Sequential Quadratic Programming (SQP) in Creo Simulate

Input: initial design x_0, bounds ℓ, u, Lagrange multipliers λ_0, Hessian approx. B_0
Output: optimal design $x^\star$, multipliers $\lambda^\star$

$k \leftarrow 0$
repeat
  Evaluate objective $f(x_k)$ and constraints $g(x_k),\ h(x_k)$
  Compute sensitivities $\nabla f(x_k),\ \nabla g(x_k),\ \nabla h(x_k)$ `/* FEA solve Creo */`
  `/* QP subproblem (local quadratic model + linearized constraints) */`
  $\min_d \ \frac{1}{2} d^\top B_k d + \nabla f(x_k)^\top d$
    s.t. $g(x_k) + \nabla g(x_k)^\top d \le 0,$
      $h(x_k) + \nabla h(x_k)^\top d = 0,$
      $\ell \le x_k + d \le u$
  Solve QP $\rightarrow$ obtain step direction d_k and multipliers $\hat{\lambda}_k$
  Choose step length $\alpha_k \in (0, 1]$ by merit-function line search
  $x_{k+1} \leftarrow \Pi_{[\ell,u]}\big(x_k + \alpha_k d_k\big)$
  $\lambda_{k+1} \leftarrow \hat{\lambda}_k$
  `/* BFGS Hessian update */`
  $s_k \leftarrow x_{k+1} - x_k$
  $y_k \leftarrow \nabla_x \mathcal{L}(x_{k+1}, \lambda_{k+1}) - \nabla_x \mathcal{L}(x_k, \lambda_k)$
  $B_{k+1} \leftarrow B_k - \dfrac{B_k s_k s_k^\top B_k}{s_k^\top B_k s_k} + \dfrac{y_k y_k^\top}{y_k^\top s_k}$
  $k \leftarrow k + 1$
until $\|\mathrm{KKT}(x_k, \lambda_k)\| < \varepsilon_{\text{opt}} \ \vee \ k \ge k_{\max}$
return $x^\star \leftarrow x_k, \quad \lambda^\star \leftarrow \lambda_k$

Goal definition: To minimise the total mass of the folded beam flexure structure

$$\text{Minimize} \ \rightarrow \ total\_modal\_mass \tag{8.7}$$

Design limits: Our prime goal during this study is to reduce the dominant frequency below a certain threshold:

$$\text{Design Measure} \ \le \ 95.5 \ \text{Hz} \quad \text{(first modal frequency)} \tag{8.8}$$

Design Variables: The design parameters that govern the folded beam were primarily considered for the design variable constraints, as the entire system's vibrational characteristics were dependent on them. Figure 8.7 shows the dimensional names for each geometrical parameter in the folded beam system, which then internally get changed during the optimisation study to meet the set design limits. Also, Table 8.2 shows the list of variables with their current, maximum, and minimum intervals, such that during the

optimisation analysis, the design is made to iterate within the range of these parameters and fix the best value that satisfies the design constraint. The interval ranges for all these parameters were determined with a multiple sensitivity analysis study by analysing which dimension mainly affects the dynamic properties of the folded beam.

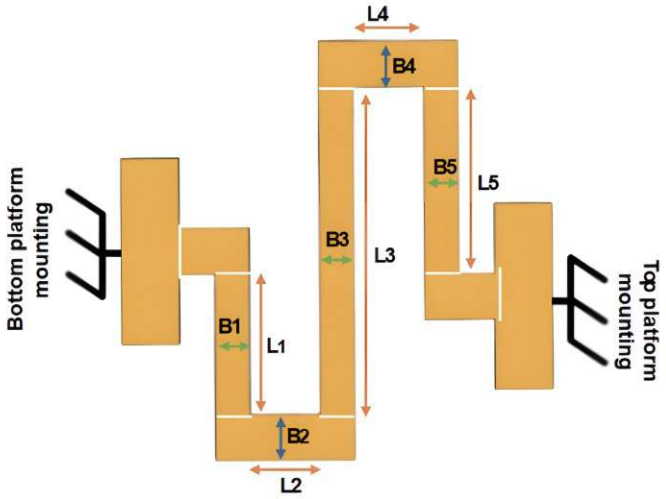

Figure 8.7: Parametric annotated design parameters for the unit folded beam element in the isolator platform.

Variable	Current (mm)	Minimum (mm)	Initial (mm)	Maximum (mm)
L1	20.00	5.00	20.00	25.00
L2 = L4	4.00	2.00	4.00	10.00
L3	40.00	30.00	40.00	50.00
L5	20.00	10.00	20.00	30.00
B1 = B5	2.00	1.50	2.00	4.00
B2 = B4	2.00	2.00	2.00	4.00
B3	2.00	1.50	2.00	3.00
T (thickness)	2.00	2.00	2.00	7.00

Table 8.2: Design variable limits for performing the optimisation study on folded beam structure.

Finally, by providing the **percentage convergence**, which is the stopping criterion that specifies the allowable relative change in the objective function between successive iterations, the optimisation is deemed to be converged if the change is below this percentage for a specified number of steps.

For the present study, the convergence threshold was set to 0.5%. The solver iterated until both the desired objective function criteria were satisfied and the required percentage convergence was achieved. Additionally, the **P-loop convergence** option was enabled to

ensure that each analysis iteration during optimisation produced numerically converged results. Enabling P-loop convergence is particularly important for the current geometric shape, as it directly influences the mode shapes. Furthermore, the **remesh after every shape update** feature was activated to maintain mesh consistency for the updated CAD model geometry at every step. Automatic remeshing avoids element-level distortion and prevents the optimisation from converging to a local minimum. A minimum of 20 iterations was specified.

8.3.4 Findings and Observations after Optimisation

Once the hyperparameters were set, the **SQP optimisation** was performed on the isolator model using its previously assigned material properties and mesh settings. The optimisation study was executed on a personal office laptop equipped with an AMD Ryzen 7 (8-core, 3.8 GHz) CPU, 32 GB DDR5 RAM, and a dedicated NVIDIA RTX-series GPU. With optimal settings, the entire study required approximately 6–7 hours due to the number of design variables and the percentage convergence requirement, which significantly increased computational time.

Upon completion of the optimisation design study, Creo generated a result summary, which included the best design parameters that satisfy the goal of achieving the first dominant modal frequency less than or equal to $95.5\ Hz$ while maintaining the least possible structural mass.

Table 8.3 showcases the design parameters of the folded beam element before and after optimisation. The modified folded beam isolator platform was then modelled by replacing the original folded beam design with the newly optimised one, as illustrated in Figure 8.8.

In the modified folded beam isolator model, the folded beam is not symmetrically offset from its neutral axis, which is evident from its unequal starting and ending vertical beam lengths. This asymmetry suggests that the current model is improved in attenuating vibrations below the targeted isolator frequency threshold. The asymmetric configuration allows for selective adjustments of stiffness in different directions, thereby shifting specific natural frequencies or altering mode shapes to avoid resonance. Additionally, this asymmetry can improve isolation efficiency in the critical axes while maintaining acceptable performance [90].

In comparison with the previous symmetric folded beam design, where the thickness and width of the beam were equal, the new optimised folded beam structure features thinner vertical beams. This design reduces stiffness and consequently lowers the natural frequency [97]. From these studies, it is validated that the current **asymmetrical folded**

Design Variables	Dimensions before optimization (mm)	Dimensions after optimization (mm)
L1	20	20
L2	4	6
L3	40	49
L4	4	6
L5	20	10
B1 = B5	2	2
B3	2	1.5
B2 = B4	2	4
T (thickness)	2	5

Table 8.3: Model design parameter comparison for the folded beam structure.

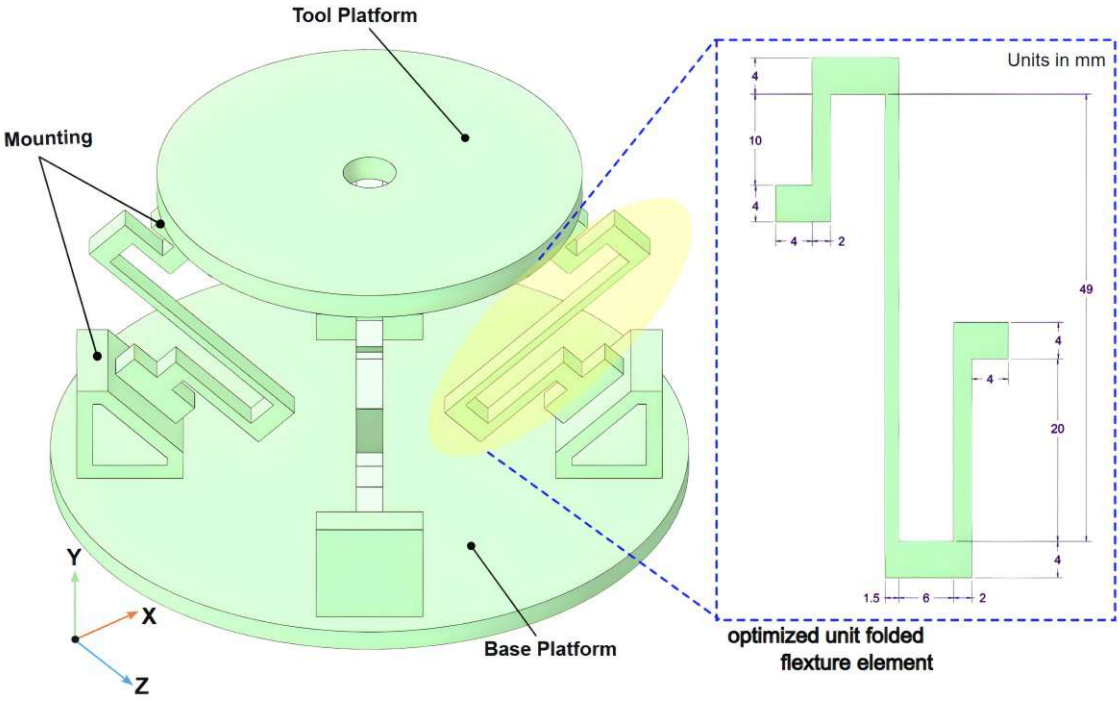

Figure 8.8: Modified optimised Conventional folded beam isolator model.

beam isolator model can more effectively suppress specific coupling modes and optimise vibration suppression for anisotropic disturbances.

8.3.5 Performing Modal and Static Analysis on the Modified Isolator Platform

After upgrading the folded beam design geometries, the new modified isolator platform was retested using modal analysis by repeating the procedural steps outlined earlier. The model's **first four fundamental frequencies and mode shapes** were inspected. The corresponding analysis result window is shown in Figure 8.9, while the first four mode shapes and their respective dominant frequencies are summarised in Table 8.4.

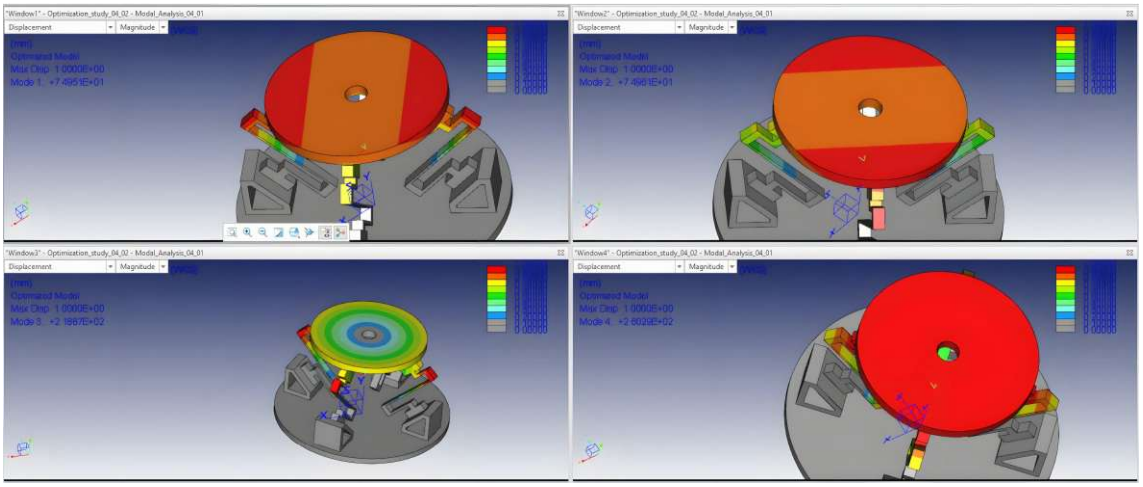

Figure 8.9: Modified optimised Conventional folded beam isolator model.

Mode #	Dominant Frequency (Hz)	Modal Description
1	74.95	**In-plane translation** along the lateral direction, **global Z-axis**
2	74.96	**In-plane translation** along the lateral direction, **global X-axis**
3	218.87	**Torsional (yaw) mode** about the vertical axis, rotation around **global Y-axis**
4	260.29	**Out-of-plane translational mode** along the vertical direction, motion primarily along **global Y-axis**

Table 8.4: First four modes of the isolator system with dominant frequencies and technical motion descriptions for the modified folded beam isolator.

It was observed that all the mode shapes remain similar to those of the previous model;

however, the **dominant frequencies**—particularly the first modal frequency—exhibit a drastic change. The current model isolator achieved a first modal frequency of $74.951\ Hz$, which is a significant reduction compared to the previous design, where the first modal frequency was $188.33\ Hz$. This reduction, achieved through the optimisation process, corresponds to more than a **50% decrease**, thereby demonstrating the effectiveness of the modified asymmetrical folded beam design.

The current model is suitable for isolating the vibrations generated by the tool because its first two natural frequencies are less than 95 Hz. Having natural frequencies below this threshold implies that the modified isolator would provide approximately 69.18 % isolation at the disturbance frequency of 135 Hz, and about 85.23 % isolation at the frequency of 195 Hz. Therefore, the new model can be considered a **good isolator platform**. However, for final confirmation, a static analysis of the resulting structure is performed to verify whether this version can safely withstand the applied loads.

8.3.6 Static Analysis of the Modified Isolator Platform

A static analysis of the isolator is performed with the same material assignment, constraining the base platform, and applying a static load of approximately 25 N on the top platform. This load replicates the sanding tool mounted on top of the isolator, which weighs about 2.492 kg including the battery, equivalent to 24.438 N. For simplicity, the load was rounded to 25 N, applied vertically downward. Figure 8.10 shows the resultant stress analysis under Von Mises criteria in MPa.

From the static analysis results, the maximum stress was found to be 455.4 MPa, occurring near the folded-beam edge. The high stress concentration indicates that under loading, the maximum stress accumulates at the end of the span beam due to the structural geometry resembling a cantilever, where the connector side experiences the highest stresses. To validate the structural integrity, the Factor of Safety (FOS) was calculated. For the chosen material ERGAL 70, the tensile yield strength is 503 MPa. Therefore, the FOS is approximately 1.104, which is only about 10% above the working stress. This low margin of safety implies that the **current design is very close to the failure threshold and is not suitable for engineering applications**.

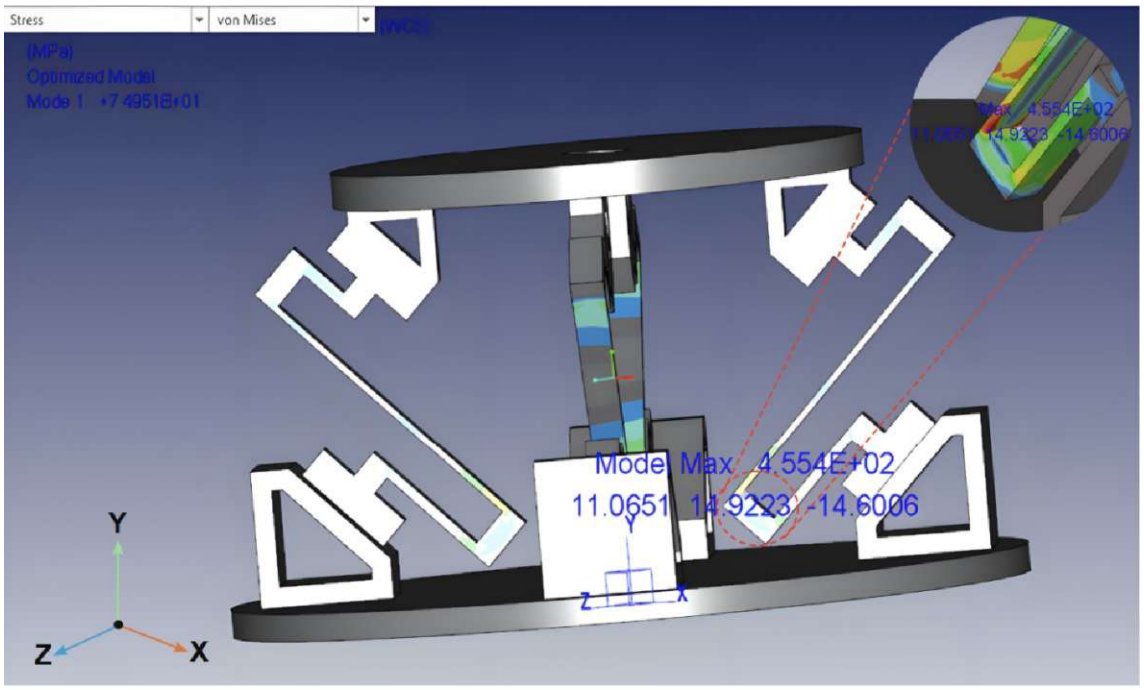

Figure 8.10: Static Analysis for the modified folded beam isolator platform.

8.4 Multi-Folded Non-Symmetric Beam Isolator

Although the optimised isolator model achieved acceptable frequency ranges, the static analysis revealed that the design failed to meet safe working limits due to its thin-span beam structure, which caused failure near the connector ends. To address this limitation, we propose a design modification by increasing the number of bends in the folded beam. By adding additional folds, the stiffness of the beam can be further reduced, thus lowering the modal frequencies of the system. This property was already observed in the previous chapter, where multi-folded beams demonstrated significantly lower stiffness compared to single-fold beams.

Based on this observation, the entire 6-DOF 45° isolator platform was redesigned using a **multi-folded beam design**. In this initial step, one additional turn was added to the folded beam structure. Furthermore, other components were modified, such as **removing the separate mounting bracket** and instead **integrating the beam structure directly into the design**. The integration of the beam structure reduces the number of individual parts, thereby lowering the overall manufacturing cost.

Since the modelling and analysis procedure for the new isolator platform follows the same approach as for the initial folded beam isolator, we again performed modal analysis to inspect the first four mode shapes and their respective frequencies. If the results showed frequencies above the desired threshold, we planned to conduct an optimisation study

by assigning the goal and objective function to reduce the system's natural frequency below the defined threshold. Once achieved, a final modal analysis would confirm the optimised frequency range of the updated model.

Figure 8.11 illustrates this entire procedure in the form of a flowchart, summarising the sequential steps followed during the design, optimisation, and analysis of the multi-folded isolator platform.

After proceeding with all the above processes, we finally obtained the desired isolator platform, as shown in Figure 8.12, which satisfies all the required objective frequency criteria and performs significantly better than its predecessors. Another noticeable design upgrade was the introduction of fillet rounds near the junctions where the span beams meet the connector beams. This modification helps distribute stresses more evenly, thereby reducing localised stress concentrations at the beam edges.

Once the final isolator model with the optimised multi-folded beam structure was complete, we assembled all the submodules into a fully integrated **passive vibration isolator end-effector interface**.

8.4.1 Complete Assembled Multi-Folded Beam Passive Vibration Isolator End-Effector

The assembly of the passive vibration isolator end-effector interface was carried out in multiple stages. First, the modelled Dewalt tool and its battery module were mounted. On top of this, a custom-designed top cap holder was fixed, serving as the connection between the tool and the rest of the end-effector interface.

Above the cap holder, a connector flange was placed, linking the cap holder (and tool) to the top platform of the multi-folded beam isolator platform. The isolator base platform was then connected to a custom-made adapter designed to hold either the ATI Mini-45 or Mini-58 Force/Torque (FT) sensor. In our current assembly, we used the Mini-45 FT sensor, which was coupled with the Doosan robot's flange interface via a sensor mount flange.

The complete assembled structure is shown in Figure 8.13, where every component mentioned was rigidly joined using appropriately sized metric screws. The completed assembly closely follows the initial schematic design of how the vibration isolator is positioned between the disturbance source (the tool) and the receiver (the robot). Ultimately, the system is mounted on the Doosan H2515 robotic arm for carrying out the instructed cleaning operations.

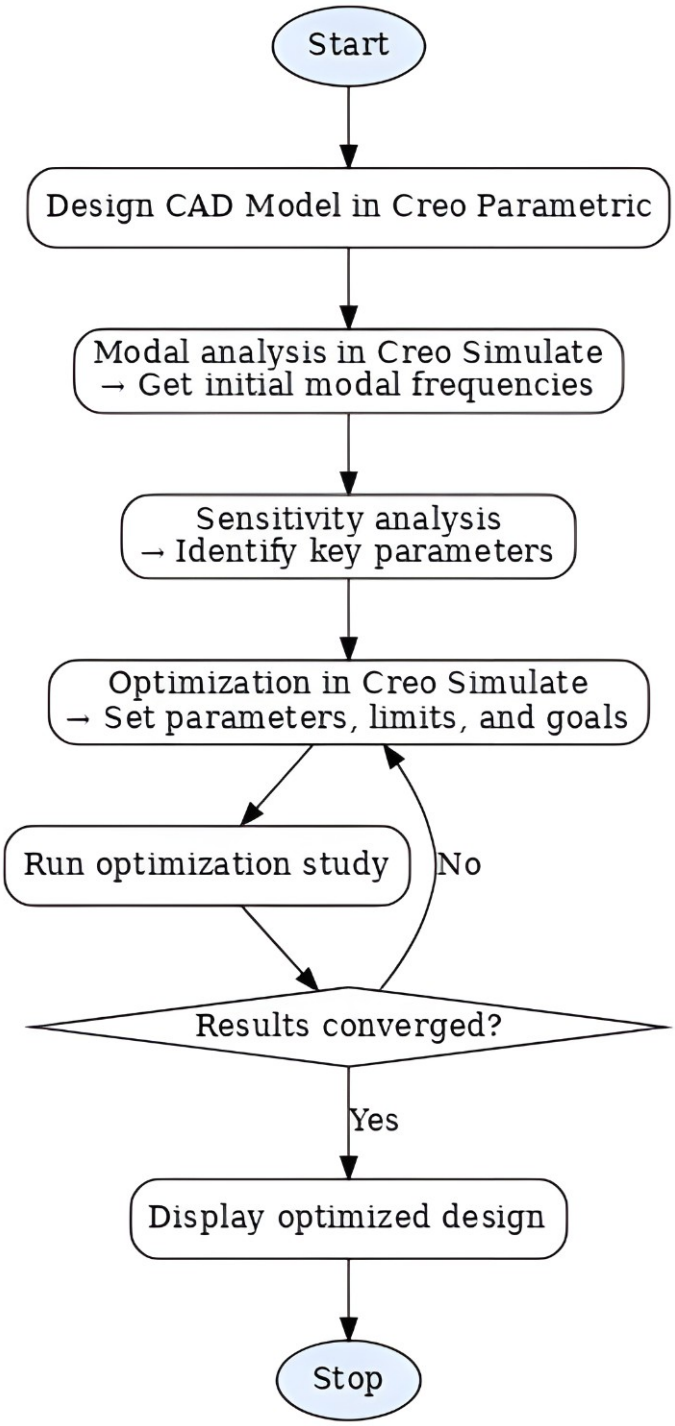

Figure 8.11: Simplified CAD-to-Optimisation Workflow for Modal Frequency Tuning for the Vibration Isolator Platform design.

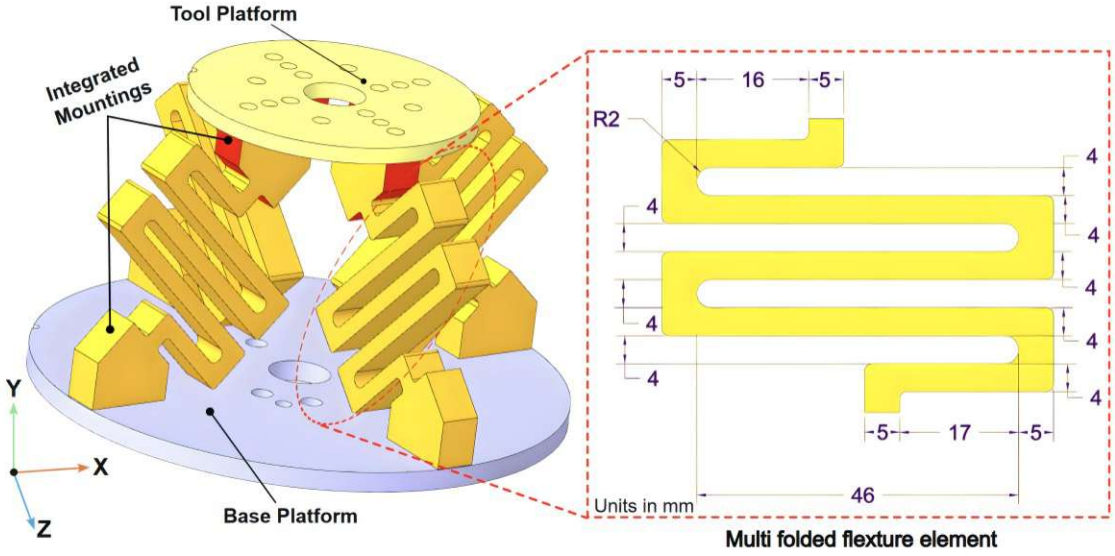

Figure 8.12: Final Model of the Multi-folded beam isolator platform.

8.4.2 Modal and Static Analysis of the Final Assembled Isolator Interface

The assembled vibration isolator, together with the mounted tool, was analysed through both modal and static analysis to verify the overall dominant frequencies and mode shapes of the integrated end-effector isolator module. The same procedure as described in the earlier sections was repeated, assigning the material ERGAL-70 with its mechanical and material properties, along with other necessary simulation parameters.

The results of this study are illustrated in Figure 8.14, showing the first four mode shapes of the fully integrated system. The corresponding descriptions of these modal shapes, together with their dominant frequencies, are summarised in Table 8.5.

From the above modal analysis for the integrated assembled structure, the dominant frequencies for the first three modes were all below the threshold range of $95.5\ Hz$, except for the fourth mode, where the system's dominant frequency was about 63.1% **above the threshold value**. We cannot state that this mode will critically affect the performance of the isolator because this particular frequency occurs in the higher harmonics, specifically in an *out-of-plane translational mode*. In practical finishing operations, the end-effector tool is subjected to an exerted force on the workpiece by the robot, which internally damps the system, making the occurrence of vibrations in the higher harmonic range improbable.

In contrast, the **first modal frequency at 20.955 Hz** has a theoretical isolation efficiency of approximately 97.5%, thereby almost completely preventing the source

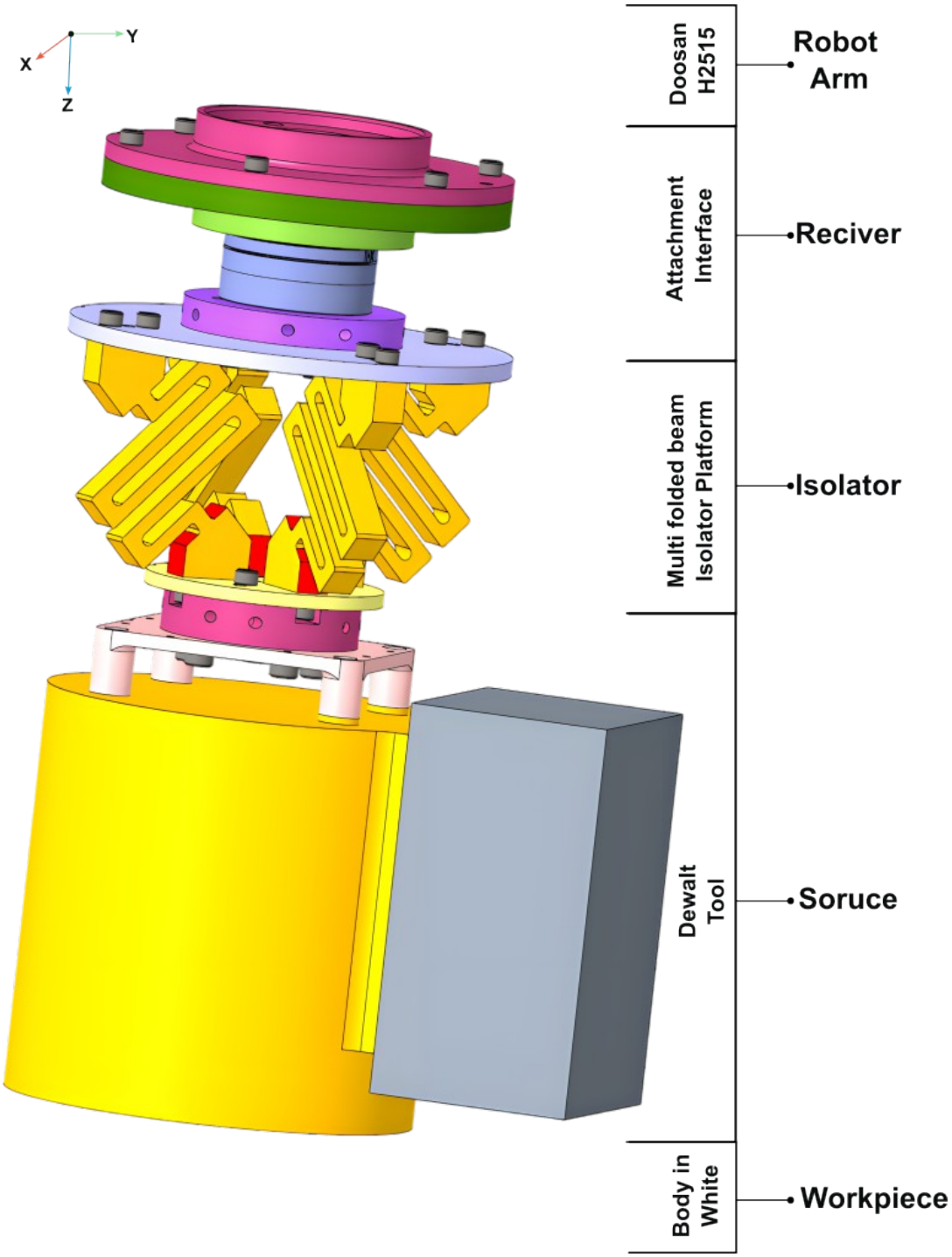

Figure 8.13: Complete Final Assembly of the Multi-folded beam passive vibration isolator End effector.

Figure 8.14: First four dominant frequencies along with their respective mode shapes for the Assembled Isolator.

Mode #	Dominant Frequency (Hz)	Modal Description
1	20.955	**In-plane translation** along the lateral direction, **global X, Z-axis**
2	22.040	**In-plane translation** along the lateral direction perpendicular to the previous translation, **global X, Z-axis**
3	59.212	**Torsional (yaw) mode** about the vertical axis, rotation around **global Y-axis**
4	106.28	**Out-of-plane translational mode** along the vertical direction, motion primarily along **global Y-axis**

Table 8.5: First four modes of the isolator system with dominant frequencies and technical motion descriptions for the multi folded beam isolator.

disturbance from transmitting to the receiver end. The high isolation efficiency ensures that the entire system remains stable and effective during the cleaning operation on automobile body parts.

For the final evaluation, the system's response to loading conditions was verified through a **static analysis study** of the integrated assembled system. In this test, the isolator base was constrained and, with the tool attached to the top platform, a vertical static load was applied. The results, shown in Figure 8.15, reveal that the maximum Von Mises stress was $22.08\ MPa$, occurring at the junction between the span beam and the connector beam. However, under resonant conditions, the maximum Von Mises stress increased to $38.24\ MPa$. Importantly, in this case, the stress was more evenly distributed across the span, reducing localised stress concentrations. Therefore, the current sys-

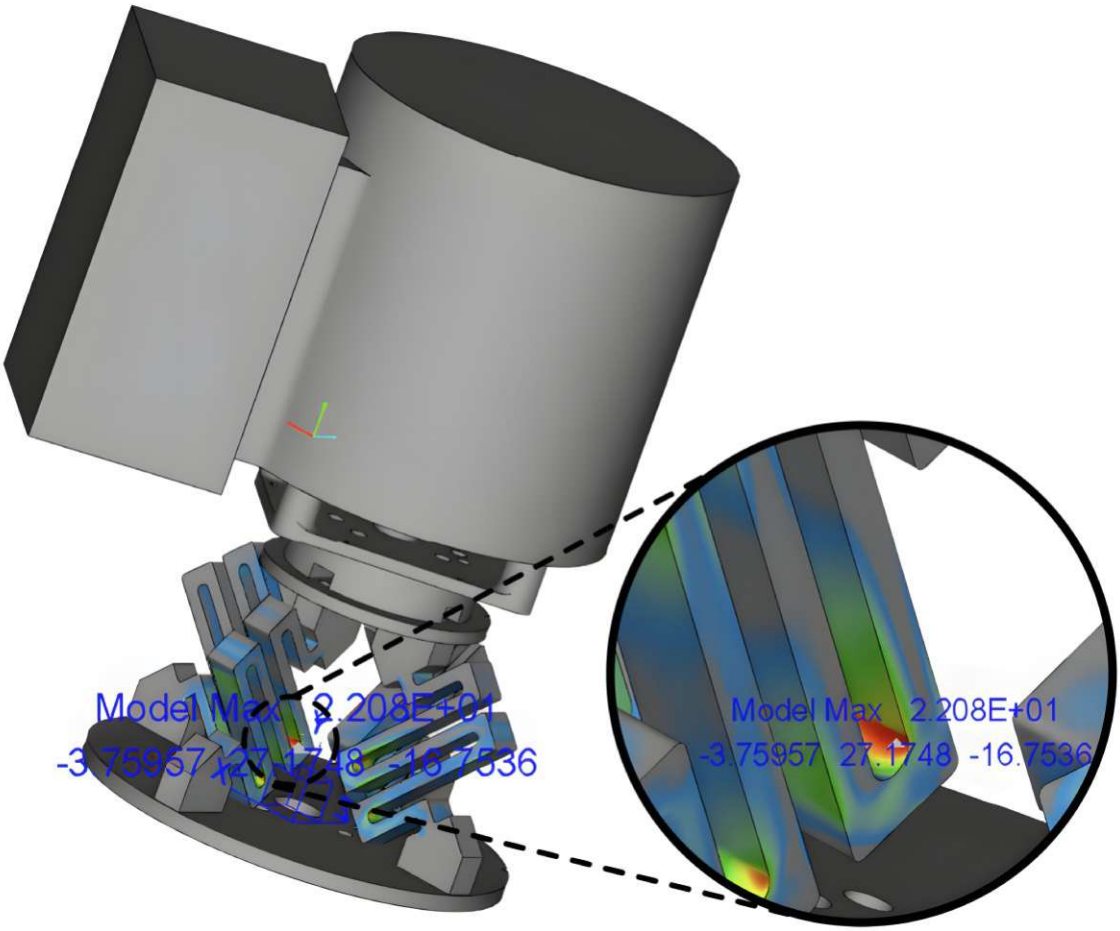

Figure 8.15: Static Analysis for the final assembled isolator End effector module.

tem was confirmed to effectively sustain static loads without significant deflections or excessive stress, making it suitable for fabrication into machined components.

8.5 Potential Limitation in the Current Conventional Folded Beam Isolator Design

- Performance can be compromised when low-order harmonics of the disturbance source align with the modal frequencies of the isolator, leading to resonance amplification at specific operating speeds [99].
- The current folded beam isolator geometry makes it challenging to achieve precise stiffness targets in specific orientations, especially for variable disturbance profiles as found in the operating random orbital sanding tool.

- This design illustrates the trade-offs between compactness, stiffness tuning, and robustness to varying disturbance characteristics, underscoring the potential need for more effective alternative isolation strategies.
- Static analysis results, illustrated in Figure 8.16, reveal that when a normal force F_n is applied along the x- or z-axis, the load is nominally distributed among the four flexure beams. For F_n acting along z, beams 1 and 4 experience predominantly in-plane loading, whereas the diagonal beams 2 and 3 carry the load as an out-of-plane component—a direction in which folded beams exhibit significantly lower stiffness. In contrast, a diagonal force F_d at 45° produces an equal in-plane load distribution across all beams.

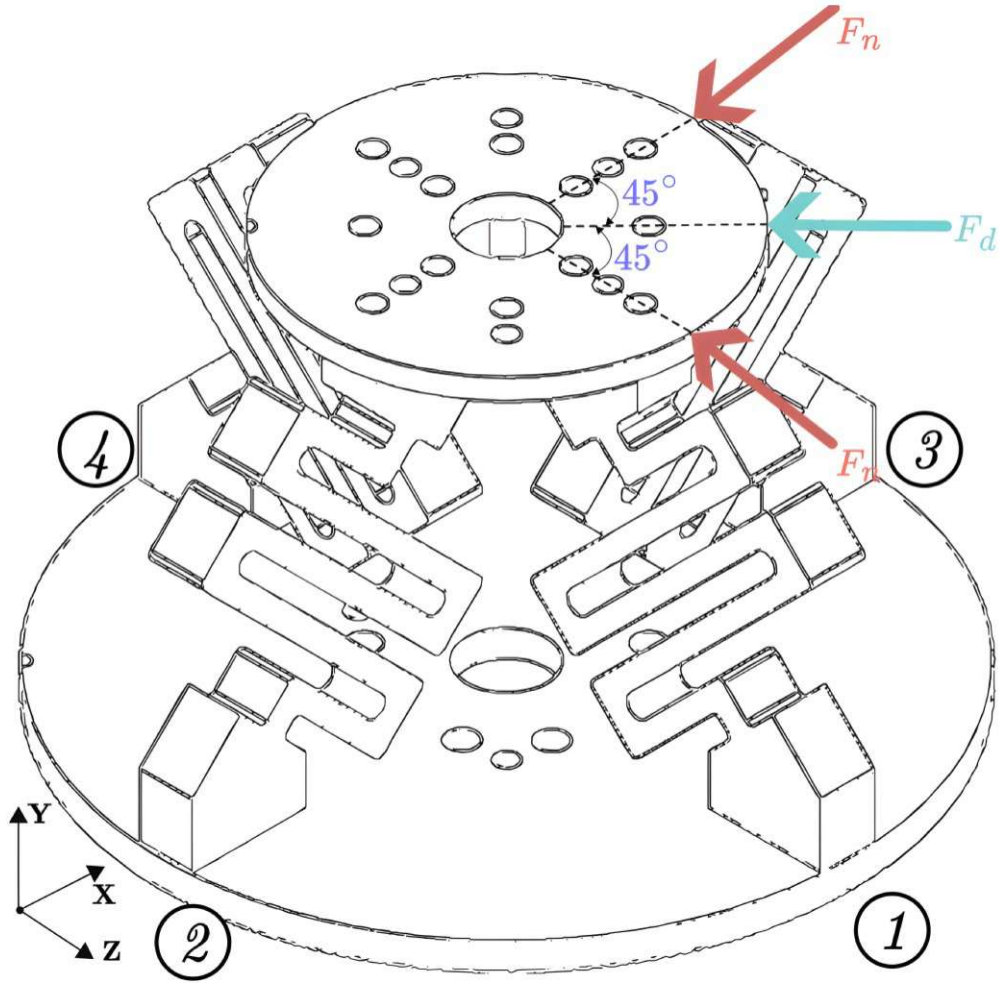

Figure 8.16: Static Analysis for the final assembled isolator End effector module.

This directional dependency leads to **unequal stiffness utilisation**, where one beam pair experiences greater deflection and higher stress while the opposing pair remains underloaded. This inherent asymmetry is a key limitation observed in the conventional passive multi–folded-beam vibration isolator configuration.

9 Passive Folded-Beam Stewart Platform Isolator Design

Until now, in this study, we have discussed in detail and developed solutions that address the issue of vibration by designing both the unit absorbing element and the platform, which mitigates these vibrations. These solutions were then modelled to fit the current use case application. In the previous chapter, we proposed a passive vibration isolation platform using folded beam structures that thoroughly met all the essential parameters. However, even with all the qualifications, the design exhibited directional stiffness anisotropy, leading to suboptimal load sharing and resonance sensitivity, which reduces the isolation performance under variable disturbance profiles. These limitations have driven us to explore further in developing a significantly better solution that addresses these shortcomings.

In this process, we first encountered a solution in a different engineering domain — an offshore access solutions company called Ampelmann — where we found a hexapod-designed structure, essentially a *Stewart Platform*, as shown in Figure 9.1, which forms the motion-compensating base in offshore applications such as cargo handling and safe personnel transfer.

Figure 9.1: Ampelmann's hexapod system used for safe personnel transfer from an offshore construction site [103].

This platform is one of the most popular and widely used parallel manipulators, known

as the *Stewart Platform* or *Gough–Stewart Platform*, named after its inventors. It has applications ranging from small-scale, high-precision positioning systems to large-scale, heavy-duty motion simulators and industrial platforms.

9.1 A General Brief Overview on the Stewart Platform

The *Stewart Platform* falls under the domain of parallel mechanisms, first proposed by V. E. (Eric) Gough and D. Stewart in 1965, which has six degrees of freedom. This platform design allows the entire mechanism to move without any ground-fixed axis during manoeuvres. This approach offers a more compact and versatile alternative to serial manipulators and other interfaces where the primary goal is to minimise the actuator count while ensuring each actuator (connecting beam) directly contributes to supporting the payload, achieving a high payload-to-structure mass ratio [104].

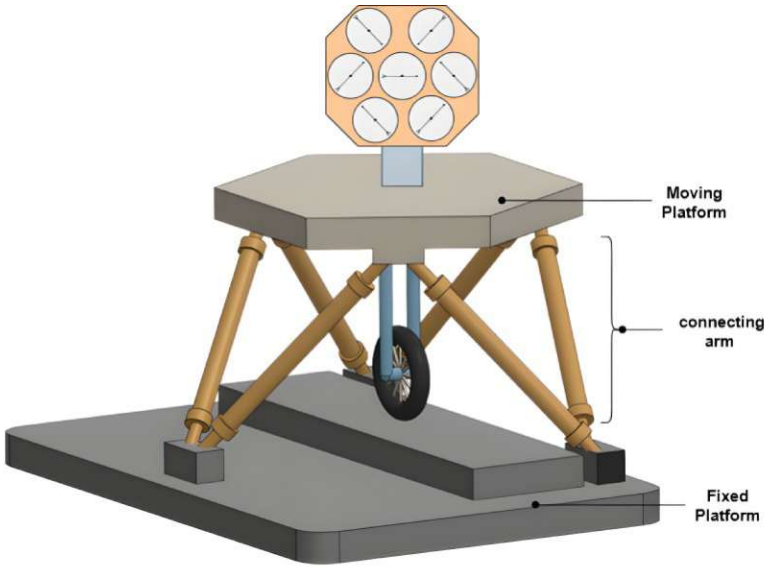

Figure 9.2: A model of the Gough platform, originally used as a type testing machine [105].

The original platform consists of a moving and a fixed platform connected by six linear actuators arranged between them in a fully triangulated hexapod layout, as illustrated in Figure 9.2. Each leg can extend or retract independently, allowing the top platform to move in all six degrees of freedom, thereby generating precise multi-axis motion. With this mechanism, the initial tyre testing was conducted by simulating complex service conditions for the tyre while keeping the test environment stationary. This concept was later adopted by Stewart into the flight motion simulator, moving from purely mechanical testing to a more immersive simulation [104]. This design laid the foundation for a model that was later adopted in various fields and applications.

9.1.1 Types of Gough–Stewart Platform Configurations

In general, these Gough–Stewart 6-DOF parallel mechanisms are mainly divided into four types: SSM (Simplified Symmetric Manipulator) or type 6-6, TSSM (Triangular Simplified Symmetric Manipulator) or type 6-3, MSSM (Minimal Simplified Symmetric Manipulator) or type 3-3, and finally a less common version called MSP (Modified Stewart Platform), as shown in Figure 9.3. These are the standardised platform configurations most widely adopted in the literature and research publications [106].

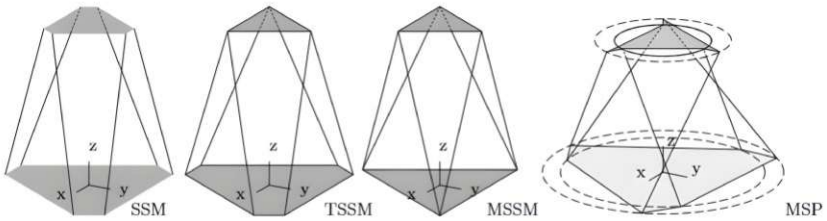

Figure 9.3: The four different Parallel Manipulator workspace configurations [106].

Here is a brief classification of each of the distinct platform configurations:

- **SSM (6–6, "Symmetric Simplified Manipulator")**: This is the classic 6-6 Gough–Stewart layout having six distinct base anchors and platform anchors, typically arranged as three symmetric pairs. This configuration forms the classic *"hexagon-on-hexagon hexapod"* [106]. In this configuration, the constant orientation workspace is larger compared to the others.
- **TSSM (6–3, "Triangular SSM")**: This platform has six distinct base anchors but only three platform anchors, where two legs meet at each vertex of a triangular moving platform. Mechanically, this compacts the top plate while preserving much of SSM's symmetry. This configuration provides a medium-sized, constant-orientation workspace, adjacent to SSM.
- **MSSM (3–3, "Minimal SSM")**: In this version, three anchors are placed on the base and three on the platform, with each anchor shared by a leg pair. Mechanically, this is the most compact arrangement but also exhibits the strongest co-location of joints. This configuration offers the smallest constant orientation workspace.
- **MSP ("Modified Stewart Platform")**: This is an optimised design for dexterity rather than workspace volume, realised by distributing anchors on both platforms. This unique distribution makes the platform optimal when dexterity is prioritised over workspace volume.

All these configurations are widely used in the domain of **micro-vibration isolation**, where they act as 6-DOF isolators to attenuate vibrations from multi-directional reaction

wheel assemblies inside spacecraft and satellites. These platforms exhibit high stiffness, large load-carrying capacity, and good dynamic performance with tractable inverse kinematics [105]. The combination of these properties makes them highly suitable and widely adopted in space applications.

9.2 State-of-the-Art Gough–Stewart Passive Vibration Isolation Designs

Since our current design for the Stewart platform integration is **passive-based**, we review some of the past research efforts. Researchers have developed several models where the connecting arms are passive; however, most designs were active, developed for higher performance and a broader frequency spectrum. Active Stewart platforms are more complex and rely on external control and power, making them effective over a wide range; however, they are less suitable for our present study.

In contrast, our application is limited to conducting cleaning operations on automobile surfaces. Since we already know the range of dominant frequencies of the tool, attenuating these frequencies can be best achieved through passive solutions. Their simple, robust, and reliable design makes them well-suited for this use case.

A general and most widely adopted **6-DOF Stewart-inspired vibration isolation system (SVIS)** is a parallel kinematic hexapod mechanism composed of a rigid base, a payload platform, and six variable-length struts arranged between the two platforms, as illustrated in Figure 9.4. Such a configuration simultaneously attenuates translational and rotational disturbances while fitting within compact volumes. Structurally, this platform is highly efficient since loads are shared across six struts, providing a high stiffness-to-mass ratio while simultaneously achieving low dynamic stiffness [107].

In much of the literature and research, the focus has been primarily on **active Stewart platform isolators** because of their wide operational bandwidth, covering frequencies from sub-Hz to approximately $10\ Hz$. In contrast, purely passive hexapods often require additional soft supports, which are challenging to model. On the other hand, **passive methods** dominate at high frequencies, where their low-frequency performance is intrinsically limited. Nonetheless, passive Stewart platform isolators remain compelling when the disturbance content lies above the platform's corner frequency. In such cases, these platforms provide compact six-degree-of-freedom compliance with high stiffness-to-mass ratios [107].

In recent years, the development of novel **flexure-based designs** has made this area

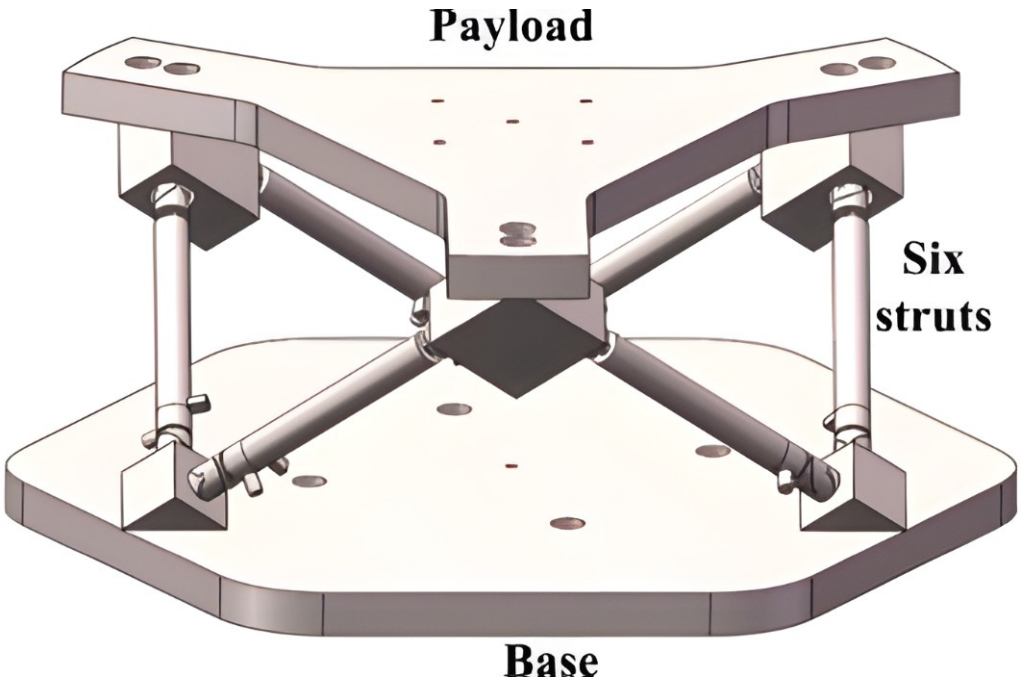

Figure 9.4: A General 6-DOF Stewart-inspired vibration isolation system (SVIS) [108].

an active research domain, as flexures introduce significant advantages in achieving high-static–low-dynamic-stiffness (HSLDS) characteristics in a compact architecture.

Here, we present a review of some past passive Stewart platform designs that inspired our own work. These include designs based first on spring structures, followed by flexure-based configurations, both of which serve as basic reference design models in the development of our new platform structure. Since one of our primary design constraints is to create a passive-based system that is compact and simple, while also allowing the sanding tool to be easily mounted and unmounted, we have particularly investigated designs utilising springs and flexures.

9.2.1 Passive Spring-Based SVIS

Several **passive spring-based Stewart Vibration Isolation Systems (SVIS)** have been developed for controlling the micro-vibrations generated by space components such as reaction wheel assemblies (RWA) and momentum wheel assemblies (MWA), preventing these vibrations from being transmitted to sensitive instruments. Most of these designs utilise X-shaped legs, as illustrated in Figure 9.5 (a–d). Collectively, these configurations aim to achieve broadband, multi-directional vibration suppression with high static–low dynamic stiffness (HSLDS) in a purely passive manner.

From Figure 9.5(a) [109], the authors presented an X-shaped structure-supporting isolation platform, where each single X-shaped module comprises two plates connected by

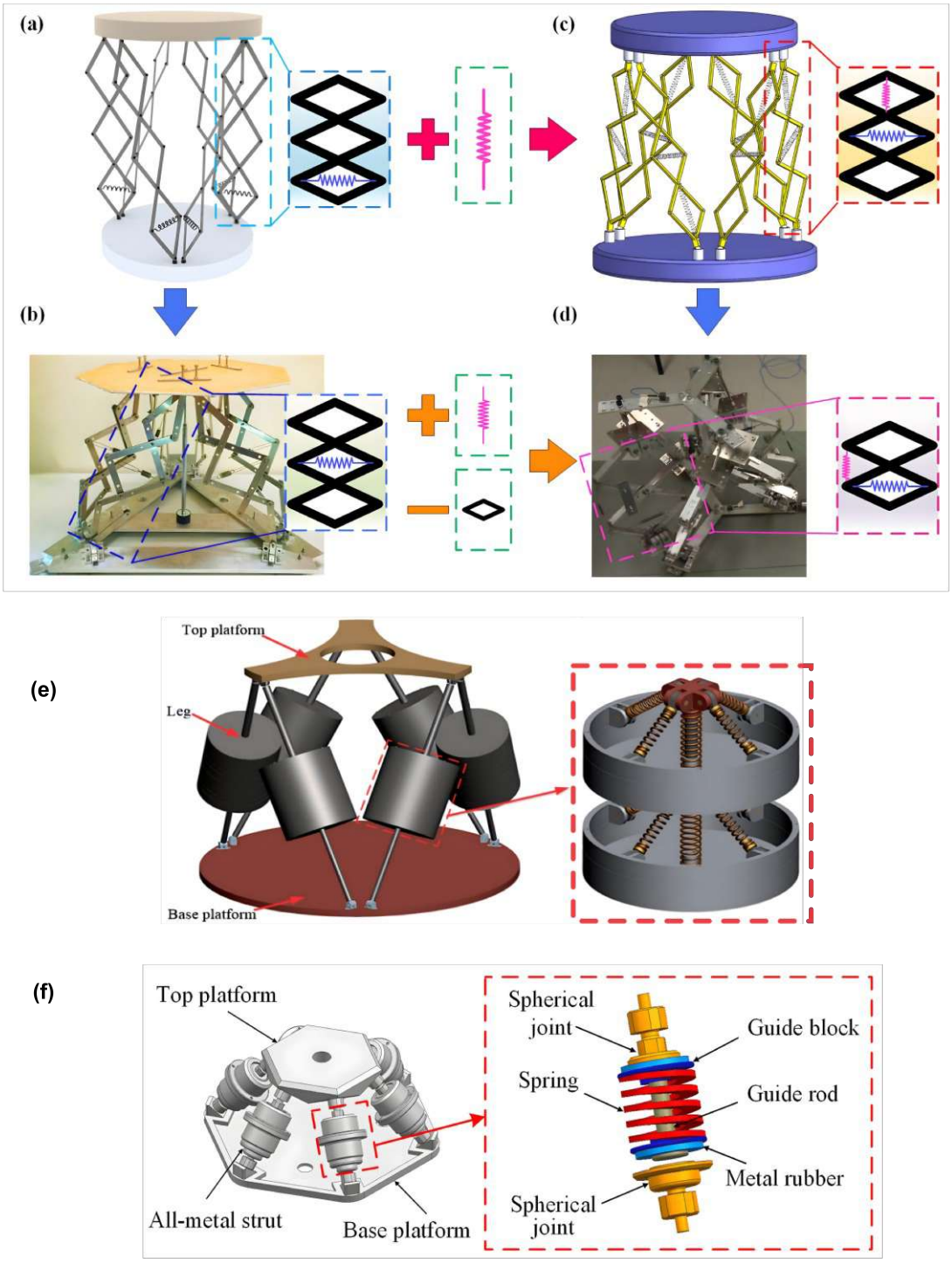

Figure 9.5: The passive spring-based SVIS structures: (a) 3D model of the SVIS with X-shaped struts [109], (b) prototype of the SVIS with n-layer X-shaped legs [110], (c) 6-DOF passive Stewart platform using asymmetrical three-layer X-shaped legs [111], (d) experimental prototype of the SVIS with X-shaped struts [112], (e) Stewart platform with quasi-zero-stiffness (QZS) based vibration isolator [113], (f) 6-DOF all-metal vibration isolator with spring–damper system [114].

crossed linkages, preloaded with springs and damping elements. These collectively generate the nonlinear stiffness profiles required for broadband isolation while maintaining load-carrying capacity. When arranged in this configuration, the research demonstrated superior multi-directional vibration suppression compared to conventional designs, particularly considering the elastic limits of springs along with their initial velocities and force inputs.

In [110], a variation employing vertically asymmetrical three-layer X-shaped structures (aXSS) as the Stewart platform legs was explored, as illustrated in Figure 9.5(b). This asymmetry in rod lengths introduces additional geometric nonlinearity, allowing further tuning of static and dynamic stiffness properties. Analytical and experimental results showed that the aXSS-based Stewart platform maintains high static stiffness for load support while achieving low dynamic stiffness across all DOFs, yielding low resonant frequencies and enhanced isolation. More importantly, this asymmetry enables more flexible installation in constrained environments and offers greater parameter adjustment than symmetric X-shaped designs.

As shown in Figure 9.5(c), the researchers in [111] proposed another X-shaped structure-based Stewart isolation platform (XSSIP) for post-capture vibration suppression in free-floating spacecraft. This under-constrained 6-DOF system consists of legs with n-layer X-structures, originally designed to be mounted between a spacecraft's robotic arm and capture mechanism. Parametric studies revealed that the optimal design of the XSSIP can significantly attenuate both tangential and normal post-capture vibrations compared to conventional spring–mass–damper Stewart platforms.

In the study [112], researchers presented a baseline complete 6-DOF passive Stewart platform with n-layer X-shaped legs, as shown in Figure 9.5(d). This design provides a clean, geometric mechanical framework by parameterising rod lengths, assembly angles, and both horizontal/vertical spring constants. It permits tailored stiffness characteristics ranging from negative to quasi-zero to positive by structural design alone, eliminating the need for active control. Experiments validated that the nonlinear legs provide markedly improved passive vibration isolation across all six directions compared to linear spring legs.

The design illustrated in Figure 9.5(e) represents a unique class of Stewart isolators that adopts a cubic hexapod architecture with six piezoelectric struts between a rigid base and a payload plate, each end joined by spherical joints to permit six degrees of freedom (6-DOF) motion. In [113], the authors reported 30 dB attenuation for tonal inputs and 10 dB to 20 dB for random disturbances in the 5 Hz to 200 Hz range. A unique feature of this system is that each leg is replaced by an n-stacked quasi-zero-stiffness (QZS) cell module to realise high static load capacity with ultralow dynamic stiffness in a passive manner.

Each QZS cell comprises one vertical spring and four symmetrically placed oblique springs connected by hinges; geometric nonlinearity in the oblique springs generates a negative-stiffness contribution that cancels the vertical spring near equilibrium extension, producing near-zero local stiffness. Consequently, QZS behaviour can be achieved in all six DOFs around the nominal configuration. This design effectively translates QZS behaviour into a full 6-DOF Stewart topology.

The Stewart platform configuration presented in [114], as detailed in Figure 9.5(f), incorporates all-metal struts designed for enhanced durability and load-bearing capacity. Each strut connects the top and base platforms via spherical joints, enabling full six-degree compliance. The internal structure of each strut integrates a spring–metal rubber composite element, positioned between guide blocks and restrained by a central guide rod to maintain axial alignment under load. The metal rubber provides nonlinear stiffness and high damping capacity, effectively dissipating vibratory energy across a broad frequency spectrum without relying on viscoelastic materials. The spring ensures elastic restoring force, while the metal rubber introduces hysteretic damping, producing a combined high-static and low-dynamic stiffness (HSLDS) effect. This design is particularly suitable for aerospace, precision manufacturing, and harsh operational environments. Experimental testing confirmed that the hybrid strut design significantly outperforms purely elastic or purely damping-based Stewart platforms in both attenuation bandwidth and load-carrying capacity.

As observed from the above spring-based SVIS designs, researchers often combine different elements to obtain nonlinear behaviour and HSLDS. However, such approaches are not cost-effective, bulky, and complex, as the number of parameters tends to increase exponentially with design complexity. Creating a low-profile design that meets the necessary behaviours will make the platform robust and compact. Additionally, as emphasised in [110], the importance of asymmetry lies in broadening the tuning range of stiffness and damping parameters, thereby enhancing performance in constrained environments.

9.2.2 Passive Flexure-based SVIS.

All the above-mentioned criteria can typically be satisfied by introducing flexures instead of traditional torsional springs. As explained in earlier chapters, these structures exhibit nonlinear behaviour and can attenuate vibrations across a broader spectrum. Furthermore, the design complexity and structural elements involved in constructing such platforms are relatively more straightforward compared to the more complex spring-based designs. Several past researchers have utilised structural flexures to achieve these functionalities effectively without resorting to conventional springs or dampers.

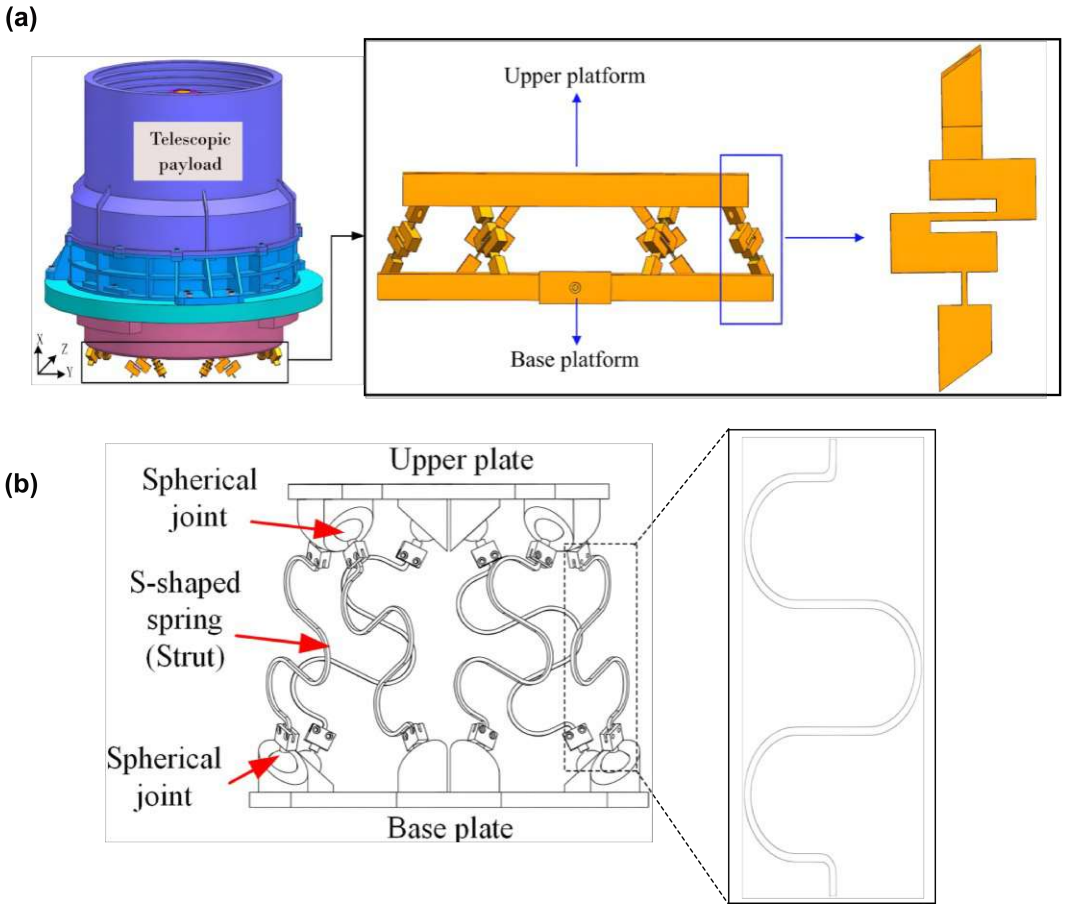

Figure 9.6: Passive flexure-based SVIS: (a) Stewart-platform–based 6-DOF micro-vibration isolator showing payload integration (left), hexapod with six canted legs (centre), and unit leg-isolator (right) [89]; (b) 6-DOF passive vibration isolator with S-shaped legs [115].

Here in this novel design [89], a Stewart hexapod was built to carry heavy payloads such as optical space telescopes, as shown in Figure 9.6(a). Each leg is realised by a beam element arranged to form an anisotropic flexure core, illustrated on the right-hand side of Figure 9.6(a), to mitigate micro-vibrations. Each lamina is a one-piece compliant structure that increases axial compliance while maintaining relatively high lateral and torsional stiffness.

The connector flexures are arranged in a special pattern around the hexapod such that the principal stiffness directions of opposing leaves are symmetric about the platform axes, thereby minimising cross-coupling. The authors also conducted optimisation studies to determine the optimal dimensional parameters for these flexures. With all these considerations, this platform is both compact and robust, capable of handling the most precise and delicate instruments.

In Figure 9.6(b), a novel Stewart platform configuration proposed by [115] replaces con-

ventional prismatic legs with *S-shaped spring beams* (flexures) to achieve multi-directional vibration isolation and increased compliance. The *S-shaped geometry* functions as a distributed-compliance mechanism, where bending deformation dominates over axial stiffness. This results in significantly reduced vertical and lateral stiffness compared to solid struts, enabling **high-static–low-dynamic-stiffness (HSLDS)** behaviour without additional mechanical complexity. The design also provides progressive nonlinear stiffness increase with deflection, which helps suppress low-frequency vibrations while preventing excessive displacement under large loads. Critical performance factors such as balanced load-carrying capacity and isolation effectiveness depend strongly on the geometry of the S-shaped beams. Static analysis revealed that the platform distributes forces evenly among the legs, and the bending-dominated deformation leads to inherently low coupling between translational and rotational stiffness.

The Stewart platform with S-shaped flexure legs forms the basis for our new design of a folded-beam vibration isolator platform. From these studies, it is evident that incorporating *flexures* into Stewart platform designs achieves **HSLDS behaviour** along with nonlinear stiffness characteristics by simply tuning the design parameters of the beam structure. The use of flexures eliminates the need for overly complex hybrid designs that fuse multiple components, as observed in spring-based Stewart platform isolators.

9.3 Geometrical and Analytical Formulation for the Stewart-based Vibration Isolator

From the literature on Stewart-based SVIS designs, it is evident that **flexure-based passive Stewart platforms** are highly desirable for our current application, where the end-effector must be compact, robust, and able to attenuate oscillations across all six degrees of freedom. The effectiveness of a Stewart platform lies in the precise interplay between its geometric design and the stiffness parameters of its legs. The geometric formulation defines critical parameters such as leg inclination, platform radii, and the overall base-to-platform dimensions, which together determine the modal frequencies necessary for effective vibration isolation.

Figure 9.7 shows the schematic representation of a general Stewart platform isolator. The geometry is defined by:

- Base radius: R_b
- Top platform radius: R_p
- Vertical separation (height): H
- Folded-beam flexure length: l_0

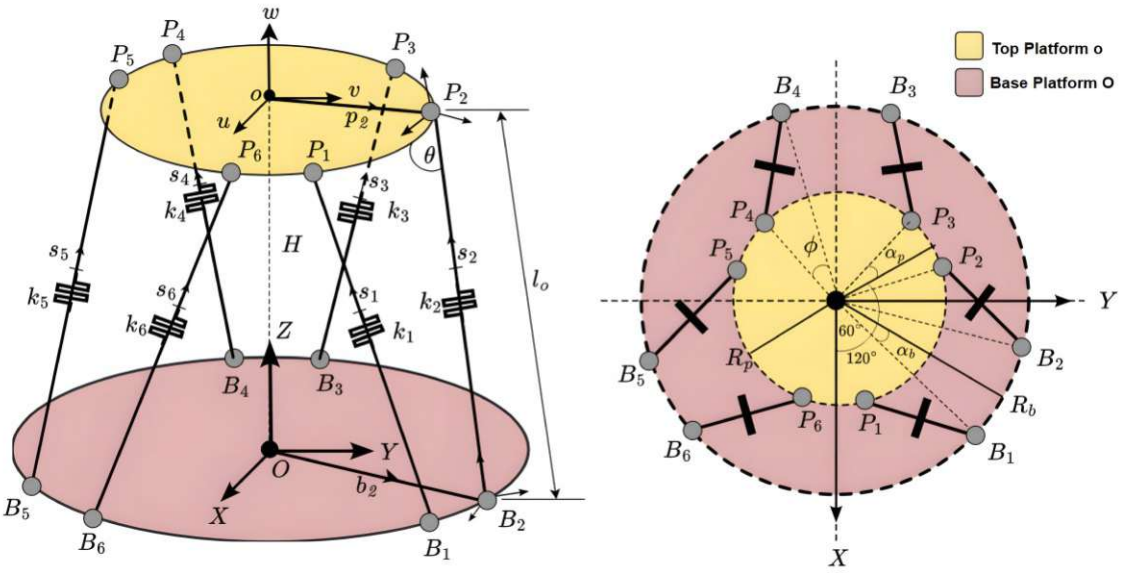

Figure 9.7: Geometrical view of Passive Stewart Platform-based Folded beam vibration isolator, the left is the front view of the isolator design and the right is the Top view of the design platform

- Stiffness of each leg: k_i
- Inclination angle: θ

Six folded-beam flexures connect the top and bottom platforms, each leg joined at base coordinates $\mathbf{B}_i$ (fixed base) and platform coordinates $\mathbf{P}_i$ (moving platform), with the origin O defined at the base centre. Each leg is associated with a screw vector $\mathbf{s}_i$ that specifies both the direction and the moment about the origin, where $i = 1, 2, \ldots, 6$. From the top view, the upper and lower platforms are offset by $60°$, with each leg attachment separated by $120°$. The half-pair angles on the base and top platforms are denoted α_b and α_p, respectively, as illustrated in Figure 9.7. The joint locations for the symmetric platform configuration are thus derived directly from this geometrical setup.

The base and platform joint locations for the symmetric Stewart platform are given as:

$$\mathbf{B}_i = R_b \begin{bmatrix} \cos\psi_b \\ \sin\psi_b \\ 0 \end{bmatrix}, \quad \mathbf{P}_i = R_p \begin{bmatrix} \cos\psi_p \\ \sin\psi_p \\ 0 \end{bmatrix}, \quad i = 1, 2, \ldots, 6 \tag{9.1}$$

where

$$\psi_b = \frac{\pi}{3} \cdot i + \alpha_b, \quad i = 1, 3, 5; \qquad \psi_b = \frac{\pi}{3}(i-1) + \alpha_b, \quad i = 2, 4, 6$$

$$\psi_p = \frac{\pi}{3}(i-1) + \alpha_p, \quad i = 1, 3, 5; \qquad \psi_p = \frac{\pi}{3} i - \alpha_p, \quad i = 2, 4, 6$$

The transformation matrix from the uvw frame to the XYZ frame is obtained by premultiplying the three basic Euler rotation matrices:

$$ {}^{B}\mathbf{R}_{P} = \text{Rot}(z,\gamma) \cdot \text{Rot}(y,\beta) \cdot \text{Rot}(x,\alpha) \tag{9.2} $$

$$ {}^{B}\mathbf{R}_{P} = \begin{bmatrix} c\alpha & -s\alpha & 0 \\ s\alpha & c\alpha & 0 \\ 0 & 0 & 1 \end{bmatrix} \begin{bmatrix} c\beta & 0 & s\beta \\ 0 & 1 & 0 \\ -s\beta & 0 & c\beta \end{bmatrix} \begin{bmatrix} 1 & 0 & 0 \\ 0 & c\gamma & -s\gamma \\ 0 & s\gamma & c\gamma \end{bmatrix} \tag{9.3} $$

Which simplifies to:

$$ {}^{B}\mathbf{R}_{P} = \begin{bmatrix} c\beta c\alpha & s\gamma s\beta c\alpha - c\gamma s\alpha & c\gamma s\beta c\alpha + s\gamma s\alpha \\ c\beta s\alpha & s\gamma s\beta s\alpha + c\gamma c\alpha & c\gamma s\beta s\alpha - s\gamma c\alpha \\ -s\beta & s\gamma c\beta & c\gamma c\beta \end{bmatrix} \tag{9.4} $$

where $s\alpha = \sin\alpha$, $c\alpha = \cos\alpha$, $s\beta = \sin\beta$, $c\beta = \cos\beta$, $s\gamma = \sin\gamma$, $c\gamma = \cos\gamma$.

From Figure 9.7, the vectors $\mathbf{p}_i$ and $\mathbf{b}_i$ are the position vectors of the connection points with respect to the platform and base origins. Thus, there are six pairs of these vectors:

$$ \mathbf{b}_i = \begin{bmatrix} b_{ix} & b_{iy} & b_{iz} \end{bmatrix}^T, \qquad \mathbf{p}_i = \begin{bmatrix} p_{ix} & p_{iy} & p_{iz} \end{bmatrix}^T $$

The vector loop equation for the i-th limb of the Stewart platform can be written as:

$$ \overline{\mathbf{B}_i\mathbf{P}_i} = \mathbf{l}_i = \mathbf{H} + {}^{B}\mathbf{R}_{P}\,\mathbf{b}_i - \mathbf{p}_i \tag{9.5} $$

Finally, the length of the i-th connector leg is obtained by:

$$ L = \|\mathbf{l}_i\| = \left\| {}^{B}\mathbf{R}_{P}\mathbf{b}_i + \mathbf{H} - \mathbf{p}_i \right\|, \quad i = 1,2,\ldots,6 \tag{9.6} $$

This results in six equations for the connecting legs, which describe their locations on the top and base platforms. In the current design, the top and bottom platforms have no relative rotation; they are only translated vertically by a distance H. The coordinates of the screw directions of the i-th leg are:

$$\mathbf{l}_i = \begin{bmatrix} -R_b \cos\left(\frac{2\pi}{3} + \alpha_b\right) - R_p \cos\alpha_p \\ -R_b \sin\left(\frac{2\pi}{3} + \alpha_b\right) + R_p \sin\alpha_p \\ H \end{bmatrix} \tag{9.7}$$

Then, the screw unit vector $\mathbf{s}_i$ of the i-th leg is the unit vector along $\mathbf{l}_i$, given by:

$$\mathbf{s}_i = \frac{\mathbf{l}_i}{L}, \qquad L = \|\mathbf{l}_i\| \tag{9.8}$$

$\forall i \in \{1, 2, \ldots, 6\}$

Thus, the components of the unit screw vector are:

$$\begin{cases} s_{ix} = \dfrac{-R_b \cos\left(\frac{2\pi}{3} + \alpha_b\right) - R_p \cos\alpha_p}{L}, \\ s_{iy} = \dfrac{-R_b \sin\left(\frac{2\pi}{3} + \alpha_b\right) + R_p \sin\alpha_p}{L}, \\ s_{iz} = \dfrac{H}{L}. \end{cases} \tag{9.9}$$

Here, s_{ix}, s_{iy}, s_{iz} are the components of the screw vector for the individual leg $\mathbf{l}_i$ projected onto the three coordinate axes. Therefore, the parametrised leg directions are defined by the unit screw vector components for each leg as:

The screw unit vector components are expressed as:

$$s_{ix} = \sin\theta\cos\psi, \qquad s_{iy} = \sin\theta\sin\psi, \qquad s_{iz} = \cos\theta.$$

Leg vector (reference pose, plates parallel):

$$\mathbf{l}_i = \begin{bmatrix} -R_b \cos A - R_p \cos\alpha_p \\ -R_b \sin A + R_p \sin\alpha_p \\ H \end{bmatrix}, \qquad A = \frac{2\pi}{3} + \alpha_b \tag{9.10}$$

Therefore, the component equations are:

$$R_b \cos A + R_p \cos \alpha_p = -L \sin\theta \cos\psi, \tag{9.11}$$

$$R_b \sin A - R_p \sin \alpha_p = -L \sin\theta \sin\psi, \tag{9.12}$$

$$H = L \cos\theta. \tag{9.13}$$

Here, θ is the leg inclination angle with respect to the top platform and ψ is the azimuth angle in the base frame. By solving for the base and platform radii from the above equations (using Cramer's rule), the closed-form solutions are:

$$\begin{cases} R_b = -\dfrac{H \tan\theta \sin(\alpha_p + \psi)}{\sin\left(\frac{2\pi}{3} + \alpha_b + \alpha_p\right)}, \\ R_p = \dfrac{H \tan\theta \sin\left(\frac{2\pi}{3} + \alpha_b - \psi\right)}{\sin\left(\frac{2\pi}{3} + \alpha_b + \alpha_p\right)}, \\ L = \dfrac{H}{\cos\theta}. \end{cases} \tag{9.14}$$

The negative sign is taken for the convenience of choosing the appropriate quadrants.

The parameters for modelling the Stewart platform were highly governed by the inclination angle θ and the vertical height H between the top and bottom platforms. With these, the initial geometrical parameters are listed in Table 9.1. All the following parameters were chosen iteratively through multiple modal and sensitivity analyses in *Creo Simulate* for determining the effective close-range parameters that satisfy the requirement of maintaining **high-static-low-dynamic-stiffness (HSLDS)** along with the tool's vibrational characteristics.

9.3.1 Global Stiffness Modelling for the SVIS

Once the design parameters were finalised, an analytical formulation for the global stiffness matrix was carried out. In general, the **global stiffness matrix** for the entire Stewart platform has been extensively studied and remains an important research topic. Therefore, in the present study, we adopt the methods derived in [115, 116, 117], which are all interconnected and formulated similarly.

Since stiffness characteristics are essential for parallel manipulators, insufficient stiffness can result in large deflections of the platform in the horizontal direction, leading to significant structural deformation issues. Suitable stiffness parameters are also critical in governing the natural frequencies of the system. Thus, in this section, a thorough

Parameter	Value (mm / °)
Base platform radius (R_b)	66 mm
Top platform radius (R_p)	66 mm
Initial connector leg length (l_0)	82 mm
Vertical height between platforms (H)	71 mm
Half-angle of adjacent mounting joints (base, α_b)	21.3°
Half-angle of adjacent mounting joints (top, α_p)	20.7°
Azimuthal offset between base and top triads (ϕ)	39°
Connector leg inclination angle (θ)	30°

Note: Multiple design iterations were conducted to refine these parameters, ensuring suitability within the targeted modal frequency thresholds.

Table 9.1: Initial geometric and design parameters of the simple symmetric Stewart-based vibration isolator.

analytical investigation of the stiffness calculation is presented.

It is stated in [117] that the stiffness of a parallel manipulator in a given workspace is termed its **stiffness matrix**. Here, the velocity relationship can be expressed as:

$$\dot{\theta} = Jv \tag{9.15}$$

Here, $\dot{\theta}$ is the vector of joint velocities and v is the vector of Cartesian velocities, which consists of a six-dimensional vector containing the linear velocity of a point on the moving base platform and the angular velocity of that platform. This vector is called the **twist** of the moving base platform. In robotics and mechanical terminology, matrices analogous to J are usually termed as **Jacobian matrices**, given by:

$$[J] = \left[\frac{\partial l}{\partial x}\right] = \begin{bmatrix} \frac{\partial l_1}{\partial x} & \frac{\partial l_1}{\partial y} & \cdots & \frac{\partial l_1}{\partial \gamma} \\ \frac{\partial l_2}{\partial x} & \frac{\partial l_2}{\partial y} & \cdots & \frac{\partial l_2}{\partial \gamma} \\ \vdots & \vdots & \ddots & \vdots \\ \frac{\partial l_6}{\partial x} & \frac{\partial l_6}{\partial y} & \cdots & \frac{\partial l_6}{\partial \gamma} \end{bmatrix}. \tag{9.16}$$

Hence, the J matrix maps the Cartesian velocity vector of the moving base platform to the joint (or leg) velocity vector. Similarly, the forces and moments applied to the moving platform under static conditions are also related to the forces or moments required at the actuator or the legs to maintain equilibrium. This relation is described by the transpose of the Jacobian matrix J, which in the case of a parallel manipulator can be written as:

$$F_{\text{plat}} = J^T F_{\text{leg}}, \tag{9.17}$$

Where F_{leg} is the vector of forces acting on the legs, struts, or actuators, and F_{plat} is the generalised vector of Cartesian forces and torques at the upper moving base platform, also referred to as the **wrench**.

Additionally, the Jacobian matrix $[J]$ also relates the platform deflection Δx to the leg deflection Δl, expressed as:

$$\Delta l = [J]\Delta x. \tag{9.18}$$

From Hooke's law, we can further write this equation as

$$F_{\text{leg}} = k\,\Delta l \tag{9.19}$$

Since $\Delta l = J\Delta x$, we can rewrite

$$F_{\text{leg}} = kJ\Delta x \tag{9.20}$$

Substituting this into the equilibrium equation gives

$$F_{\text{plat}} = J^T\big(kJ\Delta x\big), \tag{9.21}$$

which simplifies to

$$F_{\text{plat}} = K\Delta x, \tag{9.22}$$

Where the Cartesian stiffness matrix K is defined as

$$K = kJ^T J \tag{9.23}$$

The stiffness matrix K is symmetric, positive semidefinite, and configuration-dependent via J. Additional terms may arise from preload, gravity-induced geometric stiffness, or leg compliance beyond pure axial effects (e.g., bending). For the axial-spring, small-deflection model about an equilibrium, the expression $kJ^T J$ holds. If the legs have different axial stiffness values k_i, they can be arranged in a diagonal matrix $k_\ell = \text{diag}(k_1, k_2, \ldots, k_6)$, yielding the general stiffness expression:

$$K = J^T k_\ell J \tag{9.24}$$

Here, the Jacobian matrix is constructed as the stack of six screw vectors:

$$J = \begin{bmatrix} \mathbf{S}_1^T \\ \mathbf{S}_2^T \\ \vdots \\ \mathbf{S}_6^T \end{bmatrix} = \begin{bmatrix} s_{1x} & s_{1y} & s_{1z} & m_{1x} & m_{1y} & m_{1z} \\ s_{2x} & s_{2y} & s_{2z} & m_{2x} & m_{2y} & m_{2z} \\ s_{3x} & s_{3y} & s_{3z} & m_{3x} & m_{3y} & m_{3z} \\ s_{4x} & s_{4y} & s_{4z} & m_{4x} & m_{4y} & m_{4z} \\ s_{5x} & s_{5y} & s_{5z} & m_{5x} & m_{5y} & m_{5z} \\ s_{6x} & s_{6y} & s_{6z} & m_{6x} & m_{6y} & m_{6z} \end{bmatrix} \in \mathbb{R}^{6\times 6}. \tag{9.25}$$

Here, for the i-th leg in a Stewart platform, the screw direction vector $\mathbf{s}_i$ is a 6×1 column vector that encodes how a small platform displacement $\Delta x = [\Delta t \ ; \ \Delta\theta]$ projects onto the leg axis which is represented using Plücker coordinates.

$$s_i = \begin{bmatrix} \mathbf{u}_i \\ \mathbf{r}_i \times \mathbf{u}_i \end{bmatrix} = \begin{bmatrix} \mathbf{I}_{3\times 3} \\ [\mathbf{r}_i]_\times \end{bmatrix} \mathbf{u}_i, \tag{9.26}$$

where

- $\mathbf{u}_i = [s_{ix}, s_{iy}, s_{iz}]^T$ is the unit leg direction,
- $[\mathbf{r}_i]_\times$ represents the cross product in matrix form.

The cross product matrix $[\mathbf{r}]_\times$ for any vector $\mathbf{r} = [x, y, z]^T$ is expressed as:

$$[\mathbf{r}]_\times = \begin{bmatrix} 0 & -z & y \\ z & 0 & -x \\ -y & x & 0 \end{bmatrix}. \tag{9.27}$$

In the Stewart Platform, modeled as six translational flexure folded beams acting in parallel between base and platform pivots, each leg has screw directions and a current length l_i, unloaded length l_0, and individual stiffness k_i for $i \in \{1, 2, \ldots, 6\}$.

With an external wrench increment

$$\delta w = [\delta f; \delta\tau]$$

and a platform twist

$$\delta\xi = [\delta x; \delta\theta],$$

We can express the global Cartesian stiffness as

$$\delta w = K\,\delta\xi, \tag{9.28}$$

where K is the global 6×6 stiffness matrix.

The global stiffness matrix is given by [118]:

$$\begin{aligned}[K] = [j][k_\ell][j]^T + [\delta j_\theta][k_\ell(1-\rho)][\delta j_\theta]^T + [\delta j_\phi][k_\ell(1-\rho)][\delta j_\phi]^T \\ + [\delta j_\theta][k_\ell(1-\rho)][v_\theta]^T + [\delta j_\phi][k_\ell(1-\rho)][v_\phi]^T\end{aligned} \tag{9.29}$$

Here:

- $[k_\ell] = \text{diag}(k_1, \ldots, k_6)$ is the diagonal stiffness matrix of the six legs.
- $[j]$ is the Jacobian matrix mapping leg deformations to platform motions.
- $\rho = \frac{l_0}{l_i}$ is the prestrain ratio, with $\rho = 1$ for free (un-preloaded) legs.

For the special case where the legs are free (no preload), i.e., $\rho = 1$, the higher-order and mixed asymmetry terms vanish, reducing the stiffness matrix to:

$$[K] = [j][k_\ell][j]^T. \tag{9.30}$$

The second term in Equation 9.29 also captures how the Model's orientation around its own axis θ affects its stiffness, followed by the third term, which captures the sensitivity to rotation about ϕ, a slight rotation around another independent axis that introduces non-symmetric coupling. The last two terms represent the geometric cross-coupling, which produces the asymmetric and skew-symmetric parts of the global stiffness matrix. The cross-coupling terms describe the interaction between rotations and translations, playing a significant role in extreme displacement conditions where the platform is displaced significantly away from its reference pose.

Properties of the global stiffness matrix involve a high dependency on the initial prestrain condition, which is not constant unless near the unloaded configuration.

Also, this global 6×6 stiffness matrix has 21 DOF, which can reach up to 27 independent entries due to skew contributions.

A much-simplified adoption of the above global stiffness Equation 9.29 is explained in [116], where the global stiffness is expressed as a superposition of leg contributions in screw form:

$$\mathbf{K} = \sum_{i=1}^{6} \left(k_i \rho_i \, \mathbf{S}_i \mathbf{S}_i^T + k_i (1 - \rho_i) \mathbf{M}_i \right) \tag{9.31}$$

Here, $\mathbf{S}_i$ are the individual leg screw vectors, and $\mathbf{M}_i$ is an ageometric coupling block built from the skew-symmetric matrices of the base $[\mathbf{B}_i]_\times$ and the top platform $[\mathbf{P}_i]_\times$ attachment points, expressed as:

$$\mathbf{M}_i = \begin{bmatrix} \mathbf{I}_3 & -[\mathbf{P}_i]_\times \\ [\mathbf{B}_i]_\times & -[\mathbf{B}_i]_\times [\mathbf{P}_i]_\times \end{bmatrix} \tag{9.32}$$

The key difference between these two approaches is that in [116] the researchers focused on asymmetry and skew-symmetric properties, which proved that the global stiffness is not necessarily symmetric. In this case, the final global stiffness matrix is a compact expression that directly comes from summing the individual leg contributions.

On the other hand, [118] makes explicit how derivative line coordinates and moment offset contribute to the overall stiffness behaviour of the platform. The approach generalises the same physical Model with a more geometric interpretation.

In real-time Stewart platforms, connecting legs are rarely at their free length because of manufacturing tolerances and preloading conditions for rigidity. Thus, the terms in the equation 9.31 capture the actual dynamic behaviour that emphasises the coupling between translation and rotation.

Once the Global Stiffness matrix is obtained, the mass matrix is calculated by the model mass properties, which gives the total mass of the platform along with respective moments of inertia both along the centre of mass (COM) and also with respect to a defined coordinate frame. Theoretically, most of the literature expresses the Stiffness and Mass matrix as [119]:

$$\mathbf{K} = \begin{bmatrix} k_{11} & 0 & 0 & 0 & k_{15} & 0 \\ 0 & k_{22} & 0 & k_{24} & 0 & 0 \\ 0 & 0 & k_{33} & 0 & 0 & 0 \\ 0 & k_{24} & 0 & k_{44} & 0 & 0 \\ k_{15} & 0 & 0 & 0 & k_{55} & 0 \\ 0 & 0 & 0 & 0 & 0 & k_{66} \end{bmatrix} \tag{9.33}$$

Here, the Cartesian stiffness matrix $\mathbf{K}_{6\times6}$ for an identical symmetrical design model is illustrated in Figure 9.7, where all the cross terms cancel except the two translation–rotation couplings k_{15} and k_{24}, which represent the inherent cross-links between

lateral translations and pitch/roll rotations of the platform.

For the Mass matrix, if the translational coordinates are taken at the COM and axes align with the principal axes, it is given as:

$$\mathbf{M} = \mathrm{diag}(m, m, m, I_{xx}, I_{yy}, I_{zz}) \tag{9.34}$$

But if the translational coordinates are taken at a platform point $P = (x_p, y_p, z_p)^T$ which is not the COM, Then the inertia about P via the parallel-axis theorem is:

$$\mathbf{I}_0 = \mathbf{R} \begin{bmatrix} I_{xx} + m(y_p^2 + z_p^2) & I_{xy} + m x_p y_p & I_{xz} + m x_p z_p \\ I_{xy} + m x_p y_p & I_{yy} + m(x_p^2 + z_p^2) & I_{yz} + m y_p z_p \\ I_{xz} + m x_p z_p & I_{yz} + m y_p z_p & I_{zz} + m(x_p^2 + y_p^2) \end{bmatrix} \mathbf{R}^T \tag{9.35}$$

Here, $\mathbf{R}$ represents the rotation of the platform with respect to the base frame, and the rest are the principal and coupling inertial terms. Then, the Mass Matrix is the total system mass m multiplied by an $\mathbf{I}_{3\times3}$ identity matrix, followed by $\mathbf{I}_0$, which represents the inertial matrix. Thus, the final mass matrix is expressed as:

$$\mathbf{M} = \begin{bmatrix} m\mathbf{I}_{3\times3} & \mathbf{0}_{3\times3} \\ \mathbf{0}_{3\times3} & \mathbf{I}_0 \end{bmatrix} \tag{9.36}$$

With these stiffness and mass matrices, we can then find the Modal frequencies as a generalised eigenvalue problem:

$$\mathbf{K}\,\boldsymbol{\phi} = \omega^2\,\mathbf{M}\,\boldsymbol{\phi} \tag{9.37}$$

or equivalently,

$$\text{eigs of } \mathbf{M}^{-1}\mathbf{K} \quad \rightarrow \quad \omega_i^2 \tag{9.38}$$

Thus, the angular frequencies are obtained from the eigenvalues of $\mathbf{M}^{-1}\mathbf{K}$.

Here is a summarised pseudo-algorithm 9.1 that computes the stiffness matrix by using the equation 9.31 obtained from [116], and the mass matrix with respect to the COM form, which then computes the theoretical modal frequencies.

Algorithm 9.1: Computation of Global Stiffness and Modal Properties

Input : Base coords $\{\mathbf{B}_i\}$, top coords $\{\mathbf{T}_i\}$, free lengths $\{l_{0i}\}$, axial stiffness $\{k_i\}$, platform mass m, inertia tensor $\mathbf{I}_c$.

Output : Global stiffness $\mathbf{K}$ and natural frequencies f_j.

for $i \leftarrow 1$ **to** 6 **do**

$l_i \leftarrow \left\|\mathbf{T}_i - \mathbf{B}_i\right\|$

$\mathbf{s}_i \leftarrow \dfrac{\mathbf{T}_i - \mathbf{B}_i}{l_i}$

$\mathbf{S}_i \leftarrow \begin{bmatrix} \mathbf{s}_i \\ \mathbf{B}_i \times \mathbf{s}_i \end{bmatrix}$

$\rho_i \leftarrow l_{0i}/l_i$

$[\mathbf{B}_i]_\times \leftarrow \mathrm{skew}(\mathbf{B}_i), \quad [\mathbf{T}_i]_\times \leftarrow \mathrm{skew}(\mathbf{T}_i)$

$\mathbf{M}_i \leftarrow \begin{bmatrix} \mathbf{I}_3 & -[\mathbf{T}_i]_\times \\ [\mathbf{B}_i]_\times & -[\mathbf{B}_i]_\times[\mathbf{T}_i]_\times \end{bmatrix}$

$\mathbf{K}_i \leftarrow k_i\,\rho_i\,\mathbf{S}_i\mathbf{S}_i^{\mathsf{T}} + k_i(1-\rho_i)\,\mathbf{M}_i$

$\mathbf{K} \leftarrow \sum_{i=1}^{6} \mathbf{K}_i$

$\mathbf{K}_{\text{skew}} \leftarrow \frac{1}{2}\left(\mathbf{K} - \mathbf{K}^{\mathsf{T}}\right)$

$\mathbf{W} \leftarrow \sum_{i=1}^{6} k_i(l_i - l_{0i})\,\mathbf{S}_i$

$\mathbf{M} \leftarrow \begin{bmatrix} m\,\mathbf{I}_3 & \mathbf{0} \\ \mathbf{0} & \mathbf{I}_c \end{bmatrix}$

Solve the eigenproblem $\mathbf{K}\mathbf{x} = \omega^2\mathbf{M}\mathbf{x}$ for ω_j

$f_j \leftarrow \omega_j/(2\pi)$

9.4 Modelling and Analysis of the Passive Stewart-based Folded Beam Isolator Platform

Up to this point, the types of passive Stewart platform-based isolators have been described, along with an overview of the initial design parameters that form the foundation for the CAD modelling. The model corresponds to the **SSM (Simplified Symmetric Manipulator)** configuration, in which the entire structure is vertically symmetric. Based on the findings from the previous chapter, the *multi-folded beam* design was determined to be more advantageous than the plain folded beam; therefore, the present model incorporates folded-beam connecting legs with the exact dimensions as the conventional folded-beam isolator platform.

From the design parameters obtained in Table 9.1, the connector leg pairs are spaced 120° apart, with equal base and top radii, as shown in Figure 9.8.

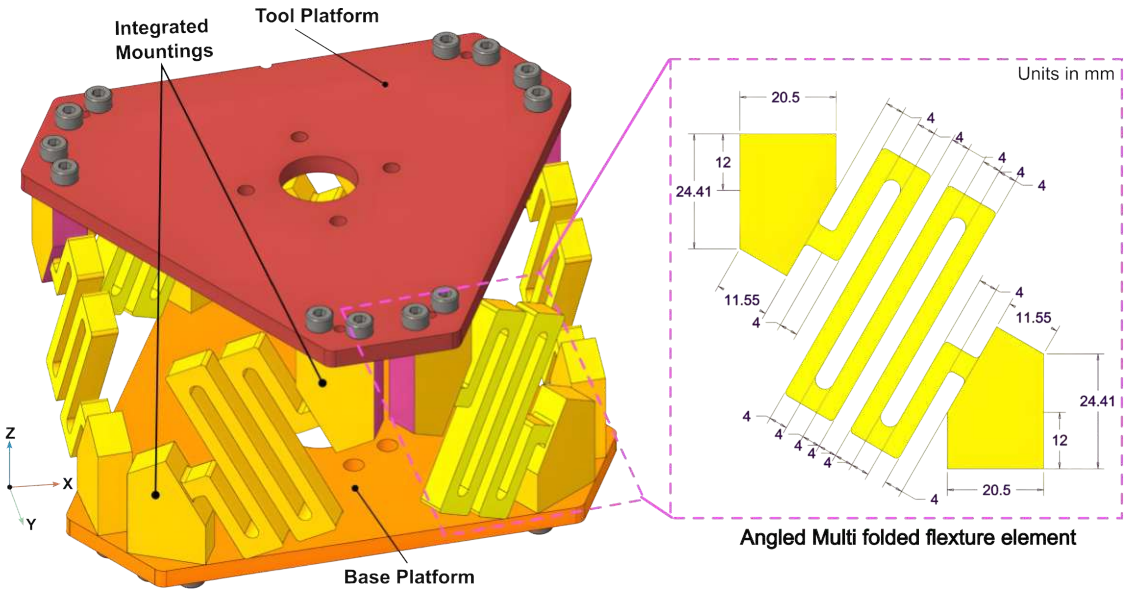

Figure 9.8: Model of the symmetric Passive Stewart-based Folded beam Vibration Isolator Platform, along with the integrated angled multi-folded element.

A modal analysis is performed in *Creo Simulate* for the entire assembled version, where the isolator is fixed with the tool. The Model was assigned material properties as ERGAL-70 and meshed using the **Auto-mesh** functionality. An adaptive mesh was generated: a finer mesh at the folded beam elements and a coarser mesh on the top and bottom platforms, as vibrations are expected to affect the folded beams primarily. The modal analysis results, given in Figure 9.9, display the first four modal frequencies along with their respective mode shapes. These are further tabulated in 9.2, listing the dominant modal frequencies and corresponding modal behaviours.

It is evident that, when compared to the conventional folded beam vibration isolator design, the first modal frequency yields an isolation percentage of approximately 93.19%. Furthermore, in the traditional Model, the fourth modal frequency occurred at 106.28 Hz; whereas, in the present configuration (with identical geometrical parameters of the folded beam but arranged differently), the fourth modal frequency was reduced to 99.398 Hz, thereby amplifying the overall system isolation by approximately 18.4%. For the first three dominant frequencies, the values remain below the threshold isolator frequency limit (i.e., < 95.5 Hz), whereas degradation is only observed in the higher harmonics. Thus, this Model remains feasible as a vibration isolator.

A design modification involving the change of the folded beam's inclination angle has a strong effect on the system's modal behaviour. This parametric feature, also observed and studied in [114], suggests that an optimal inclination angle with respect to the

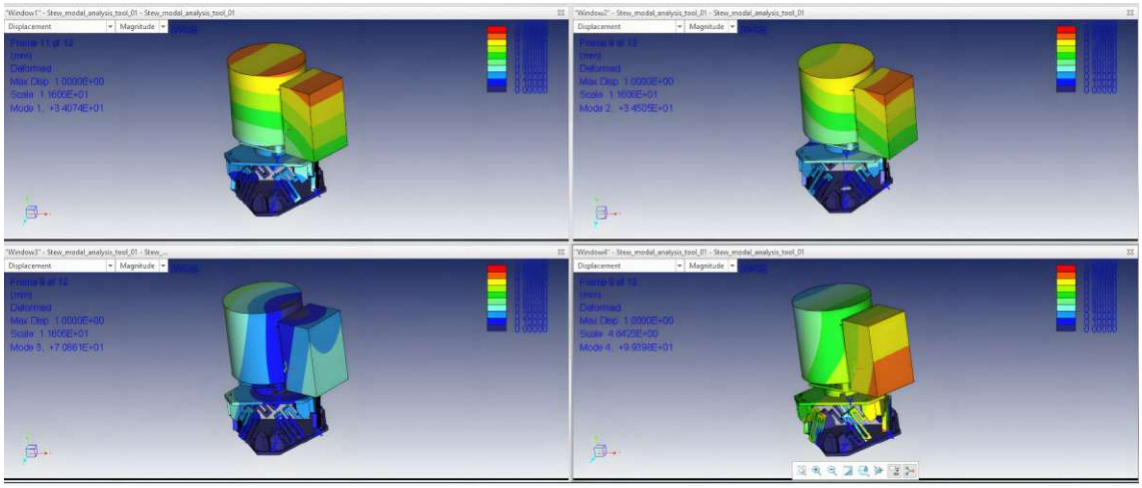

Figure 9.9: First Four dominant frequencies along with the Modal Shapes for the Stewart-based Folded beam Isolator.

Mode #	Dominant Frequency (Hz)	Modal Description
1	34.07	**In-plane translation** along the lateral direction, **global XZ-plane**
2	34.50	**In-plane translation** along the lateral direction, **global XZ-axis orthogonal to the previous mode**
3	70.86	**Torsional (yaw) mode** about the vertical axis, rotation around **global Y-axis**
4	99.398	**Out-of-plane translational mode** along the vertical direction, motion primarily along **global Y-axis**

Table 9.2: First four modes of the Stewart-based isolator system with dominant frequencies and technical motion descriptions for the modified folded beam isolator.

base platform significantly enhances performance. It is also observed that symmetric and robust isolators in the **MSSM (Minimal Simplified Symmetric Manipulator)** configuration, where the connector legs are inclined equally and arranged as equilateral triangles at the top and bottom, result in six legs grouped in three symmetric pairs. In this configuration, the horizontal stiffness is approximately $1.5\times$ greater than the vertical stiffness, which is essential for the present use case. Moreover, such a configuration ensures extreme structural symmetry.

Finally, from the previously derived equation 9.14, which describes the relation between the total leg length, it follows that a new design model is proposed which performs better than the current Stewart-based vibration isolator, ensuring that all modal frequencies remain below the threshold limit.

9.4.1 Modelling and Analysis of the Stewart-based Tilted Folded Beam Isolator Platform

During the modelling of the Stewart platform isolator, it was observed that when the folded beams are inclined at their usual elevation angle θ, an additional tilt angle Ω (treated as a zenith angle) can be introduced, as illustrated in Figure 9.10. This tilt resulted in noticeable changes in both the structural and modal characteristics of the Stewart platform. The behaviour is attributed to the redistribution of forces along the in-plane and out-of-plane stiffness components of the folded beam geometry.

With this new design feature of introducing tilted Stewart beams, the initial Stewart model was upgraded into a more compact configuration with a reduced centre of mass (COM), as shown in Figure 9.11. Unlike the initial version of the Stewart platform, where the top and base platforms had equal radii, this new model incorporates unequal base and top platform radii due to the tilted configuration of the folded beams. The design parameters are listed in Table 9.3. The tilt angle was chosen as 60° to ensure symmetric geometry, structural integrity, and efficient load distribution across the multiple legs of the Stewart platform.

9.4.2 Complete Assembled Stewart-based Tilted Folded Beam Passive Vibration Isolator End-Effector

For the updated Stewart platform model, the final assembly of the passive end-effector interface was carried out following the same standardised procedure as that described earlier for the conventional vibration isolator end-effector assembly. The main advantage of this new design is that the Stewart-based isolator can be directly swapped with

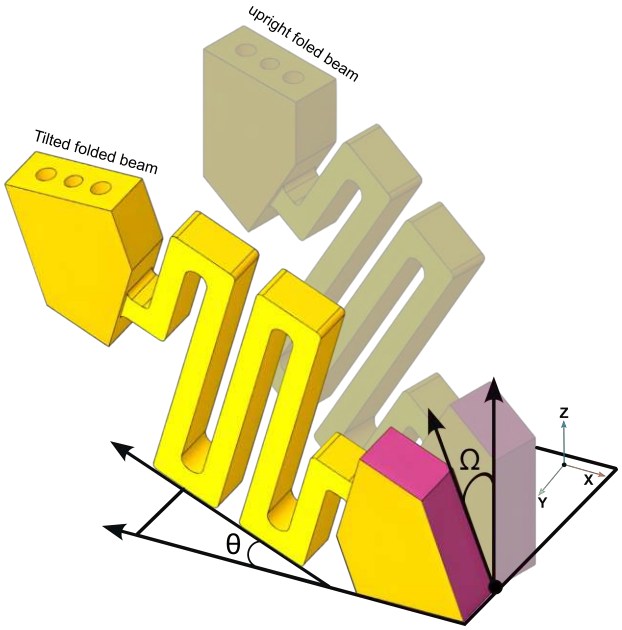

Figure 9.10: A typical folded beam isolation element along with its inclination and tilt angles.

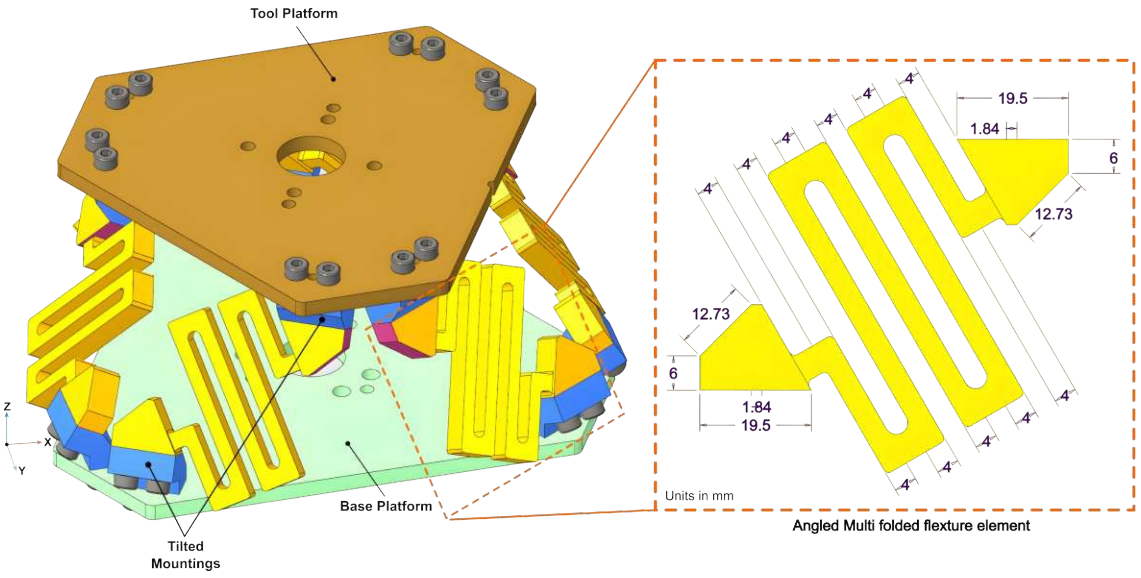

Figure 9.11: Model of the Modified symmetric Passive Stewart-based Tilted Folded beam Vibration Isolator Platform, along with the integrated angled multi-folded element.

Parameter	Value (mm / °)
Base platform radius (R_b)	78.3 mm
Top platform radius (R_p)	60.8 mm
Initial connector leg length (l_0)	81.42 mm
Vertical height between platforms (H)	66.4 mm
Half-angle of adjacent mounting joints (base, α_b)	8.4°
Half-angle of adjacent mounting joints (top, α_p)	14.6°
Azimuthal offset between base and top triads (ϕ)	37°
Connector leg inclination angle (θ)	30°
Folded beam tilt angle (Ω)	60°

Note: Multiple design iterations were conducted to refine these parameters, ensuring suitability within the targeted modal frequency thresholds.

Table 9.3: Design and geometric parameters for the Stewart-based tilted folded beam vibration isolator.

the traditional module of isolator without requiring any design changes or additional component attachments.

Special attention was given to the attachment interfaces: the connector to the Doosan robotic arm and the custom tool interface were designed to accommodate both isolator models perfectly. The final assembled Stewart-based tilted folded beam isolator end-effector is shown in Figure 9.12, where all modules and interfaces are rigidly fastened using metric-sized screws.

9.4.3 Modal and Static Analysis for the Stewart-based tilted folded beam vibration isolator end effector

The assembled Stewart-based tilted folded beam isolator was subjected to modal analysis to determine the natural frequencies of the complete system and to study the associated mode shapes. The results of this analysis are illustrated in Figure 9.13, and the first four modal frequencies along with their corresponding modal descriptions are tabulated in Table 9.4.

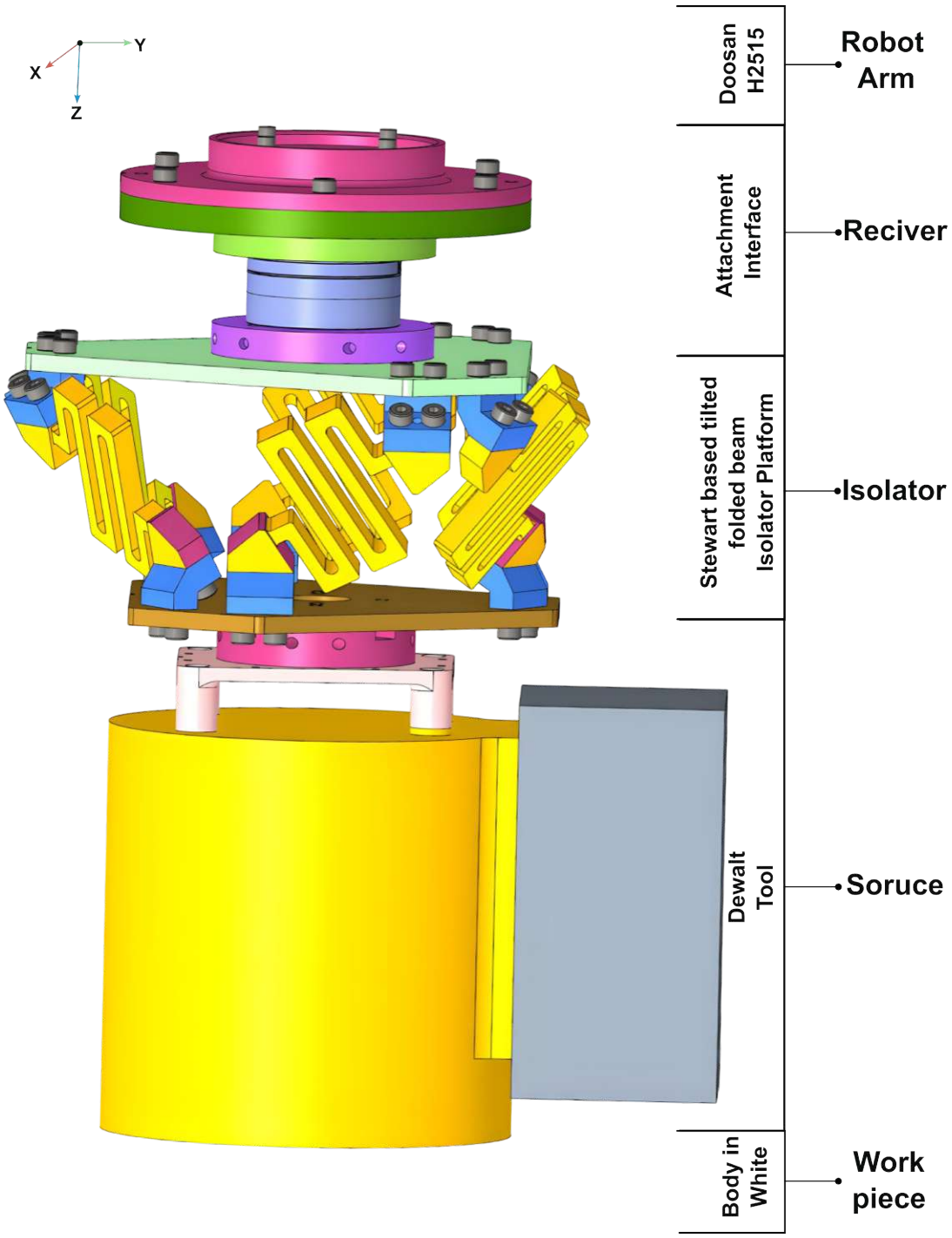

Figure 9.12: The complete assembly of the Stewart-based passive folded-beam vibration isolator end effector.

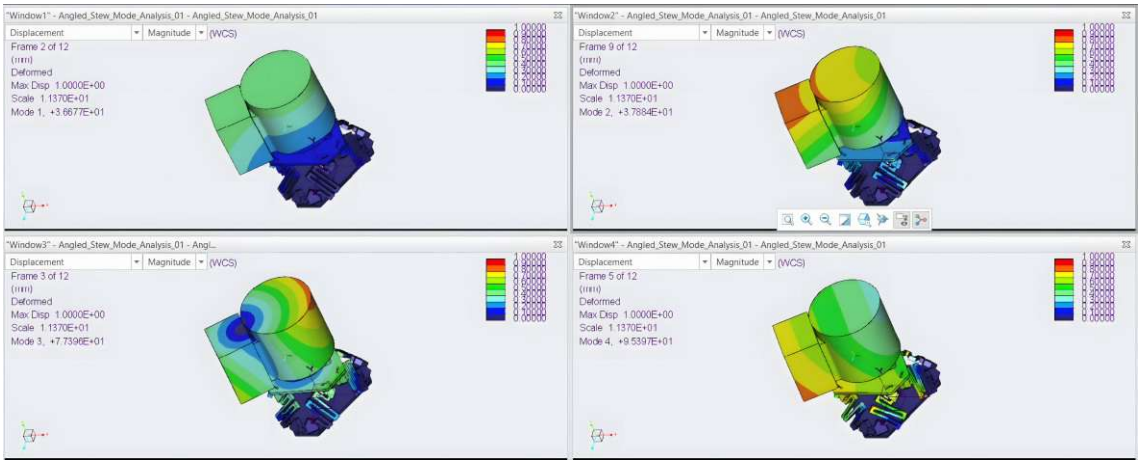

Figure 9.13: The first four dominant frequency values along with the respective modal shapes of the Stewart-based Folded beam Vibration Isolator platform.

Mode #	Freq. (Hz)	Modal Description	Isolation (%)
1	36.67	**Rolling mode** along the **global XZ-plane**	92.0
2	37.88	**Translational out-of-plane mode** along the **Y-axis**	91.5
3	77.39	**Torsional (yaw) mode** about the vertical axis, rotation around the **global Y-axis**	51.0
4	95.39	**Translational in-plane mode** in the **XZ-plane** (horizontal direction)	0.2 → borderline to isolator threshold

Table 9.4: The first four modes of the Stewart-based tilted folded-beam isolator with their dominant frequencies, mode shapes, and isolation percentages relative to the tool's first dominant frequency (135 Hz).

9.5 Results of Modal and Static Analysis for the Stewart-based Tilted Folded Beam Isolator

From the modal analysis, it is clearly evident that all the dominant modes, including the fourth mode, lie below the required isolation threshold of $95.5\,\text{Hz}$. While the lower modal frequencies are comparable to those of the conventional folded beam isolator, the tilted Stewart configuration demonstrated significant attenuation characteristics at higher harmonics.

The observed mode shapes further validate the anisotropic stiffness distribution:

- The **first mode** exhibited a rolling motion caused by the asymmetric mass distribution of the sanding tool (battery weight concentrated on one side).
- The **second mode** corresponded to an out-of-plane vertical translation, explained by the stiffness relation $K_{\text{hor}} = 1.5K_{\text{ver}}$, which enhances horizontal stiffness relative to vertical stiffness.
- The **third mode** was a torsional motion about the global Y-axis.
- The **fourth mode** revealed an in-plane translational mode in the global XZ-plane.

Since the modal results satisfied the isolation requirements, a static analysis study was performed to evaluate the structural robustness under operating loads. The maximum von Mises stress was found to be $15.32\,\text{MPa}$ (Figure 9.14), concentrated at the junction between the final span beam and the connector beam. Compared to the conventional isolator ($22.08\,\text{MPa}$), the tilted Stewart platform exhibited lower stresses, confirming its superior structural efficiency.

Under resonant conditions (worst-case scenario), the maximum von Mises stress was $66.47\,\text{MPa}$. This value remains well within the elastic limits of the chosen material, ensuring that the system is structurally rigid and free from permanent deformation.

With these results, the proposed Stewart-based tilted folded beam isolator is validated as more robust and efficient than the conventional folded beam isolator, both in modal and static analyses. This design will therefore be carried forward for experimental validation in the next chapter, where both isolator models will be compared practically for their effectiveness in mitigating tool-induced vibrations.

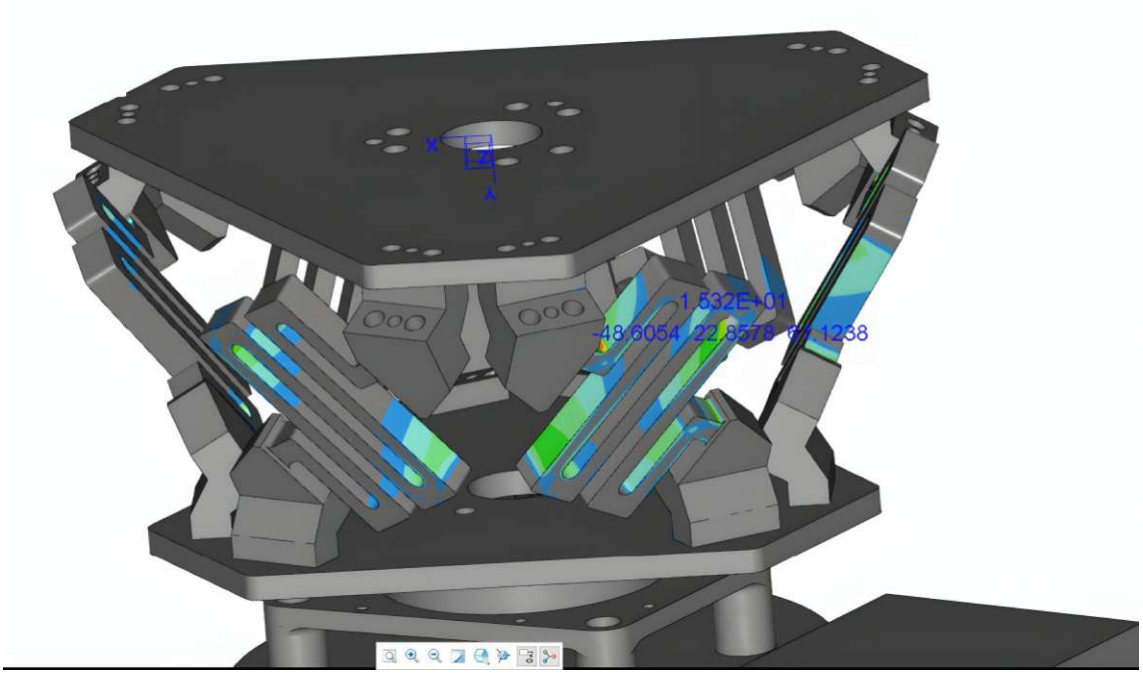

Figure 9.14: Static Analysis Maximum von Mises Stress result for the final Assembled Stewart-based isolator End effector module.

10 Isolator Prototype with Experimental Results

By now, we have completed the modelling and designing of our passive isolator interface and integrated it into the tool's end effector interface. Through both modal and static analysis studies on the respective isolator designs, we were able to theoretically and through simulations understand all the essential governing parameters that ensure the designed system satisfies the given design constraints and criteria. With this foundation, we now proceed to manufacture real isolator prototypes.

With the unconditional support and guidance from the team at HHCM Lab, Istituto Italiano di Tecnologia, two final model designs were selected to be sourced for CNC machining. The multi–folded beam design was chosen due to its effective and efficient performance, which outperformed the traditional folded beam design. For the isolator platforms, we selected:

- A **conventional isolator design** with four folded beams equally spaced.
- A **Stewart platform–based tilted folded beam model**, which has shown the most efficient isolation performance among all designs.

As illustrated in Figure 10.1, these are the final selected passive isolator models for CNC machining.

10.1 Prototype Machining and Fabrication

In this final phase of the design process, all individual components of the vibration isolator models were drafted into detailed engineering drawings, which are included in the Appendix repository section, suitable for precision machining and assembly. These drawings were prepared in compliance with established standards of Geometric Dimensioning and Tolerancing (GD&T).

The general tolerances followed were according to **UNI ISO 8015**, with dimensional tolerances specified to class **m** (medium precision) as defined in **UNI EN 22768-1**, and geometric tolerances of class **K** as specified in **UNI EN 22768-2** for linear and angular dimensioning. Furthermore, all threaded elements were designed in adherence to ISO metric thread standards.

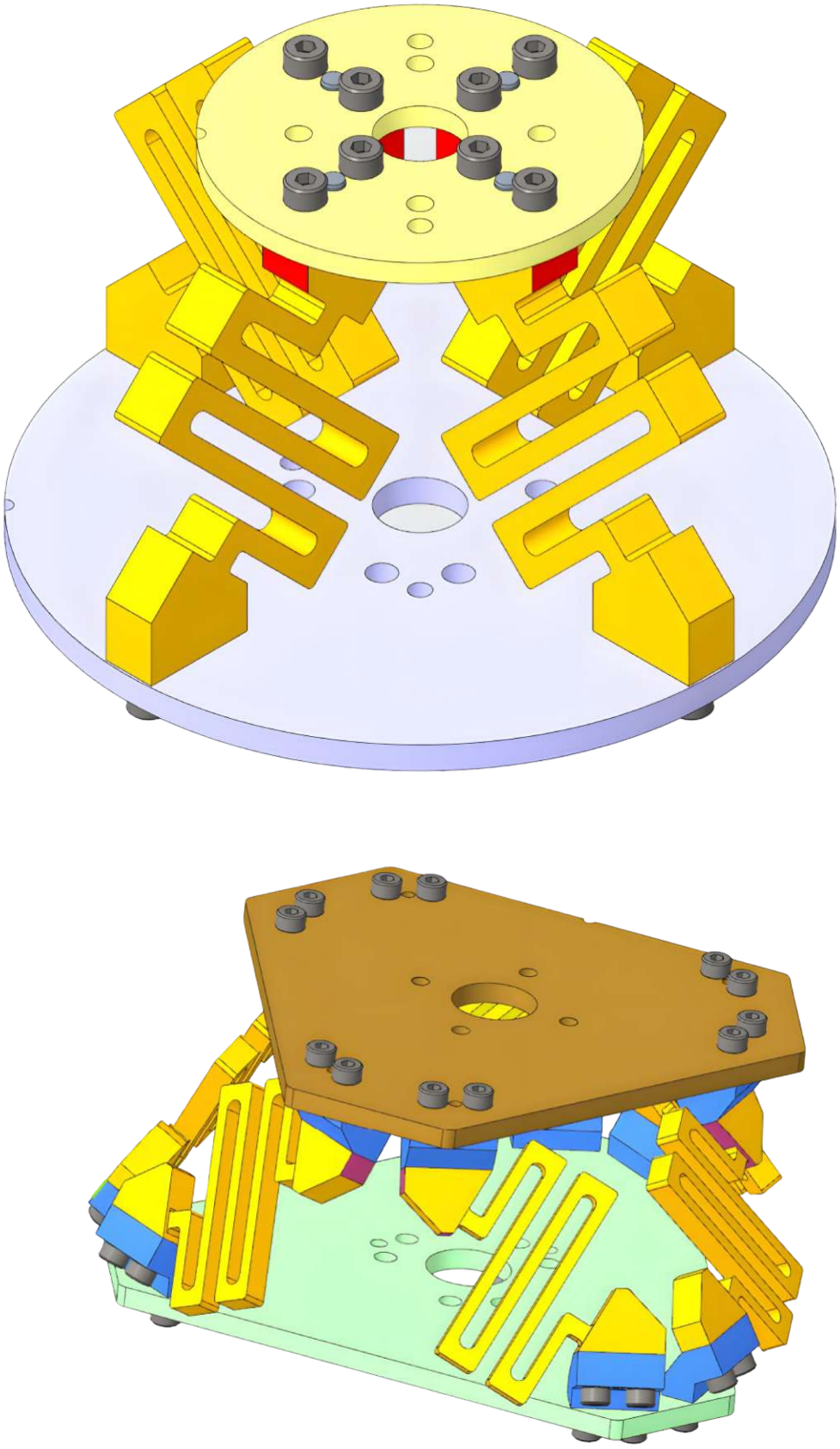

Figure 10.1: Final selected isolator models for machining operation.Top: The conventional folded beam isolator platform. Bottom: A novel Stewart-based folded beam isolator platform.

These conventions ensured that the machined parts achieved minimal tolerance accumulation and sufficient clearance, thereby safeguarding the functionality and interchangeability of components.

All components were machined from a single material to maintain consistency, namely **ERGAL 7070 (Al 7075-T6)**. The parts were carefully dimensioned considering both the mechanical properties and machinability of the alloy. Once the drafting phase was completed and reviewed, the models were forwarded for machining operations.

10.1.1 Conventional Isolator Prototype

Figure 10.2 shows the machined parts of the conventional folded beam vibration isolator platform. In addition to the main components, several auxiliary parts were also machined to facilitate the mounting of different force-torque sensors.

Once the machined parts were acquired, they were thoroughly assembled using screws to secure all components firmly in place. The final assembled metallic conventional folded beam isolator platform is shown in Figure 10.3.

10.1.2 Stewart Platform-Based Isolator Prototype

The machined parts for the Stewart-based folded beam vibration isolator platform are illustrated in Figure 10.4. The fully assembled metallic Stewart-based folded beam isolator platform is shown in Figure 10.5.

Once the assembly of the final metallic prototypes of both isolator designs was completed, we proceeded further by conducting experimental studies to evaluate the percentage of vibration isolation that these platforms exhibit under realistic operating conditions.

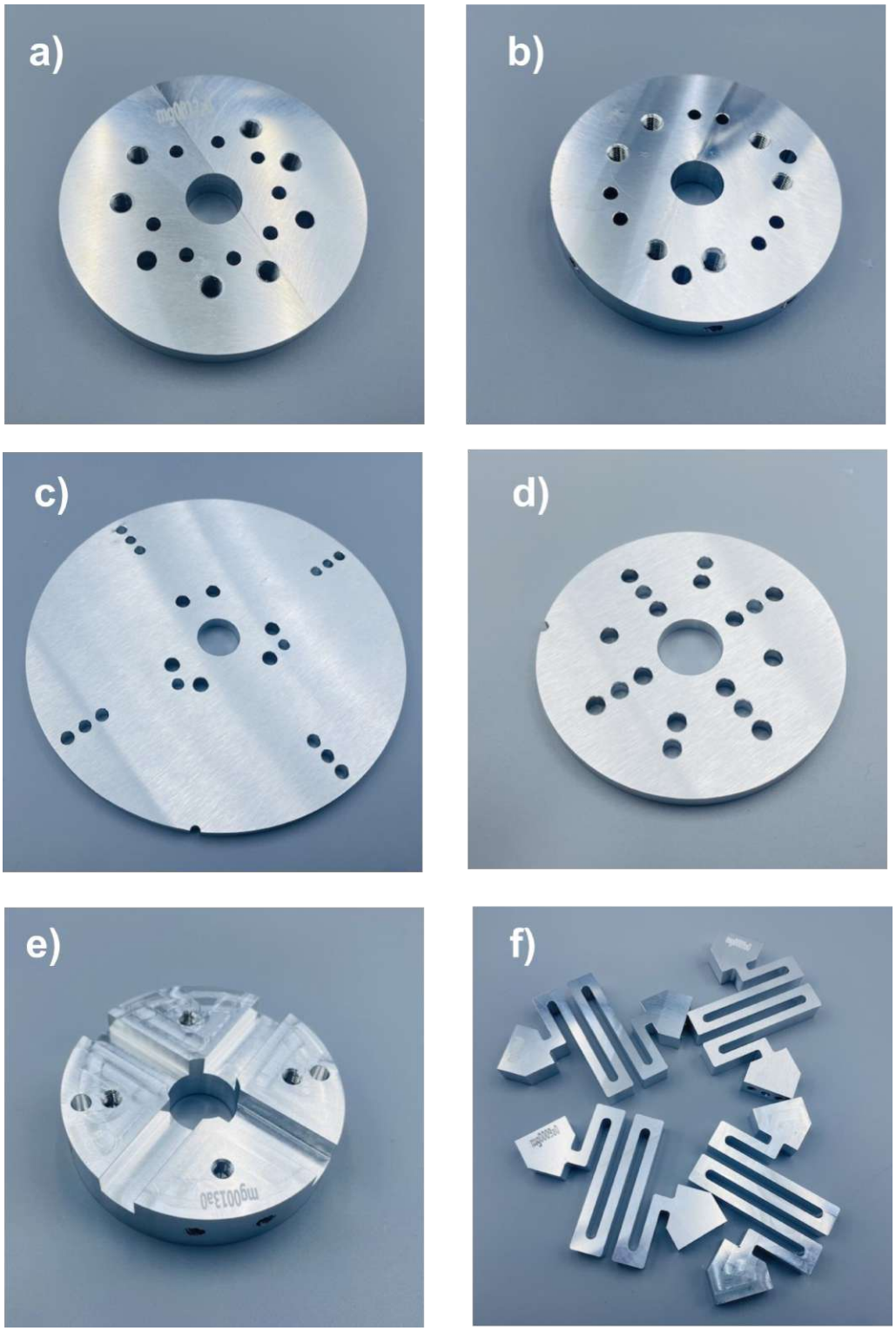

Figure 10.2: Machined parts for the Conventional Folded beam Vibration isolator, a) Top connector interface for the FT - 45 Sensor, b) Bottom Mounting Interface for the FT-45 Sensor, c) Bottom Isolator Platform which will be connected towards robotic arm, d) Top isolator platform which will be connected towards the Sanding Tool Interface, e) Connector Flange between Top isolator platform and the Sanding tool, f) Folded Beam Isolator Flexures.

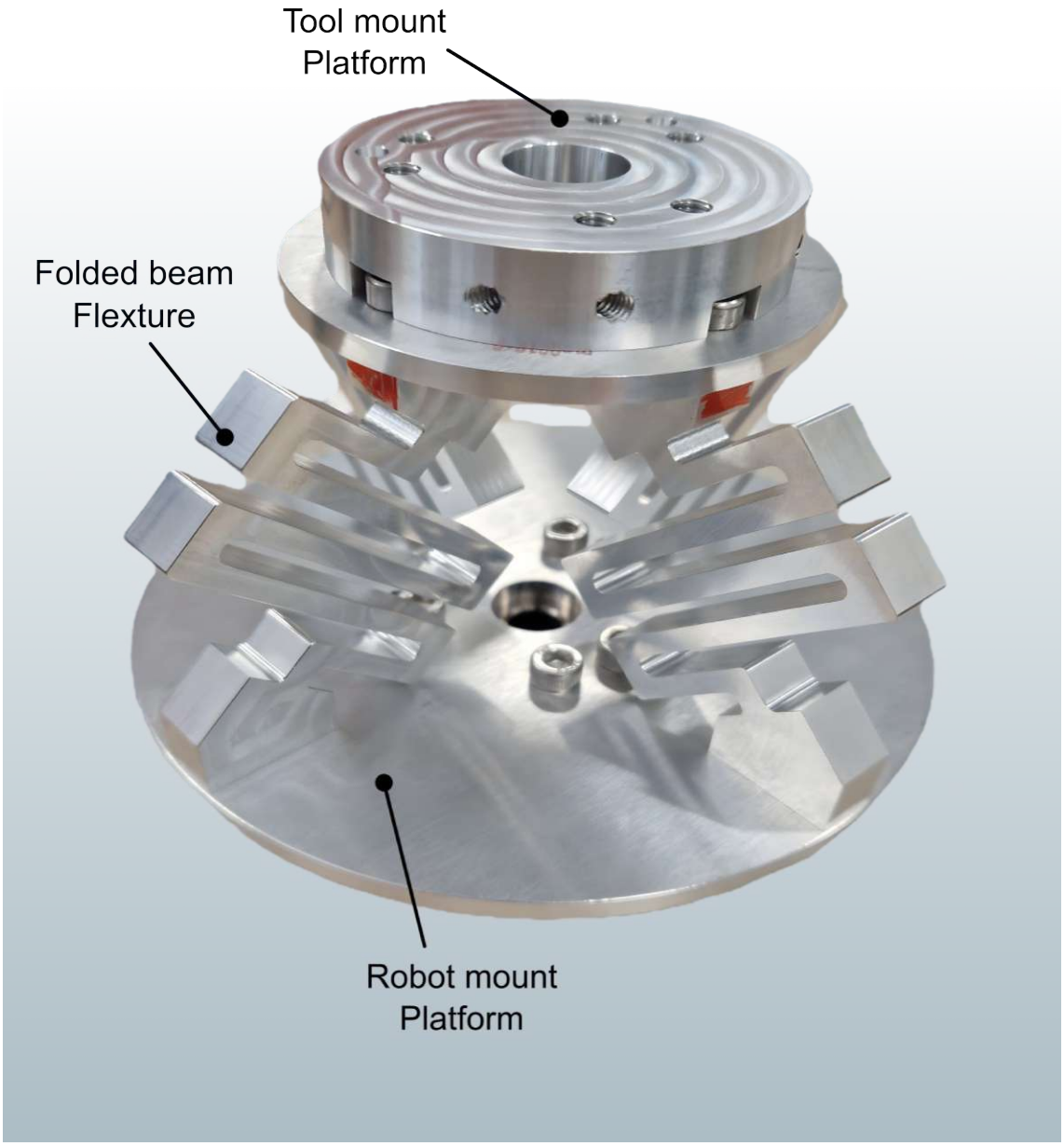

Figure 10.3: Final assembled metallic prototype of the conventional folded beam vibration isolator platform.

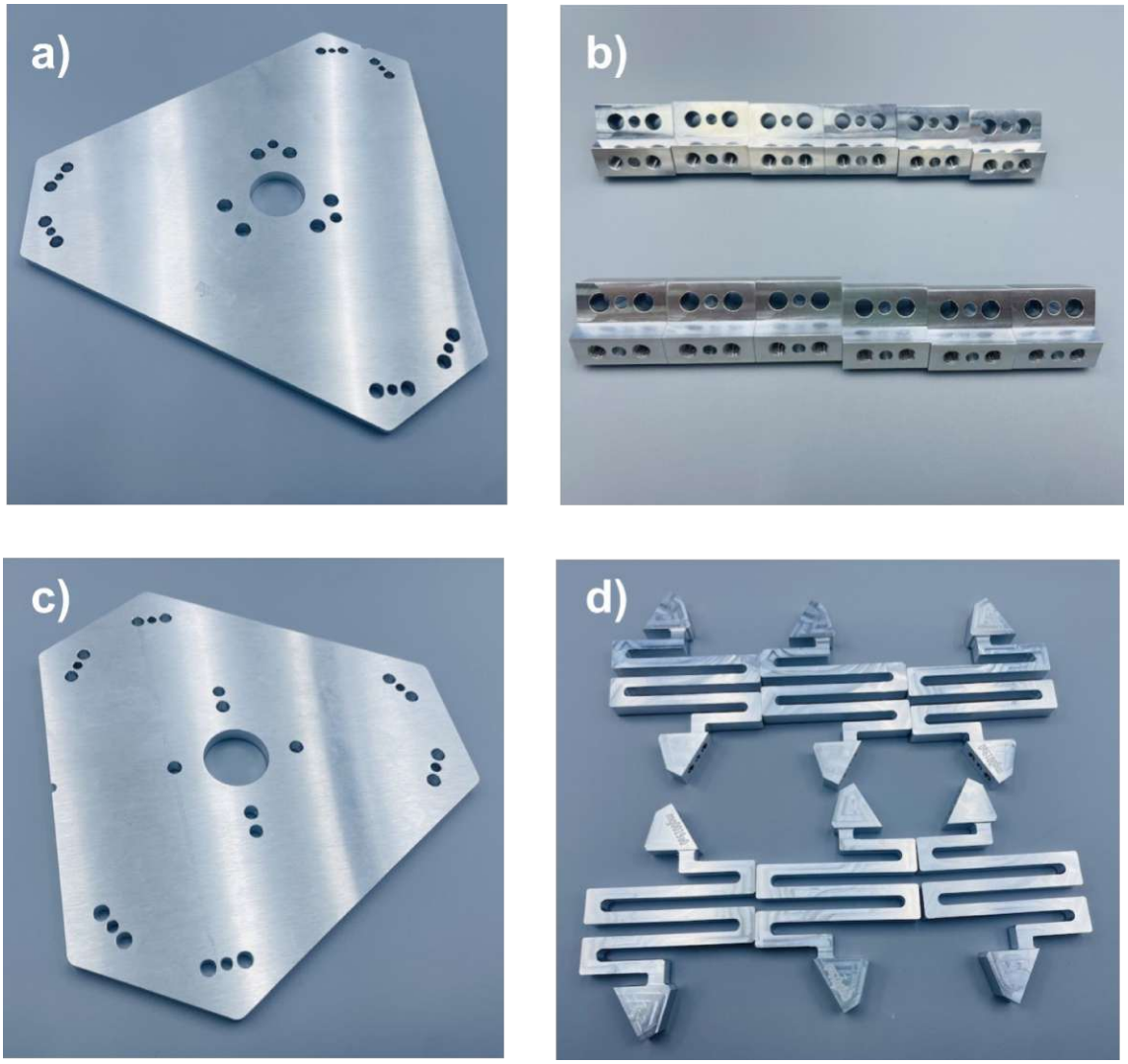

Figure 10.4: Machined parts for the Stewart-based Folded beam Vibration Isolator, a) Base isolator platform which will be mounted towards the robotic arm, b) Angular Mounting that will hold the folded beams in between the top and bottom platforms, c) Top isolator platform which will be mounted towards the Sanding tool, d) Folded beam Flexures.

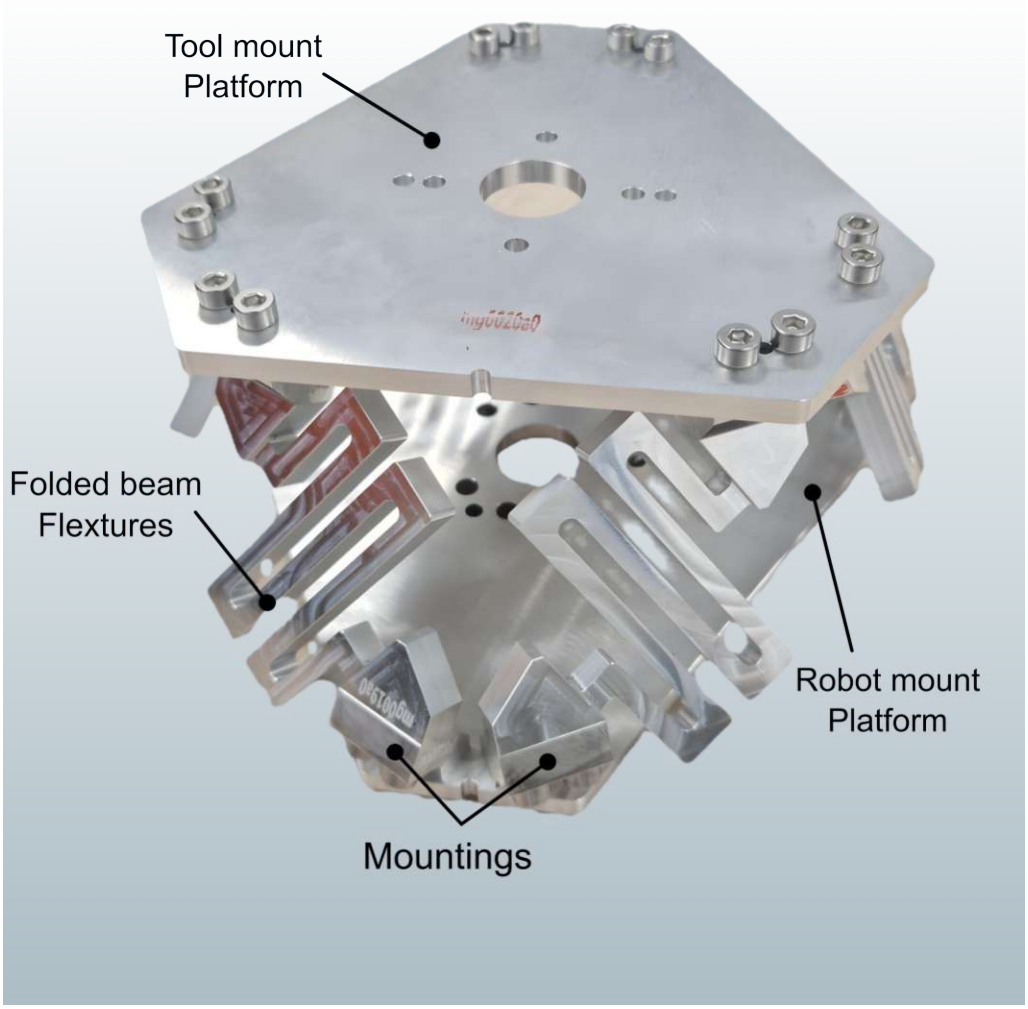

Figure 10.5: Final assembled metallic prototype of the Stewart-based folded beam vibration isolator platform.

10.2 Experimental Results

To evaluate the real-time performance of the designed isolators, an experimental analysis was conducted to assess the effectiveness of the isolation under practical operating conditions. The primary objective is to compare the attenuation performance of both isolator models and to determine which achieves better vibration suppression.

For this purpose, three experimental conditions were considered:

1. No isolator condition,
2. Conventional folded beam isolator condition,
3. Stewart-based folded beam isolator condition.

The comparison between these conditions was based on several core metrics, including the overall RMS forces, relative improvement versus a baseline (percentage isolation and dB reduction), and the transmissibility ratio, which indicates whether the isolator provides attenuation or amplification.

10.2.1 Free–Fixed Zero Degree Orientation Experiment

To compare and analyse the performance of the isolators, a similar procedure to that in earlier Chapter 5 was followed. The sanding tool was fixed to a rigid platform together with the force–torque (FT) sensor. The tool was then turned on to record force data, where vibrations were detected by the sensor as variations in strain gauge forces, producing equivalent force values. This data was collected for further study.

The experimental setup model is shown in Figure 10.6. The setup remained essentially unchanged with respect to the previous experimental configuration, with the only additional component being the vibration isolator fixed between the tool and the FT sensor, which was mounted on the rigid frame.

Test 1: Conventional Folded Beam Isolator: In the first test, the tool was connected to the conventional folded beam isolator platform, which was then mounted to the rigid extrusion frame via the FT sensor interface. The complete setup is shown in Figure 10.7a. This configuration represents the final end-effector concept that will eventually be installed on the Doosan robotic arm. For the current experiment, the tool was fixed to the rigid mounting using additional 3D-printed components.

Test 2: Stewart-Based Folded Beam Isolator In the second test, the conventional isolator was replaced with the Stewart-based folded beam isolator platform, while the rest of the experimental setup remained unchanged. The complete assembly is illustrated

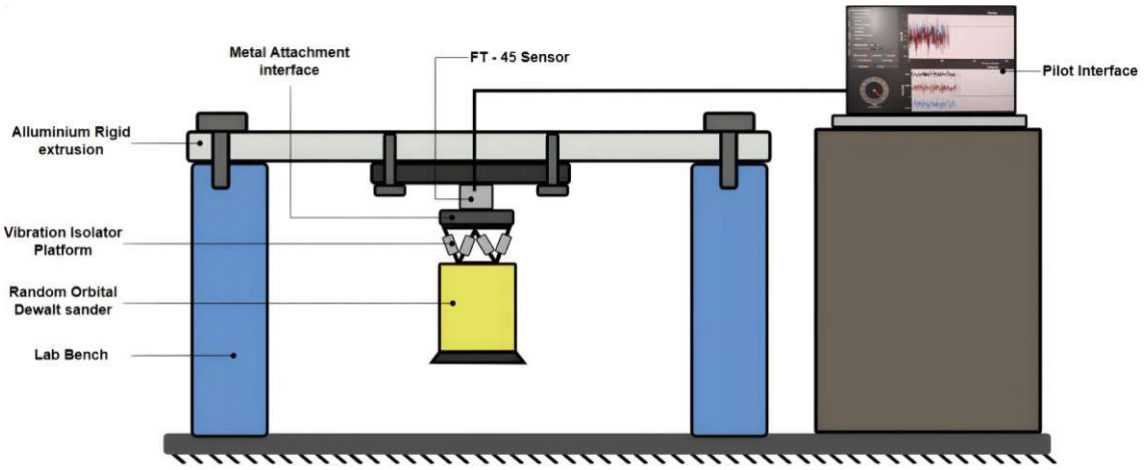

Figure 10.6: A Schematic representation of the Experimental Setup where the tool is attached to the isolator and is fixed vertically downwards from the rigid frame.

in Figure 10.7b.

For both tests, the sanding tool interfaces were operated under identical conditions. Force data was collected along all three principal axes for a duration of 20 seconds, with a sampling rate of $1000\ Hz$, across the complete tool speed range. The collected data from both isolator platforms were then analysed for comparison.

10.2.2 Final Results and Observations

Once the recorded data were collected from the respective experiments with both isolator platforms, we compared the force variations in each principal axis for three cases. The resulting force data plots, obtained in the time domain for a duration of 20 seconds under each condition, are presented in Figure 10.8. These measurements cover the entire speed range of the sanding tool.

From the time-domain force data, a clear distinction can be observed in the magnitude of forces and their fluctuations across the three cases. Since the tool is not subjected to any external forces or loads during this experiment, the reference force value is assumed to be zero Newtons.

When the tool was connected directly without an isolator, results showed comparatively better performance along the normal Z-direction. However, for the transverse lateral forces along X and Y, we observed that beyond the third tool speed level, the Stewart platform–based isolator provided superior attenuation, followed by the conventional isolator platform.

The computed force RMS, transmissibility, and insertion loss for the isolator platforms

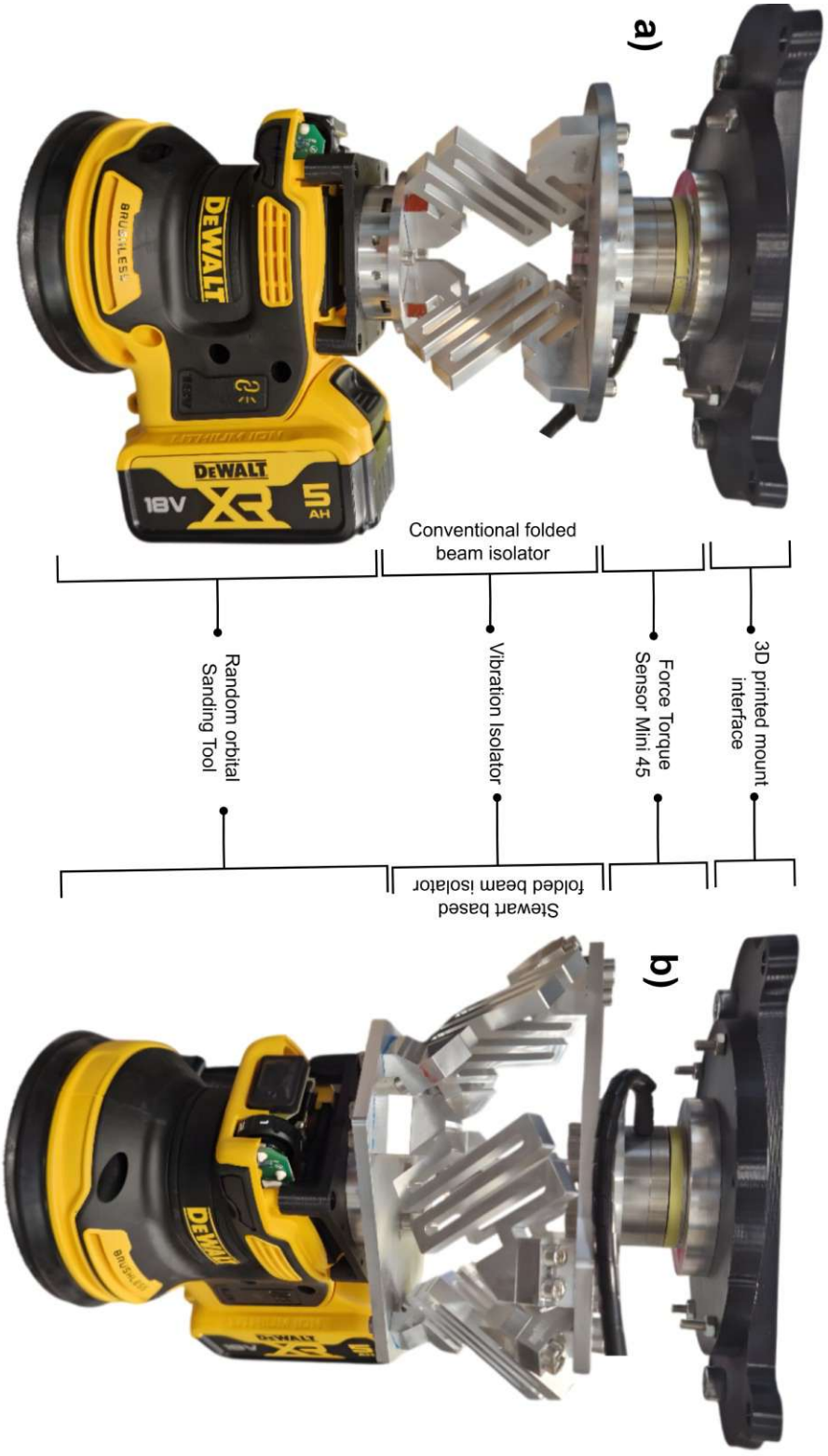

Figure 10.7: Assembled Sanding Tool Interface along with the Isolator, a) With the Conventional Isolator Platform, b) With the Stewart-based Isolator Platform.

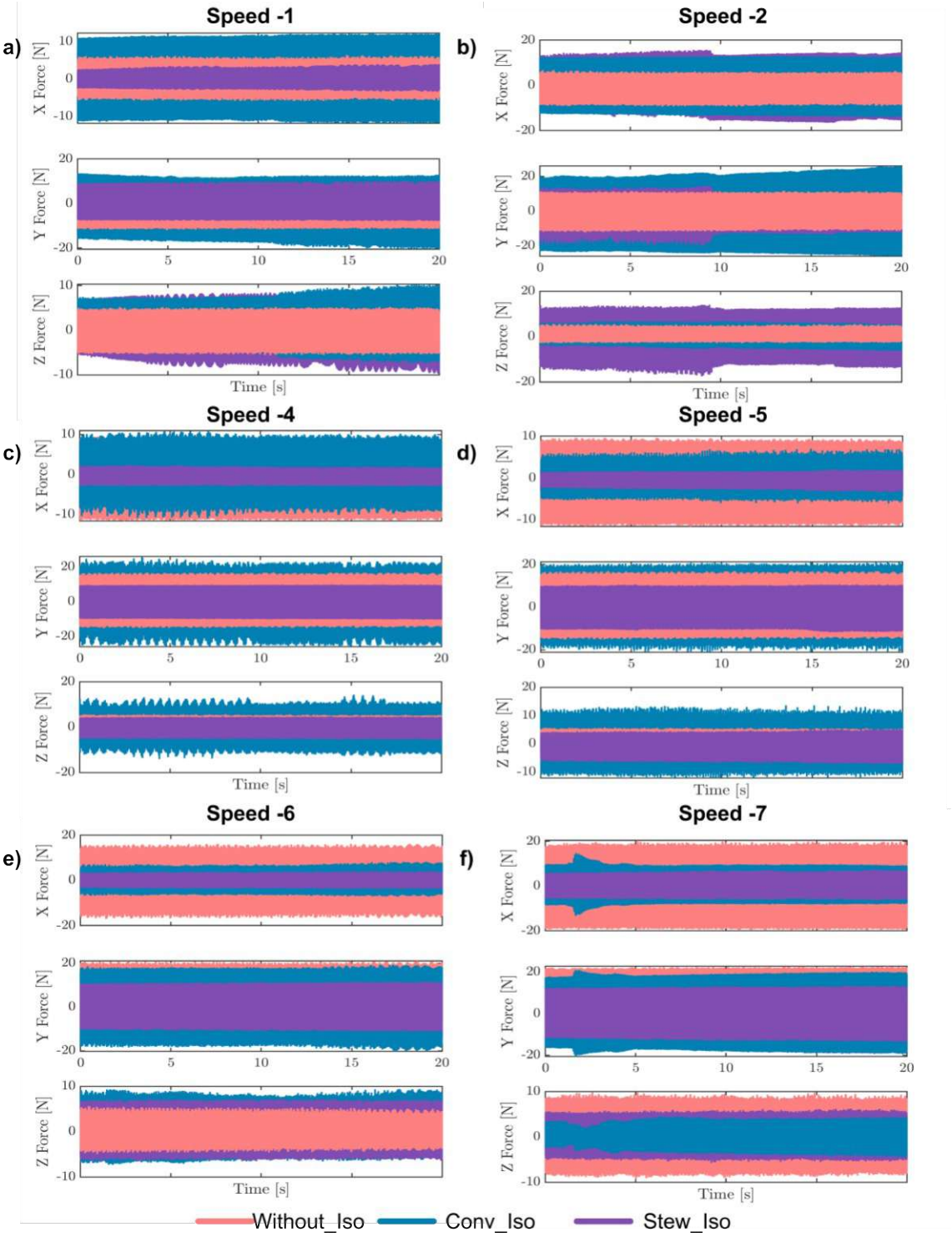

Figure 10.8: Force–time analysis across the entire tool speed range. Here, `Without_Iso` denotes the tool connected without an isolator, `Conv_Iso` denotes the tool attached to the conventional isolator, and `Stew_Iso` specifies the tool connected with the Stewart-based isolator. Subfigures (a)–(e) show the force output for each specific speed.

are presented in Table 10.1 (comparison between no isolator vs. conventional isolator) and Table 10.2 (comparison between no isolator vs. Stewart platform isolator) across the complete tool speed domain.

Speed	Axis	No Iso			Conventional Iso			T_{conv}	IL [dB]	Isolation [%]
		Mean [N]	RMS [N]	Max [N]	Mean [N]	RMS [N]	Max [N]	(linear)		
1	X	-0.034	2.966	6.384	0.027	7.937	12.204	2.676	8.55	-167.57 {outlier}
1	Y	0.001	5.413	11.911	0.049	10.393	20.427	1.920	5.67	-92.00
1	Z	0.060	2.465	5.628	0.098	4.106	10.295	1.666	4.43	-66.58
2	X	-0.022	4.646	9.427	0.052	9.229	13.980	1.987	5.96	-98.66
2	Y	0.022	6.427	12.222	0.017	15.641	26.070	2.434	7.73	-143.38 {outlier}
2	Z	0.045	1.841	5.649	0.109	3.503	6.848	1.903	5.59	-90.31
3	X	-0.045	4.662	8.155	-0.010	6.805	12.258	1.460	3.28	-45.95
3	Y	0.037	6.937	12.938	-0.430	22.424	34.749	3.232	10.19	-223.24 {outlier}
3	Z	0.071	1.947	4.263	0.189	5.741	11.064	2.949	9.39	-194.86 {outlier}
4	X	0.008	7.131	11.648	-0.092	5.708	11.040	0.801	-1.93	19.95
4	Y	0.099	8.946	16.912	0.067	12.162	26.031	1.360	2.67	-35.96
4	Z	0.074	2.417	5.744	-0.020	5.811	14.301	2.404	7.62	-140.40 {outlier}
5	X	0.008	7.131	11.648	0.019	2.794	7.012	0.392	-8.14	60.82
5	Y	0.099	8.946	16.912	0.276	12.309	21.117	1.376	2.77	-37.59
5	Z	0.074	2.417	5.744	-0.482	5.631	13.595	2.329	7.35	-132.94 {outlier}
6	X	0.018	9.685	17.073	-0.085	3.965	8.283	0.409	-7.76	59.06
6	Y	0.061	11.104	21.016	-0.102	11.722	20.171	1.056	0.47	-5.57
6	Z	0.102	2.819	5.624	0.196	4.280	9.397	1.518	3.63	-51.81
7	X	0.014	12.946	20.325	0.099	6.372	14.765	0.492	-6.16	50.78
7	Y	0.066	12.962	22.763	-0.041	13.645	20.956	1.053	0.45	-5.27
7	Z	0.084	6.015	9.942	0.025	2.273	4.512	0.378	-8.45	62.22

Note: Rows marked with {outlier} indicate outlier operating points (Speed 2–3) with atypically large errors; interpret isolation metrics there with caution.

Table 10.1: Mean, RMS, Max and Isolation (No Isolator vs. Conventional Isolator). Isolation is amplitude reduction: Isolation $= 100(1 - T)$. Color applies only to the Isolation column; values $< -100\%$ are flagged as {outlier}.

From these metrics, an important observation is that the raw forces (RMS and maximum) in the no-isolator case increased steadily with tool speed, which agrees with the expected growth in vibrational energy. When isolators were introduced, their effectiveness was found to be anisotropic, with isolation performance varying across axes and exhibiting speed-dependent dynamic behaviour.

Scenario I: Conventional Isolator Trends (Table 10.1)

1. **Amplification at Low Speeds:** With this isolator, we observed that at low speed rates (1–3), the conventional isolator amplifies vibrations rather than attenuating them. For Speed 1, along all three principal axes, the percentage isolation values are highly negative ($-167.57\,\%$, $-92\,\%$, $-66.58\,\%$), indicating that transmissibility is significantly greater than one. This behaviour is indicative of the isolator being in the stiffness-controlled regime, which is below the resonance frequency, where input forces are transmitted more efficiently, sometimes even leading to amplification of force signals.

2. **Outliers and Instabilities:** At low tool speeds (2–3), particularly along the Y- and Z-axes, extreme amplification values were observed (e.g., -223.214%, -194.86%), which were flagged as outliers. These anomalies are likely associated with resonance crossings, where the excitation frequency coincides with or approaches the isolator's natural frequency. Under such conditions, constructive interaction between excitation and system dynamics leads to uncontrolled growth in force transmission. The main causes of this behaviour will be discussed further.
3. **Improved Isolation at Higher Speeds:** From Speed 4 onward, isolation begins to show up and improve, mainly from the X axis. At Speed 5, isolation from this isolator reached around 60% with a (-8.14 dB) and in Speed 6, it also reached 59.06% with a (-7.76 dB). The isolator is entering its inertia-controlled regime, where mass dominates and effective isolation becomes possible.
4. **Anisotropy of Performance:** Even at higher speeds, the Y and Z axes exhibit less consistent isolation. At the highest speed (7), isolation is highly effective on the X-axis with -6.16 dB, corresponding to a percentage isolation just above 50%. Along the Z-axis, the highest observed isolation reaches 62.22% with -8.45 dB attenuation, whereas performance along the Y-axis is poor at -5.27% and 0.45 dB. The observed variation indicates axis-dependent transmissibility, as discussed in Chapter 8 under the limitations of conventional isolator design geometry, where a strong force and stiffness imbalance occurs when load is applied in specific transverse directions.

Scenario II: Stewart-Based Isolator Trends (Table 10.2)

1. **Superior Stability and Control:** Unlike the conventional isolator, the Stewart-based isolator shows less severe amplification at low speeds. At Speed 1, isolation ranged from 31.18% (-3.25 dB) to -93.75% (5.75 dB), with X and Y axes already showing partial attenuation, which is not observed in the conventional case.
2. **Reduced Outlier Magnitude:** Although some outliers still exist, such as the one at tool speed two along the Z-axis (-351.95%, 13.10 dB), which is not representative of standard amplification, the occurrence of outliers is less widespread compared to the conventional isolator, as observed at the first three lower tool speeds. The reduced occurrence of outliers suggests better stiffness and broader operational stability.
3. **High-Frequency Performance:** From Speed 4 onwards, the Stewart isolator consistently achieves higher positive isolation values. At Speed 4, the X-axis exhibits an attenuation of $-13.10\,\mathrm{dB}$, corresponding to 77.88% isolation. Speeds 5–7 show pronounced attenuation, with Speed 5 yielding the highest isolation values along the lateral X- and Y-axes. In particular, the X-axis demonstrates the strongest attenuation at $-14.38\,\mathrm{dB}$ (80.89% isolation). These results reflect effective control

Speed	Axis	No Iso			Stewart Iso			T_{stew}	IL [dB]	Isolation [%]
		Mean [N]	RMS [N]	Max [N]	Mean [N]	RMS [N]	Max [N]	(linear)		
1	X	-0.034	2.966	6.384	-0.007	2.041	3.963	0.688	-3.25	31.18
1	Y	0.001	5.413	11.911	-0.004	6.061	10.077	1.120	0.98	-11.96
1	Z	0.060	2.465	5.628	0.060	4.776	9.762	1.938	5.75	-93.75
2	X	-0.022	4.646	9.427	-0.006	9.508	16.602	2.047	6.22	-104.67 {outlier}
2	Y	0.022	6.427	12.222	0.000	8.271	20.064	1.287	2.19	-28.71
2	Z	0.045	1.841	5.649	0.036	8.319	17.538	4.520	13.10	-351.95 {outlier}
3	X	-0.045	4.662	8.155	0.162	5.886	9.744	1.263	2.03	-26.26
3	Y	0.037	6.937	12.938	-0.117	7.648	11.602	1.102	0.85	-10.24
3	Z	0.071	1.947	4.263	-0.176	5.633	9.272	2.893	9.23	-189.30 {outlier}
4	X	0.008	7.131	11.648	0.032	1.577	3.011	0.221	-13.10	77.88
4	Y	0.099	8.946	16.912	-0.034	6.927	10.406	0.774	-2.22	22.57
4	Z	0.074	2.417	5.744	0.115	3.240	5.621	1.340	2.54	-34.03
5	X	0.008	7.131	11.648	0.010	1.363	3.455	0.191	-14.38	80.89
5	Y	0.099	8.946	16.912	-0.025	7.123	11.816	0.796	-1.98	20.38
5	Z	0.074	2.417	5.744	0.117	3.672	7.299	1.519	3.63	-51.90
6	X	0.018	9.685	17.073	0.007	2.354	4.180	0.243	-12.29	75.70
6	Y	0.061	11.104	21.016	-0.007	7.437	11.780	0.670	-3.48	33.02
6	Z	0.102	2.819	5.624	0.021	4.191	7.442	1.487	3.44	-48.65
7	X	0.014	12.946	20.325	0.006	4.113	7.429	0.318	-9.96	68.23
7	Y	0.066	12.962	22.763	-0.030	8.560	13.800	0.660	-3.60	33.96
7	Z	0.084	6.015	9.942	0.091	3.457	6.246	0.575	-4.81	42.52

Note: Rows marked with {outlier} indicate outlier operating points (Speed 2–3) with atypically large errors; interpret isolation metrics there with caution.

Table 10.2: Mean, RMS, Max and Isolation (No Isolator vs. Stewart Isolator). Isolation is amplitude reduction: Isolation $= 100(1 - T)$. Color applies only to the Isolation column; values $< -100\%$ are flagged as {outlier}.

in the inertia-dominated region, where the Stewart configuration provides superior stiffness distribution and internal structural damping control across multiple axes.

4. **Multi-Axis Robustness:** Compared to the conventional isolator, the Stewart system demonstrates a more balanced isolation performance across all three principal directions at higher speeds. Although some negative isolation persists on the Y-axis at Speeds 6 and 7, with values of -5.83% and -13.93%, these are significantly less severe than the large amplifications observed in the conventional isolator.

The observed results indicate that the Stewart-based isolator provides more isotropic vibration suppression, which is critical for applications requiring multi-directional vibration mitigation.

10.3 Comparative Evaluation between the Isolator Platforms

The following points summarise the comparative evaluation between the conventional folded-beam isolator and the Stewart-based isolator under the zero-orientation experi-

mental setup:

- **Amplification Regimes:** The results clearly demonstrate that both isolators exhibit amplification of vibrations at low tool speeds (1–3). However, the Stewart-based isolator shows a less severe amplification compared to the conventional design and demonstrates an earlier onset of attenuation. The improved performance reflects the inherent six-degree-of-freedom isolation capability, which provides better stiffness distribution and internal damping characteristics.
- **Outlier Behavior:** The conventional isolator exhibited several severe amplification outliers, particularly in the low-speed regime. In contrast, the Stewart-based isolator, while not entirely immune to amplification, contained the effects more effectively, with the most significant outlier observed along the Z-axis at speed 2. One probable reason for this anomaly is the use of 3D-printed components sandwiched with metallic parts (Figure 10.9), combined with the weight of the 5 Ah lithium-ion battery pack.

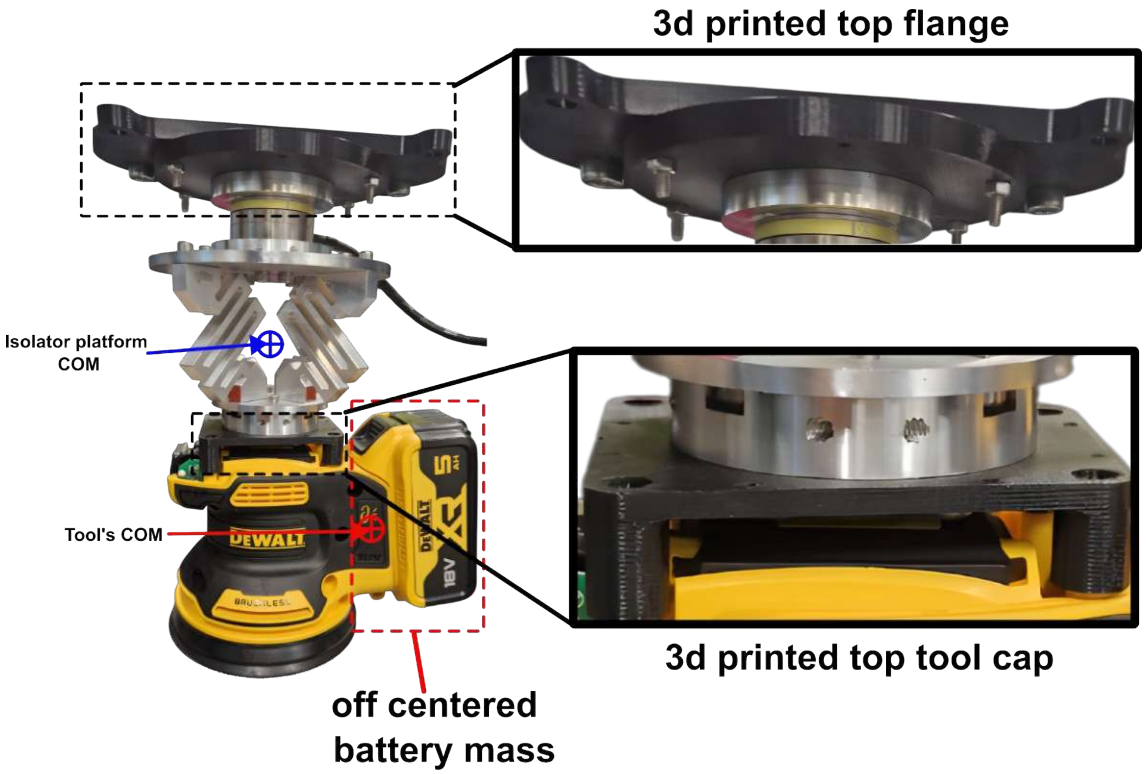

Figure 10.9: 3D-printed mountings and the heavy mass battery pack installed in the End effector of the tool.

The flexible nature of the 3D-printed parts, which differ in structural and material properties from the initially simulated ERGAL alloy design, introduced unwanted compliance. Additionally, the actual tool's centre of mass (COM) was misaligned

with that of the isolator due to the concentrated weight of the battery pack. This misalignment may have caused coupling of axial forces, which the conventional isolator's geometric configuration is poorly suited to handle. At higher speeds, however, the influence of the 3D-printed parts diminished, and fewer anomalies were observed.

- **High-Speed Performance:** At higher tool speeds (4–7), the Stewart-based isolator demonstrated significantly more consistent and effective vibration attenuation, achieving isolation levels above 60% across multiple axes. In contrast, the conventional isolator produced mixed results. For instance, at speed 7, it achieved approximately 50% isolation (-6.16 dB) along the X-axis, but simultaneously amplified vibrations along the Y-axis (-5%, 0.45 dB). This discrepancy arises from the structural design of the conventional isolator, where lateral force application leads to unequal load distribution across the four folded beams.
- **Directional Dependence:** The Stewart-based isolator exhibited a more balanced isolation performance across all three principal axes. This characteristic is particularly critical for the intended application, where the end-effector is mounted on a 6-DOF robotic arm and experiences vibrations propagating in multiple directions. In contrast, the conventional isolator exhibited a directional bias, which degraded its overall performance. Therefore, the Stewart platform emerges as the most suitable choice for the present study, offering effective multi-axis vibration suppression, stability over a wide speed range, and predictable high-frequency isolation performance.

10.4 Final Experimental Summary

Synthesising the experimental tests and results, it is evident that the designed isolators perform **more effectively at higher tool speeds**. In particular, the **Stewart-based isolator** proves to be the most suitable passive isolator platform for the end-effector interface. It consistently outperforms the conventional isolator by offering higher percentages of isolation, improved multi-degree-of-freedom performance, and more balanced directional response. Furthermore, its compact and robust design demonstrates superior dynamic stability. In contrast, the conventional isolator is more susceptible to severe resonance-driven amplification in the low- to mid-frequency ranges and exhibits strong axis-dependent behaviour.

These findings reinforce that while conventional isolators may still hold relevance for simple, single-axis vibration applications, the Stewart-based isolator provides research-grade vibration suppression and represents a more reliable choice for the current study.

Overall, the experimental metrics clearly position the **Stewart isolator as an innovative and economically viable solution** in vibration isolation technology.

11 Conclusion and Future Research Directions

11.1 Conclusion

This work provides new insights into the vibrational analysis of a commercial random orbital sanding tool by experimentally determining its excitation frequency harmonics across the working quadrants (0°, 45°, and 90°), as presented in Chapter 5. Building on these results, Chapter 6 introduces an initial end-effector interface model capable of accommodating the sanding tool, thereby laying the foundation for the final prototype design. Chapter 7 demonstrates, through both analytical and simulation studies, that the nonlinear stiffness characteristics of folded-beam elements make them suitable as the fundamental unit elements in the vibration isolator design. Consequently, Chapters 8 and 9 present the detailed design and modelling of two isolator concepts, together with their comparative performance evaluations, which were later validated through machined prototypes in Chapter 10. Specifically, two passive isolator platforms were developed in this thesis:

1. A conventional isolator platform, and
2. A Stewart-based isolator platform.

Both platforms were designed to hold asymmetric multi-folded beam flexures, which acted as the unit isolator elements. This work forms part of the larger EU-funded *MAGICIAN* project [12]. The project aims to develop modular and novel automation solutions for defect handling and reworking tasks, contributing to safer manufacturing processes.

The core objective of this study was to develop a passive, low-cost, and robust module that could be installed on a robotic arm performing reworking operations. The isolator ensures that disturbances generated by the tool do not affect the robot's trajectory control while enabling consistent real-time force monitoring. All these operations must be carried out smoothly, without interference from tool vibrations. The need for vibration-free operation and reliable force monitoring formed the guiding motivation and foundation of this research.

11.1.1 Main Aspects and Results

1. As discussed in Chapter 1, the motivation for this research stemmed from the vibratory dynamics of oscillatory finishing tools. In general manual operation, such vibrations expose workers to "Hand–Arm Vibration Syndrome," which negatively affects both physical and psychological health. This concern prompted the shift towards automated reworking solutions, one of the key criteria of the EU project *MAGICIAN*, as outlined in Chapter 2. Significantly, the project criteria extend beyond automation to the creation of a customised end-effector reworking tool interface, enabling more effective treatment of the characterised defects in automobile body parts. The first two chapters, therefore, provided the foundation upon which the present study has been developed.
2. Chapter 3 presented a thorough state-of-the-art review of both research and commercial automated robotic secondary finishing strategies and methods. These were investigated in terms of software (control approaches) as well as hardware, particularly the design of custom end-effectors and automation modules used in manufacturing. Although automation has been widely adopted since the mid-20th century, particularly in heavy industrial environments, its application to secondary machining processes such as finishing remains limited. A comprehensive literature survey revealed that while tailored solutions exist, only a few effectively address vibration control at the end-effector level. The findings highlighted an underexplored area: the development of practical, hardware-based solutions for isolating vibrations generated by finishing tools.
3. Building on the defined motivation to mitigate unnecessary vibrations from oscillating tools through the design of an isolation platform, Chapter 4 presented the fundamental science of vibration, including its characteristics, parameters, and control methods. A detailed review of existing approaches identified the random orbital sanding tool as the most suitable candidate for the present use case. Using a six-axis force–torque sensor, the vibrational characteristics of this tool were analysed, and its dominant frequency ranges were identified under defined orientations, as described in Chapter 5.
4. Once the tool's vibrational profile was understood, we designed an initial attachment interface for a DOOSAN H2515 collaborative 6-DOF robotic arm, capable of mounting both the force-torque sensor and the tool (Chapter 6). A CAD model was developed, and a metal prototype of the interface was fabricated, marking the halfway point of the project.
5. The next step, addressed in Chapter 7, was to determine an appropriate isolation approach. Our design constraints required a passive, robust, and economical solution. Given the nonlinear behaviour of the tool dynamics, conventional linear passive

elements (springs, dampers) were insufficient. We instead drew inspiration from folded beam springs, used at both macroscopic scales (e.g., space applications) and microscopic scales (MEMS technologies). Their nonlinear stiffness and geometric properties make them suitable for vibration isolation. After careful analysis of their structural and modal characteristics, folded beam elements were identified as an ideal solution for our isolator.

6. Based on prior implementations of folded beam structures, an initial conventional isolator platform was modelled with four folded beams equally distributed to provide isolation within the required frequency band. Modal analysis and optimisation studies in Chapter 8 revealed that a multi-folded beam configuration outperformed the single-beam model, leading to an improved design.
7. However, limitations in the conventional isolator design were observed, remarkably anisotropic behaviour under transverse loads, leading to uneven load distribution. To overcome this, we investigated a Stewart-platform-based isolator (Chapter 9). Its 6-DOF structure, comprising three pairs of folded beams, provides robust isolation across all translational and rotational directions. Initial design calculations and modal analyses confirmed the design's suitability for the task.
8. Finally, prototypes of both the conventional and Stewart-based isolators were fabricated and tested under real-world environmental conditions. Their performance was evaluated by attaching the tool and collecting experimental data. The results presented in Chapter 10 show that both platforms effectively attenuate high-frequency vibrations, with the Stewart-based isolator outperforming the conventional design, particularly at higher operating speeds.

Overall, this work successfully designed and modelled isolator platforms capable of attenuating dominant tool vibrations, thereby enabling smooth finishing and reworking operations. The isolators ensured stable force feedback and robust trajectory control for the robotic arm without interference. However, a subset of the larger *MAGICIAN* project, the outcomes of this study provide valuable insights and practical solutions that contribute to safer, more efficient, and more reliable manufacturing processes.

11.2 Future Research Directions

- **Implementing damping elements:** In the current isolator designs, damping elements were not included, and the system relied only on the internal structural damping properties of ERGAL-70 (the material used for the folded beam elements). Future work could involve the integration of specialised damping materials, such as Sorbothane, which can absorb vibration energy across a wide frequency range

($10\ Hz\ -\ 30,000\ Hz$), attenuating up to 50% of the vibration energy. Other polymeric damping materials, such as rubber, could also be investigated. These damping layers could be inserted between the span and connector beams of the folded beam structures, particularly at the rounded edges, as shown in Figure 11.1.

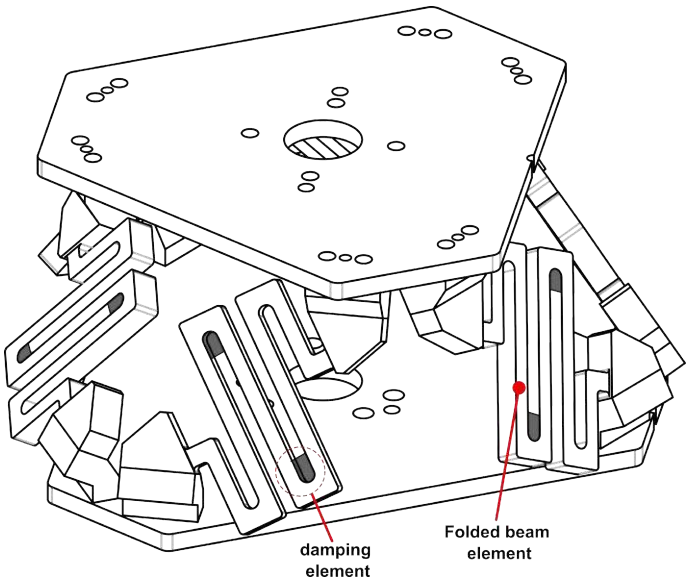

Figure 11.1: Stewart-based folded beam isolator - where the folded beams were equipped with the damping elements.

- **Conducting experiments in other tool orientations:** Due to time limitations, testing was only conducted at selected tool orientations (45° and 90°), as presented in Chapter 5. To fully understand the multi-axial performance of the isolator, future experiments should cover a broader range of tool orientations. Additionally, testing the isolator directly on the robotic arm during actual reworking operations will provide valuable insights into whether the inclusion of the isolator is genuinely beneficial. These tests should be performed with fully machined metal components, without any 3D-printed parts, to achieve a more realistic evaluation of the isolator's performance and isolation percentage. Additionally, the data collection interval shall be maintained at a longer duration to assess the force behaviour trends in each principal axis accurately.
- **Experimenting with other folded beam forms:** It has been established that folded beam elements exhibit nonlinear stiffness characteristics, and geometric modifications significantly influence their fundamental frequencies. Future studies should involve conducting static and modal analyses, along with analytical calculations, to identify geometrical variations that may outperform the current design. Some examples of alternative folded beam configurations are shown in Figure 11.2, which could be explored for improved performance.
- **Model upgrades:** The prototype revealed that assembling the isolator was time-

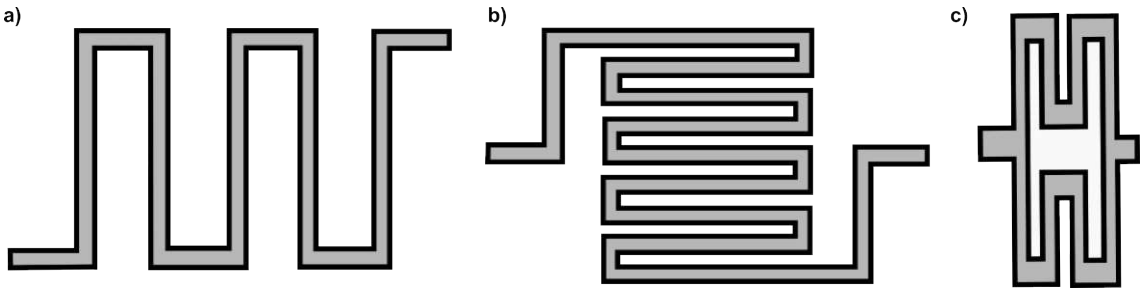

Figure 11.2: Different types of Folded beam Structures: a) Horizontal full-length folded beam Spring, b) Rotated Serpentine Spring, c) Closed loop folded beam Spring.

consuming, and attaching it to the sanding tool was not straightforward. Future versions should focus on simplifying installation and removal. Possible design improvements include quick shaft collar clamps for easy mounting and dismounting, as well as electrically actuated auto-clamping systems.

- **Extension of current research to other domains:** The Stewart-based folded beam isolator platform developed in this study is compact, robust, and entirely passive. These characteristics suggest its potential applications beyond the automotive sector. For instance, it could be adapted for space applications such as isolating reaction wheel mechanisms or supporting sensitive optical instruments like space telescopes in Figure 11.3. It may also be applied to space robotic arms. With appropriate tuning and parameter optimisation, the Stewart-based folded beam isolator platform could serve as an effective solution for micro-vibration isolation in satellites and spacecraft.

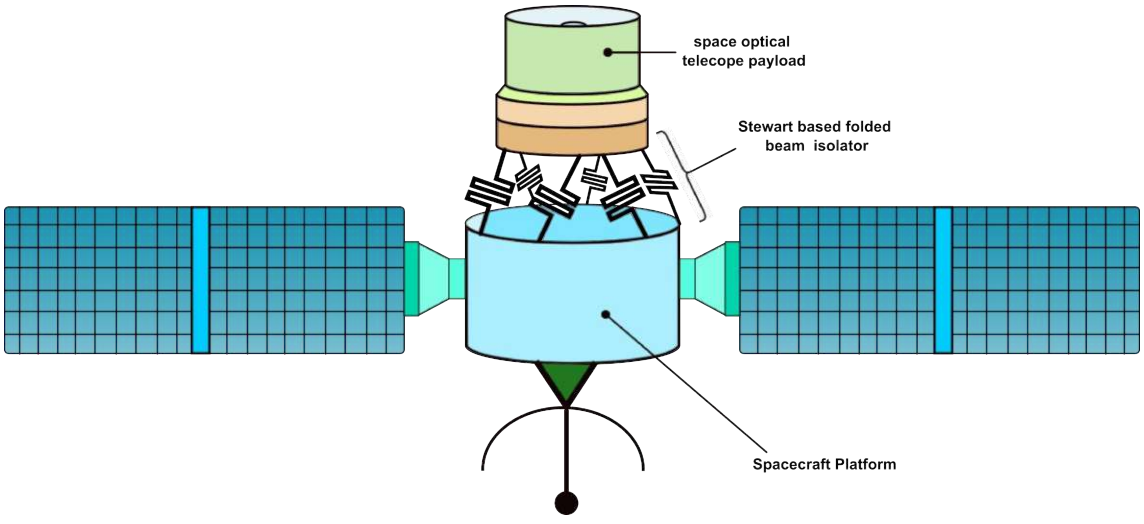

Figure 11.3: Spacecraft with a Stewart-based folded beam isolator platform carrying an optical payload.

With these final results and respective insights, followed by future directions, the present study on the design and modelling of a passive vibration isolation end-effector

tool for reworking operations in the automotive sector is brought to a close. While this work contributes only a small step within the vast domain of passive vibration isolators, it offers valuable insights into design methods and concepts that led to the development of a working prototype. As with all research, much remains to be explored and improved, particularly in finding more effective applications and reducing undesired vibrations. In this sense, the present work represents a modest but meaningful contribution—a small yet significant step within the vast landscape of innovative solutions.

References

[1] Mikell P. Groover. *Fundamentals of Modern Manufacturing: Materials, Processes, and Systems*. John Wiley & Sons, 2010.

[2] Stephen Malkin and Changsheng Guo. *Grinding Technology: Theory and Application of Machining with Abrasives*. Industrial Press Inc., 2008.

[3] Jegatheswaran Ratnasingam. "Sanding Process". In: *Furniture Manufacturing: A Production Engineering Approach*. Singapore: Springer Singapore, 2022, pp. 79–88.

[4] Robert G. Radwin et al. "Vibration exposure for selected power hand tools used in automobile assembly". In: *American Industrial Hygiene Association Journal* 51.9 (1990), pp. 510–518.

[5] M. J. Griffin et al. *Hand–arm vibration: Good practice guide (Version 7.7, 26 May 2006)*. Institute of Sound, Vibration Research, University of Southampton; Health, and Safety Laboratory; BGIA; INRS; HSE. 2006.

[6] European Union. *Directive 2002/44/EC on the minimum health and safety requirements regarding the exposure of workers to the risks arising from physical agents (vibration)*. Official Journal of the European Communities. June 25, 2002. 2002.

[7] S. Bezanson et al. "Exploring psychological impact of hand-arm vibration syndrome (HAVS)". In: *Occupational Medicine* (2025), kqae138.

[8] KML Occupational Health. *Hand-Arm Vibration Syndrome (HAVS)*. Accessed: 2025-07-18. 2025. URL: https://www.kmloh.com/hand-arm-vibration-act-now/.

[9] Raquel Nieto-Álvarez et al. "Proposal of combined noise and hand-arm vibration index for occupational exposure: application to a study case in the olive sector". In: *International Journal of Environmental Research and Public Health* 19.21 (2022), p. 14345.

[10] Norton Abrasives. *Take a deep breath, our article on car body shop dust is here*. Accessed: 2025-07-18. Mar. 2019. URL: https://www.nortonabrasives.com/en-gb/resources/expertise/take-deep-breath-our-article-car-body-shop-dust-here.

[11] European Environment Agency. *Occupational exposure and respiratory disease. In Beating chronic respiratory disease: The role of Europe's environment.* Accessed: 2025-07-18. Nov. 2024. URL: https://www.eea.europa.eu/en/analysis/publications/beating-chronic-respiratory-disease/occupational-exposure-and-respiratory-disease.

[12] European Commission. *iMmersive leArninG for ImperfeCtion detectIon and repAir through human-robot interactioN (MAGICIAN).* Horizon Europe Project Grant No. 101120731 (2023–2027). 2023. URL: https://cordis.europa.eu/project/id/101120731.

[13] MAGICIAN Project. *iMmersive leArninG for ImperfeCtion detectIon and repAir through human-robot interactioN (MAGICIAN) [Website].* European Union Horizon Europe. Accessed: 2025-07-19. 2025. URL: https://www.magician-project.eu/.

[14] Mordor Intelligence. *Global robotics market – Growth, trends, and forecast (2020–2026).* Market Report. 2020. URL: https://www.mordorintelligence.com.

[15] MarketsandMarkets. *Defect detection market by component, application, vertical, and region – Global forecast to 2026.* Market Report. 2021. URL: https://www.marketsandmarkets.com.

[16] Research and Markets. *Artificial intelligence in manufacturing market – Global forecast to 2027.* Market Report. 2022. URL: https://www.researchandmarkets.com.

[17] J. Leopold et al. "New developments in fast 3D-surface quality control". In: *Measurement* 33.2 (2003), pp. 179–187. DOI: 10.1016/S0263-2241(02)00056-8.

[18] W. J. Wills-Moren and T. Wilson. "The Design and Manufacture of a Large CNC Grinding Machine for Off-Axis Mirror Segments". In: *CIRP Annals – Manufacturing Technology* 38.1 (1989), pp. 529–532. DOI: 10.1016/S0007-8506(07)62761-9.

[19] CompositesWorld. *Automating Wind Blade Manufacture.* n.d. URL: https://www.compositesworld.com/articles/automating-wind-blade-manufacture (visited on 07/21/2025).

[20] Francesco Leali et al. "A Workcell Calibration Method for Enhancing Accuracy in Robot Machining of Aerospace Parts". In: *The International Journal of Advanced Manufacturing Technology* 85.1 (2016), pp. 47–55. DOI: 10.1007/s00170-014-6025-y.

[21] Alexander Klimchik et al. "Efficiency Evaluation of Robots in Machining Applications Using Industrial Performance Measure". In: *Robotics and Computer-Integrated Manufacturing* 48 (2017), pp. 12–29.

[22] Fabrizio Vicentini. “Collaborative Robotics: A Survey”. In: *Journal of Mechanical Design* 143.4 (2021), p. 040802. DOI: 10.1115/1.4049237.

[23] Snehal Kakade et al. “Applications of Collaborative Robots in Agile Manufacturing: A Review”. In: *Robotic Systems and Applications* 3.1 (2023), pp. 59–83. DOI: 10.1007/s43553-023-00047-0.

[24] Ewan Matheson et al. “Human–Robot Collaboration in Manufacturing Applications: A Review”. In: *Robotics* 8.4 (2019), p. 100. DOI: 10.3390/robotics8040100.

[25] Alexander Konstant et al. “Human–Robot Collaboration With a Corrective Shared Controlled Robot in a Sanding Task”. In: *Human Factors* 67.3 (2025), pp. 246–263.

[26] Xin Wang et al. “Advance on Surface Finishing Technology of Precision Bearing Cylindrical Rollers”. In: *The International Journal of Advanced Manufacturing Technology* 131.5 (2024), pp. 2341–2363.

[27] Xiaoxia Ke et al. “Review on Robot-Assisted Polishing: Status and Future Trends”. In: *Robotics and Computer-Integrated Manufacturing* 80 (2023), p. 102482.

[28] Dong Zhu et al. “Robotic Grinding of Complex Components: A Step Towards Efficient and Intelligent Machining–Challenges, Solutions, and Applications”. In: *Robotics and Computer-Integrated Manufacturing* 65 (2020), p. 101908.

[29] Qing Xie et al. “Adaptive Impedance Control for Robotic Polishing with an Intelligent Digital Compliant Grinder”. In: *International Conference on Intelligent Robotics and Applications*. Springer International Publishing, 2019, pp. 482–494.

[30] Yao Dong et al. “Contact Force Detection and Control for Robotic Polishing Based on Joint Torque Sensors”. In: *The International Journal of Advanced Manufacturing Technology* 107.5 (2020), pp. 2745–2756.

[31] Ting Zhang et al. “An Adaptive Sliding-Mode Iterative Constant-Force Control Method for Robotic Belt Grinding Based on a One-Dimensional Force Sensor”. In: *Sensors* 19.7 (2019), p. 1635.

[32] Hossam Wahballa et al. “Experimental Study of Robotic Polishing Process for Complex Violin Surface”. In: *Machines* 11.2 (2023), p. 147. DOI: 10.3390/machines11020147.

[33] Nicola Pedrocchi et al. “Design of Fuzzy Logic Controller of Industrial Robot for Roughing the Uppers of Fashion Shoes”. In: *The International Journal of Advanced Manufacturing Technology* 77.5 (2015), pp. 939–953. DOI: 10.1007/s00170-014-6483-3.

[34] Xiang Li et al. “Robotic Grinding and Polishing of Complex Aeroengine Blades Based on New Device Design and Variable Impedance Control”. In: *Robotics and Computer-Integrated Manufacturing* 92 (2025), p. 102875.

[35] Da Li et al. “Contact Force Plan and Control of Robotic Grinding Towards Ensuring Contour Accuracy of Curved Surfaces”. In: *International Journal of Mechanical Sciences* 227 (2022), p. 107449. DOI: 10.1016/j.ijmecsci.2022.107449.

[36] Yuan Qin et al. “Design and Analysis of a Compliant End-Effector for Robotic Polishing Using Flexible Beams”. In: *Actuators*. Vol. 11. 10. MDPI, 2022, p. 284. DOI: 10.3390/act11100284.

[37] Hao Chen et al. “Robotic Compliant Grinding of Curved Parts Based on a Designed Active Force-Controlled End-Effector with Optimized Series Elastic Component”. In: *Robotics and Computer-Integrated Manufacturing* 86 (2024), p. 102646.

[38] Yu Wei and Qingsong Xu. “Design of a New Passive End-Effector Based on Constant-Force Mechanism for Robotic Polishing”. In: *Robotics and Computer-Integrated Manufacturing* 74 (2022), p. 102278. DOI: 10.1016/j.rcim.2021.102278.

[39] Jintao Hong and Dong Wang. “Design of a Force-Controlled End-Effector with Low-Inertia Effect for Robotic Polishing Using Macro-Mini Robot Approach”. In: *Robotics and Computer-Integrated Manufacturing* 49 (2018), pp. 54–65. DOI: 10.1016/j.rcim.2017.05.011.

[40] Yanan Liu et al. “Vibration Coupling Characteristics and Grinding Force Control of an Elastic Component Grinding System”. In: *Mechanical Sciences* 15.1 (2024), pp. 123–136. DOI: 10.5194/ms-15-123-2024.

[41] Fang Chen et al. “Contact Force Control and Vibration Suppression in Robotic Polishing with a Smart End Effector”. In: *Robotics and Computer-Integrated Manufacturing* 57 (2019), pp. 391–403. DOI: 10.1016/j.rcim.2019.01.010.

[42] Zhen Yu and Hsien-I Lin. “Development of Robotic Polishing/Fettling System on Ceramic Pots”. In: *International Journal of Advanced Robotic Systems* 18.3 (2021), p. 17298814211012851. DOI: 10.1177/17298814211012851.

[43] A. Sharon et al. “High Bandwidth Force Regulation and Inertia Reduction Using a Macro/Micro Manipulator System”. In: *Proceedings of the 1988 IEEE International Conference on Robotics and Automation*. IEEE, 1988, pp. 126–132. DOI: 10.1109/ROBOT.1988.12058.

[44] Qingsong Xu. “Design of a Large-Stroke Bistable Mechanism for the Application in Constant-Force Micropositioning Stage”. In: *Journal of Mechanisms and Robotics* 9.1 (2017). DOI: 10.1115/1.4034943.

[45] Yajun Liu et al. “Design and Control of a Novel Compliant Constant-Force Gripper Based on Buckled Fixed-Guided Beams”. In: *IEEE/ASME Transactions on Mechatronics* 22.1 (2016), pp. 476–486. DOI: 10.1109/TMECH.2016.2619680.

[46] FerRobotics Compliant Robot Technology GmbH. *Active Contact Flange (ACF)*. n.d. URL: https://www.ferrobotics.com/leistungen/produkte/active-contact-flange/ (visited on 07/21/2025).

[47] ATI Industrial Automation. *Axially Compliant Finishing Tool, Model AOV 10*. n.d. URL: https://www.ati-ia.com/Products/deburr/deburring_ModelDetails.aspx?id=AOV-10 (visited on 07/21/2025).

[48] PushCorp. *Robotic Force Compliance Devices*. n.d. URL: https://pushcorp.com/productcat/robotic-force-compliance-devices/ (visited on 07/21/2025).

[49] Nordbo Robotics. *NAC S20 150 Documentation*. n.d. URL: https://workshop.nordbo-robotics.com/documentation/compensation/nac-s20-150-documentation (visited on 07/21/2025).

[50] Suhner. *SUHNER EFCm 02 Active Compliance System Modular*. n.d. URL: https://robotic-grinding.suhner.com/loesungen/endeffektoren/suhner-efcm-02/ (visited on 07/21/2025).

[51] OnRobot. *Sander Tool for Collaborative Robots — Sanding & Polishing*. n.d. URL: https://onrobot.com/en/products/onrobot-sander (visited on 07/21/2025).

[52] SCHUNK SE & Co. KG. *PCFC – Unità di Compensazione*. 2025. URL: https://schunk.com/it/it/tecnologia-di-automazione/tool-per-lavorazioni/pcfc/c/PGR_5500 (visited on 07/21/2025).

[53] PR – Intelligente Peripherien für Roboter GmbH. *Robot Z Axis Compliance Device*. n.d. URL: https://en.iprworldwide.com/category/compensation-modules/z-axis-compliance/ (visited on 07/21/2025).

[54] Bosch Rexroth Italia. *Smart Flex Effector: Robot con Sensibilità Umana*. n.d. URL: https://expertise.boschrexroth.it (visited on 07/21/2025).

[55] Bo Yao et al. "Sensorless and Adaptive Admittance Control of Industrial Robot in Physical Human–Robot Interaction". In: *Robotics and Computer-Integrated Manufacturing* 51 (2018), pp. 158–168. DOI: 10.1016/j.rcim.2017.12.005.

[56] Hermann Gattringer et al. "Design and Calibration of Robot Base Force/Torque Sensors and Their Application to Non-Collocated Admittance Control for Automated Tool Changing". In: *Sensors* 21.9 (2021), p. 2895. DOI: 10.3390/s21092895.

[57] Dong Zhu et al. "Analysis and Assessment of Robotic Belt Grinding Mechanisms by Force Modeling and Force Control Experiments". In: *Tribology International* 120 (2018), pp. 93–98. DOI: 10.1016/j.triboint.2017.12.022.

[58] S. S. Rao. *Mechanical Vibrations*. Harlow: Pearson, 2018.

[59] "Harris' Shock and Vibration Handbook". In: ed. by Cyril M. Harris and Allan G. Piersol. 5th. New York: McGraw-Hill, 2002, pp. 1025–1083.

[60] Z. Ma et al. "Recent Advances in Quasi-Zero Stiffness Vibration Isolation Systems: An Overview and Future Possibilities". In: *Machines* 10.9 (2022), p. 813. DOI: 10.3390/machines10090813.

[61] F. C. Nelson. "Vibration isolation: a review, I. Sinusoidal and random excitations". In: *Shock and Vibration* 1.5 (1994), pp. 485–493.

[62] E. E. Ungar and C. W. Dietrich. "High-frequency vibration isolation". In: *Journal of Sound and Vibration* 4.2 (1966), pp. 224–241.

[63] D. L. Margolis. "A procedure for comparing passive, active, and semi-active approaches to vibration isolation". In: *Journal of the Franklin Institute* 315.4 (1983), pp. 225–238.

[64] X. Tang and L. Zuo. "Passive, active and semi-active series tuned mass dampers". In: *Active and Passive Smart Structures and Integrated Systems 2010*. Ed. by M. N. Ghasemi-Nejhad. Vol. 7643. Proceedings of SPIE. 2010, 76432P. DOI: 10.1117/12.847830.

[65] H. Asada and N. Goldfine. "Optimal compliance design for grinding robot tool holders". In: *Proceedings of the 1985 IEEE International Conference on Robotics and Automation*. Vol. 2. IEEE. 1985, pp. 316–322.

[66] Patrick McCombe and Matt Higgins. *What's the Difference: Fine-Finish Sanders—Orbital vs. Random Orbit*. Issue 257 (Feb./Mar. 2016). Fine Homebuilding. Jan. 6, 2016. URL: https://www.finehomebuilding.com/2016/01/06/whats-the-difference-fine-finish-sanders-orbital-vs-random-orbit (visited on 09/05/2025).

[67] DeWalt. *DeWalt*. Accessed: 2025-08-02. n.d. URL: https://cee.dewalt.global/.

[68] L. Shi and B. Sun. "Modeling and optimization of vibration response characteristics of the orbital sander based on surrogate model". In: *Structural and Multidisciplinary Optimization* 57.6 (2018), pp. 2259–2271. DOI: 10.1007/s00158-018-1986-8.

[69] A. Z. A. Mazlan and Z. M. Ripin. "Active vibration control to attenuate hand-arm vibration from orbital sander: a mathematical model approach". In: *Indian Journal of Science and Technology* 8.30 (2015), pp. 1–8. DOI: 10.17485/ijst/2015/v8i30/84954.

[70] L. Shi and B. Sun. "Mathematical modeling and vibration simulation of an orbital sander". In: *Vibroengineering Procedia* 22 (2019), pp. 176–181. DOI: 10.21595/vp.2019.21027.

[71] M. Y. Cao et al. “Six-axis force/torque sensors for robotics applications: A review”. In: *IEEE Sensors Journal* 21.24 (2021), pp. 27238–27251. DOI: 10.1109/JSEN.2021.3114864.

[72] Alberobotics. *6-axis force torque sensors datasheet*. Accessed: 2025-08-02. n.d. URL: https://alberobotics.it/sensors-data-sheet.

[73] Doosan Robotics. *H2515 — Doosan Robotics*. Accessed: 2025-08-04. 2025. URL: https://www.doosanrobotics.com/en/product-solutions/product/h-series/h2515.

[74] ATI Industrial Automation. *Mini58 Force/Torque Sensor*. Accessed: 2025-08-04. 2025. URL: https://www.ati-ia.com/products/ft/ft_models.aspx?id=Mini58.

[75] International Organization for Standardization. *ISO 9409-1:2011 — Mechanical interfaces for manipulator robots – Part 1: Plates*. Geneva, Switzerland, 2011. URL: https://www.iso.org/standard/55882.html.

[76] Ruisheng Ma et al. “Inerter-based structural vibration control: A state-of-the-art review”. In: *Engineering Structures* 243 (2021), p. 112655. DOI: 10.1016/j.engstruct.2021.112655.

[77] Seungbo Kim and Rajendra Singh. “Multi-dimensional characterization of vibration isolators over a wide range of frequencies”. In: *Journal of Sound and Vibration* 245.5 (2001), pp. 877–913. DOI: 10.1006/jsvi.2001.3617.

[78] E. H. Hull. “The Use of Rubber in Vibration Isolation: Including the Case of Six Degree of Freedom Systems”. In: *Journal of Applied Mechanics* 4.3 (1937), A109–A114.

[79] P. S. Balaji and K. Karthik SelvaKumar. “Applications of nonlinearity in passive vibration control: A review”. In: *Journal of Vibration Engineering & Technologies* 9.2 (2021), pp. 183–213. DOI: 10.1007/s42417-020-00216-3.

[80] Zhaozhao Ma et al. “Recent Advances in Quasi-Zero Stiffness Vibration Isolation Systems: An Overview and Future Possibilities”. In: *Machines* 10.9 (2022), p. 813. DOI: 10.3390/machines10090813.

[81] Guirong Yan et al. “Bio-inspired vibration isolation: Methodology and design”. In: *Applied Mechanics Reviews* 73.2 (2021), p. 020801. DOI: 10.1115/1.4049946.

[82] Long Yan and Xianghong Gong. “Experimental study of vibration isolation characteristics of a geometric anti-spring isolator”. In: *Applied Sciences* 7.7 (2017), p. 711. DOI: 10.3390/app7070711.

[83] Thiem D. Le and Kyoung Kwan Ahn. “Experimental investigation of a vibration isolation system using negative stiffness structure”. In: *International Journal of Mechanical Sciences* 70 (2013), pp. 99–112. DOI: 10.1016/j.ijmecsci.2013.01.011.

[84] Liang Wu et al. “Mechanical metamaterials for full-band mechanical wave shielding”. In: *Applied Materials Today* 20 (2020), p. 100671. DOI: 10.1016/j.apmt.2020.100671.

[85] Yue Chai et al. “A novel quasi-zero-stiffness isolation platform via tunable positive and negative stiffness compensation mechanism”. In: *Nonlinear Dynamics* 112.1 (2024), pp. 101–123. DOI: 10.1007/s11071-023-08982-6.

[86] Saurabh Dalela et al. “Nonlinear static and dynamic response of a metastructure exhibiting quasi-zero-stiffness characteristics for vibration control: an experimental validation”. In: *Scientific Reports* 14.1 (2024), p. 19195. DOI: 10.1038/s41598-024-66467-5.

[87] Chunchuan Liu et al. “Recent advances in micro-vibration isolation”. In: *Mechanical Systems and Signal Processing* 56-57 (2015), pp. 55–80. DOI: 10.1016/j.ymssp.2014.10.007.

[88] Hui Ting Shi et al. “Vibration isolation methods in spacecraft: A review of current techniques”. In: *Advances in Space Research* 73.8 (2024), pp. 3993–4023. DOI: 10.1016/j.asr.2024.04.066.

[89] Chang Qin et al. “Design and optimization of the micro-vibration isolation system for large space telescope”. In: *Journal of Sound and Vibration* 482 (2020), p. 115461. DOI: 10.1016/j.jsv.2020.115461.

[90] D. Kamesh et al. “Passive vibration isolation of reaction wheel disturbances using a low frequency flexible space platform”. In: *Journal of Sound and Vibration* 331.6 (2012), pp. 1310–1330. DOI: 10.1016/j.jsv.2011.10.011.

[91] Kento Miyado et al. “Serpentine spring design technique for high sensitivity MEMS capacitive accelerometer fabricated by gold multi-layer metal technology”. In: *Japanese Journal of Applied Physics* 63.4 (2024), 04SP23. DOI: 10.35848/1347-4065/AD50E4.

[92] K. G. Sravani et al. “Role of dielectric layer and beam membrane in improving the performance of capacitive RF MEMS switches for Ka-band applications”. In: *Microsystem Technologies* 27.2 (2021), pp. 493–502. DOI: 10.1007/s00542-019-04630-2.

[93] S. Iyer et al. “Analytical modeling of cross-axis coupling in micromechanical springs”. In: *Modeling and Simulation of Microsystems (MSM’99)*. San Juan, Puerto Rico, Apr. 1999, pp. 632–635.

[94] Giuseppe Barillaro et al. “Analysis, simulation and relative performances of two kinds of serpentine springs”. In: *Journal of Micromechanics and Microengineering* 15.4 (2005), pp. 736–746. DOI: 10.1088/0960-1317/15/4/010.

[95] Stephen P. Timoshenko and James M. Gere. *Theory of Elastic Stability*. 2nd ed. Mineola, NY: Courier Corporation (Dover Publications), 2012. ISBN: 9780486472072.

[96] Dimitrios Peroulis et al. “Electromechanical considerations in developing low-voltage RF MEMS switches”. In: *IEEE Transactions on Microwave Theory and Techniques* 51.1 (2003), pp. 259–270. DOI: 10.1109/TMTT.2002.806943.

[97] D. Kamesh et al. “Modeling, design and analysis of low frequency platform for attenuating micro-vibration in spacecraft”. In: *Journal of Sound and Vibration* 329.17 (2010), pp. 3431–3450. DOI: 10.1016/j.jsv.2010.03.012.

[98] W. Zhou and D. Li. “Experimental research on a vibration isolation platform for momentum wheel assembly”. In: *Journal of Sound and Vibration* 332.5 (2013), pp. 1157–1171. DOI: 10.1016/j.jsv.2012.09.032.

[99] X. Yin et al. “Study on the micro-vibration suppression of a MnCu spring isolation platform with low stiffness and high damping”. In: *International Journal of Aeronautical and Space Sciences* 24.3 (2023), pp. 753–765. DOI: 10.1007/s42405-023-00630-y.

[100] Q. Luo et al. “Design and Modeling of Micro-vibration Isolation for Spacecraft Flywheel”. In: *Proceedings of the 2020 3rd International Conference on Mechatronics, Robotics and Automation (ICMRA)*. IEEE, 2020, pp. 12–17. DOI: 10.1109/ICMRA51221.2020.9348202.

[101] Jorge Nocedal and Stephen J. Wright. *Numerical Optimization*. 2nd. New York, NY: Springer, 2006. DOI: 10.1007/978-0-387-40065-5.

[102] PTC. *To create an optimization study*. https://support.ptc.com/help/creo/creo_pma/r11.0/usascii/simulate/simulate/opt_study.html. Accessed: August 11, 2025. n.d.

[103] Ampelmann. *About us*. https://www.ampelmann.nl/about-us. Accessed: 2025-08-13.

[104] D. Stewart. “A platform with six degrees of freedom”. In: *Proceedings of the Institution of Mechanical Engineers* 180.1 (1965), pp. 371–386.

[105] Z. He et al. “Progress of Stewart Vibration Platform in Aerospace Micro–Vibration Control”. In: *Aerospace* 9.6 (2022), p. 324. DOI: 10.3390/aerospace9060324.

[106] J. P. Merlet. “Determination of 6D workspaces of Gough-type parallel manipulator and comparison between different geometries”. In: *The International Journal of Robotics Research* 18.9 (1999), pp. 902–916.

[107] W. Zhang et al. “Stewart-inspired vibration isolation mechanisms for precision equipment: Current status and future research trend”. In: *Mechanism and Machine Theory* 214 (2025), p. 106153.

[108] C. Wang et al. “Investigation on active vibration isolation of a Stewart platform with piezoelectric actuators”. In: *Journal of Sound and Vibration* 383 (2016), pp. 1–19.

[109] T. Zhang et al. “Modeling of the bio-inspired vibration isolation platform supported by X-structures via D’Alembert’s principle of virtual power”. In: *Mechanical Systems and Signal Processing* 179 (2022), p. 109351.

[110] F. Hu and X. Jing. “A 6-DOF passive vibration isolator based on Stewart structure with X-shaped legs”. In: *Nonlinear Dynamics* 91.1 (2018), pp. 157–185.

[111] X. Wang et al. “Vibration suppression for post-capture spacecraft via a novel bio-inspired Stewart isolation system”. In: *Acta Astronautica* 168 (2020), pp. 1–22.

[112] Z. Wu et al. “A 6DOF passive vibration isolator using X-shape supporting structures”. In: *Journal of Sound and Vibration* 380 (2016), pp. 90–111.

[113] J. Tang et al. “A 6-DOF micro-vibration isolation platform based on the quasi-zero-stiffness isolator”. In: *Proceedings of the Institution of Mechanical Engineers, Part C: Journal of Mechanical Engineering Science* 235.22 (2021), pp. 6019–6035.

[114] C. Zheng et al. “Kinematics modeling and singularity analysis of a 6-DOF all-metal vibration isolator based on dual quaternions”. In: *Symmetry* 15.2 (2023), p. 562.

[115] H. M. Vu et al. “Kinematics design and statics analysis of novel 6-DOF passive vibration isolator with S-shaped legs based on Stewart platform”. In: *Journal of Vibroengineering* 26.1 (2024), pp. 66–78.

[116] N. Ciblak and H. Lipkin. “Asymmetric Cartesian stiffness for the modelling of compliant robotic systems”. In: *International Design Engineering Technical Conferences and Computers and Information in Engineering Conference*. Vol. 12860. ASME. 1994, pp. 197–204.

[117] C. Gosselin. “Stiffness mapping for parallel manipulators”. In: *IEEE Transactions on Robotics and Automation* 6.3 (1990), pp. 377–382.

[118] M. Griffis and J. Duffy. “Global stiffness modeling of a class of simple compliant couplings”. In: *Mechanism and Machine Theory* 28.2 (1993), pp. 207–224.

[119] Y. Tu et al. “Displacement Transmissibility Analysis of Stewart Platform Based SINS’s Bumper Under Base Vibration Excitation”. In: *Sensors* 25.11 (2025), p. 3434.

A List of Figures

B List of Tables

C List of Equations

D Repository and Data Availability

The source code, CAD drawings, simulation files, and supporting documentation related to this thesis are available in the following GitHub repository:

https://github.com/sriramrex/Master-Thesis

The repository is structured as follows:

- **Articles and References** – Relevant literature, scientific papers, and reference material on vibration isolation, robotics, and mechanical design.
- **Drafts and Notes** – Notes, draft chapters, and brainstorming material related to the thesis.
- **Matlab_files** – MATLAB code for modeling, simulation, optimization, and validation of passive vibration isolator designs.
- **Modal_Mass_End_effector_Spec_Sheet** – Technical specifications and datasheets for the robotic end-effector and modal mass characterization.
- **Presentations** – Progress presentations, internal reviews.
- **Technical Drawings** – CAD drawings, design schematics, and documentation of both the conventional and Stewart-based folded-beam isolator platforms.

For confidentiality reasons under the EU-funded MAGICIAN Project, certain experimental datasets and CAD models are not publicly accessible. These can be provided upon request to authorized collaborators.

E List of Abbreviations

AVC	Active vibration control
BIW	Body in white
CEE	Compliant end-effector
CNC	Computer numerical control
COM	Centre of mass
COPD	Chronic obstructive pulmonary disease
CR	Cleaning robot
DVA	Dynamic vibration absorbers
EMA	Experimental modal analysis
FEA	Finite element analysis
FOS	Factor of safety
FRF	Frequency response function
FFT	Frequency domain analysis
HAVS	Hand-arm vibration syndrome
HRC	Human-robot collaboration
HRI	Human–robot interaction
HSLDS	High static and low dynamic stiffness
MDOF	Multi degree of freedom
MEMS	Microelectromechanical systems
MLF	Multi-layer flexure
MSSM	Minimal simplified symmetric manipulator
MWA	Momentum wheel assemblies
NLP	Nonlinear programming
NSS	Negative stiffness structure
QZS	Quasi-zero-stiffness
RMS	Root mean square
RWA	Reaction wheel assemblies
SR	Sensing robot
SDOF	Single degree of freedom
SQP	Sequential quadratic programming
SSM	Simplified symmetric manipulator
SVIS	Stewart-inspired vibration isolation system
TSSM	Triangular simplified symmetric manipulator

End of Thesis